UTS UNIVERSITY OF TECHNOLOGY SYDNEY

Synthesis of wastewater sludge-derived TiO_2 and its composites for NO_x removal

by Sayed Mukit Hossain

Thesis submitted in fulfilment of the requirements for the degree of

Doctor of Philosophy

under the supervision of Prof. Hokyong Shon and Dr. Leonard Demegilio Tijing

University of Technology Sydney
Faculty of Engineering and Information Technology

January 2022

CERTIFICATE OF ORIGINAL AUTHORSHIP

I, *Sayed Mukit Hossain* declare that this thesis, is submitted in fulfilment of the requirements for the award of *Doctor of Philosophy*, in the *School of Civil and Environmental Engineering/Faculty of Engineering and IT* at the University of Technology Sydney.

This thesis is wholly my own work unless otherwise referenced or acknowledged. In addition, I certify that all information sources and literature used are indicated in the thesis.

This document has not been submitted for qualifications at any other academic institution.

This research is supported by the Australian Government Research Training Program.

Production Note:
Signature removed
prior to publication.

Signature: _____

Sayed Mukit Hossain

Date: 15/07/2022

DEDICATION

The thesis is wholeheartedly dedicated to my beloved parents, Sayed Md. Mostaque Hossain, and Kamrun Naher, who have been my source of inspiration and gave me strength when I thought of giving up, who continuously provided their moral, spiritual, emotional, and financial support.

To my brother and sisters who have encouraged me to finish this study.

Lastly, to my wife, Israt Zahan, for having my back, motivating me, and sharing the path with me.

ACKNOWLEDGEMENT

I would like to offer my heartfelt appreciation to everyone who has helped me along the way to finishing my Ph.D. thesis, which has been a long but rewarding journey.

First and foremost, I want to express my gratefulness to Prof. Hokyong Shon, my principal supervisor, for his excellent mentoring, professional guidance, encouragement, and unwavering support. I am thankful for bringing out the best in me during my Ph.D. studies. I would also like to express my appreciation to my co-supervisor, Dr. Leonard Demegilio Tijing, for his insightful remarks and constructive criticism during my research. Their constant supervision and support during my Ph.D. studies inspired me to develop as a researcher and do my best to accomplish this thesis.

Apart from my supervisors, I would like to express my gratitude to external collaborators Prof. Jong-Ho Kim and Dr. Young-Si Jun, for allowing me to use their labs and research facilities at Chonnam National University (CNU) in South Korea. I would like to express my gratitude to Hui-Ju Kang and Jong Seok Mun for their invaluable assistance throughout my study at CNU. I want to thank Prof. Akira Fujishima of Tokyo University of Science in Japan for his input on this study.

I would like to express my heartfelt appreciation to Dr. Md. Johir and Dr. Nirenkumar Pathak for their assistance in the laboratory. I would like to express my gratitude to my good colleagues Van Huy Tran, Syed Muztuza Ali, Nawshad Akther, Ralph Rolly Gonzales, Myongjun Park, Ugyen Dorji, Pema Dorji, Jiawei Ren, and Idris Ibrahim for their contributions.

I want to acknowledge the full financial support that I received from the UTS International Research Scholarship (UTS IRS) and the Higher Degree by Research Industry Scholarship to complete my Ph.D. study. Finally, I would like to express my gratitude to my parents and uncle Humayun Kabir for teaching me the value of education and hard work, ensuring the success of my academic journey, and inspiring me to achieve my aspirations and be self-sufficient. I am thankful to my wife, Israt Zahan, for her unwavering faith in my ability to accomplish my goals and her steadfast optimism despite the hardships we faced throughout my Ph.D. journey. It would not have been possible to achieve my research objectives without her help, collaboration, and drive.

LIST OF PUBLICATIONS

This list includes journal articles that have been prepared during the PhD candidature, which are either *part of or **not part of the thesis.

- ***Hossain, S.M.**; Tijing, L.; Suzuki, N.; Fujishima, A.; Kim, J.-H.; Shon, H.K. Visible light activation of photocatalysts formed from the heterojunction of sludge-generated TiO2 and g-CN towards NO removal. *Journal of Hazardous Materials* **2022**, *422*, doi:10.1016/j.jhazmat.2021.126919 **(Chapter 6)**.
- **Kim, J.-H.; **Hossain, S.M.**; Kang, H.-J.; Park, H.; Tijing, L.; Park, G.W.; Suzuki, N.; Fujishima, A.; Jun, Y.-S.; Shon, H.K., et al. Hydrophilic/Hydrophobic Silane Grafting on TiO2 Nanoparticles: Photocatalytic Paint for Atmospheric Cleaning. *Catalysts* **2021**, *11*, doi:10.3390/catal11020193.
- **Khan, T.; Bari, G.; Kang, H.-J.; Lee, T.-G.; Park, J.-W.; Hwang, H.; **Hossain, S.**; Mun, J.; Suzuki, N.; Fujishima, A., et al. Synthesis of N-Doped TiO2 for Efficient Photocatalytic Degradation of Atmospheric NOx. *Catalysts* **2021**, *11*, doi:10.3390/catal11010109.
- ***Hossain, S.M.**; Park, H.; Kang, H.J.; Mun, J.S.; Tijing, L.; Rhee, I.; Kim, J.H.; Jun, Y.S.; Shon, H.K. Synthesis and NOx removal performance of anatase S-TiO2/g-CN heterojunction formed from dye wastewater sludge. *Chemosphere* **2021**, *275*, 130020, doi:10.1016/j.chemosphere.2021.130020 **(Chapter 7)**.
- ****Hossain, S.M.**; Park, H.; Kang, H.J.; Mun, J.S.; Tijing, L.; Rhee, I.; Kim, J.H.; Jun, Y.S.; Shon, H.K. Facile synthesis and characterization of anatase TiO2/g-CN composites for enhanced photoactivity under UV-visible spectrum. *Chemosphere* **2021**, *262*, 128004, doi:10.1016/j.chemosphere.2020.128004.
- ***Hossain, S.M.**; Park, H.; Kang, H.-J.; Mun, J.S.; Tijing, L.; Rhee, I.; Kim, J.-H.; Jun, Y.-S.; Shon, H.K. Modified Hydrothermal Route for Synthesis of Photoactive Anatase TiO2/g-CN Nanotubes from Sludge Generated TiO2. *Catalysts* **2020**, *10*, doi:10.3390/catal10111350 **(Chapter 8)**.
- ***Hossain, S.M.**; Park, H.; Kang, H.-J.; Kim, J.B.; Tijing, L.; Rhee, I.; Jun, Y.-S.; Shon, H.K.; Kim, J.-H. Preparation and Characterization of Photoactive Anatase TiO2 from Algae Bloomed Surface Water. *Catalysts* **2020**, *10*, doi:10.3390/catal10040452 **(Chapter 5)**.
- ***Hossain, S.M.**; Park, M.J.; Park, H.J.; Tijing, L.; Kim, J.H.; Shon, H.K. Preparation and characterization of TiO2 generated from synthetic wastewater

using TiCl4 based coagulation/flocculation aided with Ca(OH)2. *J Environ Manage* **2019**, *250*, 109521, doi:10.1016/j.jenvman.2019.109521 **(Chapter 4)**.

- ***Hossain, S.M.**; Jun, Y.-S.; Kim, J.-H.; Shon, H.K. Photocatalytically enhanced TiO2/g-CN composites preparation and environmental applications. *Journal of the Research Institute for Catalysis* **2019**, *40*, 25 – 40 **(Chapter 2)**.

PREFACE

This doctoral thesis is prepared in a "Thesis by compilation" format according to the "Graduate Research Candidature Management, Thesis Preparation, and Submission Procedures, 2021" of the University of Technology Sydney. It comprises the articles that have been published or submitted for publication.

This thesis contains one published review paper in Chapter 2 and five original research articles in Chapters 4 through 8, all of which are published. The authorship of these works has been decided after discussion with the supervisory team.

Chapter 2 comprises the following article:

Hossain, S.M.; Jun, Y.-S.; Kim, J.-H.; Shon, H.K. Photocatalytically enhanced TiO2/g-CN composites preparation and environmental applications. *Journal of the Research Institute for Catalysis* **2019**, *40*, 25 - 40.

Chapter 4 is published in the Journal of Environmental Management:

Hossain, S.M.; Park, M.J.; Park, H.J.; Tijing, L.; Kim, J.H.; Shon, H.K. Preparation and characterization of TiO2 generated from synthetic wastewater using TiCl4 based coagulation/flocculation aided with Ca(OH)2. *J Environ Manage* **2019**, *250*, 109521, doi:10.1016/j.jenvman.2019.109521.

Chapter 5 is published in Catalysts:

Hossain, S.M.; Park, H.; Kang, H.-J.; Kim, J.B.; Tijing, L.; Rhee, I.; Jun, Y.-S.; Shon, H.K.; Kim, J.-H. Preparation and Characterization of Photoactive Anatase TiO2 from Algae Bloomed Surface Water. *Catalysts* **2020**, *10*, doi:10.3390/catal10040452.

Chapter 6 is published in the Journal of Hazardous Materials:

Hossain, S.M.; Tijing, L.; Suzuki, N.; Fujishima, A.; Kim, J.-H.; Shon, H.K. Visible light activation of photocatalysts formed from the heterojunction of sludge-generated TiO2 and g-CN towards NO removal. *Journal of Hazardous Materials* **2022**, *422*, doi:10.1016/j.jhazmat.2021.126919.

Chapter 7 is published in Chemosphere:

Hossain, S.M.; Park, H.; Kang, H.J.; Mun, J.S.; Tijing, L.; Rhee, I.; Kim, J.H.; Jun, Y.S.; Shon, H.K. Synthesis and NOx removal performance of anatase S-TiO2/g-CN heterojunction formed from dye wastewater sludge. *Chemosphere* **2021**, *275*, 130020, doi:10.1016/j.chemosphere.2021.130020.

Chapter 8 is published in Catalysts:

Hossain, S.M.; Park, H.; Kang, H.-J.; Mun, J.S.; Tijing, L.; Rhee, I.; Kim, J.-H.; Jun, Y.-S.; Shon, H.K. Modified Hydrothermal Route for Synthesis of Photoactive Anatase TiO2/g-CN Nanotubes from Sludge Generated TiO2. *Catalysts* 2020, *10*, doi:10.3390/catal10111350.

LIST OF ABBREVIATIONS

AOM	Algal organic matter
BET	Brunauer-Emmett-Teller
BJH	Barrett-Joyner-Halenda
BTSE	Biologically treated secondary effluent
CB	Conduction band
CPAM	Cationic polyacrylamide
DAF	Dissolved air floatation
DBP	Disinfection by-products
DOC	Dissolved organic carbon
DRA	Diffuse reflectance
DRS	Diffuse reflection spectroscopy
DW	Drinking water
DWW	Dye wastewater
EDX	Energy-dispersive X-ray spectroscopy
EOM	Extracellular organic matters
FTIR	Fourier-transform infrared spectroscopy
FWHM	Full width at half maximum
IOM	Intercellular organic matters
LMW	Low molecular weight
MB	Methylene blue
MO	Methyl orange
MW	Molecular weight
NF	Nanofiber
NHE	Normal hydrogen electrode
NOM	Natural organic matter
NP	Nanoparticle
NTU	Nephelometric Turbidity unit
PAC	Poly aluminium chloride
PAFS	Polymeric aluminium ferric sulfate
PATC	Polyaluminium titanium silicate chloride
PFC	Polyferric chloride
PFS	Polyferric sulfate

PFZS	Polymeric ferric zinc sulfate
PL	Photoluminescence
PPAC	Polymeric phosphate aluminium chloride
PPW	Printing paper wastewater
PTC	Polytitanium chloride
PVP	Poly vinylpyrrolidone
RhB	Rhodamine B
SEM	Scanning electron microscope
SWW	Synthetic wastewater
TBA	Tert butyl alcohol
TBT	Tetrabutyl titanate
TEM	Transmission electron microscopy
TNBT	Titanium (IV) n-butoxide
TNT	Titania nanotube
TP	Total phosphate
TXC	Titanium xerogel
UV	Ultraviolet
VB	Valency band
XPS	X-ray photoelectron spectroscopy
XRD	X-ray diffraction

TABLE OF CONTENTS

LIST OF FIGURES

LIST OF TABLES

ABSTRACT

This research focuses on wastewater flocculation, sludge recycling, and degrading air pollutants using recovered sludge by-products. Resource recovery from coagulation and flocculation is a holistic environmental and economic sustainability approach. Reusing treated wastewater, by-products, and residues created after treatment helps wastewater treatment protect the environment and essential resources. By calcining Ti^{4+} flocculated wastewater sludge, TiO_2 could be synthesized. However, Ti-salt-based coagulation produces acidic effluent, and the photoactivity of sludge-generated TiO_2 (S-TiO_2) is confined to UV spectra only. So, this study's broad goals are to (a) investigate the possibility of generating metal-doped and undoped photocatalyst grade titania while solving Ti-salt-based flocculation's low pH challenge, along with (b) visible light activation of S-TiO_2 for photodegradation of NO_x.

Initially, $TiCl_4$ and $Ca(OH)_2$ were employed to flocculate synthetic wastewater, and an optimum coagulant dose was determined by measuring the treated water's turbidity, DOC, and zeta potential. As a coagulant aid, $Ca(OH)_2$ attained a neutral pH, at 32.40 mg Ca/L and 14.54 mg Ti/L coagulant dose. Both Ca-doped and S-TiO_2 were produced from flocculated sludge for morphological and photocatalytic assessment. The doped Ca atoms prevented the production of anatase TiO_2, and no CaO was observed. At the optimum $Ca(OH)_2$ dose, Ca-doped TiO_2 was inferior to S-TiO_2 in acetaldehyde photodegradation. Subsequently, for the viability of A-TiO_2 production from algae blooming surface water, $TiCl_4$ was found to be better than commercially available polyaluminum chloride. In a microcosm jar test, 0.3 g Ti/L removed 99.8% of turbidity, 67% COD, and 96% TP. Under a 10 W/m^2 UV-A lamp, A-TiO_2 nanoparticles and coated mortar blocks successfully eliminated gaseous CH_3CHO and NO_x.

In addition, this study investigates the feasibility of producing TiO_2/g-CN heterojunction using Ti-incorporated dried dye wastewater sludge to enhance S-TiO_2's photoactivity. Primarily, only the dried sludge and melamine mixture were calcined, and the one-step calcination technique did not produce heterojunction, only N-doped anatase TiO_2. However, a successful TiO_2/g-CN composite was formed by calcining S-TiO_2 and melamine, and the optimum mixing ratio was evaluated as 1:3. Lastly, titanium nanotubes (S-TNT) were produced from S-TiO_2 and coupled with g-CN. The composite tripled the effective surface area (153.61 m^2/g) and reduced the energy bandgap to 3.0 eV. The as-

prepared composite's extended light absorption facilitated 19.62% and 32.44% of NO removal under 1 h of visible and UV light, respectively. In conclusion, it is feasible to make water and air safer and cleaner when considering Ti coagulants' exceptional coagulation performance.

CHAPTER 1
INTRODUCTION

1 Introduction

1.1 Background and research overview

The fundamental cause of water supply scarcity is the growing population, which is a constant source of concern for water conservation. The implementation of wastewater treatment systems has dramatically reduced environmental contamination created by polluted water runoff into natural ecosystems (Chi et al., 2019; Gan et al., 2021; Xia et al., 2018). Nonetheless, the production of perilous sludge resulting from wastewater treatment trains (primarily flocculation/coagulation) is also seen as a severe problem of the water industry (Gan et al., 2021). Handling excess sludge would cost between 25% to 65% of the overall cost of wastewater treatment facilities (Na et al., 2010). The successful reuse of treated wastewater, by-products, and residues generated during the treatment phase enabled the idea of wastewater treatment for the preservation of the environment and valuable resources (Na et al., 2010; Zhao et al., 2013; Y. X. Zhao, B. Y. Gao, G. Z. Zhang, Q. B. Qi, et al., 2014). A new technique for reusing sludge has been developed lately, using a unified titanium tetrachloride ($TiCl_4$) flocculation/sludge calcination process. TiO_2, a metal-oxide, is produced when sludge-generated by Ti^{4+} salt-based flocculation of wastewater is calcined (El Saliby et al., 2012; Okour et al., 2011; Shon et al., 2007a). The proposed sludge recycling method showed a lot of promise in lowering sludge disposal costs while still generating a useful by-product from sludge calcination. According to studies, around 40 mg of TiO_2 can be produced from a liter of flocculated wastewater. Coagulants like $TiCl_4$ and $Ti(SO_4)_2$ provide a viable solution to many environmental problems related to generating large quantities of conventional coagulant sludge (Okour et al., 2010). The production of TiO_2 from sludge, on the other hand, would substantially decrease the quantity of acidic waste generated during the sulfate and chlorine production scheme of titania (H. K. Shon et al., 2009b).

It has been reported that nearly 40 mg of TiO_2 could be produced from treating 1 liter of wastewater using $TiCl_4$ (Shon et al., 2007a). Besides, the photocatalytic and optical attributes of TiO_2 along with its strong oxidizing power for numerous potential applications made it a valuable by-product (Humayun et al., 2018; Nasirian et al., 2018; Noman et al., 2019b). Furthermore, there is better social acceptance of the use of Ti in terms of human and environmental health, in comparison to the conventional Al and Fe based coagulants (Lee et al., 2008; Zhao, Gao, Shon, Wang, et al., 2011). However, at optimum $TiCl_4$ concentration during coagulation, the hydrolysis of Ti salt causes the

release of a considerable amount of H^+ and generates an acidic effluent (pH, 3.5-5) (Shon et al., 2007a; Zhao, Gao, Shon, Wang, et al., 2011). Hence, a certain level of post-treatment is necessary to increase the pH of the final effluent. To overcome this problem, the use of coagulant aid during coagulation (H. K. Shon et al., 2009b) or the introduction of prehydrolyzed coagulant (Zhao et al., 2015) could be two viable solutions. H. K. Shon et al. (2009b) compared the effectiveness of using alkaline metallic coagulant aid, $Ca(OH)_2$, $FeCl_3$ and $Al(SO_4)_3$ with $TiCl_4$ during flocculation and showed promising results from the aspect of final pH along with adequate dissolved organic carbon (DOC) and turbidity reduction. The study characterized the prepared alkaline metal-doped TiO_2 and showed an enhanced level of optical absorbance and photocatalytic activity by the recovered metal-doped TiO_2 after calcination at 600 °C. The study inferred $Ca(OH)_2$ to be the most effective coagulant aid from the perception of final pH and photocatalytic activities of the recovered TiO_2 (H. K. Shon et al., 2009b). Nevertheless, rather than finding an optimized dose of $Ca(OH)_2$, the focus of the study was to prepare and characterize the Ca-doped TiO_2. Hence, a detailed study is necessary to optimize the dose of $Ca(OH)_2$ as a coagulant aid used with $TiCl_4$ and characterize the final Ca-doped TiO_2. Furthermore, several reviewed pieces of literature concerning doping of Ca in commercially available TiO_2 claimed improved light absorbance and photocatalytic activity (Akpan & Hameed, 2011a; Y. Li et al., 2007; Zaleska, 2008a).

Atmospheric pollution caused by nitrogen oxides (NO_x) has been identified as one of the most severe environmental problems (Song et al., 2019; Yang et al., 2019). Usually, NO_x refers to NO and NO_2, the two most common atmospheric nitrogen oxides. Anthropogenic activities such as combustion-based emission of natural gases and denitrification of nitrate salts from biogenic sources are the primary cause of atmospheric NO_x (Schwartz-Narbonne et al., 2019). Over the past decades, NO_x concentration has acutely increased, leading to dense haze events by generating secondary aerosols. Researchers have demonstrated effective removal of gaseous NO_x using several physio-chemical processes such as direct decomposition (Damma et al., 2018), selective catalytic/non-catalytic reduction (Zong et al., 2018), solid-liquid adsorption (Mamaghani et al., 2017), plasma-assisted catalytic reduction (Oskooei et al., 2019), and photocatalytic oxidation. However, most of these approaches are only useful at the source of emission where the NO_x concentration is at ppm levels and requires specific tools, tuning, or high temperatures. Photocatalytic oxidation is very efficient in removing NO_x at the ppb level

in ambient atmospheric conditions (Tsang et al., 2019). Moreover, photocatalytic NO_x oxidation facilitates sustainability by utilizing renewable solar energy, mild reaction conditions, low cost, and large-scale implementation (Schwartz-Narbonne et al., 2019; Yang et al., 2019). This promising method can effectively oxidize NO_x by generating reactive oxygen species such as superoxide ($\cdot O_2^-$) or hydroxyl ($\cdot OH$) radicals under light irradiation (Martinez-Oviedo et al., 2019).

Since the TiO_2 electrode was implemented for H_2 evolution using solar irradiation by Fujishima and Honda, it gained a growing interest in photocatalysis (Wei et al., 2016). The low cost, chemical stability, and non-toxic nature of TiO_2 made it an ideal photocatalyst (Tsang et al., 2019). Moreover, theoretical and experimental studies indicated that the dominant anatase facets ((101), (001)) of TiO_2 are more photoactive compared to the dominant rutile facets (Q. Huang et al., 2018). However, the photocatalytic activities of anatase TiO_2 are limited by its large energy bandgap (~3.6 eV) and prompt recombination of photogenerated e^-/h^+ pairs (Huang et al., 2020). Consequently, conventional TiO_2 primarily works under UV illumination, having a wavelength below 387 nm, with a low quantum efficiency. Hence, during photocatalysis, TiO_2 can only utilize a maximum of 4% – 5% of the solar spectrum (Huang et al., 2020), most of which is wasted by recombination in the bulk phase. For decades, many attempts have been made to enhance the photoactivity of TiO_2 by employing a more substantial portion of the solar spectrum and well-defined structure with high crystallinity through bandgap and crystal engineering (Lu et al., 2010; Yan & Yang, 2011), respectively. Some of the successful techniques that have been found are sol-gel method combined with inorganic/organic templates (deKrafft et al., 2012; Pan et al., 2011), hydrothermal synthesis (H. Yu et al., 2013), surface sensitization, metal/non-metal doping, noble metal deposition, self-doping, and semiconductor heterojunction (S. Zhang et al., 2019; Z. Zhang et al., 2019). In particular, the heterojunction of TiO_2 with restricted bandgap semiconductors is very efficient in utilizing the visible and solar light spectrum as well as mitigating charge recombination during photocatalysis. In recent years, polymeric derivative (g-CN) of ideal graphitic carbon nitride or polymeric melon have attracted considerable attention due to their promising optical properties, electronic structure, and photocatalytic behavior (Dong et al., 2013; Dong et al., 2011; Thomas et al., 2008). G-CN has been significant in working towards photocatalytic H_2 evolution. G-CN can easily be synthesized by thermal polycondensation of a nitrogen-rich molecular precursor such

as urea, cyanamide, dicyandiamide, melamine, and thiourea (Dong et al., 2011). Two basic tectonic units, tri-s-triazine (C_6N_7) and s-triazine (C_3N_3), each provide for the specific architecture of g-CN (Thomas et al., 2008). However, g-CN with standard C_6N_7 units has been predicted to be the most stable phase in low energy conditions (Thomas et al., 2008). Unlike TiO_2, g-CN features a two-dimensional (2D) lamellar structure consisting primarily of the π-conjugated heterocyclic aromatic compounds with a modest energy gap (~2.7 eV), leading to high thermo-chemical stability, strong visible light absorption (~450 – 460 nm), and favorable optoelectronic properties (Cui et al., 2020; Zhou et al., 2019). G-CN has the conduction band (CB) and valence band (VB) potential of −1.3 or +1.4 eV vs. normal hydrogen electrode (NHE) respectively; thus, the photoexcited e^-/h^+ pairs can be efficiently utilized for H_2O splitting (H_2 evolution), organic pollutants degradation, and CO_2 reduction (S. Zhang et al., 2019).

Thanks to its impressive π-conjugated structure and visible light absorption, g-CN has drawn tremendous attention to the removal of NO_x, one of the prominent haze precursors (Li et al., 2018; Jinzhu Ma et al., 2016; Zhenyu Wang et al., 2018). Similar to TiO_2, the photocatalytic activities of g-CN is still limited because of the low charge transfer efficiency and high recombination (i.e., the transfer of photogenerated e^- from CB to VB, to combine with photogenerated h^+) rate of the photogenerated e^-/h^+ pairs (Yu et al., 2020). Therefore, the pristine g-CN cannot effectively eliminate NO_x unless modified to inhibit the charge recombination rate and enhance charge transfer efficiency. Hence, to improve photoactivity, substantial attempts have been made for the morphology and energy bandgap amendment of the pristine g-CN. Heteroatom doping and composite preparation with compatible semiconductors through heterojunction are the prominent approaches that have been tested by many research groups. Considering the stability and the extent of the photoactivity of g-CN composites, g-CN heterojunction with other semiconductors appears to be an efficient strategy to optimize photoactivity (Cui et al., 2020; Huang et al., 2020; Yu et al., 2020). The disparity in the CB and VB levels of g-CN and TiO_2, along with the graphene-like 2D structure of g-CN, favors efficient heterojunction, which facilitates dynamic photoactivity under both UV and visible irradiation (Cui et al., 2020; Huang et al., 2020; Xia et al., 2019). Due to the position of CB and VB, TiO_2/g-CN is a type II heterostructure. Therefore, photogenerated e^- on the CB of g-CN can transfer to TiO_2, and the photogenerated h^+ from VB of TiO_2 can transmit to g-CN (Cui et al., 2020). Consequently, the recombination rate of photogenerated e^- and

h^+ can be reduced in the TiO_2/g-CN composite. In contrast, several studies reported TiO_2/g-CN to be a type Z heterostructure (Huang et al., 2020). Despite the fact that much research for NO_x elimination using TiO_2/g-CN composites have been performed, commercially accessible titania has been utilized as the precursor of TiO_2, increasing photocatalyst synthesis costs.

This research aimed to see how well $TiCl_4$ and $Ca(OH)_2$ worked together to improve flocculation in synthetic wastewater. A facile thermal treatment of flocculated sludge was utilized to prepare Ca-doped TiO_2 and tested its photoactivity under UV light. Furthermore, TiO_2 was produced from algae blooming surface water treatment, and an atmospheric photocatalytic application was described. Finally, a new TiO_2/g-CN heterojunction was constructed using various simple methods for visible light activation of the sludge-generated TiO_2, and photocatalytic performances for ambient NO_x removal were reported.

1.2 Contribution to existing knowledge

Preparation of anatase TiO_2 from flocculated sludge is a feasible option to produce photocatalytically active nanoparticles (NPs) and nanofibers (NFs). However, the produced TiO_2 can only extract a limited portion of the solar spectrum during photodegradation. Hence, activation of sludge recovered TiO_2 under visible light would enhance the extent of its application in several novel sectors. Moreover, this study would generate enhanced TiO_2 NPs which are expected to be utilized in air purification through the removal of NO_x.

1.3 Research aims and objectives

The research aimed to address the reduced pH problem of the Ti salt-based flocculation and prepare photocatalytically enhanced anatase TiO_2 from various types of wastewaters. Moreover, the novel visible light activation of sludge-generated TiO_2 was explored for the purpose of successful photooxidation of NO_x. The specific research objectives of this work are listed below:

- To investigate the coagulation performance by simultaneous dosing of $TiCl_4$ and $Ca(OH)_2$ in synthetic wastewater.
- To fabricate Ca-doped TiO_2 at optimum coagulant dose considering effluent pH, turbidity, and DOC.

- To explore the possibility of preparation of photoactive TiO_2 from algal bloom surface water.
- To perform the feasibility study for the generation of TiO_2/g-CN composite from wastewater.
- To optimize the visible light activation of the synthesized TiO_2/g-CN composite from wastewater towards atmospheric NO_x removal.
- To enhance the photoactivity of sludge-generated TiO_2/g-CN through a facile hydrothermal treatment.

1.4 Thesis outline

Chapter 1 provides a broad background and research overview including research objectives. Chapter 2 highlights some of the past research in the areas of Ti-based coagulation along with brief discussion of coagulation-flocculation mechanism and photo activity of titania.

Chapter 3 describes the lab-scale experimental investigation in evaluating flocculation performance and characterization of prepared titania. Additionally, this chapter summarizes various synthesis processes for the preparation of TiO_2/g-CN composites. Additionally, a number of prescribed applications of the TiO_2/g-CN composites in the field of energy and pollution control are briefly summarized.

Chapter 4 focuses on preparing undoped and Ca-doped titania from flocculation-generated sludge. Initially, $TiCl_4$ was used to coagulate and flocculate synthetic wastewater, and an optimal coagulant dosage was established by measuring the treated water's turbidity, DOC, and zeta potential. Later, the effects of employing $Ca(OH)_2$ as a coagulant aid on effluent pH, turbidity, and DOC removal were studied. Ca-doped and undoped anatase TiO_2 were synthesized from flocculated sludge and evaluated morphologically and photocatalytically.

The goal of Chapter 5 is to use a Ti-based coagulant ($TiCl_4$) to successfully treat algae blooming water and extract photoactive new anatase TiO_2 from flocculated sludge. Traditional jar tests were used to assess the coagulation efficiency, and $TiCl_4$ was shown to be superior to commercially available poly aluminum chloride (PAC). Furthermore, TiO_2 nanoparticles (NPs) were recovered from the flocculated sludge, and SEM, EDX, and X-ray diffraction (XRD) examination verified the existence of only the anatase phase. Under a UV-A lamp with a light intensity of 10 W/m^2, the recovered TiO_2 was shown to

be efficient in eliminating gaseous CH_3CHO and NO_x. Furthermore, the TiO_2 mixed mortar blocks produced in this research effectively eliminated ambient nitrogen oxide (NO_x) under UV irradiation.

Chapter 6 investigates the feasibility of preparing TiO_2/g-CN heterojunction from Ti salt-based flocculated dye wastewater. To create composites, two different chemical pathways were examined. In the first method, the dried sludge and melamine mixture was calcined in one-step at 600°C. The one-step calcination method did not produce TiO_2/g-CN composites; instead, only N-doped anatase TiO_2 composites were produced, according to detailed morphological and chemical characterizations. When a two-step calcination method was used, successful production of anatase TiO_2 and g-CN was seen, i.e., synthesis of anatase TiO_2 from dried sludge and subsequent generation of heterojunction by calcining (@550 °C) the TiO_2 and melamine combination. The effective heterojunction was confirmed using X-ray diffraction, infrared, and X-ray photoelectron spectroscopy.

In Chapter 7, sludges generated from Ti-based flocculation of dye wastewater is used to retrieve photoactive titania (S-TiO_2). To boost photoactivity under UV/visible light irradiance, it was heterojunctioned with graphitic carbon nitride (g-CN). Later, using photocatalysis, the as-prepared materials were used to remove nitrogen oxides (NO_x) from the atmosphere. S-TiO_2 and melamine mix was calcined (at 550 °C) to form a heterojunction between S-TiO_2 and g-CN. Advanced sample characterization was performed and thoroughly documented. The morphological and optical properties of the samples were used to demonstrate successful heterojunction. Finally, the photoactivity of the produced samples was determined by measuring NO_x photooxidation under UV and visible light irradiance. Regardless of the light types used, the prepared samples showed increased photoactivity. To understand the process of photooxidation, the optical properties of the produced composites were evaluated.

In Chapter 8, a modified hydrothermal route is used to prepare titania nanotube from sludge-generated TiO_2 (S-TNT), which was then effectively composited with graphitic carbon nitride (g-CN) through a simple calcination process. The produced samples were characterized using advanced characterization methods such as XRD, SEM, TEM, XPS, UV/vis diffuse reflection spectroscopy (DRS), and photoluminescence (PL) analysis. The morphological and optical bandgaps both improved significantly. When compared to

sludge-generated TiO_2, the produced composite's effective surface area rose thrice. The degree of photoactivity of the produced composites was examined through photooxidation of NO_x in a continuous flow reactor. The simple technique for heterojunction of S-TNT and g-CN described in this chapter may help with resource recovery from water treatment facilities and photocatalytic pollution removal in the atmosphere. Finally, the findings of the thesis are summarized and the recommendations for future work on this study are provided in Chapter 9.

CHAPTER 2
LITERATURE REVIEW

2 Literature review

2.1 Coagulation and flocculation

Coagulation and flocculation are pollutant removal technique that has been used for generation in water and wastewater treatment. Conventionally in a wastewater treatment facility, coagulation and flocculation are incorporated in the primary treatment phase to facilitate the subsequent treatment trains (DeWolfe, 2003). Based on the size of the pollutant particles they can exist in wastewater in three prominent forms, viz., solutions (< 0.002 μm), colloidal dispersions ($0.002 – 0.2$ μm) and suspensions (> 0.2 μm) (Everett, 1988). Mechanical filtration and settling can comfortably remove the pollutants in suspensions but strive to retain the colloidal particles and found ineffective. However, coagulation and flocculation can remove various water induced contaminants of the colloidal genre, e.g., materials causing turbidity, metal oxides, persistent toxic compounds, organic materials, stable emulsions, etc. The colloidal particles due to its large surface area adsorb water molecules and ions from surrounding water and develop electrostatic charges of similar nature. Hence, they repulse each other and cannot agglomerate in larger particles (Bratby, 2006). Conventionally, the colloidally dispersed particles are negatively charged and can broadly be classified into two types, viz., hydrophilic and hydrophobic colloids (Everett, 1988). Typically, hydrophilic colloids are larger organic molecules, which are thermodynamically stable when solvated in water and their charges originated from the presence of ionizable groups. On the other hand, hydrophobic colloids are thermodynamically unstable in water but remain stable in colloidal dispersion due to the formation of the charged layer through adsorption of ionic species (Bratby, 2006).

Coagulation and flocculation, despite being different in functionality in many pieces of literature they have been used interchangeably. However, there are distinct differences between the two processes. In broad terms, coagulation refers to the process through which electrically charged stable colloidal dispersion gets destabilized under favorable physiochemical condition and flocculation assists in the conglomeration of destabilized particles into larger floc, which can be separated from wastewater through settlement and/or filtration (Bratby, 2006; Jarvis et al., 2005).

2.1.1 Coagulation mechanism

Based on the reviewed pieces of literature, four significant types of coagulation (destabilization) mechanism have been observed, viz., double layer compression, adsorption & charge neutralization, bridging of colloidal particles and sweep flocculation. A brief explanation of those processes is illustrated in the following section.

2.1.1.1 Double layer compression

The negatively charged colloids, while dispersed in water remain surrounded by oppositely charged ions and produce an electric potential across its diffuse layer (Singh et al., 2009). Incorporation of cationic coagulants (i.e., Al^{3+} or Fe^{3+}) enhances the ionic strength of the solution. Which leads to compression of the diffuse (double layer) layer and reduces the exposure to which the colloidal charge affects the surrounding potential (Everett, 1988; Singh et al., 2009). Hence the effect of inter-colloidal repulsion gets reduced leading to easy aggregation of colloids in larger floc. **Fig. 2-1 (a)** illustrates the mechanism of double layer compression.

2.1.1.2 Adsorption and charge neutralization

Inorganic coagulants (viz., alum, ferrous/ferric sulfate) are found to adopt adsorption and charge neutralization during coagulation. When added to water these metallic coagulants which are good Lewis's acid get hydrolyzed into cationic species of various degree. Based on the physicochemical properties of wastewater and types of coagulant doses monomeric and polymeric hydrolyzed species are originated. These hydrolyzed species get adsorbed to the negatively charged colloids and neutralize the charges (Singh et al., 2000; Tripathy & De, 2006) (see **Fig. 2-1 (b)**). Besides, the van der walls force become dominant, which promotes agglomeration of colloids and development of larger flocs.

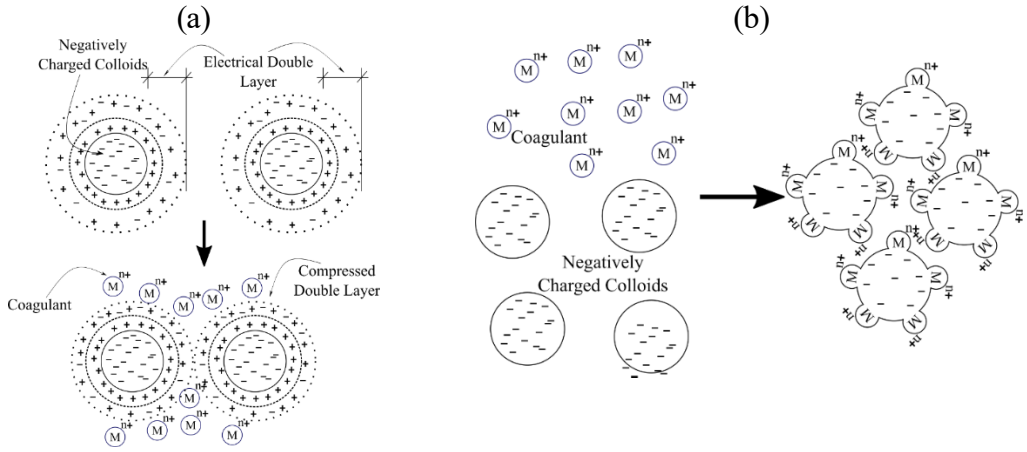

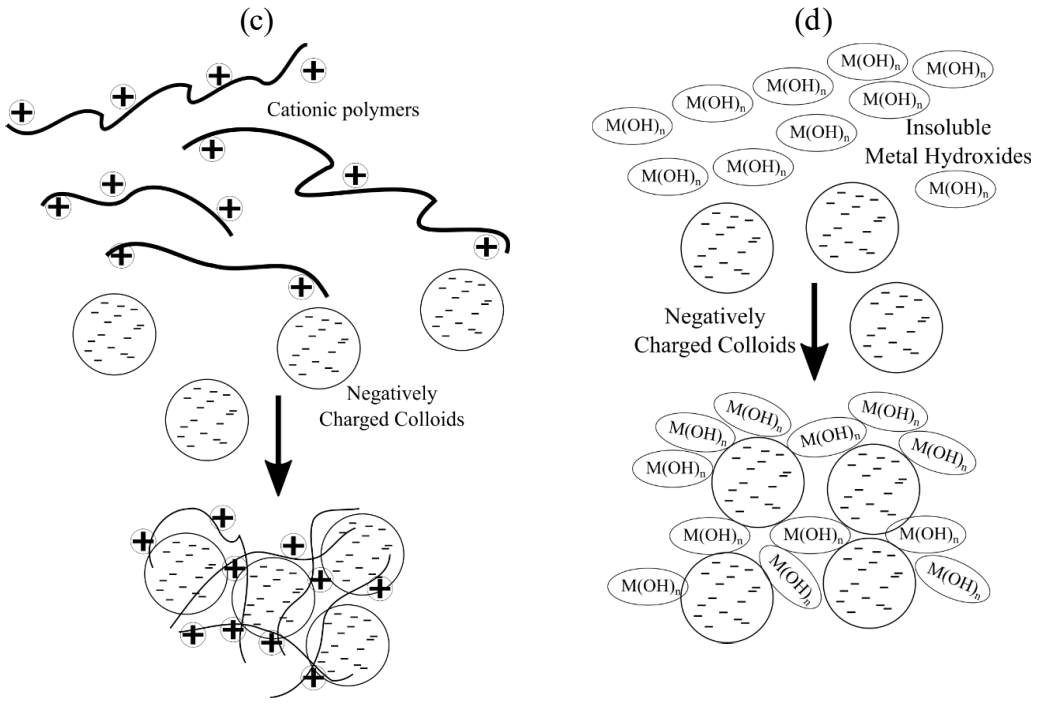

Fig. 2-1. Coagulation mechanisms: (a) Double layer compression of charged colloids, (b) Adsorption and charge neutralization (c) Bridging of colloidal particles, (d) Sweep flocculation

2.1.1.3 Bridging of colloidal particles

Addition of polyelectrolytes as coagulants or generation of polymeric hydrolyzed species could facilitate bridging of colloidal particles. While in water the ionized polymer gets attached to the colloids and hinder the motion of the colloid-polymer particle due to length and high molecular mass of the polymer. Later the extended polymer chains of the colloid-polymer particles interact with each other and form bridges, which leads to aggregation in macro flocs (Li et al., 2006)(**Fig. 2-1 (c)**).

2.1.1.4 Sweep flocculation

Generally, sweep flocculation is observed when a significant amount of inorganic metallic salt is added for coagulation. At larger dose, the insoluble metallic hydroxides, produced during hydrolysis get precipitated. While settling, the hydroxides form large polymeric structures and entrap colloids within (Li et al., 2006) (**Fig. 2-1 (d)**). Coagulation through this mechanism produces a large amount of sludge.

2.1.2 Flocculation mechanism

After destabilization of the colloid's flocculation takes place. From a broad perception, flocculation occurs in two ways, a) perikinetic flocculation and b) orthokinetic

flocculation. Perikinetic flocculation is the result of the Brownian motion of the destabilized particles. Particles with varying charges bombard on each other due to Brownian motion and agglomerate as larger flocs (Thomas et al., 1999). On the other hand, orthokinetic flocculation requires the introduction of external turbulence (i.e., stirring) in the influent. The destabilized colloidal particles in the wastewater comes in contact of each other due to bulk movement of the fluid and aggregated as macro flocs (Thomas et al., 1999). Based on theoretical principles, Orthokinetic flocculation can be modelled using the following equation,

$$ln\frac{n}{n_0} = -\frac{4}{\pi}\eta\bar{V}\bar{G}t \qquad (2\text{-}1)$$

$$\bar{G} = \sqrt{\frac{P}{V\mu}} \qquad (2\text{-}2)$$

Where,

n	Number of final colloidal particles
n_0	Number of initial colloidal particles
η	Efficiency of collision of destabilized particles
$\overline{V}$	Volume of colloidal particles per unit volume of suspension
$\overline{G}$	Mean velocity gradient
t	Time of flocculation
P	Mean power consumption
μ	Viscosity

2.2 Conventional coagulants used in water and wastewater treatment

In general, various types of metallic salts and polyelectrolytes are used for coagulation in water and wastewater treatment. Al and Fe based salts are common types of metallic coagulants. Among aluminum salts the commonly used coagulants that have been found are, aluminum sulfate ($Al_2(SO_4)_3$), aluminum chloride ($AlCl_3$) and sodium aluminate ($Na_2O.Al_2O_3$) (Bahadori et al., 2013). On the other hand, considering the use of iron-based coagulants, frequent use of ferric sulfate ($Fe_2SO_4)_3$), ferric chloride ($FeCl_3$), ferric chloride sulfate ($FeClSO_4$), and ferrous sulfate ($FeSO_4$) has been found (Sillanpaa et al., 2018). Additionally, hydrated lime ($Ca(OH)_2$) and magnesium carbonate ($MgCO_3$) are also found to be used as both coagulant and coagulant aid for water treatment (Semerjian & Ayoub, 2003). Beside metallic salts polyelectrolytes or polymers are also being used

in water and wastewater treatment facilities (Chekli et al., 2015; X. Huang et al., 2018). Considering the origins of the polymers, coagulants have been found from both natural and synthetic (organic & inorganic) origins. Among natural polymers, starch products, alginate, chitosan, etc. are found to be effective coagulants (Sillanpaa et al., 2018). Also, coagulants from synthetic origins are primarily polymerized monomers. For instance, polyamine, sulfonates, prehydrolyzed Al and Fe based salts, etc. are some established polymeric coagulants.

Following the work of DeWolfe (2003), Al (72%) and Fe (23%) based salts are the most commonly used coagulants in water and wastewater treatment. The recurring use of these two metallic salts as coagulant are attributed to two prominent factors, viz., economic feasibility and extent of availability in stable forms. Considering color and turbidity removal efficiency along with ease of handling aluminum-based coagulants are more favored in wastewater treatment comparing Fe based coagulant. However, the suspected health risk of residual Al in treated water has shifted its popularity in water treatment. With the similar physicochemical condition, ferric based coagulants are found more effective in removing natural organic matter (NOM) comparing alum. Due to higher charge density of hydrolyzed species generated from ferric coagulant it has been affirmed more efficient in eliminating NOM having a molecular weight ranging from 1000 – 4000 g/mole (Hahn et al., 2007). Furthermore, following the effect of sweep flocculation the floc size generated from ferric coagulants are larger comparing Al-based coagulants. As a result, ferric coagulant facilitates less settling time and reduction in the footprint of the corresponding treatment train. The following sections overview various types of coagulants and their general coagulation mechanisms.

2.2.1 Al-based coagulants

Aluminum sulfate ($Al_2(SO_4)_3$) and aluminum chloride ($AlCl_3$) are the most frequently utilized coagulants in water and wastewater treatment facilities (Crittenden et al., 2012). Al-based coagulants are very pH sensitive, and their coagulation mechanism varies along the changing pH profile of the target influent (Duan & Gregory, 2003). When Al-based coagulant is added to water, it undergoes hydrolysis and various monomeric dissolved species along with aluminum hydroxide precipitate are generated based on pH, species solubility and concentration of the chemical doses (Duan & Gregory, 2003)(see **Fig. 2-2**).

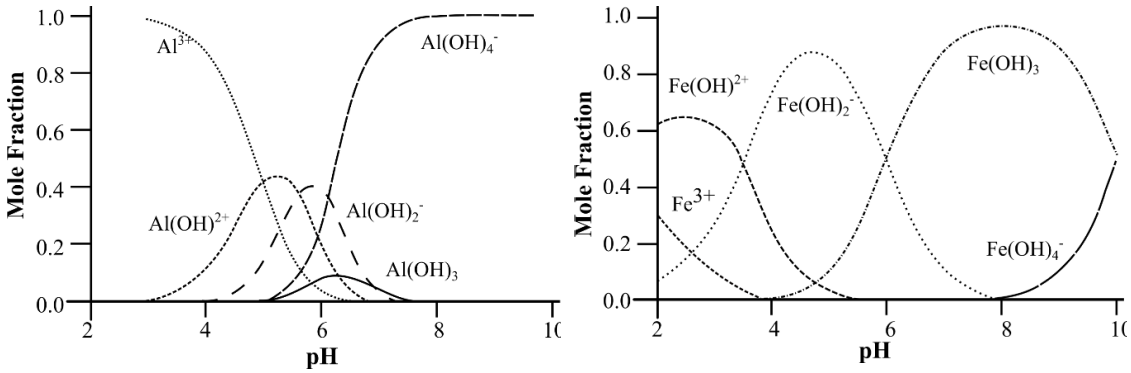

Fig. 2-2. Al (II) and Fe (III) speciation in aqueous solution. Adapted from Duan and Gregory (2003)

Gregory and Duan (2001) reported, at a dose concentration higher than 90 Al-mg/L and pH of 4.5, the dominant species is $Al(OH)_3$ precipitate. Al-based coagulants have been found ineffective outside the pH range of 3 to 11 (J. Wang et al., 2016) and theoretically, the optimum pH range for Al-based coagulation is found as 5.5 to 7.7. Within acidic and alkaline pH range cationic and anionic hydrolyzed species are found during Al-based coagulation (Duan & Gregory, 2003). Most of the time the colloidal particles (inorganic and organic) present in polluted water are found to be negatively charged (Everett, 1988). Hence, the cationic hydrolyzed species of aluminum salts assists in destabilizing the negatively charged colloid through adsorption and charge neutralization. Above the isoelectric point higher coagulant dose, the precipitating aluminum hydroxides and aluminum complexes formed with organic ligands promote sweep flocculation.

2.2.2 Iron-based coagulant

Among iron-based coagulants, the most commonly used chemicals (present in both solid and liquid form) that are found as coagulants are ferric chloride ($FeCl_3$) and ferric sulfate ($Fe_2(SO_4)_3$) (Crittenden et al., 2012). Considering the seasonal variation of wastewater and types of organic pollutants the optimum doses of ($FeCl_3$) and ($Fe_2(SO_4)_3$) could vary from 5 – 150 mg/L and 20 – 250 mg/L respectively (Crittenden et al., 2012). The coagulation mechanism of iron-based coagulant is similar to Al-based coagulant, i.e., Adsorption-charge neutralization and sweep flocculation. However, the extent of hydrolysis upon application is considerably different than Al-based coagulant (Duan & Gregory, 2003) (**Fig. 2-2**). Approximately at a pH of 6, the solubility of Fe based salt is found to be below 0.01 µM which is almost 1 µM for Al. Additionally, the hydrolysis constants of Fe are ranged at broader pH range (viz., 8 pH unit) comparing Al (Duan & Gregory, 2003; Flynn Jr, 1984; Wesolowski & Palmer, 1994). Hence at the similar

physicochemical condition, the coagulation mechanisms involved in Fe and Al-based coagulation are different. For Fe based coagulation several studies (Jarvis et al., 2012; Sillanpaa et al., 2018; Y. Zhao et al., 2014) stated the optimum pH range as 4.5 to7.

2.2.3 Polymeric coagulant

2.2.3.1 Synthetic polymers

Synthetics polymers could be developed form both inorganic and organic precursors. Inorganic synthetic polymers were introduced focusing the uncontrolled hydrolysis of metallic coagulants. Fabrication of such polymers involves the partial neutralization (using a base) of metallic salts in a controlled manner before coagulation. Previous relevant research reported, the addition of NaOH in Al-based coagulants generate a supersaturated solution of insoluble metallic hydroxides and consecutively reduces the overall surface charges of the precipitated hydroxides, leading to the formation of a large number of polymeric species (Duan & Gregory, 2003; J. Wang et al., 2016). The most studied inorganic synthetic polymers include, polyaluminium chloride (PAC), polyferric chloride (PFC), polyferric sulfate (PFS), along with some complex inorganic coagulants such as polymeric aluminum ferric sulfate (PAFS), polymeric ferric zinc sulfate (PFZS) and polymeric phosphate aluminum chloride (PPAC) (Sillanpaa et al., 2018). Charge neutralization tends to play a minor role during inorganic polymer based coagulation comparing metallic coagulant (Al and Fe based coagulant) (Wei et al., 2009). The fundamental coagulation mechanisms with polymeric coagulation are adsorption, polymeric complexation and sweep flocculation. The inorganic polymeric salts Al and Fe are found more efficient in organic pollutant removal comparing monomeric Al and Fe based coagulants. Furthermore, polymeric coagulants are found to perform more efficiently for turbidity removal at low temperature and low alkalinity (Cheng et al., 2008). The use of cationic organic polymers are found for removing organic matter from wastewater. (Matilainen et al., 2010) reported that the charge neutralization is the coagulation mechanism of such cationic organic polymers. The well-established cationic synthetic (organic) polymers would include, polydiallyldimethyl ammonium chloride (pDADMAC), cationic polyacrylamide (CPAM), polymers from epichlorohydrin and dimethylamine (Sillanpaa et al., 2018). Such organic synthetic polymers are favored for less sludge production, lower dose requirement, and reduced pH dependency.

2.2.3.2 Natural polymers

The most researched and commercially available natural coagulants primarily comprise tannin based coagulants and chitosan (Graham et al., 2008; Renault et al., 2009). Synthetic inorganic coagulants are inherently incorporated with some drawbacks, viz., voluminous sludge production, more substantial cost, tedious pH control and impacts of residual complexes. Natural polymers are found to reduce the above-mentioned problems and comes with some inherent advantages, such as regeneration, biodegradation and low toxicities.

2.3 Titanium (Ti) based coagulation

Coagulation and flocculation are a widely used mechanism to remove colloidal pollutants and dissolved organic matter from wastewater effectively. It has been illustrated in the previous sections that conventionally, Al and Fe based salts of various forms are effectively used in as coagulant. However, the use of these conventional coagulants is incorporated with some environmental and economic constraints. The two major components these constraints contain are, a) posterior handling of the generated sludge in voluminous amount, and b) impacts of residual trace metals in treated water (Okour, Shon, et al., 2009; Shon et al., 2007a). Hence to overcome such drawbacks, researchers are always looking for new types of coagulants. Following that venture, Shon et al. (2007a) reported $TiCl_4$ as an alternative coagulant for wastewater treatment. Since then, the negligible toxicity of Ti metal along with the provision of titania recovery after Ti-based coagulation has attracted scientist's attraction to a greater extent. To understand the coagulation mechanism of a metal-based salt it is imperative to have clear conception regarding their degree of hydrolysis and limit of solubility. Furthermore, to explain the coagulation mechanism the surface chemistries of hydrolyzed Ti species are important. Hence, the subsequent sections will cover these topics to grasp the coagulation mechanism of Ti-based coagulants better.

2.3.1 Hydrolysis of Ti (IV) and surface chemistry

Al and Fe based salts used as coagulant are hydrolysis prone and robust Lewis's acid (Buettner & Valentine, 2012; Duan & Gregory, 2003). Additionally, it is evident that most of the cationic metal get hydrated to some extent when in contact with water. Owning to the high charge of Ti^{4+} it is stronger Lewis's acid and more hydrolysis prone comparing Al or Fe (Buettner & Valentine, 2012; Einaga & Komatsu, 1981; Ferri & Riccio, 1985). Considering Ti, even at very low pH (< 2) doubly hydrolyzed $Ti(OH)_2^{2+}$

has been found where unhydrolyzed Al^{3+} and Fe^{3+} were found to exist below pH 2 and 5 respectively (Duan & Gregory, 2003). The high charge of the Ti^{4+} effectively polarize the surrounding water molecules in the hydration shell and depending on the H^+ concentration of the solution could promote deprotonation. With a continuous increase of the solution pH, deprotonation could proceed further and produce hydrolyzed species with lower positive charges (Sugimoto et al., 2002). The following simplified scheme showed the monomeric hydrolyzed species of Ti when the solution pH increases from left to right. For simplification, the coordinated H_2O are not shown here.

$$Ti^{4+} \rightarrow Ti(OH)^{3+} \rightarrow Ti(OH)_2^{2+} \rightarrow Ti(OH)_3^{+} \rightarrow Ti(OH)_4 \rightarrow Ti(OH)_5^{-} \quad (2\text{-}3)$$

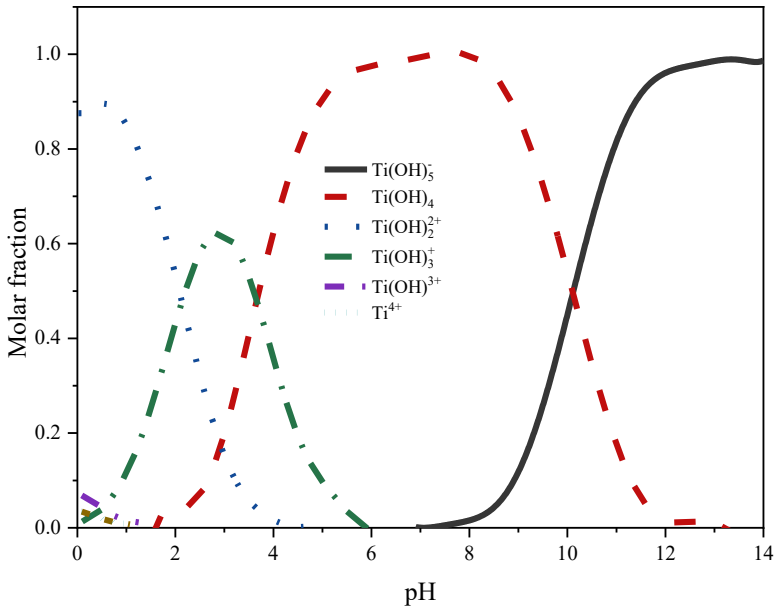

Fig. 2-3. Distribution of Ti (IV) hydrolysates along varying pH range. Adapted from X. Wang et al. (2018).

The stepwise formation constants of the hydrolyzed species shown above are tabulated in **Table 2-1** from several Ti (IV) hydrolysis studies. Based on formation constant stated in Ferri and Riccio (1985) and Buettner and Valentine (2012) the fractions of different species along varying pH (X. Wang et al., 2018) are shown in **Fig. 2-3**. From the **Fig. 2-3**, within the pH range of 4 to 10 the dominant hydrolyzed species is $Ti(OH)_4$ and in more acidic region fraction of hydrolyzed species varied in the order of, $Ti(OH)_2^{2+} > Ti(OH)_3^{+} > Ti(OH)^{3+}$. Although the authors of the study claimed the presence of $Ti(OH)_5^-$ above pH of 10, the formation constant used from the development of the of the respective fraction

curve was determined at 100 °C. On the other hand, even at pH of 12, Sugimoto et al. (2002) did not find any presence of $Ti(OH)_5^-$.

Table 2-1. Formation constants of hydrolyzed Ti (IV) species in aqueous solution from various studies

Hydrolyzed species	**Stepwise stability constant**	**Ionic strength/background electrolyte, Temperature**	**Solubility product constant (log K_{sp})**	**Ref.**
$Ti^{4+} + H_2O \rightleftharpoons Ti(OH)^{3+} + H^+$	$\log K_{s1} = 0.3$	3 M NaCl, 25 ℃		Ferri and Riccio (1985)
$Ti(OH)^{3+} + H_2O \rightleftharpoons Ti(OH)_2^{2+} + H^+$	$\log K_{s2} = 1.08$	3 M NaCl, 25 ℃		
$Ti(OH)_2^{2+} + H_2O \rightleftharpoons Ti(OH)_3^{+} + H^+$	$\log K_{s3} = -2.1$			Buettner and Valentine (2012)
$Ti(OH)_3^{+} + H_2O \rightleftharpoons Ti(OH)_4 + H^+$	$\log K_{s4} = -3.7$			
$Ti(OH)_4 + H_2O \rightleftharpoons Ti(OH)_5^{-} + H^+$	$\log K_{s5} = -10.1$	0.1 m $NaNO_3$, 100 ℃		Knauss et al. (2001)
$TiO^{2+} + 2\ OH^- \rightleftharpoons TiO(OH)_2$	-	0, 25 ℃	−29.0	Bjerrum et al. (1958)
$Ti^{4+} + 4\ OH^- \rightleftharpoons Ti(OH)_4$	-	0, 25 ℃	−53.01	
$TiO^{2+} + 2\ OH^- \rightleftharpoons TiO(OH)_2$	-	0.1, 25 ℃	−29.0	Babko et al. (1962)
$Ti(OH)_2^{2+} + OH^- \rightleftharpoons Ti(OH)_3^{+}$	$\log K_{s3} = -2.40$	0.1, 25 ℃		Liberti et al. (1963)
$Ti(OH)_3^{+} + OH^- \rightleftharpoons Ti(OH)_4$	$\log K_{s4} = -2.11$	0.1, 25 ℃		
$Ti(OH)_2^{2+} \rightleftharpoons Ti(OH)_3^{+} + H^+$	$\log K_{s3} = -2.12$	0.1, 18 ℃		

$Ti(OH)_3^+ \rightleftharpoons Ti(OH)_4 + H^+$	$\log K_{s4} = -3.37$	0.1, 18 ℃		Einaga and Komatsu (1981)
$Ti(OH)_2^{2+} \rightleftharpoons Ti(OH)_3^+ + H^+$	$\log K_{s3} = -0.92$	1, 25 ℃		Lobanov et al. (1969)
$Ti(OH)_3^+ \rightleftharpoons Ti(OH)_4 + H^+$	$\log K_{s4} = -1.05$	1, 25 ℃		
$Ti(OH)_2^{2+} \rightleftharpoons Ti(OH)_3^+ + H^+$	$\log K_{s3} = -0.64$	0, 25 ℃		Einaga and Komatsu (1981)
$Ti(OH)_3^+ \rightleftharpoons Ti(OH)_4 + H^+$	$\log K_{s4} = -0.95$	0, 25 ℃		
$TiO^{2+} \rightleftharpoons TiO(OH)_2 + 2\ H^+$	$\log K^* = -4.7 \pm 0.1$	2 M NaCl, 25 ℃	-27.3 ± 0.1	Einaga and Komatsu (1981)
$Ti(OH)_2^{2+} + OH^- \rightleftharpoons Ti(OH)_3^+$	$\log K_{s3} = 11.9$	0.1, 25 ℃		Sugimoto et al. (2002)
$Ti(OH)_3^+ + OH^- \rightleftharpoons Ti(OH)_4$	$\log K_{s4} = 10.3$	0.1, 25 ℃		
$3TiO^{2+} \rightleftharpoons Ti_3O_4^{4+} + 2\ H^+$	$K_{3,4} = 0.38 \pm 0.06$	4 m $HClO_4$, 25 ℃		Comba and Merbach (1987)
$3TiO^{2+} \rightleftharpoons Ti_3O^{\alpha}{}_3O^{\beta}{}_2H_3^{5+} + H^+$	$K_{3,3} = 1.64 \pm 0.06\ m^{-1}$	4 m $HClO_4$, 25 ℃		
$4TiO^{2+} \rightleftharpoons Ti_4O^{\alpha}{}_4O^{\beta}{}_2H_4^{8+}$	$K_{4,4} = 2.31 \pm 0.03\ m^{-3}$	4 m $HClO_4$, 25 ℃		

* Cumulative stability constant

Using the **Fig. 2-3**, the uncharged $Ti(OH)_4$ formed in the intermediate zone creates amorphous precipitate due to very low solubility. Due to the formation of the amorphous precipitate, it is challenging to determine the stability constants of the generated hydrolyzed species which reflects the variation in the results shown in **Table 2-1** from different studies. Around neutral pH, the solubility of amorphous hydroxides generated from Al and Fe was found as 10^{-7} and 10^{-12} M respectively (Buettner & Valentine, 2012). Whereas, Sugimoto et al. (2002) reported higher solubility of $Ti(OH)_4$ by dissolving freshly prepared hydrous precipitated of Ti (see **Fig. 2-4**). The slops shown in **Fig. 2-4** were generated using a theoretical model. Although at lower pH (pH < 4) hydrolyzed Ti showed a sharp increase in solubility it was found virtually constant after pH of 4. Furthermore, Comba and Merbach (1987) claimed the presence of oligomers during hydrolysis of $TiOSO_4.2H_2O$. They discovered that oligomers are present at higher pH and high Ti concentration (> 0.05 M). Also, they claimed the discovered oligomers as two types trimer and one tetramer. X. Wang et al. (2018), extensively studied the extent of surface charges and zeta potential of hydrolysate products, when $TiCl_4$ and Polytitanium Chloride (PTC) with unit basicity is hydrolyzed in water. **Fig. 2-5 (a)** and **(b)** shows the extent of surface charges and zeta potential along the changing pH profile.

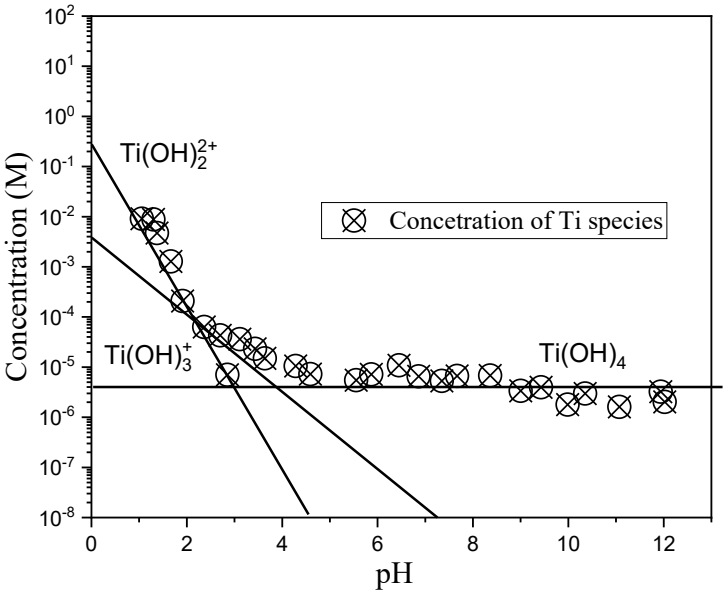

Fig. 2-4. Concentration of dissolved Ti(IV) species in aqueous solution for varying pH range. Adapted from Sugimoto et al. (2002)

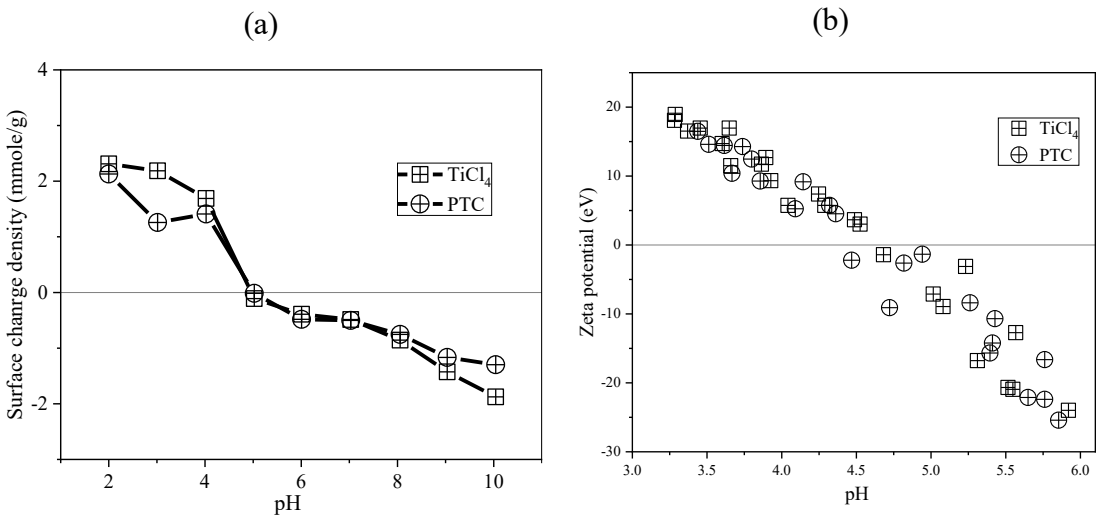

Fig. 2-5. Surface charge density (a) and Zeta potential (b) of Ti (IV) hydrolysates in aqueous solution along varying pH profile. Adapted from X. Wang et al. (2018)

2.3.2 Ti (IV) coagulation over conventional coagulants

Ti oriented salts ($TiCl_4$, $Ti(SO_4)_2$, and PTC) are found to perform on par with the conventional Al and Fe based coagulants (Chekli et al., 2015; Okour, Shon, et al., 2009; Zhao, Gao, Shon, Cao, et al., 2011). Ti (IV) coagulation has been effectively applied to treat water and wastewater enriched with various types of pollutants, such as inorganic colloids, NOM with varying molecular weight, Algae, trace nanoparticles silver, phosphorous, arsenic and many more. The provision of resource recovery as titania (TiO_2) and negligible aquatic toxicity of residual trace metal promoted the booming interest of Ti (IV) to the current researchers. Upton and Buswell (1937), was the first to report $Ti(SO_4)_2$ coagulation to remove fluoride and color from water. At a pH of 5.2, they described better color removal using $Ti(SO_4)_2$ (85%) as coagulant comparing $Fe_2(SO_4)_3$ (63%) and $Al_2(SO_4)_3$ (50%). However, the study stated very poor removal of fluoride. Later, using hydrated oxotitanium (IV) hydroxide Lokshin and Belikov (2003) claimed efficient removal of fluoride (90 – 94%) from NaF augmented water. Ti-based coagulation gained its growing interest in the sector of water and wastewater treatment when Shon et al. (2007a) affirmed equivalent pollutant removal comparing conventional coagulants ($FeCl_3$ & $Al_2(SO_4)_3$) and steady titania recovery from the flocculated sludge. They prepared photocatalytically active anatase TiO_2 through incineration of $TiCl_4$ flocculated sludge at a temperature of 600 °C to 800 °C.

Shortly after, Lee et al. (2008), studied the aquatic toxicity of residual Ti after $TiCl_4$ coagulation. They observed negligible toxicity at a coagulant dose of 150 mg/L.

Furthermore, the prepared titania from flocculated sludge showed low toxicity comparing commercially available TiO_2 (P-25). Hence Ti-based coagulation possesses the potential to mitigate the human health and high chroma index issues of residual Al and Fe after coagulation. Zhao, Gao, Shon, Kim, et al. (2011) demonstrated a comparative coagulation study concerning $TiCl_4$ and PAC for the treatment of surface water from Queshan River. Although the optimum dose of $TiCl_4$ (35 Ti-mg/L) was found higher comparing PAC (12 Al-mg/L), they claimed higher UV_{254}, COD and DOC removal for $TiCl_4$ coagulation. Moreover, Y. Sun et al. (2013) highlighted 48.10% higher As removal when they compared the coagulation efficiency of $Ti(SO_4)_2$ with $Fe_2(SO_4)_3$. Jeon and Ahn (2018) illustrated the successful application of $TiCl_4$ and PTC in a pilot scale plant for P removal from wastewater. For removing P from wastewater, they reported similar removal efficiency for $TiCl_4$ and PTC. Also, they found the optimum basicity for PTC to be 0.3. The significant comparative studies of Ti-based coagulation with conventional ones are tabulated in **Table 2-2** with claimed notable details.

Table 2-2. Key findings of Ti-based coagulation comparing coagulation associated with conventional coagulants

Ref.	Coagulant type	Influent type	Flocculation and floc morphology	Inferences (Quality of supernatant)
Upton and Buswell (1937)	Mixture of $Fe_2(SO_4)_3$ (80%) and $Ti(SO_4)_2$ (20%) prepared from ilmenite extract and $Ti(SO_4)_2$	Tap water containing fluorides (4.5 ppm of fluoride). Total solids: 380 ppm Alkalinity: 375 ppm Hardness: 296 ppm	• Mixing speed 45 to 60 rpm during coagulant addition. • Ilmenite extract produced good amount of flocs within the pH range of 2.9 to 8.2. • Lowered temperature caused reduced speed of hydrolysis and attained better flocculation.	• Above pH 5.2, floc formation using $Ti(SO_4)_2$ was very poor. And very rapid hydrolysis inhibited flocculation. At pH beneath 5 it performed better in color removal comparing alum and $Fe_2(SO_4)_3$. • Above pH 3.5, no residual Ti was found. • At an initial pH of 5.2 and coagulant dose of 34.28 ppm, color removal showed the following trend. • $Ti(SO_4)_2$ (85%) > $Fe_2(SO_4)_3$ (63%) > $Al_2(SO_4)_3$ (50%). • None of the Ti-based coagulant were found effective in fluoride removal.
Lokshin and Belikov (2003)	Hydrated oxotitanium (IV) hydroxide	NaF solutions with fluoride ion concentration of 1.0 g/L.		• Attained fluoride removal was 90 to 94% though sorption. • Maximum fluoride removal was attained at a pH range of 4 – 4.5.

Ref.	Coagulant type	Influent type	Flocculation and floc morphology	Inferences (Quality of supernatant)
				• Regeneration of sorbent was found ineffective by treating with NaOH.
Shon et al. (2007a)	$TiCl_4$ vs $FeCl_3$ & $Al_2(SO_4)_3$	Synthetic Wastewater (Mimics biologically treated sewage effluent). MW range: 70 Da - 38900 Da. Initial DOC: 10.05 mg/L Initial pH: 7.3	• Mixing: 1 min at 100 rpm → 20 min 30 rpm → 30 min of settlement. • Decantability of $TiCl_4$ coagulation was similar to $FeCl_3$ coagulation and much higher than $Al_2(SO_4)_3$ coagulation. • Order of mean floc size, $TiCl_4$ (47.5 µm) > $FeCl_3$ (42.5 µm) > $Al_2(SO_4)_3$ (16.9 µm).	• Effective removal of organic matter was observed at MW > 250 Da by all three coagulants. • At a dose of 9.79 Ti-mg/L approximately 70% of the organic matter was removed which was equivalent to Fe and Al salt flocculation. • The effluent pH after 70% organic removal was slightly higher than 3 for $TiCl_4$ and well above 6 for $FeCl_3$ & $Al_2(SO_4)_3$. • Residual Ti content in the effluent was 10 µg/L.
H. K. Shon et al. (2009b)	$TICl_4$ along with coagulant aid, $FeCl_3$, $Al_2(SO_4)_3$, $Ca(OH)_2$	Synthetic Wastewater (Mimics biologically treated sewage effluent). MW range: 70 Da - 38900 Da.	• Mixing: 1 min at 100 rpm → 20 min 30 rpm → 30 min of settlement.	• Absence of coagulant aid: Optimized dose: 8.4 Ti-mg/L Final pH: 3.25 DOC removal: 70% • Presence of coagulant aid:

Ref.	Coagulant type	Influent type	Flocculation and floc morphology	Inferences (Quality of supernatant)
		Initial DOC: 10.05 mg/L Initial pH: 7.3		Using $FeCl_3$, Optimized dose: 4.2 Ti-mg/L + 6.9 Fe-mg/L. Final pH: 4.7 DOC removal: 70% Using $Al_2(SO_4)_3$, Optimized dose: 4.2 Ti-mg/L + 8 Al-mg/L Final pH: 4.5 DOC removal: 72% Using $Ca(OH)_2$, Optimum dose: 6.3 Ti-mg/L + 15 Ca-mg/L Final pH: 7.6 DOC removal: 70%
Okour, Shon, et al. (2009)	$TiCl_4$ & $Ti(SO_4)_2$ vs $FeCl_3$, $Al_2(SO_4)_3$	Synthetic Wastewater (Mimics biologically treated sewage effluent)	• Mixing: 1 min at 100 rpm → 30 min 30 rpm → 50 min of settlement. • $Al_2(SO_4)_3$, $Ti(SO_4)_2$ in hydrated condition possess fewer positive charges	• At initial pH of 4, $Al_2(SO_4)_3$ was found ineffective. Maximum turbidity removal order and optimum coagulant dose are as follows, $TiCl_4$ (30 mg/L) > $FeCl_3$ (20 mg/L) > $Ti(SO_4)_2$ (40 mg/L)

Ref.	Coagulant type	Influent type	Flocculation and floc morphology	Inferences (Quality of supernatant)
			comparing the other coagulant. Hence, requires high amount of optimum dosses. • $TiCl_4$ and $Ti(SO_4)_2$ solutions are acidic, hence consumes more alkalinity forming coagulants species with increased positive charges which favors adsorption of organic matter. Coagulation performance was less sensitive to pH in the range of 4 to 8. • At pH range, 6-10 $Al_2(SO_4)_3$ and $Ti(SO_4)_2$ showed similar coagulation mechanism. As, colliding sulfate particles reducing electrostatic repulsion and promotes sweep flocculation.	• At initial pH 6, Maximum turbidity removal order and optimum coagulant dose are as follows, $TiCl_4$ (30 mg/L) > $Al_2(SO_4)_3$ (30 mg/L) > $FeCl_3$ (20 mg/L) > $Ti(SO_4)_2$ (50 mg/L). • At initial pH 8, Maximum turbidity removal order and optimum coagulant dose are as follows, $TiCl_4$ (40 mg/L) = $Al_2(SO_4)_3$ (50 mg/L) > $FeCl_3$ (30 mg/L) > $Ti(SO_4)_2$ (50 mg/L) • At initial pH 10, Maximum turbidity removal order and optimum coagulant dose are as follows, $TiCl_4$ (50 mg/L) = $FeCl_3$ (40 mg/L) = $Ti(SO_4)_2$ (60 mg/L) > $Al_2(SO_4)_3$ (50 mg/L) • $TiCl_4$ and $FeCl_3$ both had the same DOC, UV-254 and SUVA removal at all pH values.

Ref.	Coagulant type	Influent type	Flocculation and floc morphology	Inferences (Quality of supernatant)
			• Order of floc mean size, $TiCl_4$ (81.99 µm) > $Ti(SO_4)_2$ (63.01 µm) > $FeCl_3$ (50.88 µm) > $Al_2(SO_4)_3$ (26.29 µm).	• $Ti(SO_4)_2$ showed best color, DOC, UV-254 and SUVA removals comparing $Al_2(SO_4)_3$ at all pH ranges.
Zhao, Gao, Shon, Cao, et al. (2011)	$TiCl_4$ vs $Al_2(SO_4)_3$, Polyaluminium chloride (PAC), $FeCl_3$, and Polyferric sulfate (PFS)	Synthetic wastewater (Synthetic water was prepared using HA and kaolin. A stock solution of HA was prepared by dissolving 1.0 g of HA in 0.01 mol/L sodium hydroxide (NaOH) solution under continuous stirring for 30min.)	• $Al_2(SO_4)_3$ and PAC showed sharp rise of zeta potential was with increased doses. • $FeCl_3$ and PFS showed small increase in zeta potential with increased doses. • $TiCl_4$ showed gradual increase of zeta potential with increasing doses. • Floc growth rate showed the following order: $TiCl_4$ > PAC > PFS > $FeCl_3$ > $Al_2(SO_4)_3$. • Order for maximum floc size was,	• Optimum coagulant doses, $Al_2(SO_4)_3$: 2 Al-mg/L PAC: 3 Al-mg/L $FeCl_3$: 8 Fe-mg/L PFS: 10 Fe-mg/L $TiCl_4$: 20 Ti-mg/L • At optimum dose of $Al_2(SO_4)_3$ Residual turbidity: 0.6 NTU UV254 removal: 93.4% DOC removal: 75.98% Final pH: 7.66 • At optimum dose of PAC, Residual turbidity: 1.09 NTU UV254 removal: 91.27% DOC removal: 76.70% Final pH: 7.92

Ref.	Coagulant type	Influent type	Flocculation and floc morphology	Inferences (Quality of supernatant)
			$TiCl_4$ (800.9 µm) > $FeCl_3$ (603.9 µm) > PFS (513.4 µm) > $Al_2(SO_4)_3$ (404.8 µm) > PAC (331.9 µm). • Order of strength factor, PAC (34) > $Al_2(SO_4)_3$ (30) > PFS (29) = $TiCl_4$ (29) > $FeCl_3$ (26) • Order of recovery factor, PAC (24.55%) > $Al_2(SO_4)_3$ (17.81%) > PFS (16.66%) > $FeCl_3$ (15.07%) > $TiCl_4$ (2.13%)	• At optimum dose of $FeCl_3$, Residual turbidity: 0.93 NTU UV254 removal: 94.14% DOC removal: 80.14% Final pH: 7.10 • At optimum dose of PFS, Residual turbidity: 0.98 NTU UV254 removal: 94.10% DOC removal: 80.93% Final pH: 6.94 • At optimum dose of $TiCl_4$, Residual turbidity: 1.03 NTU UV254 removal: 98.44% DOC removal: 84.29% Final pH: 3.77 • For all the coagulant turbidity removal increased with the increase of initial pH and at lower pH Fe and Al salts performs better comparing Ti salt. At higher pH $TiCl_4$ performed better at turbidity removal.

Ref.	Coagulant type	Influent type	Flocculation and floc morphology	Inferences (Quality of supernatant)
				• Initial pH had minor influence on the DOC removal efficiency.
Zhao, Gao, Cao, et al. (2011)	$TiCl_4$ vs PAC	Surface water from Queshan River (a source of drinking water)	• At optimum doses the zeta potentials, PAC: +4.2 mV $TiCl_4$: -3.23 mV • Despite having larger floc size, floc generated using $TICl_4$ showed higher strength factor and lower recoverability comparing PAC. • Irrespective of the coagulant better revocability was observed in acidic influent. • Strength factor of $TiCl_4$ generated flocs showed gradual increase with the increase of initial pH and PAC showed the reverse pattern.	• Optimum doses, $TiCl_4$: 35 Ti-mg/L PAC: 12 Al-mg/L • At optimum dose, the removal efficiencies $TiCl_4$, UV_{254}: 71.1% COD: 50.8% DOC: 77.9% PAC, UV_{254}: 36% COD: 21.3% DOC: 40.3%

Ref.	Coagulant type	Influent type	Flocculation and floc morphology	Inferences (Quality of supernatant)
			• At short breakage period $TiCl_4$ showed higher strength and recovery factor comparing PAC and vice versa for long breakage duration.	
Y. Sun et al. (2013)	$Ti(SO_4)_2$ vs $Fe_2(SO_4)_3$	Synthetic wastewater containing As (III), using precursor $NaAsO_2$.	• Rapid mixing for 1 min (200 rpm) → Slow mixing for 20 min (40 rpm) → Settling time 20 min.	• $Ti(SO_4)_2$ effectively removed As (III) through adsorption within a large pH range of 4-9, comparing $Fe_2(SO_4)_3$. • Using a coagulant dose of 12 mg/L at pH = 4, removal efficiency of As (III) was 48.1% higher for $Ti(SO_4)_2$ comparing $Fe_2(SO_4)_3$. • The adsorption capacity of As(III) on in situ-formed Ti(IV) hydroxides was greater than that on in situ-formed Fe(III) hydroxides by about 0.151 mg/mg.

Ref.	Coagulant type	Influent type	Flocculation and floc morphology	Inferences (Quality of supernatant)
Chekli et al. (2015)	$PTC_{1.5}$, $TiCl_4$, $FeCl_3$	Synthetic wastewater containing HA and kaolin. The measured UV_{254} absorbance, DOC, zeta potential and pH of the prepared synthetic water was: 0.257 cm^{-1} ± 0.04 cm^{-1}, 8.04 mg/ L ± 0.74 mg/L, −39.1 mV ± 1.3 mV and 7.7, respectively. Turbidity ranged from 15 – 25 NTU.	• Rapid mixing for 1.5 min (200 rpm) → Slow mixing for 20 min (40 rpm) → Settling time 20 min. • The floc growth rate during the coagulation process varied in the following order: PTC (278.90 µm/min) > $TiCl_4$ (248.50 µm/min) > $FeCl_3$ (162.90 µm/min) and the order of maximum floc size was PTC (836.9 µm) > $TiCl_4$ (764.3 µm) > $FeCl_3$ (722.2 µm). • The coagulants showed comparable strength factor, but floc recovery factor was of the following order: $TiCl_4$ (42.0%) > PTC (20.5%) > $FeCl_3$ (20.4%).	• Optimum doses, PTC: 0.15 mmole Ti/L $TiCl_4$: 0.40 mmole Ti/L $FeCl_3$: 0.15 mmole Fe/L • Zeta potential at optimum dose, $TiCl_4$: −0.4 mV $FeCl_3$: −1.2 mV PTC: −2.1 mV • Order of UV_{254} and DOC removal, $TiCl_4$ (93.5%) > PTC (89.6%) > $FeCl_3$ (88.56%) $FeCl_3$ (50.2%) > $TiCl_4$ (41.7%) > PTC (36.1%).

Ref.	Coagulant type	Influent type	Flocculation and floc morphology	Inferences (Quality of supernatant)
Jeon and Ahn (2018)	$TiCl_4$, PTC. Also, a pilot scale application of Ti salt-based coagulation.	Phosphorous (2 P-mg/L) enriched synthetic wastewater.	• Rapid mixing for 1 min (120 rpm) → Slow mixing for 20 min (30 rpm) → Settling time 30 min.	• P removal efficiency of $TiCl_4$, decreased with increased alkalinity. Considering maximum P removal (99%) the doses of $TiCl_4$ were, 0.25, 0.31 and 0.49 Ti-mM for 50, 100 and 150 mg $CaCO_3$/L, respectively. • For PTC, optimum basicity was found as 0.3. Further increase in basicity reduced the P removal efficiency. Considering basicity increased from 0.3 to 3 the required PTC dose varied from 0.27 to 0.32 mM. • For P removal, both $TiCl_4$ and PTC showed similar removal efficiency.
Liao and Zhang (2018)	Polyaluminium titanium silicate chloride (PATC), with different molar ratios of the constituents.	Surface water from lake in the Hunan University of Science and Technology. Turbidity: 7 – 21 NTU Initial pH: 7.8 ± 0.2	• Rapid mixing for 2 min (210 rpm) → Slow mixing for 10 min (50 rpm) → Settling time undefined.	• At a dose of 10.8 mg/L and temperature 50 °C, maximum turbidity removal (residual turbidity < 0.5 NTU) was observed. • At temperature of 50 °C and PATC dose above 10.8 mg/L, the turbidity

Ref.	Coagulant type	Influent type	Flocculation and floc morphology	Inferences (Quality of supernatant)
				removal efficiency showed the following trend, n(Ti)/n(Al) = 0.3 > n(Ti)/n(Al) = 0.5 > n(Ti)/n(Al) = 0.6 > n(Ti)/n(Al) = 0.1. • Considering basicity, at optimized temperature and doses, n(OH)/n(Ti+Al) = 0.2, showed the minimum residual turbidity (0.44 NTU).
X. Wang et al. (2018)	TXC, PTC, $TiCl_4$	Synthetic wastewater samples (Composed of 1. humic acid + kaolin, 2. Si suspension)	• Rapid mixing for 1 min (200 rpm) → Slow mixing for 15 min (40 rpm) → Settling time 30 min. • Within the pH initial pH range of 6 to 10, considering floc growth rate and size coagulation showed following trend, TXC > PTC > TiCl4.	• For Si suspension, at low pH (< 6) and low turbidity (< 5 NTU), trend of turbidity removal efficiency, TXC > PTC > $TiCl_4$. • Considering Si suspension, at lower pH (5.8), turbidity removal efficiency of $TiCl_4$ and PTC were limited within 3 – 6 Ti-mg/L, TXC was found effective even at 12 Ti-mg/L. • The binding affinity of HA to the hydrolysates from the three coagulants followed in order of TXC

Ref.	Coagulant type	Influent type	Flocculation and floc morphology	Inferences (Quality of supernatant)
				> $TiCl_4$ > PTC. The stronger binding of HA in the TXC system might come from the anchored AcAc in the hydrolysates of TXC.
Z. Wang et al. (2018a)	$TICl_4$, $TiCl_4$ +SA, $TiCl_4$ + MSA	Ag Nano particle enriched water. Ag NPs: 5.0 ± 0.04 mg/L HA: 10 mg/L DOC: 4.544 ± 0.50 mg/L Initial pH: 8.35 ± 0.30, Zeta potential: − 14.0 ± 0.40 mV Conductivity: 6.18 µs/cm.	• Rapid mixing at for 2 min (200 rpm) → Slow mixing for 20 min (40 rpm) → Settling time 30 min. • At varying dosage and initial pH floc size varied in the following order respectively, $TiCl_4$+MSA > $TiCl_4$+SA > $TiCl_4$; $TiCl_4$ > $TiCl_4$+SA > $TiCl_4$+MSA.	• With increasing coagulant doses all the coagulant showed increased coagulation performance. • For varying initial pH, maximum Ag and DOC removal for all the coagulant was attained at pH 5. • For both Ag NP and DOC removal at varying doses and pH the coagulants performances varied in the flowing order, $TiCl_4$+MSA > $TiCl_4$+SA > $TiCl_4$ • At a dose of 4 mg/L, TiCl4+MSA could attain an Ag removal of 65%.
J. Xu et al. (2018)	$TiCl_4$, $Al_2(SO_4)_3$, PAC, $FeCl_3$	Algae (Microcystis aeruginosa) enriched water (10^6 cells/ml).	• Raw sample → Rapid mixing for 30 second (200 rpm) → Addition of coagulant → Rapid mixing	• Optimum doses, $TiCl_4$: 50 Ti-mg/L $Al_2(SO_4)_3$: 20 Al-mg/L PAC: 30 Al-mg/L

Ref.	Coagulant type	Influent type	Flocculation and floc morphology	Inferences (Quality of supernatant)
		Initial pH: 8.44–8.67 Turbidity: 12.0–14.1 NTU UV254: 0.050–0.056 cm^{-1} DOC: 2.18–2.76 mg/L	for 1 min(200 rpm) → Slow mixing for 15 min (40 rpm) → Settling time 15 min. • At optimum coagulant dose, order of growth rate: $TiCl_4$ (185.5 µm/min) > $FeCl_3$ (173.9 µm/min) > PAC (50.5 µm/min) > $Al_2(SO_4)_3$ (45.2 µm/min) Order of strength factor: PAC (71.6%) > $Al_2(SO_4)_3$ (51.9%) > $TiCl_4$ (34.7%) > $FeCl_3$ (31.6%) Order of recovery factor: $Al_2(SO_4)_3$ (26.1%) > $FeCl_3$ (11.8%) > $TiCl_4$ (3.8%).	$FeCl_3$: 40 Fe-mg/L • At optimized dose efficiency of turbidity, UV_{254}, DOC, and OD_{680} removal was of following order respectively, PAC > $FeCl_3$ > $Al_2(SO_4)_3$ > $TiCl_4$ $TiCl_4$ > PAC > $FeCl_3$ > $Al_2(SO_4)_3$ $FeCl_3$ > $TiCl_4$ > $Al_2(SO_4)_3$ > PAC PAC > $Al_2(SO_4)_3$ > $TiCl_4$ > $FeCl_3$ • $TiCl_4$ showed highest UV_{254} removal in wide range of initial pH (6-9). • At 60 Ti-mg/L, 85% Microcystis removal was achieved. • For organic removal, In the MW range of 2200 to 2900 Da, coagulant performance order, $Al_2(SO_4)_3$ > $FeCl_3$ > PAC > $TiCl_4$ For MW of 190 Da $TiCl_4$ > $FeCl_3$ > $Al_2(SO_4)_3$ > PAC.

Ref.	Coagulant type	Influent type	Flocculation and floc morphology	Inferences (Quality of supernatant)
W. Zhang et al. (2018)	PTC with different basicity	Algae (Microcystis aeruginosa) enriched water. Turbidity: 460 NTU Initial pH: 9.54 UV_{254}: 0.73 OD_{680}: 2.223 TOC: 83.24 mg/L Initial zeta potential: −63.4 mV d_{50} = 21.3 µm	• Rapid mixing at for 2 min (250 rpm) → Slow mixing for 10 min (40 rpm) → Settling time 30 min. • Based on level of alkalisation the maximum floc size varied as follows: $PTC_{0.3}$ > $PTC_{1.5}$ > $PTC_{0.5}$ > $PTC_{1.0}$ > $PTC_{2.0}$ > PTC_0 • Low alkalisation preferred superior recovery, PTC_0 (34.64%) > $PTC_{0.3}$ (34%) > $PTC_{0.5}$ (31.42%) > $PTC_{1.5}$ (3.56%) > $PTC_{1.0}$ (3.42%) > $PTC_{2.0}$ (2.86%).	• Pre-hydrolyzed Ti performed better for algae removal comparing un-hydrolyzed one. Using 70 Ti-mg/L, 90% of the turbidity removal was achieved at alkalinity of 1 ($PTC_{1.0}$). • Order of turbidity removal efficiency at optimized dose, $PTC_{1.0}$ > $PTC_{1.5}$ > $PTC_{0.5}$ > $PTC_{2.0}$ > $PTC_{0.3}$ > PTC_0 • At optimized dose, considering high pH, PTC with high alkalisation performed better for turbidity removal and vice versa. $PTC_{1.0}$ showed superior performance in broad pH range. • Increased temperature showed improved turbidity removal.
Zhao and Li (2019)	PTC, PTS, PAC, PFS	Raw municipal wastewater from Stanley sewage	• Raw sewage → Rapid mixing for 30 second (200 rpm) → Addition of coagulant → Rapid mixing	• Considering residual organics and nutrient, optimum coagulant doses, PTC: 30 Ti-mg/L PTS: 25 Ti-mg/L

Ref.	Coagulant type	Influent type	Flocculation and floc morphology	Inferences (Quality of supernatant)
		treatment works (Stanley STW). Turbidity: 66.7±15.0 NTU UV254: 0.185±0.002 cm−1 COD: 233.0±30.0 mg/L DOC: 20.19±1.95 mg/L TP: 4.21±1.81 mg/L PO_4-P: 1.50±1.68 mg/L TN: 54.62±4.21 mg/L NH_4 –N: 24.89±0.47 mg/L Initial pH: 7.02 ± 0.05 Zeta potential: −21.84 ± 1.50 mV.	for 1 min(200 rpm) → Slow mixing for 15 min (40 rpm) → Settling time 15 min. • At the end of slow mixing order of floc size PTC (1408.1 μm) > PFS (1323.9 μm) > PTS (1090.8 μm) > PAC (848.9 μm) • Order of floc strength, PTC (95.87%) > PFS (29.16%) > PTS (25.58%) > PAC (20.38%) • Order of recovery rate, PTC (225.13%) > PTS (18.17%) > PFS (16.36%) > PAC (7.60%).	PAC: 20 Al-mg/L PFS: 25 Fe-mg/L. • Considering effluent quality order of superiority of coagulation, PTC > PTS > PAC > PFS. • At optimum dose of PTC, UV_{254}, COD, TP and PO_4-P removal reached 38.5%, 80.5%, 99.1% and 98.6%, respectively. • Zeta potential at optimum doses, PTC: −5.77 mV PTS: −2.27 mV PAC: −2.00 mV PFS: −7.14 mV

2.4 Titania (TiO_2)

From the perception of abundance and bioavailability, titanium (Ti) has been considered as a ninth most abundant element in the earth's surface and ranks as second considering only the transition metal (Buettner & Valentine, 2012). In most cases, the insoluble oxide is the prominent form of Ti, which is very hydrolysis prone (Buettner & Valentine, 2012; Einaga & Komatsu, 1981; Ferri & Riccio, 1985). Besides, around neutral pH, Ti (IV) is not very soluble in aqueous solution. William Gregor invented Ti in 1791 and later in 1821 TiO_2 (titania) was discovered (Shon et al., 2008a). Since 1970 the photo electrochemistry of TiO_2 has been extensively researched focusing CO_2 conversion, water splitting and degradation of harmful pollutants in both aqueous and gaseous solution. TiO_2 has been found to exist in three stable polymorphs, viz., rutile, anatase, and brookite (Buettner & Valentine, 2012). Considering valency band gap, photo activity and stability the anatase phase of TiO_2 has been found to be one of the most effective photocatalyst. Acknowledging the scope of the work under this study the discussion on TiO_2 will be limited to the anatase phase only.

2.4.1 TiO_2 fabrication

Some of the major TiO_2 fabrication strategies reported in Shon et al. (2008a) are listed here,

- Sulfate method
- Chloride method
- Alkoxide method
- Discrete method
- Resource recovery from Ti-based coagulation

The sulfate and chloride methods are the most used for producing TiO_2 NPs, and they contribute roughly equally to the perception of production level (McKay, 1994). Both the sulfate and chloride procedures, on the other hand, generate a significant quantity of hazardous waste that is high in acid and iron salts. Some TiO_2 manufacturing facilities in the United States threatened closure due to environmental concerns and higher expenses connected with generated waste management (Shon et al., 2008b).To produce very pure TiO_2 and thin film TiO_2 alkoxide method is utilized. TiO_2 prepared from this method is free of counter anion hence the photocatalytic activity is not hampered (Kaneko & Okura, 2002). This method is preferred for coating purposes. Some of the discrete methods are

stated in Shon et al. (2008a), and mostly these methods are utilized for production of TiO_2 thin film, viz., thermal decomposition of titanium isopropoxide vapor, thermal reaction of titanium oxyacetyleaectonate in organic media, thermal decomposition of alkoxide in an inert organic solvent, thermal oxidation of titanium metal in an autoclave, laser-induced decomposition of alkoxide, ultrasonic technique. Resource recovery from Ti-based coagulation is explained in detail in following section.

2.4.2 Fabrication of TiO_2 from Ti-based flocculated sludge

Shon et al. (2007a) was the first to prepare TiO_2 from flocculated sludge through flocculation of synthetic wastewater using $TiCl_4$. They prepared anatase TiO_2 NPs using incineration at 600 °C, and the prepared TiO_2 was found with higher BET surface area (76.3 m^2/g) comparing commercially available TiO_2 (P-25). The study showed, calcination above 800 °C produces rutile phase TiO_2, thus the authors suggested calcination temperature for anatase TiO_2 fabrication to be 600 °C. Moreover, the prepared TiO_2 NPs were found more efficient in degrading acetaldehyde upon UV irradiation comparing P-25. Shon and his team claimed, a wastewater treatment plant with a capacity of 25000 m^3/day could generate 446.5 kg/day TiO_2 NPs (Shon et al., 2007a). Later, H. K. Shon et al. (2009b) with the help of coagulant aids ($FeCl_3$, $Al_2(SO_4)_3$ & $Ca(OH)_2$) prepared metal-doped TiO_2 having increased BET surface area. They claimed Ca-doped TiO_2 as the most efficient for acetaldehyde removal comparing P-25, Al-doped, and Fe-doped TiO_2 under UV irradiation.

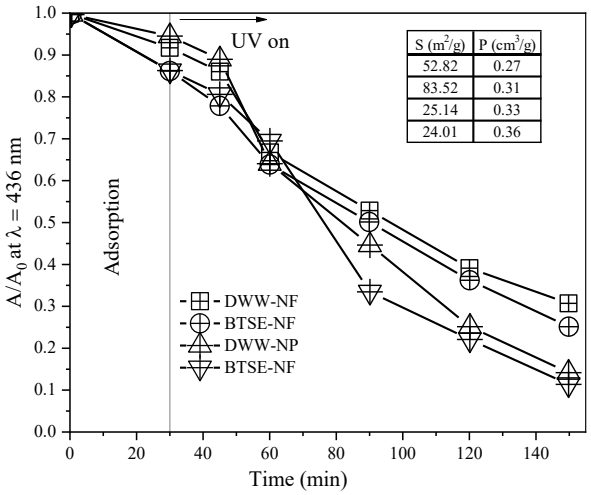

Fig. 2-6. Normalised absorbance of dissolved organics in synthetic wastewater. S = BET surface area; P = Total pore volume. Adapted from El Saliby et al. (2012)

Okour et al. (2010) using the complexation of hydrothermal treatment (130 °C for 14 h) and incineration (600 °C for 2 h) developed Thiourea-doped titanate nanotubes. The prepared Thiourea-doped TiO_2 showed an enhanced photodegrading of acetaldehyde under UV irradiation (Okour et al., 2010). Moreover, Liu et al. (2011) developed photoactive titania, containing metallurgical slag by treating metallurgical slag waste using Ti-based flocculation. Under visible light, their prepared titania exhibited 50% photodegradation of 2,4-dichlorophenol. Besides, El Saliby et al. (2012) conducted a comparative study concerning Titania NPs, and NFs generated from flocculated sludge of different genre, viz., biologically treated secondary effluent (BTSE) and dye wastewater (DWW). They claimed to observe the absorbance of dissolved organics under UV irradiation at a larger wavelength (λ = 436 nm). **Fig 2.6** briefly illustrates some of their prominent findings. Park et al. (2014) prepared TiO_2 from DWW flocculated sludge and applied it to enhance photocatalytic properties of mortar to remove NO_x. At a weight ratio of 3 and 5% for titania to mortar ratio, they stated the similar extent of NO_x removal comparing P-25. Very recently, Z. Wang et al. (2018b) studied the Ag removal from aqueous solution using modified sodium alginate assisted $TiCl_4$ flocculation. From the collected flocculated sludge, they prepared doped titania through calcination at 600 °C for 12 h. Moreover, they affirmed the presence of AgCl-TiO_2 anatase composite phase utilizing XRD analysis and stated equivalent photodecomposition of reactive brilliant red K-2BP under UV irradiation comparing commercially available TiO_2 (Z. Wang et al., 2018b).

2.4.3 Application of Nano TiO_2

The optical properties of TiO_2 play a vital role behind the diverse application of TiO_2. With the energy band gap larger than 3.0 eV, application of TiO_2 showed most promising results in the photocatalytic and photovoltaic sector (Noman et al., 2019b). Considering the scope of this study this section will only discuss the photocatalytic applications of TiO_2. The photodegradation ability and environmentally inert nature of TiO_2 triggered some extensive application concerning numerous organic pollutants removal. Fujishima et al. (2008) reported the possible use of TiO_2 in the sector of water treatment and H_2 production. Moreover, they discussed the potential application of self-cleaning and self-sterilizing surfaces. Using atomic layer deposition technique, Xiao et al. (2015) successfully deposited TiO_2 nanolayers on polyamide fabric and reported effective UV light resistance. Harifi and Montazer (2014) illustrated co-doping of Iron (Ferric) and Ag

with TiO_2 NPs. Using XPS analysis, they confirmed Fe (III) doping on TiO_2 crystal along with the deposition of Ag on TiO_2 surface. The combined effect of doping reduced the energy band gap and showed enhanced photodegradation of MB upon both UV and visible light irradiation. Ghanem et al. (2014), developed a hyperbranched TiO_2 nanocomposite with PET and reported higher photocatalytic performance along with reduced degradation time. Additionally, antimicrobial efficiency of cotton fabric was enhanced by treating with chitosan and AgCl-TiO_2, although chitosan played the major role behind the antimicrobial property (Arain et al., 2013). Using a low amount of binder Gupta et al. (2007) fabricated TiO_2 and ZnO coated cotton fiber and studied the self-cleaning characteristic of finished fabric. They claimed continuous improvement in self-cleaning with a corresponding increase of TiO_2 NPs concentration under light irradiation.

Deposition of TiO_2 NPs on glass fabric showed promising results. Ghanem et al. (2014) fabricated TiO_2 treated glass fabric using laser light irradiations technique. The enhanced glass fabric affirmed continuous degradation of orange II dye upon UV irradiation. Behzadnia et al. (2014) utilized titanium butoxide as a precursor and synthesized TiO_2 on cotton fabric using a direct sonochemical method. The modified fabric showed notable antimicrobial and self-cleaning attribute. Perelshtein et al. (2012) on the other hand used simple ultrasonic irritation to deposit TiO_2 NPs of cotton fabric. They examined the antimicrobial property of the fabric and stated significant impact on S. aureus bacteria. To reduce the recombination rate of the electron-hole pair during photodegradation, Zhou et al. (2005) using the sol-gel technique effectively developed Fe-doped TiO_2. Photodegradation performance of Fe-doped TiO_2 was compared against commercially available p-25 to oxidize acetone. Fe-doped TiO_2 resulted in reduced recombination rate and improved photocatalytic oxidation. Dougna et al. (2015), conducted a comparative study using the commercially available photocatalyst for photodegradation of phenol under UV irradiation. The study affirmed superior photoactivity of p-25 comparing other catalysts.

2.4.4 Photocatalytic activity of pure TiO_2

The photocatalytic activity of semiconductor generates from the development of electron-hole pair with the assistance of UV light irradiation. TiO_2 is an n-type semiconductor, whose conduction band (CB) and valence band (VB) are at an energy level of -0.03 eV and 2.9 eV respectively, which results in the band energy gap to be 3.2 eV (Humayun et al., 2018; Noman et al., 2019b). Considering the band energy gap, the extent of optical

absorption of TiO_2 is within the range of the UV spectrum ($\lambda < 400$ nm) (Nasirian et al., 2018). Hence, during solar irradiation against TiO_2, when the energy of the incident photon (E_p) is equivalent to the band energy gap (E_{gap}), it gets absorbed. This phenomenon leads to the excitement of electrons (e^-) from VB to CB and could assist in reduction reaction on the surface of the catalyst. As a consequence, holes (h^+) are created on the VB and eventually aid in an oxidation reaction. A simplified schematic of the whole process is illustrated in **Fig 2-7**.

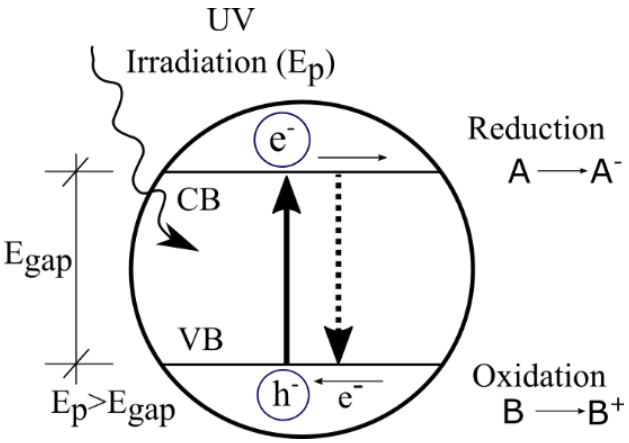

Fig. 2-7. Photogenerated charge carrier movement in TiO_2. A → Electron acceptor, B → Electron donner. Adapted Humayun et al. (2018)

Considering the redox potential of H^+/H_2 (0 eV) and O_2/H_20 (1.23 eV), the photo activated TiO_2 can carry out redox reaction and produce H_2 and O_2 respectively (Noman et al., 2019b). Similarly, chemical fuels from CO_2 and pollutant oxidation to inorganic minerals are some potent outcome of TiO_2 assisted photocatalysis. However, the photocatalytic applications of TiO_2 are still very limited as the wide band energy gap and fast recombination of the photogenerated electron-hole pair. To overcome these limitations, various forms of TiO_2 modification has been considered over time. Some prominent modification strategies are, metal and non-metal doping, dye sensitization, noble metal deposition, etc. Considering the scope of the work this report will only focus on the metal and non-metal doping for modification of TiO_2.

2.4.5 Modification strategies of TiO_2 to perform under visible light

Many researchers established that the optical absorption and electron-hole pair recombination of a nanoparticle could be altered upon introduction of secondary species in the crystal lattice. Following the substitution theory, Ti^{4+} in TiO_2 lattice can be replaced using metals with equivalent diameter and could alter the position of VB or CB by

creating a mix (Nasirian & Mehrvar, 2016). Furthermore, doped metal has also been found on the surface of TiO_2 and found to introduce a new energy level in the existing band gap. Due to having the same ionic radius Fe doping through an ultrasonic assisted hydrothermal method in TiO_2 seems to substitute Ti^{4+} from crystal lattice and reduce the energy band gap from 3.2 eV to 2.9 eV. Hence, Fe doping using this method was found to extend the optical absorption of TiO_2 from UV to visible spectrum (Sood et al., 2015). Furthermore, Roy et al. (2014) fabricated Cu doped TiO_2 using the facile hydrothermal method. The author claimed the generation of an intermediate surface state in between the VB and CB of TiO_2. As a result, the energy band gap reduced from 3.2 eV to 2.06 eV and the optical absorption was extended to visible light range. Another metal-doped TiO_2 was fabricated by Tahir and Amin (2015), using sol-gel method and indium (In) as the dopant. The energy band gap was enlarged, and optical absorption was slightly shifted towards reduced wavelength. Besides, surface active sites were significantly increased, and electron-hole pair recombination was suppressed. Hence, photocatalytic reduction of CO_2 was increased considerably.

Although metal doping effectively improved the photocatalytic properties of TiO_2, the effectiveness of metal dopant is greatly dependent on its role as a photo-induced electron trapper (Humayun et al., 2018). Incident light intensity, dopant concentration along with the level of distribution and the electron donner density seems to play a complex role towards effectivity of metal-doped TiO_2. It has been observed under high light intensity when all the electron trapping sites are fully occupied the doped metal ion tends to work as a recombination center. Based on the reviewed pieces of literature, the redshift (UV to visible spectrum) of optical absorption for non-metal-doped TiO_2 can be explained by three fundamental mechanisms, viz., a) reduction in energy band gap resulting from mixing of orbitals (Banerjee et al., 2015), b) introduction of oxygen vacancies through enhancement of catalyst density (Banerjee et al., 2015; J. Lu et al., 2017), and c) development of localized energy level in the band gap due to substitutional and interstitial doping (Banerjee et al., 2015). Hou et al. (2014) successfully developed nitrogen (N) doped TiO_2 nanotubes hydrothermally and showed enhanced degradation of methyl orange (MO) under visible light irradiation. The band gap narrowing was explained using orbital mixing and oxygen vacancies. The band gap was effectively reduced to 2.84 from 3.2 eV. Lately, McManamon et al. (2015) fabricated sulfur (S) doped TiO_2 using a sol-gel method and reported enhanced photodegradation of malachite green under visible

light. The author described a generation of surface state within VB and CB though interstitial attachment of S. The energy band gap was significantly reduced from 3.2 to 1.7 eV. Furthermore, it was affirmed that the doping of carbon (C) on TiO2 nanoparticles, substitute oxygen and creates oxygen vacancies (Wu et al., 2013). Hence, the optical absorbance was significantly altered, and the band gap was reduced to 2.39 eV. The reported C doped TiO_2 showed enhanced oxidation of nitric oxide (NO) and MO.

2.5 TiO_2 based composites

In the recent few decades, wastewater and air treatment technology have experienced a new development on a semiconductor based photocatalysis that is considered environmentally friendly and highly effective in destroying numerous inorganic and organic pollutants. Currently, several semiconductors, including ZnO, CdS, V_2O_5, WO_3, and TiO_2, exhibited high photocatalytic ability in photodegradation of many organic pollutants (Zhou et al., 2016). Among them TiO_2 has been considered a very effective photocatalyst because of its lower price, non-toxicity, and enhanced stability (Asahi et al., 2014; Diker et al., 2014). The practical applications of TiO_2, however, has been a challenge because of the fast electron recombination rate and considerable energy bandgap of about 3.2 eV (Nasirian et al., 2017). In this regard, efforts have been made to decrease the photogenerated charge recombination and enhance light absorption by TiO_2 into the region of visible light (Asahi et al., 2014). Hence, several methods have been suggested to develop superior TiO_2. These methods include; formations of heterojunctions with semiconductors that have narrow band gaps and doping the TiO_2 with other metallic or non-metallic elements (Y. Huang et al., 2019; H. Liu et al., 2019). High photocatalytic performance has been realized due to the synergistic effect that results from coupling TiO_2 with visible light-sensitive semiconductors. The synergetic effects may include; improved photostability, efficient photoexcited charge separation, and increased light harvesting (Baca et al., 2019). However, to ensure smooth charge transfer through the heterojunction, it is necessary to consider the close interfacial connection of the two semiconductors concerning the recommended CB and VB (Jo et al., 2019).

Graphitic carbon nitride (g-CN) has recently sparked interest over its potential visible light-induced photoactivity. In normal condition g-CN is characterized by a polymeric system that is conjugated and developed by tri-s-triazine or interconnected s-triazine units having tertiary amines (Naseri et al., 2017). The atomic layer of g-CN takes a honeycomb

configuration arrangement that is covalently bonded, and the polymeric sheets are connected by weak van der Waals forces (Thomas et al., 2008). In correspondence with the H_2 electrode at pH 7, the g-CN presents a small bandgap of about 2.7 eV with its CB and VB positions at −1.3 eV and +1.4 eV respectively (Kandi et al., 2017). Hence, theoretically, g-CN can effectively generate photogenerated e^-/h^+ pairs under visible light irradiation. Additionally, the fast photo-induced charge separation and slow recombination of charges in the process of electron transfer provided by the delocalized conjugated p structure of g-CN makes it a lucrative candidate in designing more efficient visible light driven photocatalyst (S. Kumar et al., 2018). In this regard, preparation of photocatalytic composites through coupling of TiO_2 and g-CN could be one of the best strategies to synthesis superior visible light sensitive photocatalysis. Several studies have been conducted to investigate the use of g-CN in the preparation of composite photocatalyst (Baca et al., 2019; Fajrina & Tahir, 2019; Haider et al., 2019). This review mainly focuses on the major developments and modification of composite photocatalysts of g-CN utilizing titania. To date, a number of techniques have been employed for the preparation of TiO_2/g-CN composite. Researchers have utilized simple impregnation (Sun et al., 2019), ball milling (Zhou et al., 2015), electrospinning (Wei et al., 2016), solvothermal treatment (Pan et al., 2019), modified sol-gel method (Li et al., 2016), electrodeposition (Zhou et al., 2012), microwave assisted synthesis (Wang et al., 2013), ultrasonic exfoliation (Du et al., 2019), chemical vapor deposition (Ma et al., 2018), and facile annealing (Wang et al., 2015) for the preparation of TiO_2/g-CN composites. Moreover, The TiO_2/g-CN composite catalysts have several applications due to their excellent performance of the photocatalytic activity. The following sections discusses the current development of the studies related to the composite catalysts produced by g-CN and TiO_2 concerning its synthesis routes and environmental applications.

2.5.1 Preparation of TiO_2/g-CN composites

Because the TiO_2/g-CN composite is composed of two kinds of single component catalyst g-CN and TiO_2, the preparation of TiO_2/g-CN can be attained by either direct mixing of g-CN and TiO_2 or mixing of their corresponding precursors. Regardless of the method used, the target is to ensure g-CN, and TiO_2 contact forms a composite structure.

2.5.1.1 Direct mixing of g-C_3N_4 and TiO_2

This method of synthesis is usually done by independent preparation of TiO_2 and g-CN, after which the components are blended by processes such as evaporation of the dispersed

solution, ball milling and thermal treatment. Yan and Yang (2011) obtained TiO_2/g-CN by mixing TiO_2 and g-CN powder by a ball milling technique with a changing wt.% of g-CN. They prepared TiO_2 by the hydrolysis of $TiCl_4$ in ammonia, while the g-CN was synthesized from melamine by thermal decomposition at 600 °C in the presence of Ar gas. Similarly, Zhou et al. (2015) used the ball milling process to synthesis g-CN/TiO_2 composite photocatalysts whose photocatalytic performance was enhanced. They, too, synthesized the g-CN through direct calcination of melamine, thereby mixing (350 rpm) the powder of TiO_2 and g-CN in a ball mill. This resulted in the formation of a structure of g-CN on the TiO_2 surface. Most notably, this study also discovered that there is enhanced photocatalytic efficiency when the rate of milling is increased. A study on the visible light driven photocatalyst, brookite (br)-TiO_2 hybridized with g-CN was first conducted by Zang et al. (2014). The preparation of this hybrid was done through pyrolysis of br-TiO_2 and g-CN in air. The br-TiO_2/g-CN composite performed better under visible light compared to conventional anatase and rutile titania coupled with g-CN. Very recently, Kočí et al. (2017) prepared TiO_2/g-CN composite by mere calcination of pre-synthesized TiO_2 and g-CN. They have prepared the TiO_2 through thermal hydrolysis and the g-CN was prepared by calcining melamine at 620 °C. Jiang et al. (2018) on the other hand, prepared N-TiO_2/g-CN through ultrasonication followed by calcination at 450 °C for 2 h. Compared to standalone use of N-TiO_2 and g-CN the prepared composite showed superior atmospheric NO removal under visible light. A WO_3/TiO_2/g-CN composite was prepared by Tahir et al. (2019) by using facile calcination of hydrothermally treated mix of WO_3, TiO_2 and g-CN. Before calcination they kept the corresponding mix in an autoclave chamber at a temperature of 180 °C for 12 h.

Other than the ball milling and simple annealing technique, solvent evaporation as a physical mixing method is also largely being used for the preparation of the TiO_2/g-CN composite catalyst. This process involves the uniform dispersion of g-CN and TiO_2 in any solvent (e.g., methanol) before evaporating so that the g-CN and TiO_2 combine to form the heterogeneous structure. For instance, Gu et al. (2014) used this method to hybridize anatase TiO_2 nanosheets having (001) facets with g-CN. In their study, urea was calcined for the preparation of polymeric g-CN, while the synthesis of anatase TiO_2 nanosheets of dominant (001) facets were done through the solvothermal reaction of tetrabutyl titanate (TBT). Both g-CN and washed precipitate were then uniformly dispersed in methanol through sonication. After this, it was put in a fume hood for twelve

h. Upon complete evaporation, the mixture was dried at 100 °C for about 4 h. The solvent evaporation technique on the solution of g-CN and TiO_2 (B) allotrope in methanol, was also used by Zhang et al. (2014) to synthesis TiO_2(B)/g-CN with enhanced visible light photoactivity. In this process, melamine was thermally decomposed in a muffle furnace at 550 °C for 4 h to prepare g-CN while the preparation of TiO_2(B) nanofibers was done using a hydrothermal method and subsequent calcination technique. Similarly, Chen et al. (2014) prepared Ag-TiO_2/g-CN microspheres with enhanced performance under visible light irradiance. However, they synthesized the protonated g-CN sheets via the thermal treatment of melamine in a solution of HCl. TiO_2 was formed using a conventional hydrothermal process. Deposition of Ag was done through photodeposition, and then the g-CN was mixed by forming a suspension at 70 °C with Ag/TiO_2 microspheres. A Pt decorated TiO_2 nanotube (TNT)/g-CN composite was prepared by Gao et al. (2016) using a facile chemical vapor deposition technique. They have used a Ti substrate in fluoride based electrolytes for the development of TNT through anodization. Lately, using $C_6H_{12}O_6$ as a template Ma et al. (2018) reported a technique to synthesize TiO_2/g-CN hollow microsphere. The detailed synthesis route is elaborated in the **Fig. 2-8**. Based on their analysis, they have argued that the g-CN can be easily coated on the hollow microsphere of TiO_2, and the photocatalytic activity was severely increased. To prepare the hollow sphere, they have used $C_6H_{12}O_6$ and $(NH_4)_2TiF_6$ as precursor during the solvothermal treatment. Furthermore, Y. Huang et al. (2019) successfully prepared a photocatalytically enhanced composite using self-doped TiO_2 and protonated g-CN (p-CN) at room temperature. For the preparation of p-CN they have mixed g-CN with HCl (37%) vigorously stirred for 12 h. For self-doped TiO_2 they completely dispersed TNT in HCl solution and recrystallized at the room temperature. TiO_2/g-CN composite synthesis through direct mixing of the respective components is an easy method to use and can be scaled up for use in large scale production. However, uniform mixing has been a challenge since it may not be easily achieved. Besides, the morphology of the photocatalysts plays a vital role in promoting enhanced photoactivity, which may not be precisely controlled through this method.

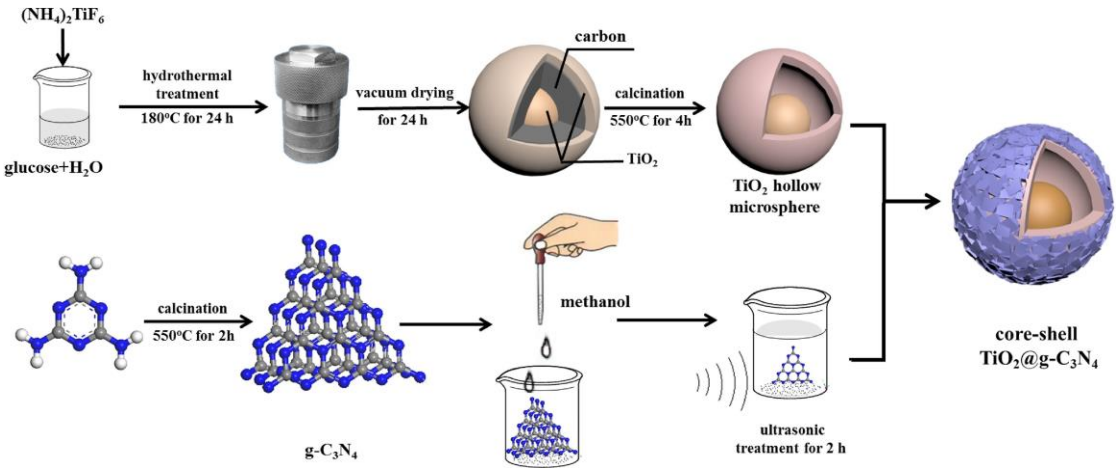

Fig. 2-8. Preparation route for the TiO_2 hollow microsphere composited g-CN (Ma et al., 2018).

2.5.1.2 Direct mixing of the corresponding precursors

In this method, either g-CN or TiO_2 is firstly prepared using conventional processes. Then the prepared nanomaterials (g-CN or TiO_2) are blended with the precursor of the alternative, making the in situ growth of TiO_2/g-CN composite. For instance, Lu et al. (2010) used such strategy in the synthesis of TiO_2/g-CN. They prepared g-CN by polymerizing dicyandiamide at 600 °C for 5h in the N_2 environment, and then the g-CN was dispersed into a hydrolyzed $Ti(OC_4H_9^n)_4$ solution. The corresponding TiO_2/g-CN composite was synthesized after the hydrothermal reaction and showed superior rhodamine B (RhB) degradation under both UV and visible light irradiation. Furthermore, Zhao et al. (2012) used a similar method to synthesis TiO_2/g-CN by dispersing g-CN into hydrolyzed $TiCl_4$ solution. They have reported TiO_2/g-CN composite with light absorption wavelength ranging from 300 nm to 450 nm. Their prepared composite showed enhanced photoactivity under visible light, and the TEM image showed well-dispersed TiO_2 on g-CN sheets. A study done by Shen et al. (2014) reported a novel and template free technique for the development of a network structure of mesoporous g-CN/TiO_2 with improved photocatalytic activity. The detailed method is elaborated in **Fig. 2-9**. Briefly, this method involved an initial synthesis of g-CN through the calcination of melamine and addition of g-CN into Ti $(SO_4)_2$ solutions in a hydrothermal reaction to obtain the TiO_2/g-CN.

More studies have recently been done on N doped titania (N-TiO_2) concerning its high environmental applicability. In this regard, many studies have successfully grown the N-

TiO_2 on g-CN to form a heterojunction (Han et al., 2014; Jiang et al., 2018; Sun et al., 2019; Wang et al., 2013). For instance, in the synthesis of N-TiO_2/g-CN, composite, Wang et al. (2013) utilized a microwave assisted synthesis method with H_2TiO_3 being a precursor for TiO_2, and NH_3H_2O as the source of N-doping. When preparing the catalyst, g-CN was taken in together with H_2TiO_3 in a microwave stimulated reaction. The prepared composite revealed significant enhancement in surface area and porosity. Hence, it showed superior photoactivity compared to standalone use of TiO_2 or g-CN. The author reported that the presence of 40 wt.% of N-TiO_2 in TiO_2/g-CN exhibited the highest photocatalytic activity. A simple electrospinning process, along with a modified heat etching technique, has been used by Han et al. (2014) to synthesis nitrogen doped titania nanotube (N-TNT)/g-CN composite. This method involved a thermal polymerization of melamine to obtain g-CN, which was later dispersed into a solution of acetic acid together with titanium (IV) n-butoxide (TNBT) and poly vinylpyrrolidone (PVP). N was doped into TiO_2 to reduce the energy bandgap, promote the extension of light absorption and ensure higher photocatalytic efficiency under visible light. Recently, Sun et al. (2019) used a simple impregnation technique to couple N doped TiO_2/diatomite with g-CN for the purpose of Cr (IV) reduction. For doping N on TiO_2/diatomite, they have used simple impregnation technique. Later, the final N-TiO_2/g-CN@diatomite was prepared though calcination of the mixture of N- TiO_2/diatomite and urea.

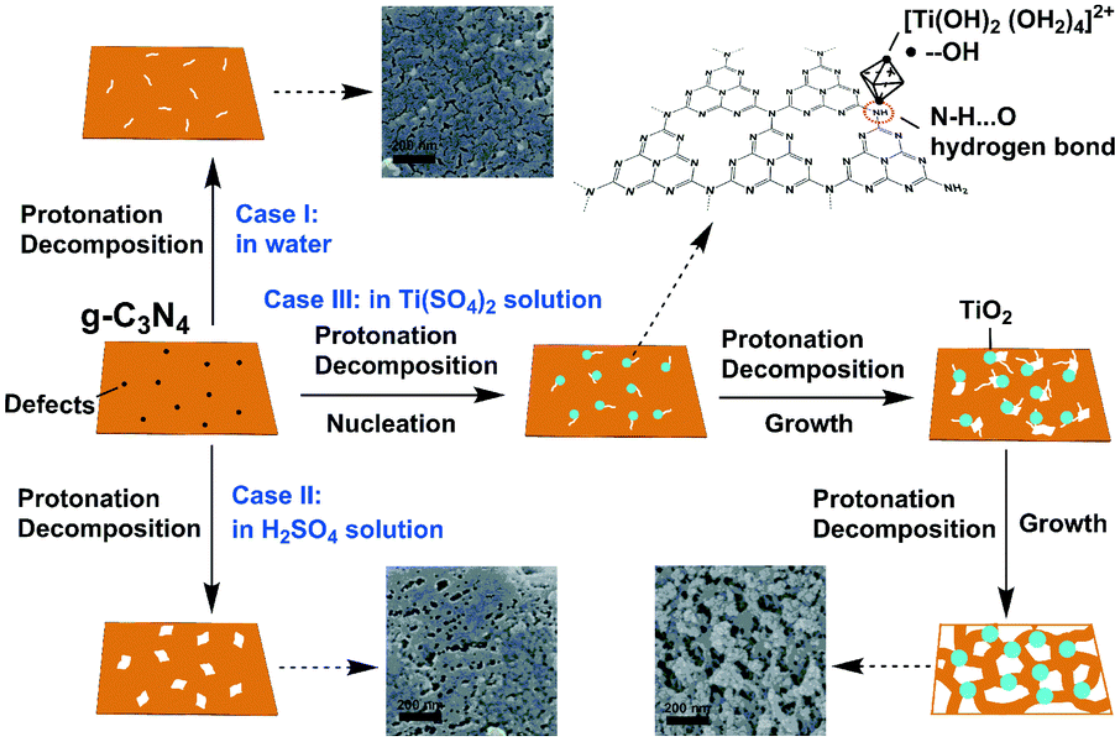

Fig. 2-9. Preparation route of TiO_2/g-CN in template free synthesis (Shen et al., 2014).

It is well established that the exposure of a high energy surface of a crystal can be controlled by the solvothermal reaction. Hence, Huang et al. (2015) synthesized TiO_2 hollow nano box (TiO_2-HNB) assemble in TiO_2-NS on g-CN to form the TiO_2/g-CN composite. They also did some comparative study on the impacts of high energy interfaces of TiO_2 (101) and (001) facets, concerning the activity of photocatalysis. They prepared the catalyst using a tert butyl alcohol (TBA) solvent in a solvothermal process. Song et al. (2016) on the other hand used facile solvent free calcination for the preparation of TiO_2 (001)/g-CN heterostructure. Initially, they prepared the (001) facet exposed TiO_2 nanosheets using hydrothermal method. As TiO_2 precursor they have used TNBT mixed with HF. In another work, H. Li et al. (2015) elaborated on the in situ growth of TiO_2 on g-CN through a solvothermal strategy. They have grown TiO_2 crystal on g-CN using solvothermal treatment of TBOT in the presence of ammonium acetate. K. Li et al. (2015) prepared Ti^{3+} doped TNT-g-CN composite utilizing a one-step pyrolysis of $H_2Ti_3O_7$ nanotubes with melamine. The TNTs were prepared through the hydrothermal treatment of TiO_2 powder in 10 M NaOH solution. For successful growth of the nanotubes, they have heated the mixture of TiO_2 and NaOH in a teflon lined autoclave for 48 h at a temperature of 180 °C. Moreover, Wang et al. (2015) used facile ball milling induced calcination of commercially available P25 and melamine to prepared visible light

activated photocatalyst. To formulate less energy-intensive techniques, Zou et al. (2011) synthesized mesoporous TiO_2 spheres by using a synthetic light-driven strategy. Under mild conditions, this strategy may be used for the activation of urea to produce g-CN. Besides, to prepare the composite in mild condition Zhou et al. (2012) used a simple electrochemical method to synthesize TiO_2/g-CN nanotube array (TNT/g-CN). In their method, electrodeposition resulted in the deposition of g-CN polymer in the crystallized TiO_2 nanotubes.

A number of current studies have reported successful synthesis of TiO_2/g-CN composite through simple calcination of the mixture of commercially available TiO_2 and any other g-CN precursors (e.g., melamine, urea). For example, Giannakopoulou et al. (2017) successfully prepared TiO_2/g-CN composite through simple calcination of the of the dry mixture of P25 and melamine. Using varying wt.% of melamine in the mixture they have successfully modified the energy band gap and edge potentials of the TiO_2/g-CN composites. Papailias et al. (2017) also synthesized TiO_2-g-CN composites by calcining TiO_2 and melamine mixture in a tube furnace at a temperature of 550 °C for 3 h. Both of the TiO_2/g-CN composites prepared by Giannakopoulou et al. (2017) and Papailias et al. (2017) showed superior atmospheric NO_x removal compared to commercially available P25. Although, template free preparation of TiO_2/g-CN composites were favored by the researchers, very recently Pan et al. (2019) used a SiO_2 template based method for the preparation of self-doped black TiO_2/g-CN. They have used continuous hydrothermal deposition and sculpture reduction technique for this method. Using SiO_2 as a template and titanium(IV) isopropoxid as TiO_2 precursor they have prepared TiO_2 microspheres though ultrasonic mixing followed by drying and annealing at 450°C for 4 h. Later, g-CN was coupled though conventional calcination. Based on the aforementioned discussion it is very clear that the strategy of growing either TiO_2 on g-CN or vice versa is an effective technique to prepare TiO_2/g-CN composites. Besides, composites prepared in such manner are chemically stable and can sustain multiple cycles of experiments. However, in case of template free facile synthesis, it may be difficult to attain a very uniform distribution of TiO_2 on the g-CN sheets because of the rapid hydrolysis of TiO_2 precursors. Hence, it is still a big challenge to control the TiO_2 with the desired size distribution and dispersity.

2.5.2 The applications of TiO_2/g-CN composites

Both TiO_2 and g-CN are very effective photocatalysts; however, they have their shortcomings towards practical applications due to prevailing crystal and electronic structure. Meanwhile, the development of TiO_2/g-CN could mitigate each other's flaws and improve photoactivity. Most of the current research regarding the application of TiO_2/g-CN is vested majorly in H_2 evolution, inorganic and organic pollutants degradation, inactivation of bacteria, treatment of heavy metals, and CO_2 reduction. Some of the applications concerning H_2 evolution and degradation of pollutants in gaseous and aqueous mediums are briefly discussed here.

2.5.2.1 H_2O splitting towards H_2 evolution

The global energy crisis due to limited amounts of fossil fuel urges for the invention of new kinds of sustainable energy sources. From that perspective, several methods of production of H_2 have largely been studied. Among them, H_2 evolution through photocatalysis of H_2O using titania has been favored by many researchers. However, TiO_2 can only absorb the light spectrum in the UV region. Hence, scientists have extensively studied the visible light active TiO_2/g-CN composite for H_2O splitting. **Table 2-3** summarizes the significant studies conducted towards H_2 evolution by using TiO_2/g-CN composites. Yan and Yang (2011) prepared TiO_2/g-CN composite materials by varying the wt.% of g-CN and used the samples in photocatalytic H_2 evolution. Their work showed that the rate of evolution of H_2 was higher, using the as prepared TiO_2/g-CN in the photocatalysis experiment. Additionally, Chai et al. (2012) developed a porous Pt decorated TiO_2/g-CN and reported that the method exhibited maximum catalytic ability with excellent production of H_2 under visible light irradiation. Gao et al. (2016) also prepared a Pt decorated TNT/g-CN using a chemical vapor deposition approach for H_2 generation under visible light irradiation. Their prepared Pt-TNT/g-CN showed 98 times higher H_2 generation compared to standalone use of TNT under visible light. Per cm^{-2} of the prepared electrode they have reported an H_2 generation of 15.62 $\mu L.h^{-1}$. Wei et al. (2016), on the other hand, synthesized nanofibers with a ternary heterostructure exhibiting nanosheets of g-CN, plasmonic noble metal (Au, Ag, or Pt) nanoparticles (NPs), and TiO_2. The prepared TNT/g-CN composites decorated with noble metals showed high charge carrier mobility and enhanced production of H_2. Chen et al. (2016) developed an anatase boron-doped TiO_2 (B-TiO_2) with exposed (001) facets and composited it with the g-CN. The catalyst showed 25 times higher catalytic activity for

the production of H_2 compared to standalone use of TiO_2. The author stated that the reduced charge recombination, and high absorption of visible light are the main reasons of enhanced photoactivity. Tan et al. (2018) synthesized a Ti^{3+} TiO_2/g-CN mesoporous nanosheet for visible light based H_2 evolution. They have reported a successful reduction in energy band gap ($E_g \approx 2.21$ eV) and improvement of specific surface area (73.8 $m^2.g^{-1}$). Hence, the photoactivity under visible light was significantly increased, compared to g-CN (4 times) and TiO_2 (14 times). A maximum generation of 290.2 $\mu mol.h^{-1}.g^{-1}$ H_2 was reported in their study. For the purpose of H_2 generation Wu et al. (2018) prepared a noble metal free N-TiO_2/g-CN 3D structure. To enhance photoactivity they have photochemically deposited Ni_xP on N-TiO_2/g-CN composite. The resulted composite showed 5.3 times higher photoactivity under visible light compared to Ni_xP deposited g-CN. The maximum H_2 generation they have reported was 5438 $\mu mol.h^{-1}.g^{-1}$ H_2.

Table 2-3. Salient features of the significant studies concerning TiO_2/g-CN based H_2 evolution

Refs.	**Composite**	**Light source**	**Intensity ($mW.cm^{-2}$)**	**Sacrificial donor, catalyst**	**Irradiation time (min)**	**H_2 evolution**
Yan and Yang (2011)	TiO_2/g-CN	450 W mercury lamp (λ = 436 nm)		CH_3OH, Pt	180	22.4 $\mu mol.h^{-1}$
Chai et al. (2012)	Pt-TiO_2/g-CN	300 W Xe lamp ($\lambda \geq$ 420 nm)		Triethanolamine		178 $\mu mol.h^{-1}$
Han et al. (2014)	N-TNT/g-CN	300 W Xe lamp (Full spectrum)		CH_3OH, Pt	120	8931.3 $\mu mol.h^{-1}.g^{-1}$
Zang et al. (2014)	TiO_2(Br)/g-CN	300 W Xe lamp ($\lambda \geq$ 420 nm)		Triethanolamine, H_2PtCl_6	180	1058 $\mu mol.h^{-1}.g^{-1}$
Chen et al. (2016)	B-TiO_2-(001)/g-CN	300 UV Xe arc lamp ($\lambda \geq$ 400 nm)	150	CH_3OH, Pt		45.1 $\mu mol.h^{-1}$
Gao et al. (2016)	Pt-TNT/g-CN	Simulated sunlight AM 1.5	100	C_2H_5OH		15.62 $\mu L.h^{-1}.cm^{-2}$
Jian Ma et al. (2016)	TiO_2-(001)/g-CN	300 W Xe lamp ($\lambda \geq$ 420 nm)	90	Triethanolamine, Pt	180	32.98 $\mu mol.h^{-1}$
Wei et al. (2016)	Ag- TiO_2/g-CN	500 W Xe lamp (Solar spectrum)	100	Triethanolamine	120	1.50 $\mu mol.h^{-1}$
	Au- TiO_2/g-CN					1.19 $\mu mol.h^{-1}$
	Pt- TiO_2/g-CN					0.89 $\mu mol.h^{-1}$

Refs.	**Composite**	**Light source**	**Intensity ($mW.cm^{-2}$)**	**Sacrificial donor, catalyst**	**Irradiation time (min)**	**H_2 evolution**
Tan et al. (2018)	Ti^{3+}-TiO_2/Meso-g-CN	300 W Xe lamp (Solar spectrum)			180	290.2 $\mu mol.h^{-1}.g^{-1}$
Wu et al. (2018)	N-TiO_2/g-CN@Ni_xP	300 W Xe lamp (Solar spectrum)		Triethanolamine	150	5438 $\mu mol.h^{-1}.g^{-1}$
Pan et al. (2019)	Ti^{3+}-Black-TiO_2/g-CN	300 W Xe lamp (Solar spectrum)	100	Triethanolamine	300	808.97 $\mu mol.h^{-1}.g^{-1}$

2.5.2.2 Degradation of pollutants in the gaseous phase

Photocatalysis has been found as an effective mechanism for the degradation of air pollutants, and TiO_2/g-CN is one of the widely researched composites in this aspect. To date, scientists have successfully applied TiO_2/g-CN for degrading several harmful atmospheric pollutants, such as HCHO (J. Yu et al., 2013), C_3H_6O (Jian Ma et al., 2016), CO_2 (Thanh Truc et al., 2019; Zhou et al., 2014), NO_x (Jiang et al., 2018; Papailias et al., 2017), N_2O (Kočí et al., 2017; Troppová et al., 2018), and many more. **Table 2-4** illustrates on some of the important studies in this regard. In an attempt to mitigate interior air pollution generating from HCHO, J. Yu et al. (2013) developed a TiO_2/g-CN composite using a mixture of urea and P25. The author has observed Z scheme photocatalysis during photodegradation of HCHO using the as prepared composite, under UV irradiation. Their prepared TiO_2/g-CN showed a maximum of 7.36 x 10^{-2} min^{-1} reaction rate by considering a pseudo 1st order reaction, which was nearly 2 times higher than standalone use of P25. Similarly, Jian Ma et al. (2016) photodegraded acetone under visible light irradiance. Using a solvothermal method, they have prepared (001) facet dominated TiO_2/g-CN composite. The as prepared composite was found to remove approximately 76.55% of acetone within 2 h under visible light (λ = 420 nm) irradiance. Zhou et al. (2014) used TiO_2/g-CN composite prepared from facile calcination of P25 and urea for photoreduction of CO_2 into CO and showed a successive increase in the extent of photoreduction. They have compared the reduction rate of CO_2 with commercially available P25 and prepared g-CN. After 12 h irradiation under a 300 W Xe lamp, TiO_2/g-CN, P25, and g-CN had produced 14.73 µmol , 3.19 µmol and 4.21 µmol of CO, respectively. In a recent study, Thanh Truc et al. (2019) emphasized on the evolution of valuable fuel from photoreduction of CO_2 by utilizing the photoactivity of Nb doped TiO_2/g-CN. They have reported a maximum generation of 562 $\mu mol.h^{-1}.g^{-1}$, 420 $\mu mol.h^{-1}.g^{-1}$ and 698 $\mu mol.h^{-1}.g^{-1}$ of CH_4, CO and HCOOH respectively using photoreduction of CO_2, under visible light. The maximum photoactivity was found when the Nb-TiO_2 to g-CN ratio was 1:1.

Over the past decades, a substantial increase in atmospheric NO_x ($NO+NO_2$) has been observed, and photocatalytic oxidation of NO_x is one of the prominent solutions towards this problem. Many research groups nowadays have focused on this topic and developed a number of efficient photocatalysts to oxidize NO_x into a more neutral product. Giannakopoulou et al. (2017) have tried an easy solvent free mechanical mixing followed

by calcination technique to tailor the energy bandgap of TiO_2/g-CN, to facilitate NO oxidation. They have tried to oxidize an initial concentration of 1 ppm NO under both visible (7000 lux) and UV (10 Wm^{-2}) light irradiation. After 40 min of irradiance, they have attained a maximum of 38% and 42% of removal for visible and UV light, respectively. Papailias et al. (2017), also tried removal of NO_x using TiO_2/g-CN and attained a removal rate of 18% and 22.5% after 30 min by using visible and UV irradiation, respectively. They have modified the surface morphology of the as prepared composites with the assistance of $CaCO_3$. Recently, Y. Huang et al. (2019) used a simple ultrasonic exfoliation technique and synthesized Ti^{3+} TiO_2/p-CN composite for the purpose of NO oxidation. Using an initial NO concentration of 400 ppb, they have attained a removal percentage of 25.8% after 30 min of irradiation. Research has also been conducted for the breaking down of N_2O into N_2 and O_2 in a gaseous medium using TiO_2/g-CN composites. Kočí et al. (2017) reported accelerated oxidation of N_2O using as prepared TiO_2/g-CN under both UV-C and UV-A light. The rate of decomposition of N_2O was fitted with a 1st order kinetic model, and the resulted reaction rates were 8.50×10^{-2} h^{-1} and 6.63×10^{-2} h^{-1} for UV-C and UV-A type lights respectively. In both cases, the decomposition rates were superior compared to standalone use of P25 and as prepared g-CN. Troppová et al. (2018) also reported N_2O decomposition under UV-A light. However, they have proposed a novel low energy-intensive synthesis technique by using pressurized water. After 20 h of irradiance, they have decomposed nearly 70.6% of 928 ppm of N2O. The primary factor influencing photocatalytic activity in the gaseous medium is the adsorption capacity of the catalyst. Altering the morphologies and structures is the new and significant trend in the study of TiO_2/g-CN composite for breaking down atmospheric pollutants.

Table 2-4. Salient features of the significant studies concerning TiO_2/g-CN based atmospheric pollutant degradation

Refs.	**Composite**	**Light source**	**Light intensity**	**Pollutant**	**Flowrate, conc.**	**Irradiation time (min)**	**Rate of degradation**
J. Yu et al. (2013)	TiO_2/g-CN	15 W UV lamp ($\lambda \approx 365$ nm)	2.5 $mW.cm^{-2}$	HCHO	170 ppm	60	$K = 7.36\times10^{-2}$ min^{-1}
Zhou et al. (2014)	N-TiO_2/g-CN	300 W Xe lamp (UV-Vis)	100 $mW.cm^{-2}$	CO_2	15 $mL.min^{-1}$	720	14.73 µmol
Jian Ma et al. (2016)	TiO_2-(001)/g-CN	300 W Xe lamp ($\lambda \geq 420$ nm)	90 $mW.cm^{-2}$	C_3H_6O		120	76.55%
Jinzhu Ma et al. (2016)	TiO_2/g-CN	500 W Xe lamp ($\lambda \geq 420$ nm)	35.8 $mW.cm^{-2}$	NO	1.2 $L.min^{-1}$, 400 ppb	30	44%
		500-W Hg lamp ($\lambda \approx 366$ nm)	84.7 $mW.cm^{-2}$				55%
Song et al. (2016)	TNS-(001)/g-CN	500 W halogen lamp ($\lambda \geq 420$ nm)	0.7 $mW.cm^{-2}$	NO	200 $mL.min^{-1}$, 40 ppm	60	12.6%
		125 W mercury lamp ($\lambda \approx 365$ nm)	1.6 $mW.cm^{-2}$				59.4%

Refs.	Composite	Light source	Light intensity	Pollutant	Flowrate, conc.	Irradiation time (min)	Rate of degradation
Kočí et al. (2017)	TiO_2/g-CN	UVC (λ = 254 nm)		N_2O	1020 ppm		$K = 8.50\times10^{-2}\ h^{-1}$
		UVA (λ = 365 nm)					$K = 6.63\times10^{-2}\ h^{-1}$
Giannakopoulou et al. (2017)	TiO_2/g-CN	Visible light	7000 lux	NO	3 $L.min^{-1}$, 1 ppm	40	38%
		UVA light	10 $W.m^{-2}$				42%
Papailias et al. (2017)	$CaCO_3$-TiO_2/g-CN	8W - 4000 K lamp	7000 lux	NO_x	3 $L.min^{-1}$, 1 ppm	30	18%
		UVA light	10 $W.m^{-2}$				22.5%
Jiang et al. (2018)	N-TiO_2/g-CN	8 W Hg lamp (UVA)		NO	2.4 $mL.min^{-1}$, 600 ppb	30	46.1%
Troppová et al. (2018)	TiO_2/g-CN	150 W Xe lamp		N_2O	978 ppm	1200	70.6%
Y. Huang et al. (2019)	Ti^{3+}-TiO_2/p-CN	300 W Xe lamp (λ > 420 nm)		NO	1.2 $L.min^{-1}$, 400 ppb	30	25.8%
Thanh Truc et al. (2019)	Nb-TiO_2/g-CN	30 W white bulb		CO_2	20 $mL.min^{-1}$, 99.99%		CH_4 - 562 $\mu mol.h^{-1}.g^{-1}$
							CO - 420 $\mu mol.h^{-1}.g^{-1}$

Refs.	Composite	Light source	Light intensity	Pollutant	Flowrate, conc.	Irradiation time (min)	Rate of degradation
							O_2 - 1702 $\mu mol.h^{-1}.g^{-1}$
							HCOOH - 698 $\mu mol.h^{-1}.g^{-1}$

2.5.2.3 Abatement of pollutants in aqueous medium

A lot of research works have been done to determine the degradation level of organic dyes using TiO_2/g-CN composite photocatalyst. Among them, rhodamine B (RhB) degradation using TiO_2/g-CN has been extensively studied. **Table 2-5** briefly summarized some of the important studies. Lu et al. (2010) prepared a TiO_2/g-CN composite following a hydrothermal treatment induced calcination route and has reported superior RhB degradation under both visible (80%) and UV (55%) light irradiation. Wang et al. (2013) on the other hand, had used a microwave assisted synthesis route to prepare N doped TiO_2/g-CN composite for degrading RhB. N-TiO_2/g-CN containing 40% of N-TiO_2 showed maximum removal efficiency. Using an initial RhB concentration of 10 $mg.L^{-1}$, they have demonstrated a pseudo 1^{st} order degradation rate constant of 0.91 min^{-1} under visible light. Jian Ma et al. (2016) reported a (001) facet dominated TiO_2/g-CN for RhB degradation under visible light and have shown the removal of 96.55% within 50 min of visible light irradiation. Quite recently, another fascinating study was conducted by Ma et al. (2018) towards RhB removal by using a composite prepared from TiO_2 hollow microsphere (HM) and g-CN. They have developed TiO_2/g-CN HM composite by varying the mass ratio of g-CN and TiO_2 in the range of 0.01 to 0.2. The optimum mass ratio by considering maximum removal of RhB was found as 0.15. It was reported that the photocatalytic activity of the as prepared TiO_2/g-CN HM was 3 times higher than a single use of TiO_2 HM.

Beside RhB, many researchers have used photodegradation of MB in an aqueous medium, to assess the photoactivity of TiO_2/g-CN composites. Boonprakob et al. (2014) by using a sol-gel method, prepared a TiO_2/g-CN composite film to get enhanced MB degradation under visible light. They have reported, a 50% g-CN loading on TiO_2 was optimum for getting maximum MB removal. Based on their analysis, 68% MB could be removed within 180 min of photodegradation by using the as prepared TiO_2/g-CN film. However, K. Li et al. (2015) showed a g-CN loading of 40% is optimum to get maximum MB removal using Ti^{3+} doped TNT/g-CN under UV-Vis light spectrum. Moreover, they have compared the rate of MB degradation by using Ti^{3+}-TNT/g-CN with pure TiO_2 and g-CN. Ti^{3+}-TNT/g-CN showed 7.6 and 26.76 times higher MB degradation rate constant compared to g-CN and TiO_2 under 30 W LED light irradiance. H. Liu et al. (2019), used surface alkalisation technique to enhance the extent of MB degradation using TiO_2/g-CN. Initially, they have alkalinized the surface of g-CN using $NaHCO_3$ as a precursor and then

prepared the TiO_2/g-CN composite through annealing. The prepared composite demonstrated superior adsorption efficiency due to strong electrostatic interaction. In addition, 90% - 100% of 20 $mg.L^{-1}$ MB was removed within only 120 min under visible light.

Furthermore, scientists have also used sulforhodamine B (SRB) (Zhang et al., 2014), Brilliant Red X-3B (X3B) (Zang et al., 2014), Acid orange 7 (AO7) (Lei, Chen, Shen, et al., 2015), and MO (Zang et al., 2014) dye to assess the level of photoactivity of TiO_2/g-CN composites under visible light, and stated superior dye removal compared to standalone use of g-CN and TiO_2. Photodegradation of organic compounds like phenol has also being used by many researchers to assess the photoactivity of TiO_2/g-CN. Tan et al. (2018) reported a composite concerning mesoporous g-CN nanosheets and Ti^{3+} doped TiO_2 towards superior phenol removal in an aqueous medium. The as prepared Ti^{3+}-TiO_2/g-CN was found with a larger specific surface area (73.8 $m^2.g^{-1}$) and a tailored narrow energy bandgap (2.21 eV). Hence, the Ti^{3+}-TiO_2/g-CN composite showed higher phenol removal. TiO_2/g-CN composites are also found to photodegrade pharmaceutical pollutants like ciprofloxacin (Wang et al., 2015) and acetaminophen (Du et al., 2019) from wastewater effectively. G. Li et al. (2015) used TiO_2/g-CN composite to remove Escherichia coli from polluted water. They have stated that by using visible light irradiance and TiO_2/g-CN composite, it is possible to remove 100% of Escherichia coli (107 $cfu.mL^{-1}$) within only 180 min.

Table 2-5. Salient features of the significant studies concerning TiO_2/g-CN based pollutant degradation in aqueous medium

Refs.	**Composite**	**Light source**	**Light intensity**	**Pollutant**	**Conc.**	**Irradiation time (min)**	**Rate of degradation**
Lu et al. (2010)	TiO_2/g-CN	500 W Xe lamp ($\lambda > 365$ nm)		RhB	0.01 g.mL^{-1}	300	80%
		250 W UV source (λ = 200 - 400 nm)					55%
Zhao et al. (2012)	TiO_2/g-CN	500 W Xe lamp ($\lambda \geq 420$ nm)	94 mW.cm^{-2}	Phenol	5 mg.L^{-1}	180	67.7%
		500 W Xe lamp (UV-Vis)	100 mW.cm^{-2}			60	96.6%
Zhou et al. (2012)	TNT/g-CN	500 W Xe lamp ($\lambda \geq 400$ nm)		MO	20 mg.L^{-1}	150	100%
	N-TiO_2/g-CN			RhB	10 mg.L^{-1}	60	K = 0.91 min^{-1}

Refs.	Composite	Light source	Light intensity	Pollutant	Conc.	Irradiation time (min)	Rate of degradation
Wang et al. (2013)		300 W Xe lamp ($\lambda > 400$ nm)	0.16 k $W.m^{-2}$	MB			$K = 0.07\ min^{-1}$
Boonprakob et al. (2014)	TiO_2/g-CN film	50 W Halogen lamp ($\lambda \geq 400$ nm)	640 $W.m^{-2}$	MB	10 $mg.L^{-1}$	180	68%
Chen et al. (2014)	Ag-TiO_2/g-CN	300 W Xe lamp ($\lambda > 420$ nm)		MO	13.5 $mg.L^{-1}$	360	94%
				Phenol	16.6 $mg.L^{-1}$		95%
(Han et al., 2014)	N-TNT/g-CN	300 W Xe lamp (Solar spectrum)		RhB	10 $mg.L^{-1}$	120	$K = 0.0321\ min^{-1}$
Shen et al. (2014)	TiO_2/g-CN	50W Halogen lamp ($\lambda > 420$ nm)		MO		180	$K = 0.0038\ min^{-1}$
Zang et al. (2014)	TiO_2(Br)/g-CN	300 W Xe lamp ($\lambda \geq 420$ nm)		MO	10 ppm	180	$0.00443\ min^{-1}$
				As^{3+}	5 ppm	180	55%

Refs.	Composite	Light source	Light intensity	Pollutant	Conc.	Irradiation time (min)	Rate of degradation
Zhang et al. (2014)	TNT(B)/g-CN	108 W lamp (Philips) ($\lambda >$ 400 nm)		SRB	25 $\mu mol.L^{-1}$	300	K = 0.0021 min^{-1}
		108 W lamp (Philips) ($\lambda <$ 300 nm)					K = 0.034 min^{-1}
Huang et al. (2015)	TiO_2/g-CN HNB (1 0 1)	3 W LED lamp ($\lambda \approx 365 \pm 10$ nm)		X3B	1×10^{-4} $\mu.L^{-1}$	45	K= 107.76 min^{-1}
	TiO_2/g-CN (0 0 1)						K = 84.40 min^{-1}
Lei, Chen, Shen, et al. (2015)	TiO_2/g-CN	500W halogen lamp ($\lambda \geq 420$ nm)		AO7	20 $mg.L^{-1}$	300	99%
		300 W mercury lamp (UV)				120	100%
Lei, Chen, Wang, et al. (2015)	TiO_2/g-CN	500 W halogen lamp ($\lambda \geq 420$ nm)		AO7	20 $mg.L^{-1}$	180	99%

Refs.	Composite	Light source	Light intensity	Pollutant	Conc.	Irradiation time (min)	Rate of degradation
		300 W mercury lamp (UV)				120	96%
G. Li et al. (2015)	TiO_2/g-CN	300 W Xe lamp ($\lambda > 420$ nm)	100 $mW.cm^{-2}$	E. coli K-12	10^7 $cfu.mL^{-1}$	180	100%
H. Li et al. (2015)	TiO_2/g-CN	300 W Xe lamp		Phenol	10 $mg.L^{-1}$	90	100%
K. Li et al. (2015)	Ti^{3+}-TNT/g-CN	30 W LED light (no filter)		MB	20 $mg.L^{-1}$	100	$K = 0.038$ min^{-1}
Wang et al. (2015)	TiO_2/g-CN	150 W tungsten lamp		Ciprofloxacin	10 $mg.L^{-1}$	60	95%
Zhou et al. (2015)	TiO_2/g-CN	500 W Xe lamp ($\lambda > 420$ nm)		MB	0.03 mM	120	3 times higher than pure g-CN
		15 W mercury lamp (UV)					1.3 times higher than anatase TiO_2

Refs.	Composite	Light source	Light intensity	Pollutant	Conc.	Irradiation time (min)	Rate of degradation
Li et al. (2016)	TiO_2/g-CN	500 W Xe lamp (λ > 420 nm)		MB	10 $mg.L^{-1}$	360	3.5 times higher than pure g-CN
Jian Ma et al. (2016)	TiO_2-(001)/g-CN	300 W Xe lamp (λ > 420 nm)	90 $mW.cm^{-2}$	RhB	10 $mg.L^{-1}$	50	96.55%
Wei et al. (2017)	TiO_2/g-CN film	500 W Xe lamp (λ > 420 nm)	35 $mW.cm^{-2}$	Phenol	5 $mg.L^{-1}$	120	100%
				Coking wastewater	25 ppm TOC	300	45%
		500 W Xe lamp (Solar)	0.69 $mW.cm^{-2}$	Phenol	5 $mg.L^{-1}$	90	100%
				Coking wastewater	25 ppm TOC	180	100%
Ma et al. (2018)	TiO_2/g-CN HM	300 W Xe lamp (λ > 420 nm)		RhB	1×10^{-5} M	100	K = 0.021 min^{-1}
Tan et al. (2018)	Ti^{3+}-TiO_2/Meso-g-CN	300 W Xe lamp		Phenol	10 $mg.L^{-1}$	90	K = 0.028 min^{-1}

Refs.	Composite	Light source	Light intensity	Pollutant	Conc.	Irradiation time (min)	Rate of degradation
		(λ > 420 nm)					
H. Liu et al. (2019)	TiO_2/Na-g-CN	300 W Xe lamp (λ > 400 nm)		MB	20 $mg.L^{-1}$	120	90% - 100%
Du et al. (2019)	TiO_2/g-CN-PS	300 W Xe lamp (λ > 400 nm)		AAP	5 $mg.L^{-1}$	30	99.3%
Sun et al. (2019)	N-TiO_2/g-CN@diatomite	500 W Xe lamp (λ > 400 nm)		Cr(VI) reduction	5 $mg.L^{-1}$	300	100%
Tahir et al. (2019)	WO_3/TiO_2/g-CN	500 W halide lamp (UV-Vis)		Acetylsalicylate	10 $mg.L^{-1}$	90	98%
				Methyl-theobromine			97%

2.6 Feasibility of the generation of sludge-derived TiO_2 from economic perspective

2.6.1 Cost benefit analysis

The Earth's crust contains 0.44–0.66 % Ti elements, making it the sixth most abundant metal globally. The main ores that have titanium in them are ilmenite ($FeTiO_3$) and rutile (TiO_2) (Gan et al., 2021; Thomas et al., 2020). The former is the most important source of Ti, and it may be found in the form of black sand on a significant number of ocean beaches. 2018 US Geological Survey figures indicate that Australia (28.33 %), China (26.06 %), India (9.63 %), South Africa (7.14 %), and Kenya (6.12 %) account for the majority of ilmenite production (Gan et al., 2021). As a result, the manufacturing of Ti coagulant precursors in large quantities is supported by a strong material and technological basis. According to data from the world's leading trade websites (**Table 2-6**), $TiCl_4$ is marginally more expensive than $AlCl_3$ and $FeCl_3$, although $Ti(SO_4)_2$ or $TiOSO_4$ is much more expensive than $Al_2(SO_4)_3$ and $Fe_2(SO_4)_3$. At the moment, $TiCl_3$ costs about five times as much as $AlCl_3$ and $FeCl_3$, which is too much to use directly. Hence, the most acceptable precursors for producing titanium-based coagulants by the sol-gel technique are $TiCl_4$, isopropyl titanate, and tetrabutyl titanate, with the lowest unit costs of $1,000/tonne, $2,000/tonne, and $2,000/tonne, respectively. Considering economic costs, $TiCl_4$ is most likely to be a precursor to titanium coagulants.

Table 2-6. Prices of the raw materials for cost analysis (tentative prices have been collected from https://www.alibaba.com/ accessed on 08.06.2022).

Raw materials	**Price ($/tonne)**
$AlCl_3$	500 – 700
$FeCl_3$	500 – 600
$Al_2(SO_4)_3.18H_2O$	100 – 250
$Fe_2(SO_4)_3.7H_2O$	100 – 200
$TiCl_4$	1,000 – 1,200
$TiCl_3$	3,100 – 3,800
$TiOSO_4$	3,100 – 3,800
Titanium (IV) isopropoxide	2,000 – 4,500

Raw materials	Price ($/tonne)
Titanium(IV) butoxide	2,000 – 5,000

The high growth rate and settling velocity of large flocs in Ti coagulation lead to short mixing and residence times (Chekli, Corjon, et al., 2017; Chekli, Eripret, et al., 2017; Hossain, Park, Kang, Kim, et al., 2020; Hossain, Park, Kang, Mun, et al., 2020). Consequently, mixing the wastewater requires less energy, and consolidating the flocculation and sedimentation tanks requires less infrastructure. Typically, sludge treatment accounts for at least 50% of the overall cost of water treatment (Na et al., 2011; Okour et al., 2011; Shon et al., 2007a). Most conventional Al/Fe coagulants end up in landfills as garbage, where they cause inevitable secondary contamination and the encroachment of land resources. In contrast, the most significant benefit of Ti coagulants is that the coagulation sludge may be recycled to create TiO_2 by calcining the settling flocs at high temperatures (Hossain, Park, Kang, Kim, et al., 2020; Hossain, Park, Kang, Mun, et al., 2020; Hossain et al., 2021). TiO_2 could be prepared from the Ti coagulation sludge from different types of water and wastewater, such as seawater(Chekli, Corjon, et al., 2017), biochemical effluent (Gan et al., 2021), printing and dyeing wastewater (Jong Beom Kim et al., 2010), and wastewater from composing paper (Na et al., 2011). Using Ti coagulation, it is projected that 446.5 kg/d of valuable TiO_2 by-products may be recovered from a 25,000 m^3/d medium-sized sewage treatment facility. The photocatalyst materials ($TiO_{1.42}C_{0.44}P_{0.14}$) produced from $TiCl_4$ coagulation sludge performed better in the photodegradation of acetaldehyde than the commercial P25 (Hossain et al., 2019; H. Shon et al., 2009a; H. K. Shon et al., 2009b; Shon et al., 2007a). The nano-TiO_2 produced from sludge using $TiCl_4$ as a coagulant showed higher electrochemical capacity and cycling performance than pure commercial TiO_2. The photocatalytic activity of TiO_2 produced from coagulation sludge was unaffected by seasonal changes in sewage treatment plant water quality (Okour et al., 2011). Adding a metal-based coagulant to facilitate Ti coagulation may improve the effluent pH while also assisting in preparing metal-doped TiO_2 (Shon et al., 2014). Because the doping lowered the band gap of the semiconductor, the visible-light photocatalytic activities of Fe-doped TiO_2 recovered from the coagulation sludge were better than certain commercial ones, such as P25.

Table 2-7. Cost-benefit study of TiO_2 recovery from $TiCl_4$ coagulation for the removal of phosphorus from wastewater (Adapted from (Gan Yonghai, 2020)).

Types	**Process**	**Item**	**Standard**	**Treatment amount (Ton)**	**Consumption**	**Unit**	**Cost (USD, avg.)**	**Total Cost (USD)**
Coagulant ($TiCl_4$)				12		kg	$0.34	$4,058.51
Resource recovery	Drying	Oven (Electricity)	300 °C, Moisture content (80% - 40%)		1500	kW	$0.06	$95.12
	Calcination	Furnace (Electricity)	600 °C, Moisture content (80% - 40%)		850	kW	$0.06	$53.90
	Grinding	Grinder (Electricity)	Grinding and separation	1	250	kW	$0.06	$15.85
	Packing	Packer	Ton	1	1	EA	$25.37	$25.37
	Others	Labors		1	3	Persons	$67.64	$202.93
				1	30%		$393.17	$117.95

Types	Process	Item	Standard	Treatment amount (Ton)	Consumption	Unit	Cost (USD, avg.)	Total Cost (USD)
Total production cost of TiO_2				1				$4,569.63

To determine the economic feasibility of using $TiCl_4$ to remove phosphorus from wastewater and synthesize photocatalyst grade TiO_2, Gong and his team conducted an economic study in a water treatment facility with a capacity of 330,000 m^3/d, and the prices of $TiCl_4$ and commercial PAC were compared (Gan et al., 2021; Gan Yonghai, 2020). We have adapted these results and converted them to USD equivalents (**Table 2-7**). It is possible to recover about 1 ton of TiO_2 from the coagulated sludge produced by 12 tons of $TiCl_4$. And by taking into account the impurity of recovered TiO_2, the selling price was adjusted to be ten times lower than the commercial P25. Interestingly, the selling price of sludge TiO_2 can offset the high cost of Ti coagulant and generate a profit of 3000 USD per day (**Table 2-8**). In addition to being utilized as photocatalysts, the TiO_2 products produced from coagulation sludge may also be used as pigments, coatings, and other applications. Furthermore, the resource-utilization of coagulation sludge has certain environmental advantages, such as resolving the issue of soil degradation and land use caused by sludge landfills. It is presently unclear to determine how much more money will be generated due to these advantages.

Table 2-8. Cost comparison between commercial PAC and $TiCl_4$ sewage treatment

Items	**PAC(10%)**	**$TiCl_4$**	**Unit**
Total amount of sewage	330000.00	330000.00	m^3/day
Coagulant dosage amount	13.50	26.40	ton/day
Generated sludge amount	14.40	27.30	ton/day
Total Coagulant cost	$1,712.18	$8,928.72	USD/day
	$126.83	$338.21	USD/ton
Sludge treatment cost	$1,461.06	$1,127.25	USD/day
	$101.46	$41.29	USD/ton
Total sewage treatment cost	$3,173.25	$10,055.97	USD/day
Balance (PAC cost - $TiCl_4$ cost)		$6,882.73	USD/day
Amount of titanium dioxide produced		2.20	ton/day

Items	PAC(10%)	$TiCl_4$	Unit
TiO_2 Selling price		$10,053.18	USD/day
Profit		$3,170.46	USD

2.7 Conclusion

Natural water and wastewater both include a variety of inorganic and organic chemical substances with varying physicochemical characteristics and toxicity to aquatic life. Consequently, they must go through a number of purification procedures before they are used for human consumption or industrial uses or before they may be released into the environment. Coagulation and flocculation are used in these procedures, which use a variety of traditional coagulants, primarily Fe^{2+}, Fe^{3+}, and Al^{3+} salts. A number of recent studies suggest that the use of Ti^{4+} salts as coagulants may replace conventional coagulants. By utilizing titanium compounds in coagulation operations, it is feasible to recover TiO_2 from sludge produced during coagulation processes, contributing to the circular economy's advantages. Aside from their low toxicity, titanium coagulants have several benefits such as low residual concentration in water, high Ti concentration values for taste and smell thresholds, and the maximum allowable concentration in drinking water suggested by some authors (not greater than 0.1 mg/L), but the concentration is usually lower (using factors such as an adequate acidity level and dose of Ti^{4+}). Coagulants made of titanium chloride and Ti(IV) compounds were utilized to treat water, synthetic wastewater, textile wastewater, underground coal gasification wastewater, and coal mining wastewater. It is also feasible to use it at low temperatures (as low as 3 °C). Additionally, these coagulants were noted for their outstanding effectiveness in lowering water or wastewater characteristics (e.g., color, turbidity, UV254, etc.). As a result, titanium coagulants may serve as an alternative to the more frequently employed iron and aluminum coagulants. While there are many advantages associated with titanium-based coagulants, there is currently a lack of published data. In certain instances, titanium-based coagulants outperform traditional coagulants, but additional study is needed before they may be used more widely.

The aforementioned novel coagulation and flocculation process effectively used Ti-salt sludge, and through a series of facile steps of flocculation followed by calcination synthesized valuable TiO_2, which could substantially minimize waste disposal costs. The

flocculated sludge from Ti-salt flocculation generated a beneficial byproduct when it was incinerated at 600 °C. Previous research has looked at the flocculation of drinking water, seawater, and various wastewater to produce different kinds of TiO_2. TiO_2 from different water sources mainly was doped with 3-5% carbon atoms, whereas the maximum doped impurities in TiO_2 generated from synthetic wastewater was C and P atoms up to 20%. The anatase structure was prominent in all TiO_2 generated from various water sources, with surface areas of 76.3, 103.5, and 68.1 m^2/g for TiO_2 made from synthetic wastewater, wastewater, and seawater, respectively. Interestingly, the photocatalytic activity of TiO_2 synthesized from synthetic wastewater was found to be greater than that of commercial P25 when exposed to UV light for the photodecomposition of gaseous acetaldehyde.

Since its discovery in the 1950s, titanium dioxide (TiO_2) has gained widespread recognition as one of the most promising photocatalysts owing to its unique characteristics such as high oxidation ability, thermal and chemical durability, and cheap cost. However, its photocatalytic effectiveness is restricted because of the rapid recombination of photo-induced electron-hole pairs and the high bandgap energy (~3.2 eV). Extensive attempts have been made to improve TiO_2's photocatalytic performance. Metal/metal oxide deposition, nonmetal element doping, composite semiconductor coupling, and surface sensitization have all proven successful in enhancing TiO_2's photocatalytic activity. The photocatalytic oxidation of pollutants using TiO_2/g-CN composites has been extensively studied, with the addition of g-C_3N_4 shown to significantly improve photocatalytic activity. Due to its strong resistance to heat (up to 600 °C in the air) and chemical attacks (e.g., acid, base, and organic solvents) and an attractive electronic structure with a medium bandgap, g-C_3N_4 has emerged as an intriguing photocatalyst candidate. The photocatalytic elimination of NO in the air has been implemented using g-C_3N_4. However, the use of g-C_3N_4 is not optimal due to its limited surface area and rapid electron-hole recombination. Mesoporous g-C_3N_4 with a specific surface area of 200 – 500 m^2/g may offer additional reaction sites; nevertheless, the preparation typically dictates the use of a template, which is time-consuming and complicated. To enhance photocatalytic activity, a combination of TiO_2 and g-C_3N_4 may increase the surface area of the photocatalyst and facilitate the separation of photogenerated electrons and holes. Moreover, g-C_3N_4's conduction band electrons have a higher reduction capacity than conventional TiO_2 photocatalysts and can efficiently activate molecular oxygen and generate more superoxide radicals for photocatalytic

destruction of contaminants. The photocatalytic removal of pollutants using TiO_2/g-CN composites has been extensively studied, and g-C_3N_4 alteration has been shown to significantly improve photocatalyst activity.

Even though TiO_2/g-CN composites are effective photocatalysts for NO removal, little progress has been made in removing the released NO_2. While the direct oxidation of NO_2 results in the production of innocuous nitrates (NO_3^-), the oxidation of NO to NO_3^- requires a number of intermediary stages before it is completely oxidized, the most significant of which is the generation of NO_2. Because NO_2 is more hazardous than NO, it's emission significantly reduces photocatalytic efficiency. Unconditional improvement in air quality can only be achieved via the use of a selective photocatalyst that both inhibits the production and the release of undesirable intermediates. As a consequence, selectivity has lately gotten a lot of press. Furthermore, to the best of our knowledge, no research has been published on the utilization of sludge-generated TiO_2 to synthesis TiO_2/g-CN materials for photocatalytic NO_x removal.

CHAPTER 3
MATERIALS AND METHODS

3 Materials and Methods

3.1 Materials

3.1.1 Synthetic wastewater

For the studies, synthetic wastewater (SWW) that mimics biologically treated sewage effluent (BTSE) was prepared. The detailed composition of the prepared wastewater can be found elsewhere (Seo et al., 1997; Shon et al., 2007a). A breakdown of the chemical contents and molecular weight ranges of the synthesized SWW is shown in **Table 3-1**. The SWW constituents were selected to distribute the prevailing organic matters among a wide range of molecular weights. In summary, tannic acid, sodium lignin sulfonate, sodium lauryle sulphate peptone, and arabic acid contributed to the large molecular weight organic matters, while the small molecular weight organic matters came from peptone, beef extract, and humic acid.

Table 3-1. Constituents of the prepared synthetic BTSE[a]

Compounds	**Concentration (mg/L)**	**Fraction by organic matter**	**Molecular wt. (Da)**
Beef extract	1.8	0.065	300,100,70
Peptone	2.7	0.138	34300,100,80
Humic acid	4.2	0.082	1,500,300
Tannic acid	4.2	0.237	6300
Sodium lignin sulfonate	2.4	0.067	12100
Sodium lauryle sulphate	0.94	0.042	34300
Arabic gum powder	4.7	0.213	900,300
Arabic acid (polysaccharide)	5	0.156	38900
$(NH_4)_2SO_4$	7.1	-	-
K_2HPO_4	7	-	-
NH_4HCO_3	19.8	-	-
$MgSO_4.7H_2O$	0.71	-	-

[a] BTSE: Biologically treated sewage effluent

3.1.2 Algal surface water

Algae bloomed water was collected from Daecheongho Lake, one of the largest manmade lakes in South Korea, and fulfills various water demands of Daejeon and Cheongju. The raw lake water was diluted using tap water, and the pH was adjusted using 1.0 N NaOH (> 97% purity; Daejung Chemicals and Metals, South Korea). The physicochemical properties of the simulated water were determined as follows: pH 7 ± 0.5, temperature 22 ± 2 °C, turbidity 500 ± 10 NTU, COD 117 ± 5 mg/L, and TP 3.61 + 3 mg/L.

3.1.3 Dye wastewater

The wastewater produced by a dye wastewater (DWW) treatment plant located in Daegu, South Korea, was collected for the purposes of this study. The initial physicochemical properties were as follows: pH 11.7 ± 0.6, COD 449 ± 5 mg/L, TN 72 ± 3 mg/L, TP 3.2 ± 0.5 mg/L.

3.1.4 Chemical reagents

For the algal surface water, the flocculation efficiency of $TiCl_4$ is compared with commercially available polyaluminium chloride (PAC). The stock solution of $TiCl_4$ was prepared using concentrated $TiCl_4$ (> 99% purity, density 1.73 g/ml, Sigma-Aldrich, Australia). A 20 wt.% $TiCl_4$ solution was prepared by adding (dropwise) 46.4 ml of concentrated $TiCl_4$ to a predetermined volume (400 ml) of deionized (DI) water (frozen cubes) under continuous stirring. Industry grade PAC was directly utilized, having 10.2 wt.% of Al_2O_3 and 64% basicity.

In the studies concerning dye wastewater, melamine ($C_3H_6N_6$, assay: 99%, Sigma-Aldrich) and NP400 (anatase titania) precursors were purchased in powder form from Sigma-Aldrich (Seoul, South Korea) and Bentech Frontier Co. Ltd. (Gwangju, South Korea) and used during the study without any additional change. $TiCl_4$ (Assay: 99%, Sigma-Aldrich, Korea) was used for coagulation and subsequent flocculation. Additionally, for the hydrothermal treatment, sodium hydroxide (NaOH) (97%, w/w) and hydrochloric acid (HCl) (37%, v/v) were procured from Sigma-Aldrich, Korea. All the chemical reagents were used without any further modification.

3.2 Experimental methods

3.2.1 Coagulation and flocculation of SWW

Jar tests were conducted in two phases: (a) coagulation/flocculation using varying doses of $TiCl_4$ and (b) coagulation/flocculation with varying doses of $Ca(OH)_2$ at optimized

doses of $TiCl_4$. During the jar tests, the doses of $TiCl_4$ and $Ca(OH)_2$ were varied from 2.9 to 23.3 mg Ti/L and 2.16 to 54 mg Ca/L, respectively. In both cases, the wastewater was stirred rapidly for 2 min at 200 rpm, followed by 20 min of slow mixing at 30 rpm and 30 min of settling. Dissolved organic carbon (DOC), which represented the organic content, was measured using a Dohrmann Phoenix 8000 UV-Persulphate DOC analyzer equipped with an autosampler. All the samples were filtered through a 0.45 μm filter paper before organic carbon measurement. The pH at varying doses of coagulants was measured using a pH meter (Orion, model 920A). Finally, the turbidity was measured using a NTU turbidity meter, and the results were expressed as a turbidity ratio, which was determined as follows:

$$Turbidity\ ratio = \frac{Turbidity\ (NTU)\ of\ the\ sample\ after\ flocculation}{Initial\ turbidity\ (NTU) of\ the\ sample} \quad (3\text{-}1)$$

3.2.2 Coagulation and flocculation of algal surface water

Standard jar tests were conducted to compare the coagulation efficiencies of $TiCl_4$ and PAC using a programmable jar tester (PB-900TM, Phipps and Bird, USA). Simulated algal surface water of 500 ml was filled in a 1.0 L beaker, and the coagulant doses (as Ti or Al) were varied from 0.1 g/L to 0.3 g/L at an increment of 0.1 g/L. The addition of coagulant was followed by rapid mixing at 100 rpm for 1 min and a slow mixing at 20 rpm for 20 min. Finally, the samples were settled for 20 min before analyzing the target physicochemical properties of the effluent. The coagulation efficiency of the coagulants was compared from the perception of residual turbidity, COD, and TP. Sample water after coagulation was collected from 2.0 cm below the water surface in the beaker, and turbidity was determined immediately using a turbidity meter. Besides, COD and TP were determined using UV/Vis spectrophotometry, utilizing potassium permanganate ($KMnO_4$) as an oxidizing agent. All the experiments were conducted in triplicates, and the average values with standard errors are reported.

3.2.3 Preparation of TiO_2 from SWW

After completion of the jar tests, the settled sludge following coagulation/flocculation was collected and further concentrated using a centrifuge. Afterward, the concentrated sludge was dried overnight at 120 °C, which was followed by grinding. Then the grinded samples were incinerated for 2 h at a temperature of 600 °C to obtain anatase titania (**Fig. 3-1**). Finally, two types of powdered TiO_2 were prepared: one from flocculation using only $TiCl_4$ and the other from flocculation using both $TiCl_4$ and $Ca(OH)_2$. The TiO_2

preparation process in this study was adapted from (El Saliby et al., 2010b; J. B. Kim et al., 2010; Jong Beom Kim et al., 2010; Na et al., 2010). For ease of discussion, TiO_2 prepared from only $TiCl_4$ flocculation is termed as U-TiO_2 (undoped TiO_2) and TiO_2 fabricated using $Ca(OH)_2$ as coagulant aid is termed as Ca-TiO_2 (Ca-doped TiO_2).

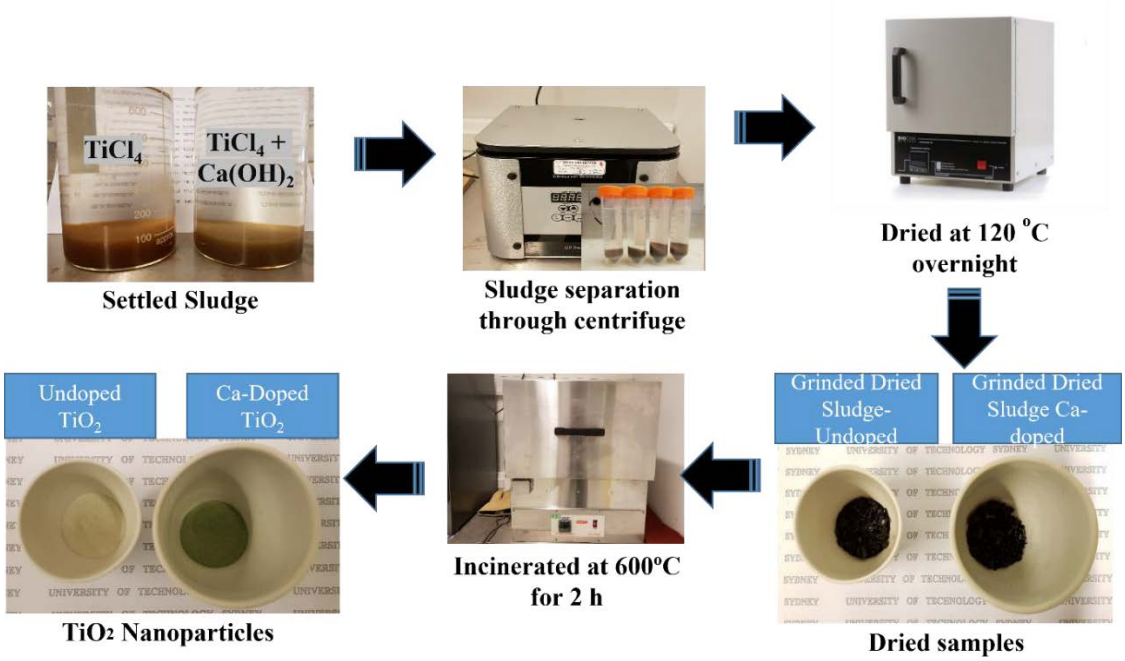

Fig. 3-1. Preparation of undoped anatase TiO_2 and Ca-doped TiO_2 from SWW.

3.2.4 Preparation of TiO_2 from algal surface water

Following the jar tests, Ti-based algal flocculated sludge was collected, and titania (TiO_2) nanoparticles (NPs) were prepared following the protocols described in literature (Y. Zhao et al., 2014), and are illustrated in **Fig. 3-2**. The prepared A-TiO_2 NPs were characterized using a scanning electron microscope associated with energy dispersive X-ray spectroscope (SEM/EDX, Rigaku, Japan). The specific surface area of the prepared A-TiO_2 was determined using physisorption at 77K accompanied with N_2 gas (Micromeritics Gemini 2360, USA). Multi-point Brunauer-Emmett-Teller (BET) method was adopted to calculate the specific surface area using isotherm data from $P/P_0 = 0.058$ to $P/P_0 = 0.188$.

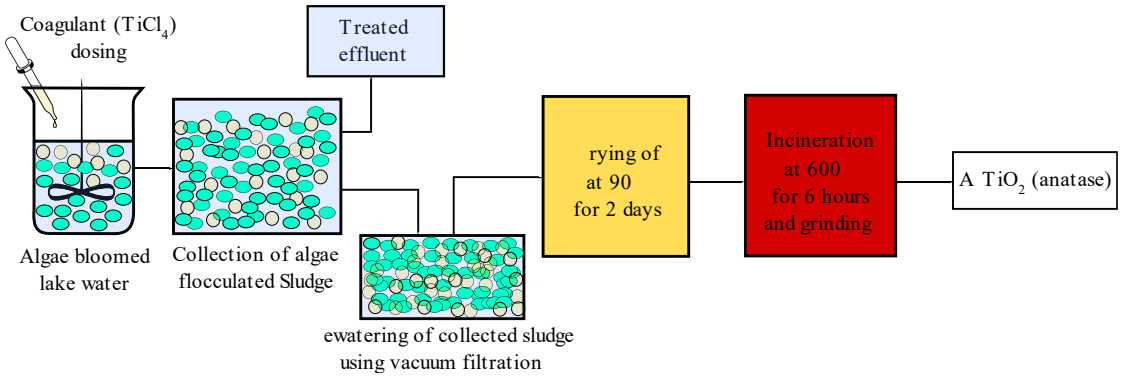

Fig. 3-2. Preparation of A-TiO_2 using Ti flocculated algal sludge.

3.2.5 Preparation of A-TiO_2 mixed mortar blocks

Removal of NO_x using A-TiO_2 was assessed for both A-TiO_2 NPs and A-TiO_2 mixed mortar. The mortar blocks were prepared following the protocols stated in ISO 679:2009 (ISO, 2009). In the prepared sample, sand to cement ratio and cement to water ratio were maintained at 3:1 and 2:1, respectively. Mortar blocks (100 mm × 50 mm × 10 mm) were prepared incorporating 5.0 wt.% and 10.0 wt.% of A-TiO_2. Additionally, to compare the results with commercially available TiO_2 (Degussa (Evonik) P25), mortar blocks were prepared containing 5.0 wt.% of P25.

3.2.6 Preparation of TiO_2 from DWW

The wastewater was treated with an optimized dose of $TiCl_4$, which was first rapidly mixed within the sample at a rate of 100 rpm for 1 min before being slowly mixed at a rate of 30 rpm for a further 20 min. The flocculated wastewater was subsequently stored to allow the flocks to settle, after which the settled dye wastewater sludge was extracted dried overnight in a laboratory oven at a temperature of 100℃. A pestle and mortar were used to mill the dried material into a powder form before the anatase S-TiO_2 was synthesized by placing the powder into an alumina crucible and calcining it at 600 ℃ (@10℃/min) for 3 h.

3.2.7 Preparation of TiO_2/g-CN composites from DWW

For the preparation of TiO_2/g-CN composites, two reaction routes were followed, as shown in **Fig. 3-3**. Initially, a facile one-step synthesis approach was employed to prepare the composite set 1 (see **Table 3-2**), where the prepared dried sludges in the laboratory were uniformly mixed with specific amounts of melamine (30%, 50%, 70%, 90%, and 100%) by using a mortar and pestle. Later the precursor mix was calcined in a box furnace at a controlled temperature of 600 ℃ over 3 h at a heating ramp of 2.3 ℃/min for the

composite preparation. Following the conventional calcination temperature of 550 °C, the dried sludge and melamine mix was calcined, but it produced blackish particles, as shown in **Fig. 3-2** (upper right Fig.) with negligible photoactivity. The composite set 1 was termed as SM0, SM30, SM50, SM70, SM90, and SM100, corresponding to the wt.% of melamine.

On the other hand, a two-step calcination approach was employed to prepare the composite set 2 (see **Table 3-3**). The dry melamine and SM0 mixtures were annealed under atmospheric pressure for the composite preparation. Different composites were generated by varying the wt.% of melamine (30%, 50%, 70%, 90%, and 100%) and subsequently calcinated at 550 °C. A fixed temperature was applied within the box furnace that rose by 2.3 °C every min over a period of 3 h. Similar to composite set 1, composite 2 was termed as TM0, TM30, TM50, TM70, TM90, and TM100.

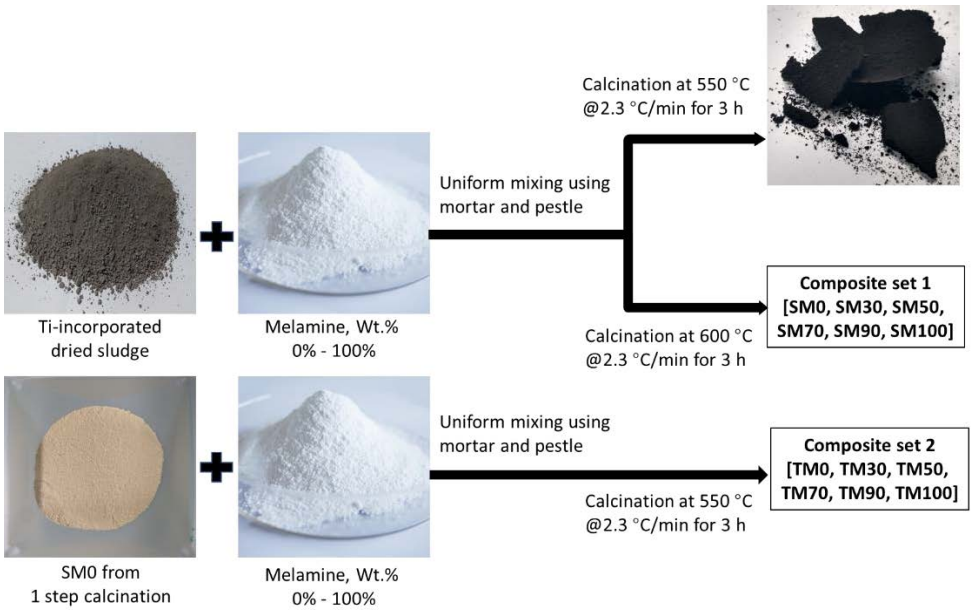

Fig. 3-3. Synthesis scheme for TiO_2/g-CN composite sets 1 and 2 through one and two-step calcination routes.

Table 3-2. Composites from 1 step calcination of sludge and melamine mix.

Name	Amounts(g)		Prepared sample (g)	Temperature (°C)	Ramp (°C/minute)	Duration (h)
	Sludge	Melamine				
SM0	15	0	5.7	600	2.3	3

Name	Amounts(g)		Prepared sample (g)	Temperature (°C)	Ramp (°C/minute)	Duration (h)
	Sludge	Melamine				
SM30	10.5	4.5	3.98	600	2.3	3
SM50	7.5	7.5	2.85	600	2.3	3
SM70	4.5	10.5	1.71	600	2.3	3
SM90	1.5	13.5	0.8	600	2.3	3
SM100	0	15	1.8	600	2.3	3

Table 3-3. Composites from 2 step calcination of SM0 and melamine mix.

Name	Amounts(g)		Prepared sample (g)	Temperature (°C)	Ramp (°C/minute)	Duration (h)
	SM0	Melamine				
TM0	10	0	9.8	550	2.3	3
TM30	7	3	6.7	550	2.3	3
TM50	5	5	6.4	550	2.3	3
TM70	3	7	5.5	550	2.3	3
TM90	1	9	4.7	550	2.3	3
TM100	0	10	4.7	550	2.3	3

3.2.8 Preparation of TiO_2/g-CN composites from DWW generated TiO_2

The pure g-CN and conjugated S-TiO_2/g-CN was prepared via a facile one-step synthesis scheme. A box furnace was utilized for annealing the dry mixture of S-TiO_2 and melamine (Sigma-Aldrich, 99%) for the sample preparation. The annealing was performed under atmospheric pressure. Various samples were created by differing the ratio of wt.% of melamine to S-TiO_2, and a calcination temperature of 550 °C was applied. The temperature of the box furnace was fixed such that it rose at 10 °C/min with a calcination duration of 3 h. **Table 3-4** presents an overview of the nomenclature of the prepared samples together with details of the mixing ratios of the precursors.

Table 3-4. Nomenclatures and salient features of the prepared samples. STC indicates the S-TiO_2/g-CN samples at various melamine concentrations.

ID	Amount(g)		Prepared sample (g)	Mixing ratio	Temperature (°C)	Ramp (°C/min)	Duration (h)
	S-TiO_2	Melamine					
STC 1	4	2	4.8	2:1	550	10	3
STC 2	4	4	5	1:1	550	10	3
STC 3	4	8	7.8	1:2	550	10	3
STC 4	4	12	8.1	1:3	550	10	3
STC 5	4	16	11	1:4	550	10	3
STC 6	4	20	13.2	1:5	550	10	3
g-CN		5	1.1		550	10	3

3.2.9 Preparation of S-TiO_2 and H-TNT from DWW

The flocculated DWW sludge was collected and dried for 48 h in the laboratory oven at a controlled temperature of 100 °C. Then the blackish dried flocculated sludges were powdered in a mortar and pestle. Finally, the milled powder was calcined at a constant temperature of 600 °C for 3 h in a box furnace at a heating ramp of 10 °C/min for the preparation of S-TiO_2. For the nanotube, initially, 3 g of S-TiO_2 and 80 ml of NaOH (10 N) was mixed in a glass beaker for 1 h by using a conventional magnetic stirrer. Then the uniform suspension was collected and placed in a teflon lined autoclave. Later, the laboratory oven temperature was prefixed at 180 °C, and the autoclaves were placed there for 48 h for hydrothermal treatment. After the completion of hydrothermal treatment, centrifugation at 3000 rpm was utilized to recover Na-titania nanotubes (Na-TNTs) from

the residual suspension. The recovered solids were treated for ion exchange in a magnetic stirrer at pH 2 using 1 N HCl solution. After ion exchange, the sample was washed with ultra-pure water until the pH reaches 7. Finally, H-titania nanotubes (H-TNTs) were prepared through the sample's overnight drying at 100 °C.

3.2.10 Preparation of S-TNT/g-CN composite from DWW

To form heterojunction, the dry mixture of H-TNT and melamine (Sigma-Aldrich, 99%) was calcined in a laboratory-scale box furnace at a temperature of 550 °C for 3 h. The rate of temperature rise in the furnace was maintained at 10 °C/min. Three samples were prepared by varying the melamine content from 0 – 100%. The salient features of the prepared samples are tabulated in **Table 3-5**.

Table 3-5. Nomenclatures and salient features of the preparation method for prepared composites.

ID	**Amount(g)**		**Prepared sample (g)**	**Mixing ratio**
	H-TNT	**Melamine**		
S-TNT	2.5	-	2.4	-
S-TNT1	2.5	1.25	2.1	2:1
S-TNT2	2.5	2.5	2	1:1

3.2.11 Evaluation of the photocatalytic activities of the prepared photocatalysts

3.2.11.1 Removal acetaldehyde under UV irradiation

In order to assess the level of photocatalytic activity of the prepared photocatalysts, photodecomposition of acetaldehyde (> 99.9% purity, Fox Chemicals) was carried out under UV irradiation. An airtight cuboid (220 × 125 × 80 mm) reactor with a volume of 2 L and assimilated with a gas chromatograph/flame ionization detector (GC/FID) (HP5890 series II, Wilmington, USA) was utilized to study the extent of photodegradation (**Fig. 3-4**). Two 10 W, 341 nm ± 10 nm UV-A lamps (Sankyo Denki, F10T8BL, Japan) were used to facilitate UV irradiation in the reactor. The reactor was equipped with 3 rubber openings, the first and second openings were respectively connected to acetaldehyde containing cylinder and air pump to ensure mixing of air inside the reactor, while the third was connected to the attached gas chromatograph having

super-Q PLOT capillary column (30 m × 0.52 mm) to measure the acetaldehyde concentration change. A petri-dish was used to place 0.5 g of sample in the reactor at a distance of 10 cm from the UV lamps. The photodegradation of acetaldehyde (2000 ppmv) was carried out for 200 min at a temperature of 24 °C. The experiments were conducted under dark conditions for 80 min with acetaldehyde gas mixtures exposed to the photocatalysts to assess the degradation rate due to adsorption and desorption. Finally, in the presence of UV-A light, experiments with the above-mentioned acetaldehyde gas mixtures were performed to determine the rate of degradation due to UV-photocatalysis. The decomposition of acetaldehyde concentration versus irradiation time was followed up to 200 min and was measured every 15 min. The acetaldehyde removal efficiency using synthesized photocatalysts were compared with the commercially available NP400 and P25.

Fig. 3-4. Experimental setup for the UV-based photocatalysis of acetaldehyde (a), sample holder in the reactor (b).

3.2.11.2 Photooxidation of NO_x under UV and visible light irradiation

A laboratory-scale photocatalytic reactor was utilized to assess the extent of photooxidation of the prepared samples through photooxidation of NO_x under both UV and visible light. For UV light-induced NO_x removal, ISO 22197-1 (ISO, 2016) was followed, where ISO 17198-1 (ISO, 2018) was followed for visible light irradiated NO_x removal. For UV irradiation, according to ISO 4892-3, so-called black light (UV-A, Sanyo-Denki, Japan) with a wavelength range of 300 nm to 400 nm (maximum 351 nm) was utilized. Additionally, cool fluorescent light with a UV cut-off filter for wavelengths below 400 nm was employed for the visible light, which adheres to ISO 14605. The experimental setup has been previously documented (Park et al., 2014; Rhee et al., 2018).

The schematic of the utilized system to evaluate the photocatalytic performance of the as-prepared samples is illustrated in **Fig. 3-5**. Following the ISO protocols, the utilized photoreactor can hold the test sample within a 50 mm wide trough having a surface parallel to an optical window for photoirradiation. The sample piece was separated from the window by a 5 ± 0.5 mm thick air layer. The gap was carefully controlled by using height adjusting plates, as shown in **Fig. 3-5 (b)**. 1 g of sample was mildly pressed in a rectangular sample holder with a surface area of 50 cm^2. For the removal of organic matters from the as-prepared samples, the sample holders with samples were pretreated under UV irradiance for 5 h at a light intensity of 10 W/m^2. Finally, the sample holder (with sample) was placed in the reactor attached with a NO_x analyzer (CM2041, Casella) to record the variation in NO, NO_2, and NO_x concentrations profile during light (UV/visible) irradiation. The experimental parameters were locked according to the aforementioned ISO protocols. Throughout the experiments, the flow of NO at the inlet of the reactor was maintained as 1 ppmv with an airflow of 3 L/min. Besides, the moisture content and the internal temperature of the reactor was maintained as 50% and 25 °C, respectively. Each experiment was carried out for 100 min, 20 min of gas adsorption followed by 1 h of light irradiation, and 20 min of purging. During UV irradiated NO_x oxidation, light intensity was maintained as 10 W/m^2 ± 0.5 W/m^2, and during visible light irradiance, it was 6000 lx ± 300 lx according to the followed ISO protocols. The average values of the three experiments were reported. The rate of NO removal, NO_x removal, NO_2 generation, and nitrate (NO_3^-) selectivity was confirmed according to the following equations:

$$NO_{removal} = \frac{NO_{in} - NO_{out}}{NO_{in}} \times 100\% \qquad (3\text{-}2)$$

$$NO_{2,generation} = \frac{NO_{2,out} - NO_{2,in}}{NO_{in}} \times 100\% \qquad (3\text{-}3)$$

$$NO_{x,removal} = \frac{NO_{x,in} - NO_{x,out}}{NO_{in}} \qquad (3\text{-}4)$$

$$NO_{3^-_{selectivity}} = \frac{NO_{x,removal}}{NO_{removal}} \times 100\% \qquad (3\text{-}5)$$

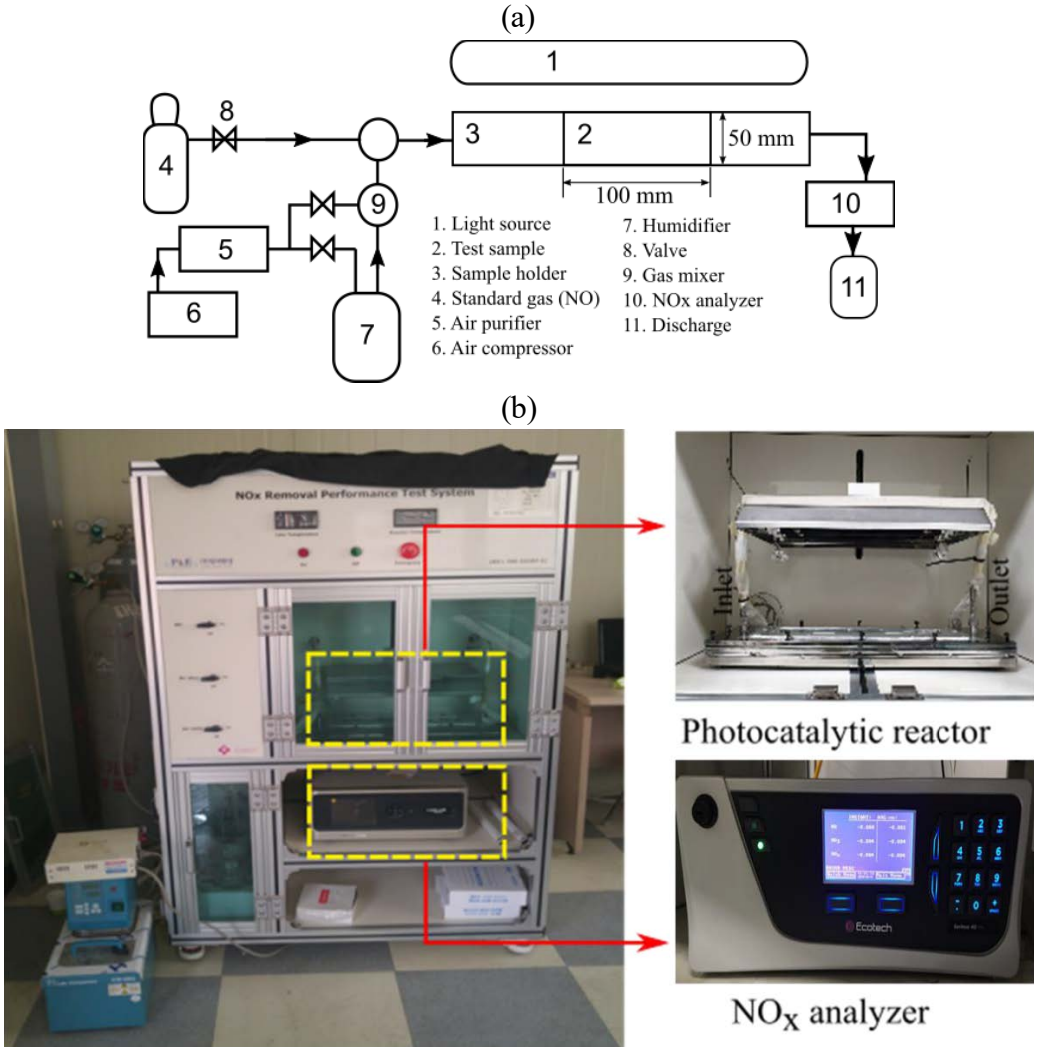

Fig. 3-5. (a) Simple schematic, and (b) visual representation of the experimental setup for photooxidation of NO.

3.3 Analytical methods

3.3.1 Analysis of morphological attributes

X-ray diffraction (XRD) analysis was performed to characterize the crystalline phase of the synthesized samples. XRD patterns were generated on an MDI Jade 5.0 X-ray diffractometer (D/MAX Ultima III, Rigaku, Japan) operating at 40 kV and 40 mA that was fed with a Cu Kα radiation source. By using the Bragg-Brentano experimental method, the patterns of XRD were documented at a scanning rate of 0.02/sec. Besides, the patterns were generated within the scattered angle (2θ) array of 5° to 90°. The X-ray beam was operated with limiting parameters of 2/3° divergence, 10 mm divergent altitude, 0.3 mm receiving slits, and 2/3° scattering.

A scanning electron microscope (S-4700, Hitachi, Japan) that was operated at 15 kV in a vacuum with a working gap of 7 mm was used to examine the morphology of the powdered S-TiO_2/g-CN. A scanning electron microscope that was supplied with an energy dispersive X-ray detector (55VP SEM) operating at 15 kV was employed to perform the elemental composition analyzes. To further investigate the samples' crystallinity and internal structure, a transmission electron microscope (FE-TEM, JEOL Ltd., JEM-2100F, Japan) was utilized. The TEM samples were prepared by evaporating a droplet of the powders placed on a Cu grid coated with holey carbon support films in ethanol. The as-prepared samples' effective surface area was estimated using the BET theory. The adsorption-desorption isotherms were generated in Belsorp mini II, BEL, Japan. The desorption data was subsequently used in combination with the Barrett-Joyner-Halenda (BJH) framework to investigate the pore volume distributions.

To confirm the presence of anatase titania and g-CN, the IR Prestige-21, Shimadzu, Japan, was utilized to generate the Fourier transform infrared (FT-IR) patterns of the as-prepared samples. The range of wavenumbers was prefixed between 400 cm^{-1} and 4000 cm^{-1}; moreover, the samples were prepared using the KBr pellet preparation method. The X-ray photoelectron spectroscopy (XPS) spectra of the dry samples were generated on a MultiLab2000, VG, UK, to validate the various chemical bonds present in the samples.

3.3.2 Analysis of optical attributes

The photoluminescence (PL) spectra were generated on a dual microplate spectrofluorometer, Horiba, Piscataway, NJ, USA, to evaluate the charge recombination rates of the prepared samples during photoactivity. A sample excitation wavelength of 300 nm was utilized in the fluorometer. A UV-Vis-NIR spectrometer (Lambda 950, Perkin Elmer, KBSI Daegu center, South Korea) that was fitted with a diffuse reflectance (DRA) accessory was used to obtain the UV-VIS spectra, which were documented in a spectral range of between 400 and 800 nm. The optical bandgaps of the as-prepared samples were determined by using the modified Kubelka-Munk functions illustrated in the following equations,

$$F(R) = \frac{K}{S} \qquad (3\text{-}6)$$

$$K = (1 - R)^2 \qquad (3\text{-}7)$$

$$S = 2R \qquad (3\text{-}8)$$

Here, F(R) is the Kubelka-Munk function, and the K, R, and S are molar absorption coefficient, scattering factor, and reflectance data, respectively. Additionally, for sludge generated titania (anatase), an indirect energy bandgap was considered, and it was determined through extrapolation of $F(R)h\nu)^{1/2}$ vs. hν. In contrast, the bandgaps of the as-prepared samples were estimated considering direct energy bandgap $(F(R)h\nu)^2$ vs. hν).

CHAPTER 4
Preparation and characterization of TiO_2 generated from synthetic wastewater using $TiCl_4$ based coagulation/flocculation aided with $Ca(OH)_2$

STATEMENT OF CONTRIBUTION OF AUTHORS

Title of Paper	Preparation and characterization of TiO_2 generated from synthetic wastewater using $TiCl_4$ based coagulation/flocculation aided with $Ca(OH)_2$		
Publication Status	☒Published ☐Accepted for Publication ☐Submitted for Publication		
Publication Details	**Hossain, S. M.**, Park, M. J., Park, H. J., Tijing, L., Kim, J. H., & Shon, H. K. (2019). Preparation and characterization of TiO_2 generated from synthetic wastewater using $TiCl_4$ based coagulation/flocculation aided with $Ca(OH)_2$. *J Environ Manage*, *250*, 109521. https://doi.org/10.1016/j.jenvman.2019.109521		
PRINCIPLE AUTHOR			
Name of Principle Authors	Sayed Mukit Hossain **(Candidate)**		
Contribution	**Conceptualization, Data curation, Formal analysis, Investigation, Methodology, Validation, Writing – original draft.**		
Certification	This paper reports on original research I conducted during my Higher Degree by Research candidature and is not subject to any obligations or contractual agreements with a third party that would constrain its inclusion in this thesis. I am the primary author of this paper.		
Signature	Production Note: Signature removed prior to publication.	Date	30/11/2021
CO-AUTHOR CONTRIBUTIONS			
Name of Co-Author 1	Myoung Jun Park		
Contribution	Methodology, Formal analysis.		
Name of Co-Author 2	Hee Ju Park		
Contribution	Methodology, Formal analysis.		
Name of Co-Author 3	Leonard Tijing		
Contribution	Writing - review and editing, Funding acquisition, Supervision.		
Name of Co-Author 4	Jong-Ho Kim		
Contribution	Writing - review and editing, Funding acquisition, Supervision.		
Name of Co-Author 5	Ho Kyong Shon		
Contribution	Supervision, Project administration, Resources, Funding acquisition, Validation, Writing - review and editing.		

4 Preparation and characterization of TiO_2 generated from synthetic wastewater using $TiCl_4$ based coagulation/flocculation aided with $Ca(OH)_2$

4.1 Abstract

This study focused on the preparation of undoped and Ca-doped titania from flocculation generated sludge. Initially, $TiCl_4$ was utilized to perform coagulation and flocculation in synthetic wastewater and an optimized dose of coagulant was determined by evaluating the turbidity, dissolved organic carbon (DOC) and zeta potential of the treated water. Later, using $Ca(OH)_2$ as a coagulant aid, the effects on effluent pH, turbidity and DOC removal were investigated. Both Ca-doped and undoped anatase TiO_2 were prepared from the flocculated sludge for morphological and photocatalytic evaluation. During the standalone use of $TiCl_4$, maximum turbidity and DOC removal were found at 11.63 and 14.54 mg Ti/L, respectively. At the corresponding coagulant dose, rapid deprotonation of water caused the pH of the effluent to reach below 3.77 mg Ti/L. Whereas, when using $Ca(OH)_2$ as a coagulant aid, a neutral pH (7.26) was attained at a simultaneous dosing of 32.40 mg Ca/L and 14.54 mg Ti/L. When aided with $Ca(OH)_2$, the turbidity removal was further increased by 54.28% and the DOC removal was somewhat similar to the standalone use of $TiCl_4$. TiO_2 was prepared by incinerating the collected sludge at 600°C for 2 h. Both XRD and SEM analysis were conducted to observe the morphology of the prepared titania. The XRD pattern of the TiO_2 showed only an anatase phase along with the presence of a high atomic proportion of Ca (4.14%). Consequently, a high amount of Ca atoms inhibited the level of TiO_2 phase and no obvious presence of CaO was observed. The prepared Ca-doped TiO_2 at the optimized dose of $Ca(OH)_2$ was found to be inferior to the undoped TiO_2 during the photodegradation of acetaldehyde. However, a reduced dose of $Ca(OH)_2$ (< 15 mg Ca/L) exhibited a substantial increase in photoactivity under UV irradiance.

4.2 Introduction

For more than 100 years, coagulation has been found to be very effective for treating wastewater from varying sources containing diverse types of pollutants. Conventionally, different forms of iron (Fe) and aluminium (Al) salts are used for the purpose of coagulation, and they are found very useful for improving the physicochemical properties of wastewater (Hameed et al., 2018; Z. Wang et al., 2018a). However, coagulation using Fe and Al salts possesses two significant drawbacks: i) the generation of voluminous amounts of sludge, which requires further treatment and a complex disposal scheme (Xia

et al., 2018) and ii) the toxicity of the residual chemicals present in the effluent (Barakwan et al., 2019; Lee et al., 2008). Subsequently, the presence of residual Al has been found to be harmful to both human health and the environment (Cheng & Chi, 2002). In addition, the effluent generated from using Fe salts as the coagulant has been found to have a high chroma index and has shown corrosive properties (Y. Wang et al., 2016). Hence, for conventional wastewater treatment facilities, the post-treatment of sludge consumes a substantial portion of operating costs and requires critical attention considering its environmental aspects (Y. X. Zhao, B. Y. Gao, G. Z. Zhang, S. Phuntsho, et al., 2014; Y. X. Zhao, B. Y. Gao, G. Z. Zhang, Q. B. Qi, et al., 2014). Moreover, the recycling of valuable resources from Al- and Fe-based flocculation has not had many promising results (J.-H. Kim et al., 2011). To overcome the aforementioned drawbacks, Ti-based coagulation was introduced for the treatment of wastewater (Shon et al., 2007a). A number of studies involving Ti-based coagulation have reported equivalent coagulation efficiencies compared to conventional coagulants and the alleviation of the residual impacts of the trace elements. Another very important aspect of Ti-based flocculation is the recovery of anatase TiO_2 from flocculated sludge.

Upton and Buswell (1937) first utilized a Ti-based coagulant to remove fluoride ions and colour from drinking water. Using a dry feed of $Ti(SO_4)_2$, they compared the level of coagulation with commercially available alum and inferred that Ti-based coagulation is cheaper than conventional coagulants. Nonetheless, the full extents of the benefits were not realised as the dry feed of Ti salts was found to be partially hydrolyzed and ineffective concerning the removal of colour from the influent (Upton & Buswell, 1937). Afterward, a number of relevant studies found that Ti-based coagulants exhibit superior performance compared to conventional coagulants in removing DOC and a broad range of colloidal particles (Chekli, Corjon, et al., 2017; Hussain et al., 2019; X. Wang et al., 2018). Besides, the flocs generated using $TiCl_4$ were found to be larger, and the floc generation rate was higher with respect to Al- and Fe-based coagulants (Chekli, Corjon, et al., 2017; Chekli, Eripret, et al., 2017; Zhao et al., 2017). In addition, the introduction of Ti salts as a coagulant facilitated the recovery of resources such as TiO_2 from the generated sludge (J. H. Kim et al., 2011; X. Wang et al., 2016). The photocatalytic and optical attributes of TiO_2, along with its strong oxidising power, make it a valuable by-product (Sulaiman et al., 2018). TiO_2 is one of the most studied and utilized semiconductor in the field of photocatalysis under a wide range of light spectrum. As a photocatalyst, TiO_2 has received

vast recognition primarily due to its environment friendly nature, chemical stability, nontoxicity and high rate of electron (e^-)/hole (h^+) pair formulation ability (Reddy et al., 2018; Siwinska-Stefanska et al., 2018). It has been reported that nearly 40 mg of TiO_2 could be produced from treating one litre of wastewater using $TiCl_4$ (El Saliby et al., 2009; Okour, El Saliby, et al., 2009). Furthermore, there is better social acceptance of the use of Ti in terms of human and environmental health in comparison to the conventional Al- and Fe-based coagulants (Lee et al., 2008; Zhao, Gao, Shon, Cao, et al., 2011).

However, at an optimum $TiCl_4$ concentration during coagulation, the hydrolysis of Ti salts causes the release of a considerable amount of H^+ and generates an acidic effluent (pH, 3.5-5) (Chekli, Eripret, et al., 2017; Hussain et al., 2019). Hence, a certain level of post-treatment is necessary to increase the pH of the treated effluent. To overcome this problem, the use of coagulant aids during flocculation (H. K. Shon et al., 2009b) and/or the introduction of pre-hydrolyzed coagulants (Zhao et al., 2015) are two possibly viable solutions. H. K. Shon et al. (2009b) compared the effectiveness of using alkaline metallic coagulant aids, for example $Ca(OH)_2$, $FeCl_3$ and $Al(SO_4)_3$, with $TiCl_4$ during flocculation and this showed promising results from the aspect of final pH along with adequate DOC and turbidity removal. The study prepared alkaline metal doped TiO_2 from flocculated sludge and showed an enhanced level of optical (UV) absorbance and photoactivity. In addition, they inferred that $Ca(OH)_2$ was the most effective coagulant aid from the perception of the final pH and photocatalytic activities of the recovered TiO_2 compared to $FeCl_3$ and $Al_2(SO_4)_3$. Nevertheless, rather than finding an optimized dose of $Ca(OH)_2$, the focus of the study was on the preparation of Ca-doped TiO_2 from flocculated sludge. Hence, a detailed study to optimize the dose of $Ca(OH)_2$ as a coagulant aid and the characterization of the prepared Ca-doped TiO_2 at the corresponding dose could be a significant addition. Furthermore, several related studies report that Ca doping on commercially available P25 could promote a redshift and enhance photoactivity through band gap narrowing (Akpan & Hameed, 2011b; Y. Li et al., 2007; Zaleska, 2008b).

The aim of the present study was the effective fabrication of a Ca-doped anatase TiO_2 photocatalyst from Ti-based flocculation utilizing simultaneous coagulant ($TiCl_4$ and $Ca(OH)_2$) dosing. Insufficient amounts of studies were found regarding this topic. Most importantly, to the authors' knowledge, this is one of the first studies to evaluate the morphological and photocatalytic attributes of flocculation generated Ca-doped TiO_2 prepared from the optimized dosing of coagulant ($TiCl_4$) and coagulant aid ($Ca(OH)_2$).

Hence, the specific objectives were: (a) the attainment of a neutral final pH in treated effluent using $Ca(OH)_2$ as a coagulant aid, (b) the evaluation of turbidity and DOC removal during simultaneous dosing of $TiCl_4$ and $Ca(OH)_2$ (c) the preparation of undoped and Ca-doped TiO_2 utilizing flocculated sludge and (d) the characterization of the prepared TiO_2 from morphological and photocatalytic aspects.

4.3 Optimization of $TiCl_4$ dose

To determine the optimum dose of Ti to use as a coagulant, simple jar tests were conducted using $TiCl_4$. The removal rates of DOC and the turbidity of the effluent were used as indicators for coagulant dose optimization. The initial pH, DOC, turbidity, and zeta potential of the synthetic wastewater was determined as 7.38, 7.44 mg/L, 3.17 NTU and -19.2 mV, respectively. **Fig. 4-1** shows the gradual increase in DOC removal for increased doses of $TiCl_4$ along with the corresponding decrease in pH. At a maximum dose of 23.26 mg Ti/L, the final pH was found to be 3.05. Evidently, the decrease in pH of the effluent resulted from the continuous release of H^+ during the hydrolysis of $TiCl_4$ (Y. X. Zhao, B. Y. Gao, G. Z. Zhang, Q. B. Qi, et al., 2014). The maximum DOC removal was found at 14.54 mg Ti/L with a corresponding pH and zeta potential of 3.77 and +1.25 mV, respectively. A slightly positive zeta potential indicates that charge neutralisation plays a significant role in the removal of DOC from synthetic wastewater (Hussain et al., 2019).

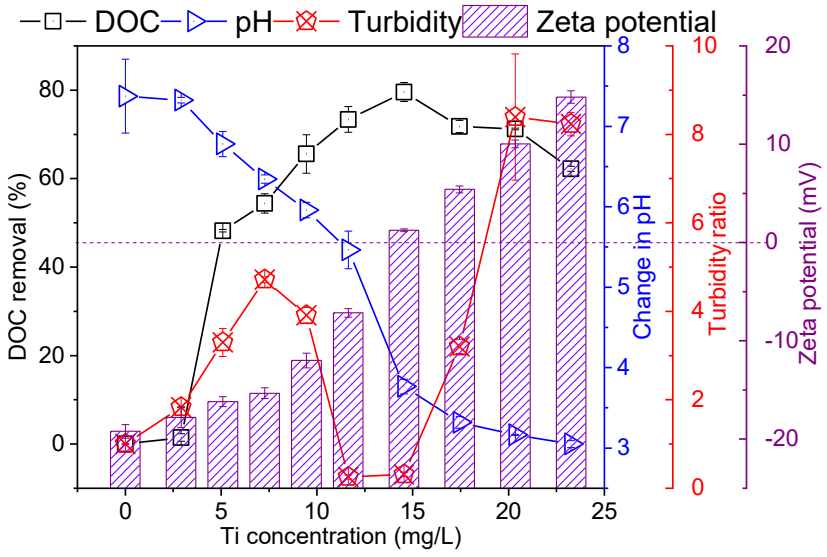

Fig. 4-1. Flocculation efficiency using $TiCl_4$: illustrates changes in % DOC removal, pH, turbidity ratio and zeta potential at varying doses of $TiCl_4$.

From **Fig. 4-1**, it is clear that at lower doses of $TiCl_4$, the rate of increase in zeta potential was very low and the isoelectric point was reached at between 11.63 and 14.54 mg Ti/L. Hence, at a lower dose, $TiCl_4$ was unable to destabilize the negatively charged colloids, causing inefficient DOC and turbidity removal. However, at a dose higher than 7 mg Ti/L, the turbidity ratio started to reduce abruptly. The maximum turbidity removal was attained at a coagulant dose of 11.63 mg Ti/L, at which the pH and zeta potential were found to be 5.46 and -7.16 mV, respectively. A relatively high negative zeta potential at maximum turbidity removal indicates the dominance of sweep flocculation and adsorption on the cationic hydrolyzed species of $TiCl_4$ as the core flocculation mechanism (Z. Wang et al., 2018d). As two different doses of $TiCl_4$ were found for maximum turbidity and DOC removal, the doses of $Ca(OH)_2$ were optimized against both of these doses.

4.4 Optimization of $Ca(OH)_2$ dose as a coagulant aid

Two series of jar tests were conducted using $Ca(OH)_2$ as a coagulant aid of $TiCl_4$. **Fig. 4-2** presents the test results of coagulation/flocculation using $TiCl_4$ and $Ca(OH)_2$. From **Fig. 4-2(b),** it is clear that a continuous increase in $Ca(OH)_2$ dose results in a subsequent increase of effluent pH. This augmented pH may have resulted from the introduction of OH^- ions coming from the increased doses of $Ca(OH)_2$. At a coagulant dose of 11.63 and 14.54 mg Ti/L, an approximately neutral pH was obtained when the Ca concentration in the wastewater was 21.60 and 32.40 mg/L, respectively. Thus, from **Fig. 4-2(a)**, it can be seen that at a neutral pH, the DOC removal was 69.69% and 75.54%, respectively. In addition, the estimated turbidity ratio (**Fig. 4-2(c)**) was substantially low (high turbidity removal) compared to the standalone use of $TiCl_4$ at a neutral pH for corresponding doses of $Ca(OH)_2$.

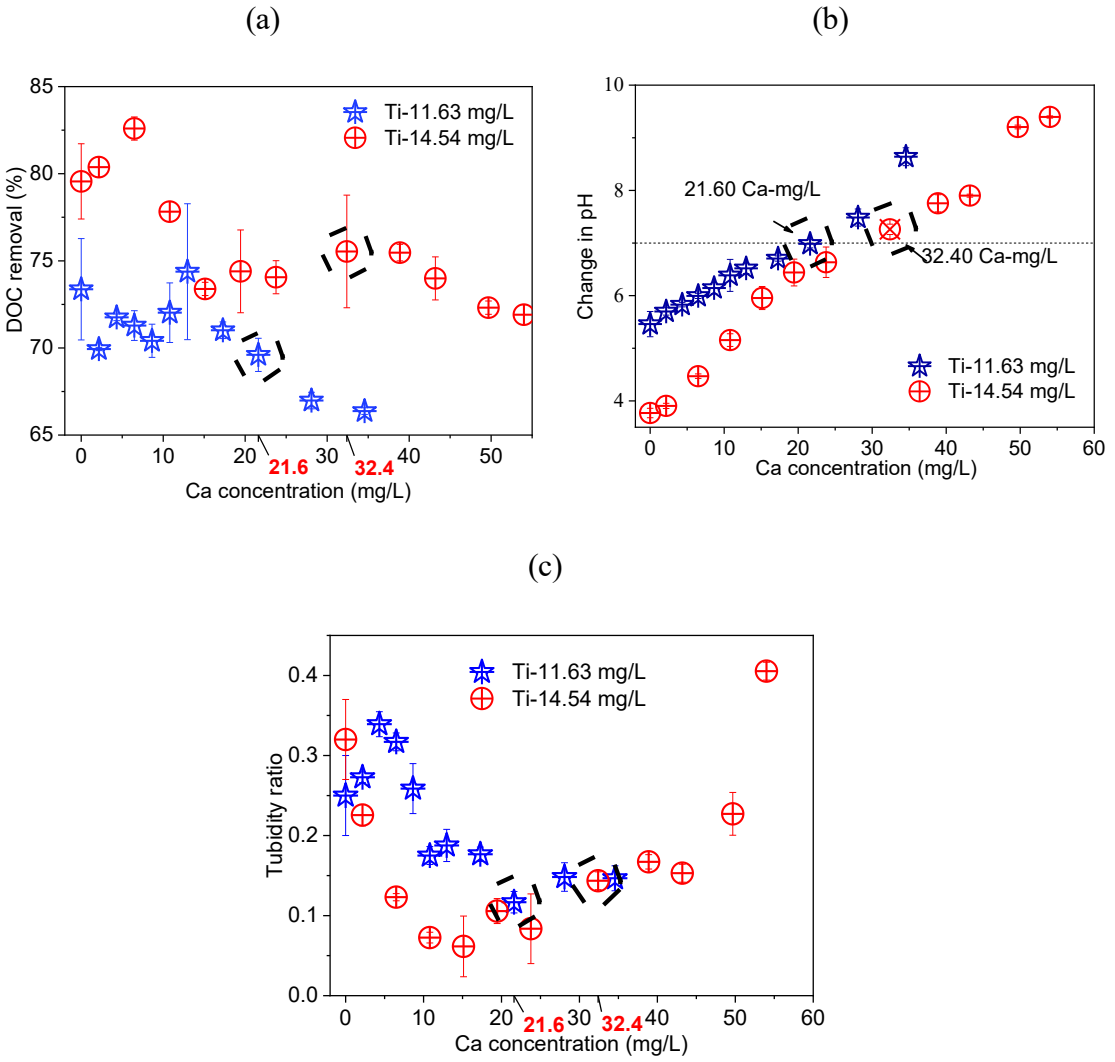

Fig. 4-2. Flocculation efficiencies using simultaneous dosing of $TiCl_4$ and $Ca(OH)_2$: a) % DOC removal, b) pH variance, and c) turbidity ratio at varying doses of $Ca(OH)_2$ for selected concentrations (11.63 mg Ti/L and 14.54 mg Ti/L) of $TiCl_4$.

At a coagulant dose of 14.54 mg Ti/L, the inclusion of $Ca(OH)_2$ on an incremental basis showed an initial increase in DOC removal, which was followed by a sinusoidal (successive decrease and increase) shape like trend (**Fig. 4-2(a)**). The introduction of divalent Ca^{2+} increased the amount of cationic species in the influent, which might have increased the rate of DOC removal through charge neutralisation and colloids adsorption of oppositely charged hydrolyzed products (Z. Liu et al., 2019). On the other hand, a possible explanation for the reduction in DOC removal at a Ca dose greater than 6.48 mg/L could be the substantially increased zeta potential of the effluent. In fact, the zeta potential at a coagulant dose of 14.54 mg Ti/L was +1.25 mV (see **Fig. 4-1**) and the introduction of Ca^{2+} might have further increased the zeta potential of the effluent.

Apparently, a significantly high zeta potential tends to promote charge reversal (restabilization of the destabilized colloidal particles) and introduce repulsion between similarly charged particles, causing a reduction in coagulation efficiency (i.e., the rate of DOC removal) (Dobias & Stechemesser, 2005). Meanwhile, a further increase in the $Ca(OH)_2$ dose increased the pH. Consequently, at a pH range of 6 to 8, the dominant hydrolyzed product of $TiCl_4$ is $Ti(OH)_4$, which could facilitate sweep flocculation (X. Wang et al., 2018; Zhao et al., 2017). As a result, the DOC removal started to increase again at a dose greater than 32.40 mg Ca/L (**Fig. 4-2(a)**). A similar trend was observed for DOC removal using a coagulant dose of 11.63 mg Ti/L.

Comparing **Fig. 4-1** and **Fig. 4-2**, the addition of $Ca(OH)_2$ seems to further increase the turbidity removal of the effluent compared to the standalone use of $TiCl_4$. Additionally, the DOC removal was found to be equivalent in both cases. Interestingly, when using $Ca(OH)_2$, the turbidity removal was increased by 54.28% and after maximum removal, any increase in the Ca dose showed a successive reduction in turbidity removal (see **Fig. 4-2(c)**). This increased turbidity removal can be explained by increased cationic species due to the incorporation of $Ca(OH)_2$. Based on the above discussion and **Fig. 4-2**, it is clear that a coagulant dose of 14.54 mg Ti/L performed better than 11.63 mg Ti/L when $Ca(OH)_2$ is used as a coagulant aid. Hence, focusing on the neutral pH and the corresponding DOC and turbidity removal, the optimum concentrations of Ti and Ca that were selected are 14.54 and 32.4 mg/L, respectively.

4.5 Characterization of produced TiO_2

4.5.1 EDX and SEM analysis

An EDX analysis was conducted to determine the elemental composition of the prepared TiO_2. The detailed compositions are illustrated in **Table 4-1**. The primary constituents found in the analysed U-TiO_2 and Ca-TiO_2 were C, O, P, Ca, and Ti. Presumably, the prevailing organic matters and nutrients of synthetic wastewater contributed towards the presence of C and P. Some trace elements that were found in the EDX analysis were attributed to instrument factors. Related research reports that most doped C and P atoms substitute O atoms and Ca is placed at the substitutional or interstitial site of Ti atoms (M. M. Mian & G. Liu, 2019).

Table 4-1. Elemental composition of prepared TiO_2 determined via an EDX analysis.

Element	**U-TiO_2 atomic % (wt. %)**	**Ca-TiO_2 atomic % (wt. %)**
C	8.49 (4.48)	12.45 (6.45)
O	67.06 (46.16)	61.15 (43.87)
Si	0.18 (0.21)	0.73 (0.89)
P	1.55 (2.00)	1.14 (1.53)
Ti	22.47 (46.27)	15.75 (33.76)
Fe	0.08 (0.19)	-
Cu	0.19 (0.53)	0.46 (1.30)
Zn	0.13 (0.35)	0.18 (0.50)
Ca	-	4.14 (7.47)
Mg	-	0.32 (0.36)
S	-	0.21 (0.27)
Cl	-	0.07 (0.11)

A number of salient features of the prepared TiO_2 in the current study was compared with related studies and tabulated in **Table 4-2**. Although, (Na et al., 2011) prepared titania using printing paper wastewater (PPW) flocculated sludge, the U-TiO_2 prepared in this study had a remarkable resemblance in elemental composition, especially concerning the proportion C, O, and Ti. A similar annealing temperature and duration may have played a vital role. However, the Ca-TiO_2 showed a higher atomic proportion of C (12.45%) and Ca (4.14%). This high C and Ca content could be attributed to the change in the preparation process when preparing the TiO_2. While the TiO_2 preparation strategy used for this study was adapted from (J.-H. Kim et al., 2011), rather than using natural settlement, a centrifuge was utilized to separate the sludge. This may be the reason for the higher C and Ca content of the Ca-TiO_2. The high C content resulted greyish colour in the prepared Ca-TiO_2 (Figure not shown).

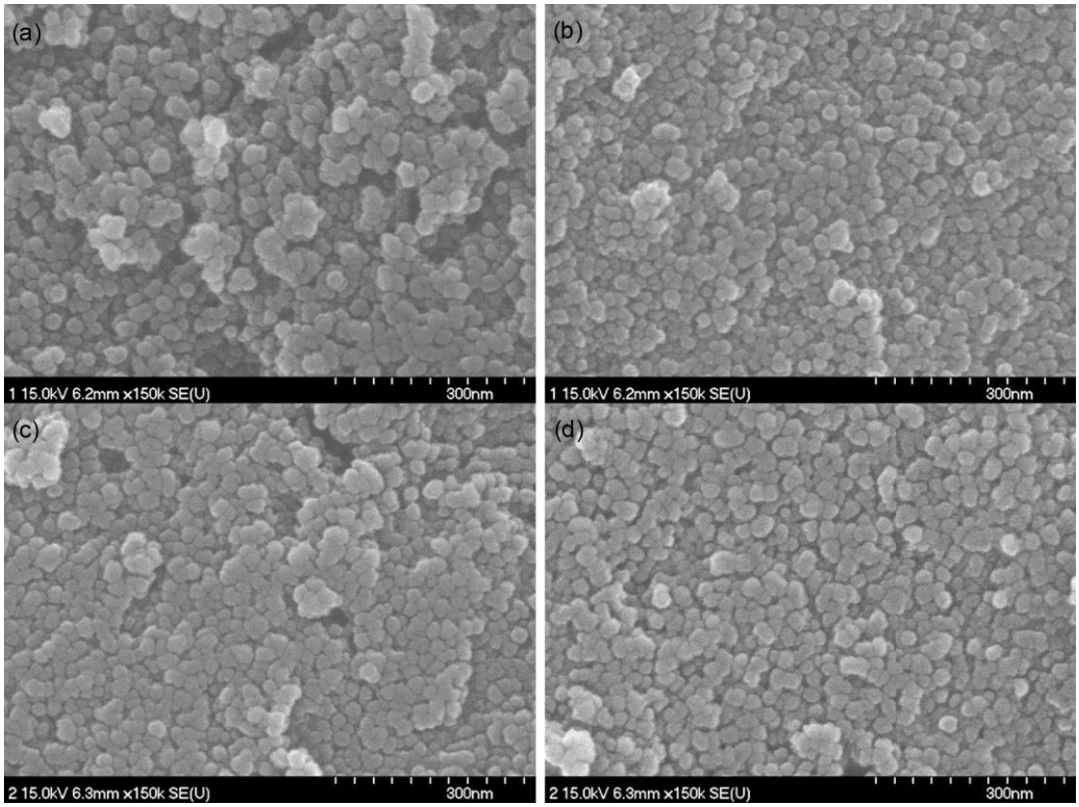

Fig. 4-3. SEM image of U-TiO_2 (a, b) and Ca-TiO_2 (c, d).

Fig. 4-3 depicts the SEM images of the U-TiO_2 and Ca-TiO_2. Both the U-TiO_2 and Ca-TiO_2 displayed similar particle sizes, which varied from 10 to 20 nm. **Table 4-2** shows that in the majority of the reported studies on flocculation generated TiO_2, the particle size was approximately similar to the U-TiO_2 prepared for this study despite the varying physicochemical properties of the wastewater used. On the other hand, the presence of Ca in the Ca-TiO_2 does not show any notable differences in particle size, which contrasts with related studies. (Sendi, 2018) inferred that a trace amount of substantially doped Ca in TiO_2 can cause a significant reduction of particle size by enhancing the crystal density through the development of oxygen vacancies. In addition, both Sendi (2018) and Liu et al. (2014) reported that at a high atomic proportion of Ca doping (>2%), an increase in the amount of doping causes an increase in particle size. Presumably, the large portions of the doped Ca atoms were interstitially placed on the Ca-TiO_2 crystals, causing negligible deformation of the structure of TiO_2 (Humayun et al., 2018).

4.5.2 XRD results and BET surface area

The XRD pattern and S_{BET} of both U-TiO_2 and Ca-TiO_2 are presented in **Fig 4-4**. Comparing the peak of the XRD pattern with pure TiO_2, the majority of U-TiO_2 and Ca-

TiO_2 were in the anatase phase. Evidently, Ti-based flocculated sludge calcined at 600°C produces only the anatase phase of the TiO_2. The rutile phase is only detectable above 800°C (Shon et al., 2007a). Additionally, no peak was observed on the XRD pattern for CaO, which corresponds with previous studies (Akpan & Hameed, 2011b; Y. Li et al., 2007). For instance, Akpan and Hameed (2011b) reported that TiO_2 generated by incinerating at 360°C with 0.3% to 1% by weight of Ca dopant showed no presence of CaO when conducting a XRD analysis. However, Liu et al. (2014) prepared Ca-doped TiO_2 by modifying commercially available TiO_2 and they claim that a Ca-O bond is present when there is a high Ca content (3.67 atomic %) and a high annealing temperature (595 °C).

Perhaps the presence of the rutile phase facilitates the formation of CaO during calcination, which was not the case in the present study. Moreover, compared to U-TiO_2, Ca-TiO_2 had a lower peak (see **Fig. 4-4**) for the TiO_2 phase, which indicates that the presence of a high proportion of the Ca atom inhibits the peak of the TiO_2 phase (Burnat et al., 2015). The S_{BET} of the prepared U-TiO_2 was found to be 116 m^2/gm (**Fig. 4-4**), which is two folds higher than the commercial P25 (50 m^2/gm) (J.-H. Kim et al., 2011) and in good coherence with previous studies (see **Table 4-2**). However, the specific surface area of Ca-TiO_2 was found to be 38 m^2/gm, which is even less than commercial P25 and in contrast with related studies. Due to the presence of a significantly high amount of Ca in the prepared Ca-TiO_2, the formation of TiO_2 was inhibited (see **Fig 4-4**), which may be the reason for the reduced S_{BET}. Moreover, regarding transitional metal, (Zhu et al., 2006) elaborated that an increase in the proportion of dopant could reduce the specific surface area.

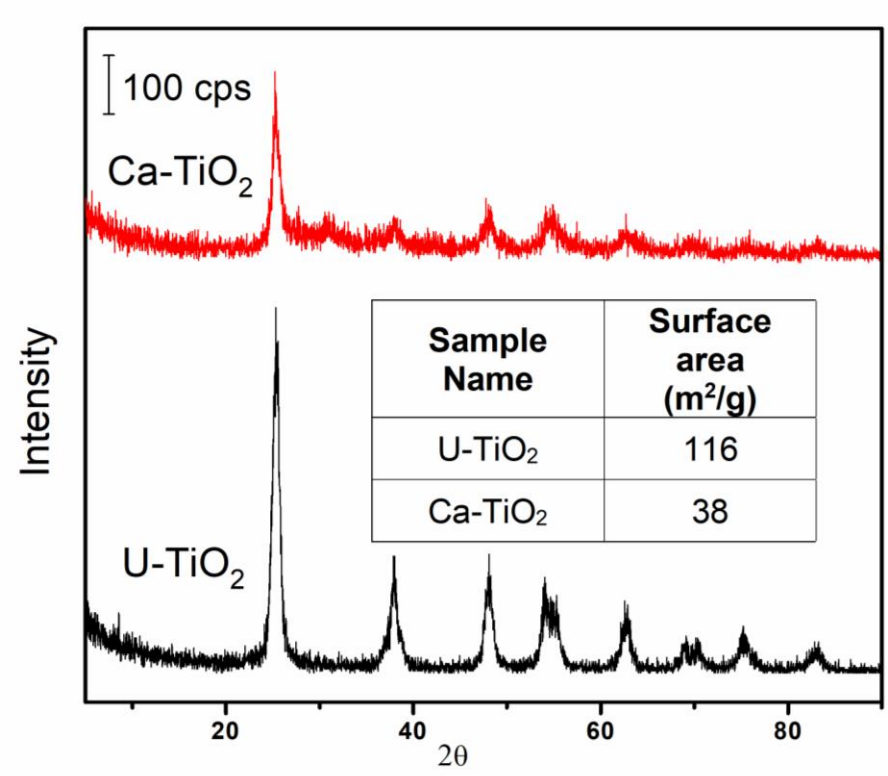

Fig. 4-4. XRD pattern of U-TiO_2 and Ca-TiO_2 along with S_{BET} determined using the BET method.

Table 4-2. Synopsis of the preparation of photoactive anatase TiO_2 from flocculated sludge and their salient features.

Refs	**Coagulant**	**Wastewater types[a]**	**Temperature, Duration**	**Crystal phase**	**Size (nm)**	**S_{BET} (m^2/g)**	**Atomic %**	**Photoactivity under UV irradiance**
Shon et al. (2007a)	$TiCl_4$	Synthetic BTSE	600 ℃ - 800 ℃	Anatase TiO_2 NPs	6	76.30	Ti (26.90%); O (51.50%); C (15.80%); P (5.80%)	Superior photodegradation of CH_3CHO compared to P25.
Okour, El Saliby, et al. (2009)	$TiCl_4$	SW	600 ℃, 24 h	Anatase TiO_2 NPs	40	68.10	Ti (23.75%); O (76.02%); Si (0.23%)	Superior photodegradation of CH_3CHO compared to P25.
H. Shon et al. (2009b)	$TiCl_4$	DW	600 ℃	Anatase TiO_2 NPs	13	90.20	Ti (27.65%); O (65.92%); C (3.87%)	Superior photodegradation of CH_3CHO compared to P25.
		BTSE	600 ℃	Anatase TiO_2 NPs	15	103.50	Ti (32.19%); O (67.08%); C (4.82%)	Superior photodegradation of CH_3CHO compared to P25.

Refs	Coagulant	Wastewater types[a]	Temperature, Duration	Crystal phase	Size (nm)	S_{BET} (m^2/g)	Atomic %	Photoactivity under UV irradiance
H. K. Shon et al. (2009b)	$TiCl_4$ + $Al_2(SO_4)_3$	Synthetic BTSE	600 ℃	Anatase Al doped TiO_2 NPs	11 – 5		Ti (18.9 – 23.74%); O (69.5 – 71.14 %); C (6.74 – 9.37%); Al (0.10 – 0.46%)	Equivalent photodegradation of CH_3CHO compared to P25.
	$TiCl_4$ + $FeCl_3$		600 ℃	Anatase Fe doped TiO_2 NPs	11 – 8		Ti (19.66 – 22.40%); O (59.07 – 68.7%); C (7.84 – 8.00%); Fe (0.27 – 9.83%)	Rate of CH_3CHO photodegradation reduced by 50%, when Fe content was above 1.89 at.%.
El Saliby et al. (2010b)	$TiCl_4$	DWW	600 ℃, 24 h			68.24	Ti (30.20%); O (62.80%); C (5.09%)	Slightly reduced rate of CH_3CHO photodegradation compared to P25.

Refs	Coagulant	Wastewater types[a]	Temperature, Duration	Crystal phase	Size (nm)	S_{BET} (m^2/g)	Atomic %	Photoactivity under UV irradiance
Na et al. (2010)	$TiCl_4$	Sludge from final settling tank	600 ℃				Ti (17.49%); O (65.00%); C (8.56%); P (5.72%)	After 200 minutes of irradiance, CH_3CHO photodegradation rate reached 60%.
Na et al. (2011)	$TiCl_4$	PPW	600 ℃, 3 h		10 – 15		Ti (30.90%); O (65.00%); C (8.56%)	After 200 minutes of irradiance, CH_3CHO photodegradation rate reached 60%.
El Saliby et al. (2012)	$TiCl_4$	BTSE	600 ℃, 4 h		20 – 30	83.52	Ti (25.20%); O (68.03%); C (5.27%)	Superior compared to P25, 85 – 89% UV_{254} and $color_{436}$ removal in SWW.
		DWW	600 ℃, 4 h		40 – 50	52.81	Ti (23.73%); O (68.07%); C (5.47%)	Superior compared to P25, 85 – 89% UV_{254} and $color_{436}$ removal in SWW.

Refs	Coagulant	Wastewater types[a]	Temperature, Duration	Crystal phase	Size (nm)	S_{BET} (m^2/g)	Atomic %	Photoactivity under UV irradiance
J. B. Kim et al. (2013)	$TiCl_4$ + $FeSO_4$	DWW	640 ℃	Rutile Fe doped TiO_2 NPs	15 – 20		Ti (19.40%); O (68.60%); Fe (6.80%)	Slightly reduced rate of CH_3CHO photodegradation compared to P25.
Z. Wang et al. (2018b)	$TiCl_4$ + MSA	Ag NP enriched wastewater	600 ℃, 12 h	Anatase Ag doped TiO_2 NPs				Equivalent photodegradation of reactive brilliant red K-2BP compared to P25.
Current study	$TiCl_4$	Synthetic BTSE	600 ℃, 2 h	Anatase TiO_2 NPs	10 – 20 nm	116	Ti (22.47%); O (67.06%); C (8.49%)	Equivalent photodegradation of CH_3CHO compared to NP-400.
	$TiCl_4$ + $Ca(OH)_2$			Anatase Ca-doped TiO_2 NPs	10 – 20 nm	38	Ti (15.75%); O (61.15%); C (12.45%); Ca (4.14%)	Negligible photoactivity under UV-A light.

[a] BTSE: Biologically treated sewage effluent; SW: Seawater; DW: Drinking water; DWW: Dye wastewater; PPW: Printing paper wastewater; SWW: Synthetic wastewater; MSA: Modified sodium alginate.

4.6 Photocatalytic activity

To observe the extent of photocatalytic activity, the photodecomposition of gaseous acetaldehyde was observed for both U-TiO_2 and Ca-TiO_2 under UV irradiation. **Fig. 4-5** shows the comparative evaluation of the percentage removal of CH_3CHO using the prepared TiO_2 and commercially available NP-400 (Bentech Frontier). Due to the synergistic effect of large surface areas and photoactivity, initially, the U-TiO_2 showed superior acetaldehyde removal efficiency compared to NP-400 (see **Fig. 4-5**). The degradation of acetaldehyde using U-TiO_2 confirms the formation of an electron/hole (e^-/h^+) pair under UV irradiation (Noman et al., 2019a). When TiO_2 is placed under UV irradiance, related studies reported the formation of hydroxyl ($OH^{\cdot}$) and superoxide ($O_2^{\cdot}$) radicals by utilizing surrounding O_2 and H_2O, respectively (see **Equations. (4-1), (4-2), (4-3)**) (Nasirian et al., 2017). Later, the aforementioned oxidising agents oxidised the CH_3CHO into CO_2 and H_2O, as shown in **Equations (4-4) and (4-5)**. The primary reactions associated with photooxidation of acetaldehyde are illustrated sequentially in the following Equations (Deng et al., 2019; Lin et al., 2018):

$$TiO_2 + hv \rightarrow e^- + h^+ \qquad (4\text{-}1)$$

$$e^- + O_2 \rightarrow O_{2^{\cdot}}^- \qquad (4\text{-}2)$$

$$h^+ + OH^- \rightarrow OH^{\cdot} \qquad (4\text{-}3)$$

$$CH_3CHO + OH^{\cdot} \rightarrow CH_3COOH + CO_2 + H_2O \qquad (4\text{-}4)$$

$$CH_3COOH + O_{2^{\cdot}}^- \rightarrow CO_2 + H_2O \qquad (4\text{-}5)$$

Although, initially, the U-TiO_2 had a higher rate of photoactivity compared to the NP-400 (see **Fig 4-5**), after 50 min, both exhibited equivalent CH_3CHO removal efficiency. The presence of C (8.49 atomic %) and P (1.55 atomic %) in the U-TiO_2 crystal may have acted as e^-/h^+ pair recombination sites and reduced the extent of photooxidation (Karafas et al., 2019). Moreover, Bianchi et al. (2014) reported that acetic acid (CH_3COOH) is one of the intermediate products of CH_3CHO photooxidation, which seems to compete with H_2O for physisorption on photoactive sites (Batault et al., 2015). As a result, the generation of oxidising species may have been reduced, leading to decreased photoactivity.

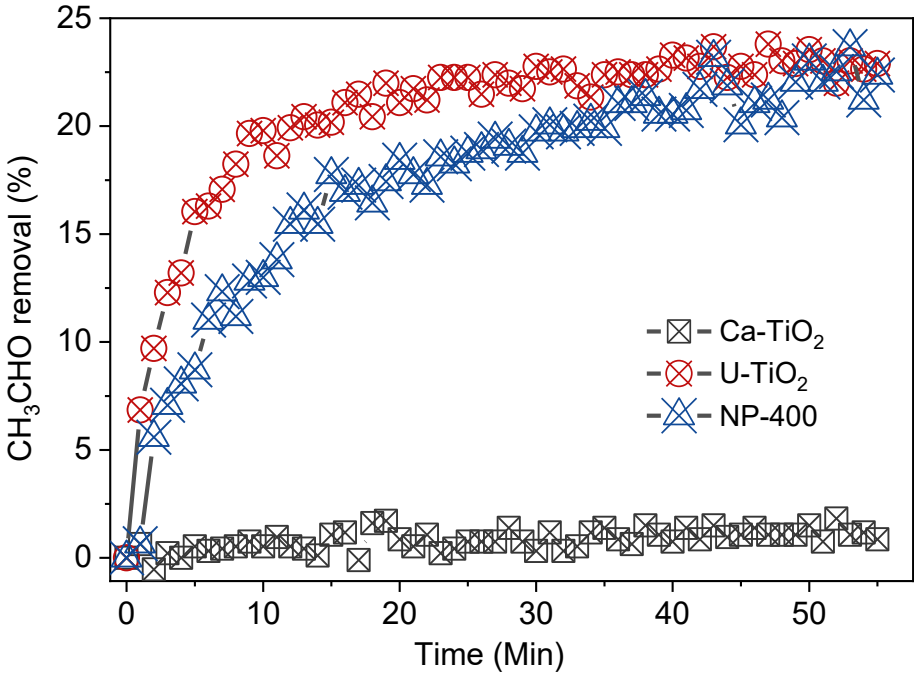

Fig. 4-5. Photodegradation of acetaldehyde under UV irradiation.

On the other hand, Ca-TiO_2 with a smaller specific surface area of 38 m^2/g showed a negligible percentage of acetaldehyde removal (**Fig. 4-5**). Apparently, the prime factors that contributed to this phenomenon are: (a) a low effective surface area and (b) a high atomic percentage of Ca in the final product. It is well established that a reduction in the effective surface area contributes to the depletion of adsorption sites, leading to limited photocatalytic activity. Presumably, most of the doped Ca is interstitially placed on the Ca-TiO_2 crystals, causing an increased rate of e^-/h^+ pair recombination (Sulaiman et al., 2018). Besides, the particle size would have changed if the doped Ca atoms were placed, replacing the Ti^{4+} from the TiO_2 crystal. According to Zhu et al. (2006), the presence of an excess amount of dopant could reduce the level of photocatalytic activities. They state that using transitional metal, during photocatalysis, the presence of an excess amount of dopant could trap an excess number of holes, which could facilitate the recombination of photoinduced electrons. Similarly, Akpan and Hameed (2011b) showed degrading photoactivity compared to P25 when the percentage of the weight of the doped Ca increased to above 1%. Furthermore, when degrading methyl orange using Ca-doped TiO_2, Castro and Durán (2016) proved that a 1% molar ratio of doped Ca^{2+} was more superior than higher proportions of dopant.

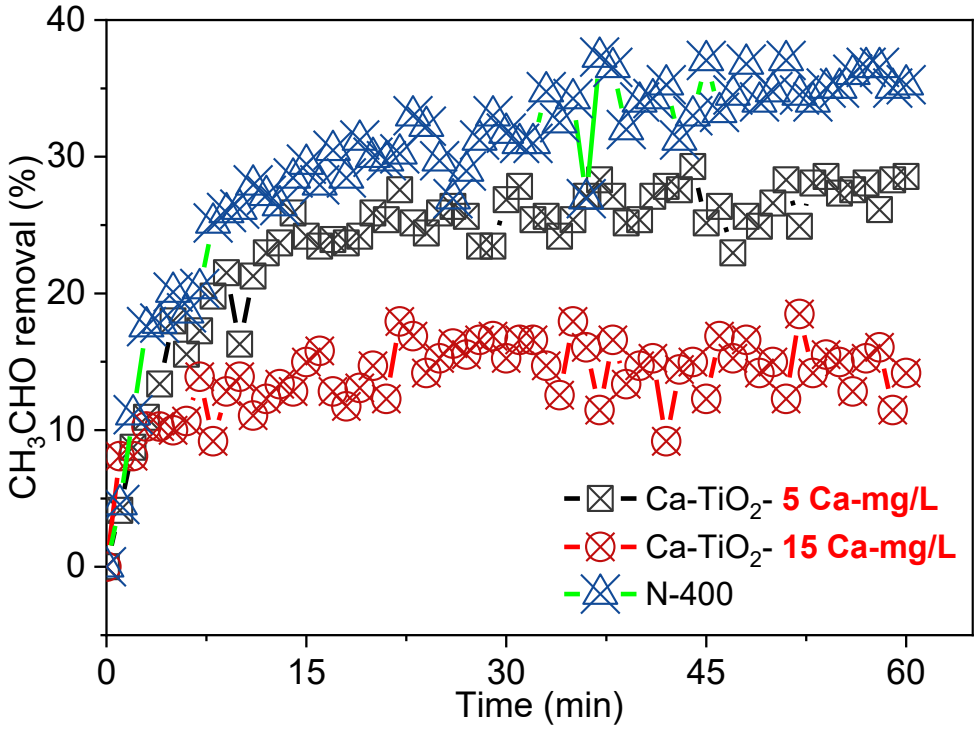

Fig. 4-6. Degradation of CH_3CHO under UV irradiance using Ca-TiO_2 (with reduced Ca doses) and NP-400.

To evaluate the impact of a high Ca content, an additional set of experiments was conducted, and the results are presented in **Fig. 4-6**. The photoactivity (under UV irradiance) of prepared Ca-TiO_2 using reduced doses (5 mg Ca/L and 15 mg Ca/L) of $Ca(OH)_2$ was compared with NP-400 (see **Fig. 4-6**). With the successive reduction of the Ca dose, the photodegradation of CH_3CHO showed significant improvement, but even at 5 mg Ca/L, the extent of photooxidation using Ca-TiO_2 was less than NP-400. Nevertheless, related research exhibits that Ca doping in TiO_2 could promote redshift (photoactivity under visible spectrum), which might cause an absorbance trade-off between the visible and UV light spectrum (Liu et al., 2014). Hence, photoactivity is reduced under UV light, which may have been why CH_3CHO removal was decreased in the current study. Further research on this novel Ca-TiO_2 regarding the internal chemical bonds and the shift in the absorbance spectrum could explore several practical implications. Moreover, in terms of economic values, the flocculation generated Ca-TiO_2 would obviously be superior to the commercial one.

4.7 Resource recovery and applicability

The process of TiO_2 generation by calcinating Ti incorporated flocculated sludge is yet to get simplified. In addition, the features of the flocculation generated TiO_2 depends on several external factors, such as quality of effluents, types of coagulant used, calcination temperature, etc. (Z. Wang et al., 2018a; Y. X. Zhao, B. Y. Gao, G. Z. Zhang, Q. B. Qi, et al., 2014). A simplified explanation could be the generation and accumulation of hydrolyzed species of Ti-based coagulants during coagulation and flocculation along with trapped impurities. Later, upon calcination of the dried sludge at 600 °C, 55% of water and 20% of organic matters get evaporated resulting to $TiO_{1.42}C_{0.44}P_{0.14}$ (H. Shon et al., 2009b). To date flocculation generated TiO_2 has been prepared from biologically treated sewage effluent (H. Shon et al., 2009b), seawater (Okour, El Saliby, et al., 2009), drinking water (Y. X. Zhao, B. Y. Gao, G. Z. Zhang, Q. B. Qi, et al., 2014), dye wastewater (El Saliby et al., 2012), printing paper wastewater (Na et al., 2011), and dewatered sewage sludge (M. M. Mian & G. Liu, 2019). It has been reported that using $TiCl_4$ as a coagulant in secondary sewage effluent 40 mg of TiO_2 can be produced from 1 L of wastewater (El Saliby et al., 2009; Okour, El Saliby, et al., 2009).

The synthetic wastewater used in this study was to mimic BTSE. Consequently, the organic components found in BTSE are mainly residue from raw sewage and metabolic derivatives of biological treatment. Based on analytical results concerning real sewage water, a number of highly cited studies used the chemical composition shown in **Table 4-2** and reported similar attributes (J.-H. Kim et al., 2011; Lee et al., 2008; Seo et al., 1997; Shon et al., 2007a). Additionally, several studies, illustrated in **Table 4-2** reported the preparation of photoactive TiO_2 from real secondary sewage effluents (El Saliby et al., 2012; Na et al., 2010; Zhao & Li, 2019). The anatase titania prepared from real secondary sewage effluents were found with high S_{BET} and reduced rate of e^-/h^+ pair recombination during photooxidation under UV light (M. M. Mian & G. Liu, 2019). Besides, the elemental composition of as prepared TiO_2 in this study showed remarkable resemblance with TiO_2 prepared from real secondary sewage effluents (see **Table 4-2**). Using varying sources of wastewater, the flocculation generated TiO_2 showed superior photoactivity compared to commercially available titania. Hence, application of this process could facilitate the sustainable management of wastewater sludge and contribute towards the growing demand of photoactive TiO_2.

4.8 Conclusion

This study explored the effects of using $Ca(OH)_2$ as a coagulant aid has on the coagulation performance of $TiCl_4$ and the properties of the recovered TiO_2. The results of the coagulation efficiency were systematically compared with the standalone use of $TiCl_4$ and the photoactivity of the prepared TiO_2 was compared with NP-400 under UV-A irradiance. The incorporation of $Ca(OH)_2$ as a coagulant aid resulted in a neutral pH in the treated water and superior turbidity removal. Using the optimized coagulant dose (14.54 mg Ti/L), the prepared U-TiO_2 showed equivalent CH_3CHO removal rate compared to commercially available NP-400 under UV irradiation. However, the Ca-TiO_2 developed using the optimized dose of $Ca(OH)_2$ showed negligible photoactivity under UV light. A high proportion of Ca (4.14 atomic %) within the doped TiO_2 seemed to reduce the S_{BET} and photoactivity under UV. On the other hand, at a reduced $Ca(OH)_2$ dose (15 and 5 mg Ca/L), photodegradation (under UV-A) of the CH_3CHO using Ca-TiO_2 exhibited significant improvements.

CHAPTER 5
Preparation and characterization of photoactive anatase TiO_2 from algae bloomed surface water

STATEMENT OF CONTRIBUTION OF AUTHORS

Title of Paper	Preparation and Characterization of Photoactive Anatase TiO_2 from Algae Bloomed Surface Water		
Publication Status	☒Published ☐Accepted for Publication ☐Submitted for Publication		
Publication Details	**Hossain, S. M.**, Park, H., Kang, H.-J., Kim, J. B., Tijing, L., Rhee, I., Jun, Y.-S., Shon, H. K., & Kim, J.-H. (2020). Preparation and Characterization of Photoactive Anatase TiO_2 from Algae Bloomed Surface Water. *Catalysts*, *10*(4). https://doi.org/10.3390/catal10040452		
PRINCIPLE AUTHOR			
Name of Principle Authors	Sayed Mukit Hossain **(Candidate)**		
Contribution	**Conceptualization, Data curation, Formal analysis, Investigation, Methodology, Validation, Writing – original draft.**		
Certification	This paper reports on original research I conducted during my Higher Degree by Research candidature and is not subject to any obligations or contractual agreements with a third party that would constrain its inclusion in this thesis. I am the primary author of this paper.		
Signature	Production Note: Signature removed prior to publication.	Date	30/11/2021
CO-AUTHOR CONTRIBUTIONS			
Name of Co-Author 1	Heeju Park		
Contribution	Formal analysis, investigation, and data curation.		
Name of Co-Author 2	Hui-Ju Kang		
Contribution	Formal analysis, investigation, and data curation.		
Name of Co-Author 3	Jong Beom Kim		
Contribution	Formal analysis, investigation, and data curation.		
Name of Co-Author 4	Leonard Tijing		
Contribution	Writing - review and editing.		
Name of Co-Author 5	Inkyu Rhee		
Contribution	Writing - review and editing, Funding acquisition.		
Name of Co-Author 6	Young-Si Jun		
Contribution	Writing - review and editing, Resources.		
Name of Co-Author 7	Ho Kyong Shon		
Contribution	Supervision, Project administration, Resources, Funding acquisition, Validation, Writing - review and editing.		
Name of Co-Author 8	Jong-Ho Kim		
Contribution	Supervision, Project administration, Resources, Writing - review and editing.		

5 Preparation and characterization of photoactive anatase TiO_2 from algae bloomed surface water

5.1 Abstract

The purpose of the study was to effectively treat algae bloomed water using a Ti-based coagulant ($TiCl_4$) and to recover photoactive novel anatase TiO_2 from the flocculated sludge. Conventional jar tests were conducted to evaluate the coagulation efficiency, and $TiCl_4$ was found superior compared to commercially available poly aluminum chloride (PAC). At a dose of 0.3 g Ti/L, the removal rate of turbidity, COD and TP were measured as 99.8%, 66.7%, and 96.9% respectively. Besides, TiO_2 nanoparticles (NPs) were recovered from the flocculated sludge and presence of only anatase phase was confirmed using SEM, EDX and XRD analysis. The recovered TiO_2 was found effective in removing gaseous CH_3CHO and NO_x under UV-A lamp at a light intensity of 10 W/m^2. Additionally, TiO_2 mixed mortar blocks prepared in this study successfully removed atmospheric NO under UV irradiance. This study is one of the first to prepare anatase TiO_2 from flocculated algal sludge and showed promising results. Further research on this novel TiO_2 concerning internal chemical bonds and shift in the absorbance spectrum could explore several practical implications.

5.2 Introduction

Surface water is one of the primary sources of natural water resources to fulfill a prominent portion of diverse water demands around the world. However, a major concern for surface water is rapid algal bloom resulting from eutrophication, due to seasonal variation in physicochemical properties of surface water along with numerous anthropogenic activities (e.g., uncontrolled dredging, inappropriate effluent discharge, etc.) (Naceradska et al., 2019; Reichwaldt & Ghadouani, 2012). Consequently, algae enriched water could facilitate the generation of various algal organic matter (AOM), which may include both extracellular organic matters (EOM) and intercellular organic matters (IOM) (An et al., 2019). Algae cells together with corresponding EOMs and IOMs can cause the development of disinfection by-products (DBPs), toxins (e.g., hepatoxins and neurotoxins), unpleasant tastes and odors in surface water, resulting significant deterioration of water quality (Chen et al., 2009; Jiang & Kim, 2008). In general, negatively charged algae forms a heterogeneous stable colloidal suspension in eutrophic water (Z. Wang et al., 2018d). Besides, the low structural rigidity and high hydrophilicity of algal cells make them very difficult to remove from water (An et al.,

2019; Henderson et al., 2010). As a result, conventional treatment facilities face plenty of convoluted difficulties, while treating algae-induced water, (e.g., requirement of higher coagulant dose, clogging of filter media, the formation of DBPs from cell lysis, and microbial regrowth in the effluent side of the distribution system) (Ghernaout et al., 2012; X. Lu et al., 2017).

To date, a number of treatment processes have been developed to alleviate or remove algal cells from surface water. Broadly, the prevailing methods can be categorized as, (a) physical processes such as dissolved air floatation (DAF), direct media filtration and membrane filtration (Ma & Liu, 2002); (b) chemical process (both inorganic and organic) such as coagulation/flocculation and pre-oxidation (using chlorine, ozone, permanganate), EOM as flocculation aid (Shen et al., 2011); and lastly (c) electromagnetic irradiation such as UV irradiated disinfection (L. Liu et al., 2016) and ultrasonic irradiation assisted algae removal (C. Liu et al., 2016). However, from the aspect of economic limitations and practical implications, chemical processes have been used conventionally to treat algae enriched water. More precisely, coagulation/flocculation is the mostly used method for the removal of algal cells (Naceradska et al., 2019; Z. Wang et al., 2018d). Nevertheless, the conventional coagulation/flocculation (using Al and Fe based coagulants) produces a voluminous amount of sludge in addition to residual impacts of the trace metals (Al and Fe), needing extensive post-treatment and appropriate disposal schemes (J. Xu et al., 2018). In other words, the corresponding treatment train gets convoluted. Later, to overcome this difficulty, Ti-based coagulants have been used as an alternative to conventional Al and Fe based coagulants, and previous studies reported superior coagulation efficiencies related to physicochemical properties of effluent and floc morphology (Shon et al., 2007b; Y. Zhao et al., 2014).

Chekli, Eripret, et al. (2017) reported comparable coagulation performance of Ti-based coagulants in algal turbid water compared to $FeCl_3$ and argued that at a lower coagulant dose (< 9 mg/L), $TiCl_4$ performed better to remove turbidity. Moreover, related study (Chekli, Corjon, et al., 2017) affirmed superior coagulation efficiency of $TiCl_4$ over $FeCl_3$ in algae augmented synthetic seawater and reported more than 90% removal of EOM, which generated low molecular weight organics (LMWs). Recently, J. Xu et al. (2018) used $TiCl_4$ to conduct flocculation in laboratory simulated algae (10^6 cells/mL) contained reservoir water and demonstrated the microcystins (MCs) removal of 85% at a dose of 60 mg/L. On the other hand, F. Sun et al. (2013) claimed that conventional PAC is ineffective

in removing MCs from wastewater. In addition, most of the Ti-based coagulation studies are performed on algae cultured synthetic wastewater, hence, evaluation of Ti-based coagulation in real algae bloomed surface water would be a significant addition. Besides, the Ti-based flocculated sludge can be recycled to produce highly valuable titania (TiO_2) nanoparticle (NPs) (El Saliby et al., 2010a; Na et al., 2011; Shon et al., 2007b). It has been reported that around 446.5 kg TiO_2 NPs can be generated from a water treatment facility, having a treatment capacity of 25000 m^3/d (Chekli, Corjon, et al., 2017; Shon et al., 2007b). Also, TiO_2 NPs from Ti-based flocculated sludge are found morphologically superior with equivalent photocatalytic activities compared to commercially available P25 (H. Shon et al., 2009c). TiO_2 is a widely applied compound in the photocatalytic and photovoltaic sector, due to its unique optical and electronic properties (Noman et al., 2019a; Wetchakun et al., 2019). Although the use of photocatalyst in the degradation of gaseous pollutants is not yet a well-accepted practice due to low effectiveness and release of toxic intermediates (Gallus et al., 2015; Hay et al., 2015), the photocatalytic application of TiO_2 in the field of air purification has received significant attention. Mostly, photodegradation of atmospheric nitrogen oxide (NO_x) using TiO_2 incorporated substrate showed very encouraging outcomes (Chen et al., 2018; Maggos et al., 2008). Reports indicated that even a very low short-term concentration of NO (0.05 ppm to 0.2 ppm) could cause respiratory problems, such as, asthma and bronchitis (McConnell et al., 2010; Seo & Yun, 2017). Moreover, NO_x could cause the formation of photochemical smog and tropospheric ozone, along with the hazardous phenomena like acid rain (Angelo et al., 2013). Hence, abatement of NO_x using photocatalytic TiO_2 bears immense significance.

TiO_2 is an n-type semiconductor, whose conduction band (CB) and valence band (VB) are at an energy level of -0.03 eV and 2.9 eV respectively, which results in the band energy gap of 3.2 eV (Humayun et al., 2018; Noman et al., 2019a). Hence, during solar irradiation of TiO_2, when the energy of the incident photon (E_p) is equivalent to the band energy gap (E_{gap}), it gets absorbed. This phenomenon leads to the formation of hydroxyl ($OH\cdot$) and superoxide ($\cdot O_2$) radicals by utilizing surrounding O_2 and H_2O respectively (Wetchakun et al., 2019). Finally, the active $OH\cdot$, and $\cdot O_2$ oxidizes the adsorbed NO_x into nitrate (NO_3^-) ions. A schematic of the whole process is illustrated in **Fig. 5-1** (Chen et al., 2018; Karapati et al., 2014). Photodegradation of NO_x has been exclusively studied using TiO_2 blended cementitious materials in both laboratory and pilot scale setup (Boonen & Beeldens, 2012). Moreover, a number of real life applications of TiO_2 blended

substrate for atmospheric NO_x removal showed convincing results (Boonen & Beeldens, 2014; Ohama & Van Gemert, 2011). Photocatalytic (TiO_2 mixed) pavement blocks are found to effectively remove NO_x using UV irradiance above the light intensity of 1 W/m^2, and more than 80% NO_x removal were reported at an initial NO concertation of 0.05 ppm to 1.0 ppm (Ohama & Van Gemert, 2011). One of the recent studies (Kim et al., 2017) evaluated the NO_x removal of sprayed TiO_2 on the retaining wall of an expressway (Gyeongbu, Korea) and reported a maximum average daily removal of 22%.

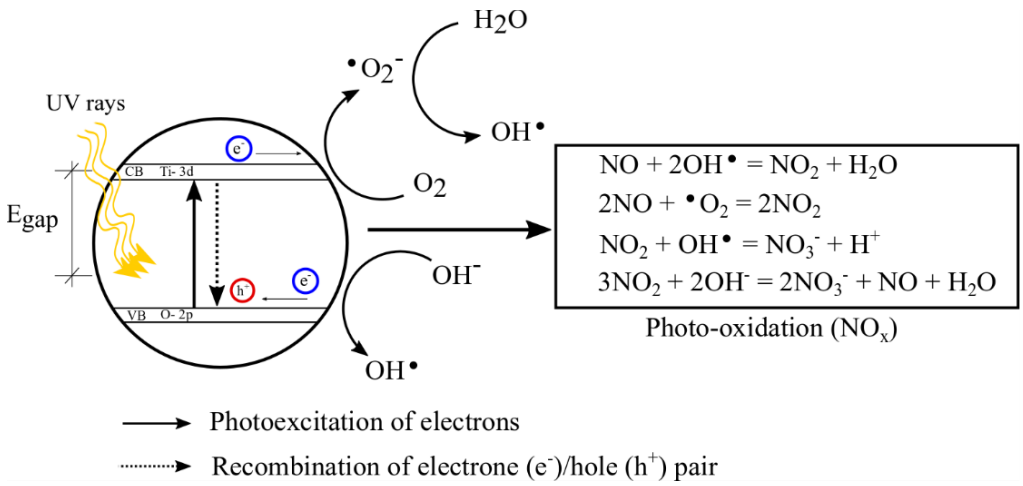

Fig. 5-1. NO_x removal mechanism using TiO_2.

The conventional TiO_2 production processes are not very environmentally friendly, and generates hazardous wastes, requiring advanced management (H. Shon et al., 2009c). Hence, an alternative TiO_2 production scheme, which is economic and environmentally friendly, is always appreciated. The novelty of the present work is the preparation of photocatalytic anatase TiO_2 from flocculated algal sludge to remove gaseous CH_3CHO and NO_x. Consequently, the flocculation efficiency of $TiCl_4$ was compared with commercially available PAC in algae bloomed surface water. Later, TiO_2 NPs were recovered from algae flocculated sludge, and the extent of photodegradation of prepared TiO_2 was compared with P25.

5.3 Coagulation efficiency of $TiCl_4$ comparing PAC

The coagulation efficiency of the $TiCl_4$ was assessed in comparison with commercially available PAC in algae bloomed lake water. The coagulant doses were varied from 0.1 to 0.3 g/L and coagulation efficiency was measured based on turbidity, COD and TP. **Table**

5-1 shows the variations in coagulation efficiency along with the standard errors for the utilised coagulants. Irrespective of the coagulants, coagulation efficiencies increased with continuous increments in coagulant doses. Interestingly, at an equal amount of coagulant doses, $TiCl_4$ was found superior in the removal of turbidity compared to PAC. Using 0.1 g Ti/L, approximately 85% turbidity and 70% of TP were removed. Whereas 0.1 g Al/L removed only 42% and 50% of turbidity and TP, respectively. Both the coagulants were found inefficient in removing COD from algae bloomed water at a dose of 0.1 g/L. In comparison with other studies on the treatment of algae bloomed water (Chekli, Eripret, et al., 2017; Ghernaout et al., 2012) the coagulant doses required in the present work were very high, mostly because of the variation in feed water quality. Additionally, the extent of turbidity, COD and TP were several folds higher compared to all the cited studies. For instance, J. Xu et al. (2018) analysed the coagulation efficiency of $TiCl_4$ and PAC, and reported an optimum dose of 0.05 g Ti/L and 0.03 g Al/L, respectively. They found that at an optimum dose, PAC performed better in removing turbidity compared to $TiCl_4$, which is in contradiction with the current study. This could be due to the lower basicity of the utilised PAC in the current study, leading to the formation of less amount of positively charged $Al(OH)_n^{(3-n)+}$ hydrolyzates (Li et al., 2010; Tang et al., 2015). Besides, the number of valence electrons in Ti is higher than that of Al and upon hydrolysis, vigorously generates highly charged positive hydrolyzates ($Ti(OH)_n^{(4-n)+}$), attributing to elevated charge neutralization capacity (Jeon & Ahn, 2018; J. Xu et al., 2018).

Table 5-1. Turbidity, COD and TP results with different concentrations of $TiCl_4$ (as Ti) and PAC (as Al) in algal turbid water.

Dosage (g/L)	**Ti**			**Al**		
	Turbidity (NTU)	**COD (mg/L)**	**TP (mg/L)**	**Turbidity (NTU)**	**COD (mg/L)**	**TP (mg/L)**
0.0	500 ± 0.018	117 ± 0.503	3.61 ± 0.261	500 ± 0.018	117 ± 0.503	3.61 ± 0.261
0.1	75 ± 0.050	115 ± 0.362	1.08 ± 0.251	290 ± 0.052	113 ± 0.233	1.81 ± 0.050
0.2	1.9 ± 0.178	115 ± 0.308	0.59 ± 0.122	65 ± 0.051	84 ± 0.328	0.32 ± 0.102

Dosage (g/L)	Ti			Al		
	Turbidity (NTU)	COD (mg/L)	TP (mg/L)	Turbidity (NTU)	COD (mg/L)	TP (mg/L)
0.3	1.0 ± 0.156	39 ± 0.135	0.11 ± 0.051	21 ± 0.044	86 ± 0.244	0.16 ± 0.057

Using **Table 5-1**, the successive increase in coagulant dose up to 0.3 g/L as Ti and Al showed a continuous improvement of coagulation efficiency. At a dose of 0.3 g Ti/L, the turbidity, COD and TP removal were 99.8%, 66.7% and 96.9%, respectively. Alternatively, at a similar dose, PAC showed equivalent turbidity (95.8%) and TP (95.5%) removal, but the COD removal was 40.2% lower (see **Table 5-1**). In general, coagulation using PAC is suitable for removing high molecular weight organic matter with hydrophobic nature (Ghernaout et al., 2012). However, PAC was found inefficient in removing uncharged and hydrophilic biopolymers (i.e., polysaccharides) (F. Sun et al., 2013). On the other hand, $TiCl_4$ was found efficient in removing organic matters with a very low molecular weight (< 350 Dalton) and can remove uncharged biopolymers to some extent through sweep flocculation and bridging of formed complexes with AOM (Chekli, Corjon, et al., 2017). Previous report indicated that at 0.06 g Ti/L of coagulant, $TiCl_4$ can remove 85% of algae originated microcystins (J. Xu et al., 2018). From the COD removal values tabulated in **Table 5-1**, it can be expected that the AOM in the collected lake water contained a large portion of LMW organic compounds. Hence, in this study, $TiCl_4$ was found more efficient in abating COD compared to PAC.

Furthermore, high doses of the coagulants may have degraded the algae cell membrane causing the release of IOMs, making it hard to reduce COD (Naceradska et al., 2019). Presumably, $TiCl_4$ coagulation in this study may have caused algal cell damage, thus, COD remained approximately the same, while the coagulant dose was increased from 0.1 g Ti/L to 0.2 g Ti/L. Although, zeta potentials of the flocculated flocs were not measured in this study, previous studies using optimum Ti dose for coagulation of synthetic water containing AOM indicated that zeta potential remained within the range of -5.0 to 0.0 mV (Chekli, Corjon, et al., 2017; Chekli, Eripret, et al., 2017). To be exact, Chekli, Corjon, et al. (2017) calculated the zeta potential at optimum dose of 0.05 g Ti/L and found the optimum zeta potential to be -2.03 mV. The coagulation mechanisms of $TiCl_4$ in algae

bloomed water could be attributed to charge neutralization, sweep flocculation, and bridging of developed Ti hydrolyzates incorporated AOM complexes (J. Xu et al., 2018; W. Zhang et al., 2018). Another prominent advantage of $TiCl_4$ coagulation in this study was larger floc size compared to PAC, which was detectable even with bare eyes. The larger and more compact flocs during the Ti-based flocculation are mainly due to the large atomic radius and a high number of valence electrons (H. Shon et al., 2009c; Shon et al., 2007b; Y. Zhao et al., 2014).

$TiCl_4$ has been found very efficient in removing phosphorous from wastewater. Jeon et al. (2017) reported, both Ti and Al-based coagulants perform similarly when the initial pH of the feed water is 7, which is in agreement with the current study. At an alkalinity level of 100 mg $CaCO_3$/L, they have reported 99% phosphorous removal using a coagulant dose of 0.02 g Ti/L and 0.01 g Al/L, respectively. It was reported that an increase in alkalinity of feed water was responsible for the requirement of elevated coagulant doses (Jeon et al., 2017). Consequently, in the current study, the presence of algae in feed water may have increased the alkalinity causing an augmented demand of coagulants to remove TP.

5.4 Physicochemical properties of the prepared A-TiO_2

The physicochemical properties of the prepared algae bloomed water treated TiO_2 (A-TiO_2) NPs were evaluated via SEM/EDX, XRD, and physisorption of N_2. The prevailing physicochemical properties were also compared with annealed algal sludge (A-Residue) from the collected raw lake water sample. **Fig. 5-2** shows the SEM image of A-Residue and A-TiO_2. The particles present in A-TiO_2 were well dispersed, and the average particle size was between 20 – 30 nm (see **Fig. 5-2(b)**). On the other hand, particles present in A-Residue were partially agglomerated, and the average particle size was approximately 50 nm. The particles of the prepared A-TiO_2 corresponds well with the TiO_2 NPs prepared by Park et al. (2014) and El Saliby et al. (2012) through flocculation of dye wastewater and biologically treated sewage effluent respectively, using Ti-based coagulant.

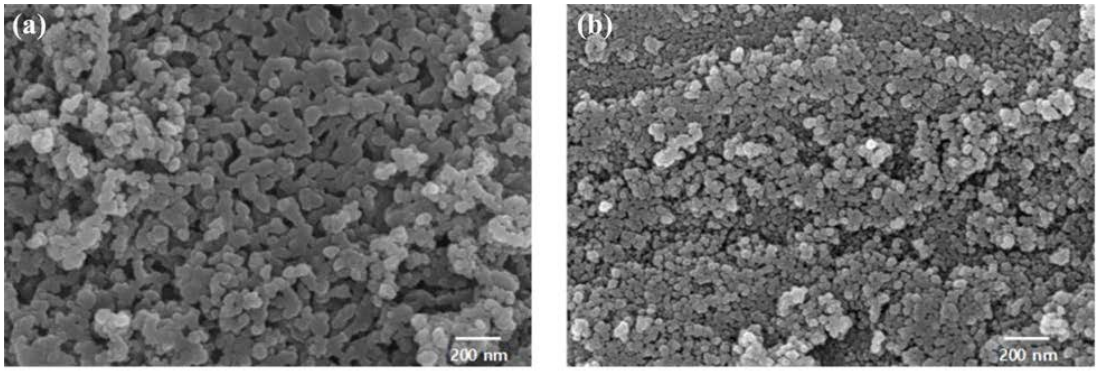

Fig. 5-2. SEM images of (a) A-Residue; (b) A-TiO_2.

In contrast, TiO_2 prepared from secondary sewage effluent, and paper mill wastewater showed a smaller (< 20 nm) particle size (Na et al., 2011; H. Shon et al., 2009c). It has been reported that the particle size of TiO_2 NPs developed through Ti-based flocculation primarily depends on the quality of the feed water that has been used (M. M. Mian & G. Liu, 2019; Shon et al., 2014; Z. Wang et al., 2018d). Moreover, the substitutional and interstitial doping of impurities from the feed water can significantly affect the particle size of the prepared TiO_2 NPs (Cheng et al., 2016; Wetchakun et al., 2019). For instance, the high Ca (large atomic radius comparing Ti) content (see Table 2) in A-TiO_2 crystal may have contributed towards the enhancement of crystal size through substitutional doping (Humayun et al., 2018).

Table 5-2. EDX and BET surface area results of A-Residue and A-TiO_2

Material	**Weight (%)**											**S_{BET} (m^2/g)**	
	O	**Na**	**Mg**	**Al**	**Si**	**P**	**S**	**Cl**	**K**	**Ca**	**Fe**	**Ti**	
A-Residue	45.5	2.0	3.8	4.4	13.7	3.5	3.1	2.4	5.0	11.1	5.5		9
A-TiO_2	49.3	1.9	1.3	-	0.6	-	1.1	2.7	0.6	3.3	-	39.2	40

Table 5-2 demonstrates the elemental composition of prepared A-Residue and A-TiO_2 from EDX analysis along with the estimated BET specific surface area (S_{BET}). Noticeable increase (approximately 4 times) in S_{BET} has been observed in A-TiO_2 compared to A-Residue, which support the obtained results of smaller particle size of A-TiO_2 presented in **Fig. 5-2**. Using **Table 5-2**, various elements were found in the analysed A-Residue with a notable amount of Si (13.7%), Ca (11.1%), Fe (5.5%) and O (45.5%). Possibly,

the prevailing AOMs (EOMs and IOMs) of the feed water were the sources of the elements observed in A-Residue. In general, AOMs contain biopolymers (i.e., polysaccharides and proteins) (38.5%), humic substances (9.9%), building blocks (27.1%) and low molecular weight organics (i.e., alcohols, aldehydes, ketones and monoprotic organic acids) (23.9%) thus possibly contributing to impurities on A-Residue (Chekli, Corjon, et al., 2017). Surprisingly, certain amounts of Cl were found in both A-Residue and A-TiO_2, which could have been attributed from the existing residual chlorine of the lake water. Nevertheless, the fraction of impurities was reduced in prepared A-TiO_2 NPs (see Table 2) as Ti hydrolyzates develop chemical complexes (J. Xu et al., 2018) with existing AOM and at 600°C, anatase TiO_2 is the dominant crystal structure (Na et al., 2011).

Despite the presence of varying impurities, the S_{BET} of the prepared A-TiO_2 was approximately similar to that of commercially available P25 (42.3 m^2/g) (Shon et al., 2007b). However, the S_{BET} of the A-TiO_2 NPs were found lesser compared to the TiO_2 NPs prepared from Ti-based flocculation of drinking water (90.2 m^2/g) (H. Shon et al., 2009c), secondary sewage effluent (103.5 m^2/g) (H. Shon et al., 2009c), seawater (68.1 m^2/g) (Okour, El Saliby, et al., 2009) and dye wastewater (76 m^2/g) (El Saliby et al., 2010a). Substantial doping of the impurities in A-TiO_2 crystal may have been the possible reason of the reduced specific surface area (Noman et al., 2019a), which is evident from the reduced fraction of Ti (39.2%) in relation to O (49.3%) (see **Table 5-2**).

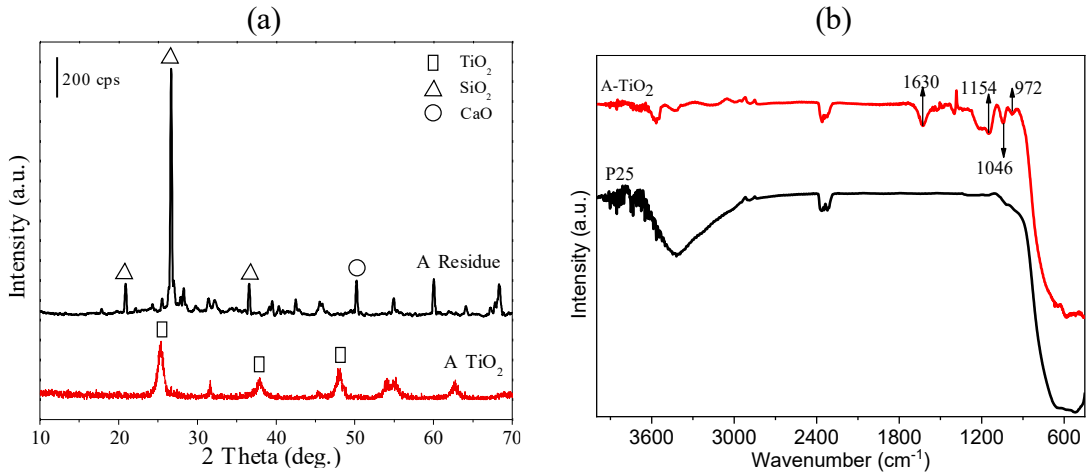

Fig. 5-3. (a) XRD patterns, (b) FT-IR spectra of A-Residue and A-TiO_2 prepared from algal turbid water.

The X-ray diffraction patterns of A-Residue and A-TiO_2 are compared in **Fig. 5-3**, and the result bears convincing resemblance with the elemental composition found in EDX analysis (see **Table 5-2**). In A-Residue, SiO_2 crystal diffraction peaks at 20.9°, 26.7° and 36.6°, and CaO crystal diffraction peak at 50.2° were observed. Alternatively, A-TiO_2 mostly showed anatase TiO_2 crystal peaks at 25.3°, 37.9° and 47.9°, which is in agreement with a reported study that incineration of Ti flocculated sludge at 600 °C generates photocatalytically active anatase TiO_2 (Na et al., 2011). An insignificant diffraction peak for SiO_2 was observed at 26.7°; however, it was presumed to be primarily present in an amorphous state. Furthermore, **Fig. 5-3** depicts, the presence of doped pollutants (substantially/interstitially) in A-TiO_2, which inhibited the crystalline diffraction intensity of anatase TiO_2 (H. Shon et al., 2009c).

The FT-IR spectra of commercially available P25 and A-TiO_2 are illustrated in **Fig. 5-3(b)**. For both A-TiO_2 and P25, a range of absorption broad peak was observed in between 400 cm^{-1} to 900 cm^{-1}, which is characteristics spectra for TiO_2 representing the vibration of Ti-O-Ti (M. M. Mian & G. Liu, 2019). Another broad absorption band around 3435 cm^{-1} in P25 indicated the characteristic vibration mode of Ti-OH (Cheng et al., 2016), could not be observed in A-TiO_2. However, the absorption peak around 1630 cm^{-1} in A-TiO_2 indicated the presence of hydroxyl group (M. M. Mian & G. Liu, 2019). The shift vibration peaks around 1154 cm^{-1}, 1046 cm^{-1} and 972 cm^{-1} in A-TiO_2, represented the presence of C-O-C, C-O and Si-O-Si in lower intensity, which exhibited the presence of C and Si on prepared A-TiO_2 (Chi et al., 2019; M. M. Mian & G. Liu, 2019). Several previous studies concerning sludge generated TiO_2 showed the traces of C, which was found beneficial during photocatalysis due to tailored energy bandgap from doping effect.

A thorough quantitative study on the XPS spectra of A-TiO_2 and P25 was conducted to compare the surface chemical compositions. **Fig. 5-4(a)** illustrates the survey spectra of the as-prepared photocatalysts. The survey spectra delineate the presence of Ti 2p and O 1s region, confirming the formation of TiO_2 from the prescribed methodology in this manuscript (M. M. Mian & G. Liu, 2019). Using high-resolution XPS, the Ti 2p and O 1s region were further assessed, and the dominant peaks were deconvoluted using Lorentz line fit and presented in **Fig. 5-4(b)** and **5-4(c)** respectively. The Ti 2p spectra of A-TiO_2 showed two characteristic peaks around 459.39 eV and 465.07 eV. Whereas, P25 depicted the Ti 2p characteristic peaks around the binding energies of 458.41 eV and 464.31 eV, which can be attributed to Ti $2p_{3/2}$ and Ti $2p_{1/2}$, respectively, of Ti^{4+} (Pérez-Nicolás et al.,

2017). A major shift (465.07 eV) in the Ti $2p_{3/2}$ peak of A-TiO_2 was observed compared to the P25, which can indicate the generation of Ti^{3+} as local trap state (Lisowski et al., 2017). Such local trap states can restrict the recombination rate of photogenerated e^-/h^+ pairs along with the narrowing of energy bandgaps (Wetchakun et al., 2019).

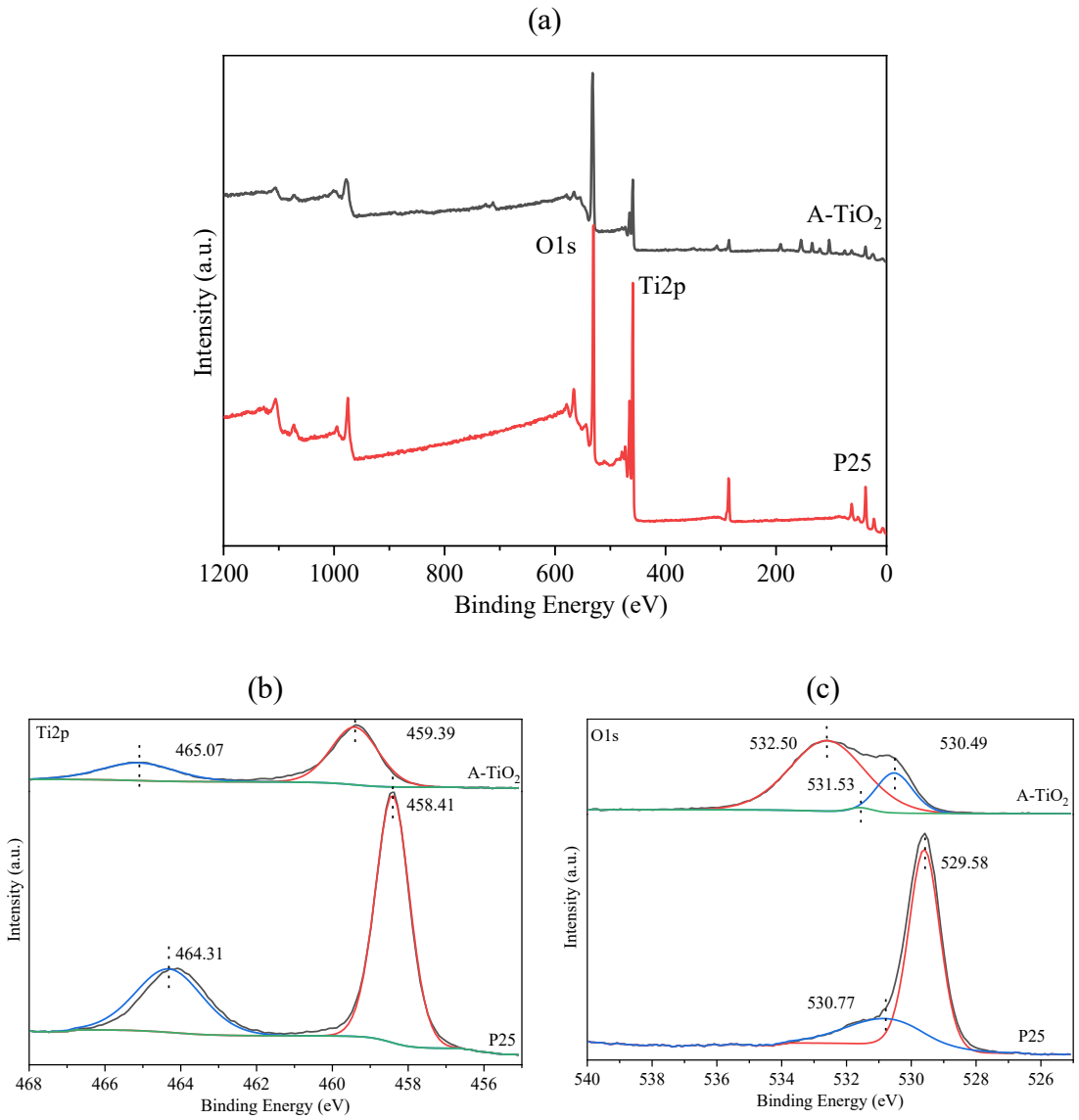

Fig. 5-4. (a) XPS survey spectra, (b) Ti 2p spectra, and (c) O 1s spectra of A-TiO_2 and P25.

Although this study did not report any visible light photocatalysis experimental results, narrowed energy bandgap of the as-prepared A-TiO_2 could mean visible light activation. Moreover, the EDX results presented in **Table 5-2** showed the presence of Ca in the chemical composition of A-TiO_2, and the shift of Ti 2p towards higher binding energy could be due to the presence of dopant in A-TiO_2. Similar changes in chemical compositions were observed in some of the relevant studies. For instance, Shon et al. (2007b) performed XPS analyses on sludge generated TiO_2 from the coagulation of synthetic wastewater to determine the composition of the TiO_2, and to classify the valence states of different atoms present. Using multi-scan recording mode, they have recorded the sample spectrum for Ti, O, C, and P, which revealed that the atomic percentages were

26.9%, 51.5%, 15.8%, and 5.8%, respectively. In addition, they have the Ti 2p line's binding energy at about 458.96 eV, confirming Ti was mainly present as Ti^{4+}. This phenomenon suggests that a higher degree of oxidation occurred during the calcination of Ti incorporated sludge. Whereas, following a similar scheme used in this manuscript and Shon et al. (2007b), M. M. Mian and G. Liu (2019) prepared TiO_2 by sewage sludge coagulation and stated that the Ti 2p line was moved to higher binding energy as 459.1 eV. Accordingly, they concluded that sludge produced TiO_2 could facilitate the development of local trap state Ti^{3+} and increase the photocatalytic efficiency. The O 1s spectra of A-TiO_2 illustrated in **Fig. 5-4(c)** showed characteristic peaks of anatase TiO_2 around 530.49 eV and 531.53 eV, which can be dedicated to Ti-O and Ti-OH bond, respectively (Lisowski et al., 2017). Presumably, due to the presence of trace amounts of dopants, the O 1s peaks shifted towards higher binding energies compared to P25. Additionally, the peak around 532.50 eV is a characteristic peak of the C=O bond, which may have resulted from the impurities present in the as-prepared A-TiO_2 (Lisowski et al., 2017).

5.5 Photocatalytic activity of prepared A-TiO_2 NPs

The photocatalytic activities of developed A-TiO_2 NPs were assessed under UV irradiation through photodegradation of gaseous acetaldehyde (**Fig. 5-5**) and NO_x (**Fig. 5-6**). Additionally, the degree of photoactivity was compared with commercially available P25. In case of acetaldehyde decomposition under UV irradiation, to exclude the losses to photodecomposition along with other heterogenous losses, i.e., uptake and hydrolysis, initially blank experiments were performed with 2000 ppmv of acetaldehyde gas mixture in the reactor under UV-A irradiation without any presence of photocatalysts. During UV irradiation for over 200 min, no such observable losses or systemic patterns were observed. Acetaldehyde was adsorbed on A-TiO_2 and P25 for 80 min in dark condition (no UV irradiation), and at the initiation of UV-A lamp the concentration of acetaldehyde was found as approximately 1820 ppmv for both A-TiO_2 and P25 (see **Fig. 5-5**). Using **Fig. 5-5**, under UV irradiation at the end of 200 min A-TiO_2 and P25 removed almost 85.7% and 96.7% of the imparted acetaldehyde gas, respectively. Past studies have shown that the TiO_2 photocatalytic degradation rate adopted the traditional pseudo-first-order kinetics pattern of Langmuir-Hinshelwood (Karafas et al., 2019). The kinetic equation can be expressed as $\ln C/C_0 = -kt$. Where, k is the pseudo-first-order reaction rate constant (min^{-1}), C is the concentration at reaction time t, and C_0 is the initial

concertation. In **Fig. 5-5(b)**, the value k was calculated from the slope, where ln C/C_0 versus t was plotted. Thus, the reaction rate constant of A-TiO_2 and P25 were found as 0.0169 min^{-1} and 0.0311 min^{-1}, respectively.

Similarly, following ISO 22197-1 the NO_x removal efficiency of A-TiO_2 was compared with P25 (**Fig. 5-6**). At the beginning of UV irradiation, both A-TiO_2 and P25 exhibited a rapid reduction of NO, probably due to the combined effect of adsorption and photodegradation (Park et al., 2014). Moreover, the maximum removal of NO, achieved under UV irradiation was 57.10% and 78.22% for A-TiO_2 and P25, respectively. Apparently, the HNO_3 developed during photooxidation of NO may have adsorbed on the surface of TiO_2 and diminished the level of photodegradation (Seo & Yun, 2017). Hence, both A-TiO_2 and P25 indicated consecutive increase in concentration of NO. After 60 min of UV irradiation, the NO removal efficiency of A-TiO_2 and P25 were determined as 16% and 50%, respectively. As illustrated in **Table 5-3**, in the continuous flow reactor, the average initial concentration of NO was found as 6.95 µmol and 7.01 µmol for A-TiO_2 and P25, respectively. Under UV irradiation for 60 min, the prepared A-TiO_2 removed 1.95 µmol of NO on average, which is approximately 27.99% of the initial concentration. Whereas, used P25 showed an average removal of 54.17% for the same duration of UV exposure. Meanwhile, under UV light, the average NO_2 concentration was increased by 16.50% and 19.79% for A-TiO_2 and P25, respectively, which shows higher selectivity of A-TiO_2 towards NO_2 production.

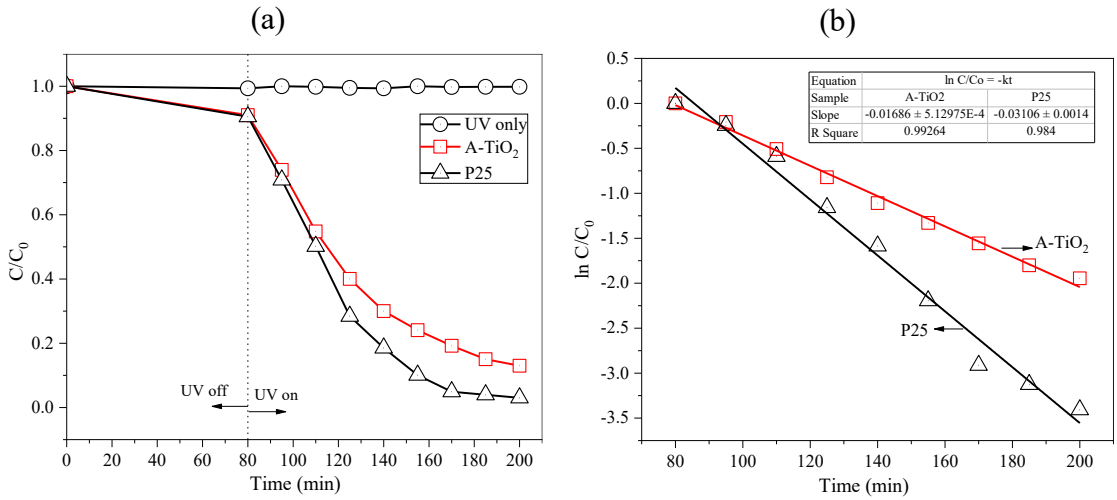

Fig. 5-5. Removal of acetaldehyde under UV irradiation over A-TiO_2 and P25 NPs.

Table 5-3. Average NO removal and NO_2 generation rates for the prepared samples

Sample	**$NO_{(initial)}$**	**$NO_{(removal)}$**	**$\%NO_{(removal)}$**	**$NO_{2(initial)}$**	**$NO_{2(production)}$**	**$\%NO_{2(production)}$**
	µmol	**µmol**		**µmol**	**µmol**	
NPs						
A-TiO_2	6.95	1.95	27.99%	0.45	1.15	16.50%
P25	7.01	3.80	54.17%	0.65	1.39	19.79%
Mortar blocks						
A-TiO_2 (5%)	7.46	0.24	3.24%	0.03	0.08	1.08%
A-TiO_2 (10%)	7.49	0.46	6.14%	0.01	0.13	1.78%
P25 (5%)	7.45	0.45	6.02%	0.02	0.14	1.88%

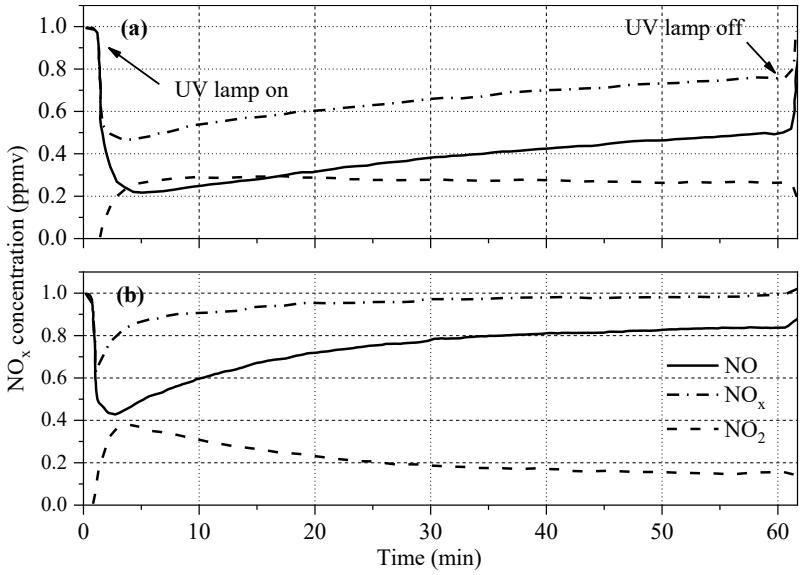

Fig. 5-6. Removal of NO_x under UV irradiation over (a) P25 and (b) A-TiO_2 NPs.

From **Figs. 5-5** and **5-6**, it is clear that the prepared A-TiO_2 was found inferior to photodegrade acetaldehyde and NO_x compared with P25. The aforementioned is in contrary with most of the previous studies where TiO_2 NPs produced from Ti-based flocculation were found either superior or almost similar to P25 with regards to photodegradation of volatile organic compounds (El Saliby et al., 2012; Park et al., 2014;

Z. Wang et al., 2018d). The following postulates may explain the reduced photocatalytic activities of the prepared A-TiO_2:

Firstly, the apparent density of A-TiO_2 was estimated as 1.2 g/mL which is approximately 6 times larger than that of P25 (0.19 g/mL), causing a small number of adsorption sites for A-TiO_2. However, considering the substantial difference in available adsorption sites the reduction in maximum removal of acetaldehyde and NO_x was only 11% and 20% respectively, comparing A-TiO_2 to P25 NPs.

Secondly, it is evident that doped metals and nonmetal significantly affect the photo activity of a photocatalyst (Noman et al., 2019a). The EDX analysis of the current study showed notable amounts of Ca (3.3%) and Cl (2.7%) in A-TiO_2. Castro and Durán (2016) reported that Ca doping on TiO_2 at a very low concentration (< 3 wt.%) could reduce the band energy gap of TiO_2 and enhance photodegradation of methyl orange under solar irradiation. However, doped Ca of substantial amount can act as recombination site for e^-/h^+ pair generated during photodegradation (see **Fig. 5-1**) and may cause a reduced level of photoactivity (Humayun et al., 2018). Similarly, Wang et al. (2012) illustrated that a certain amount (2 at.% – 4 at.%) of Cl as the dopant in TiO_2 could activate TiO_2 under visible light, and the extent of light absorption within UV range can get reduced, so as the photoactivity. Hence, in the current study, the dual effect of the doped Ca and Cl may have reduced the photocatalytic activity of A-TiO_2.

Fig. 5-7 depicts the NO_x removal performance of photocatalytic mortars prepared by adding 5 wt.% and 10 wt.% of A-TiO_2. The results were compared with mortar prepared using 5 wt.% of P25. Under UV irradiation, regardless of the mortar used, NO concentration in the reactor gradually reduced and stabilized approximately after 5 min. The UV-A lamp remained turned on for 60 min, and the stabilized NO concentration was found constant throughout this time irrespective of the employed photocatalytic mortar. In the photocatalytic mortar containing 5 wt.% and 10 wt.% of A-TiO_2, NO concentration was stabilized at 0.96 ppmv and 0.93 ppmv, respectively.

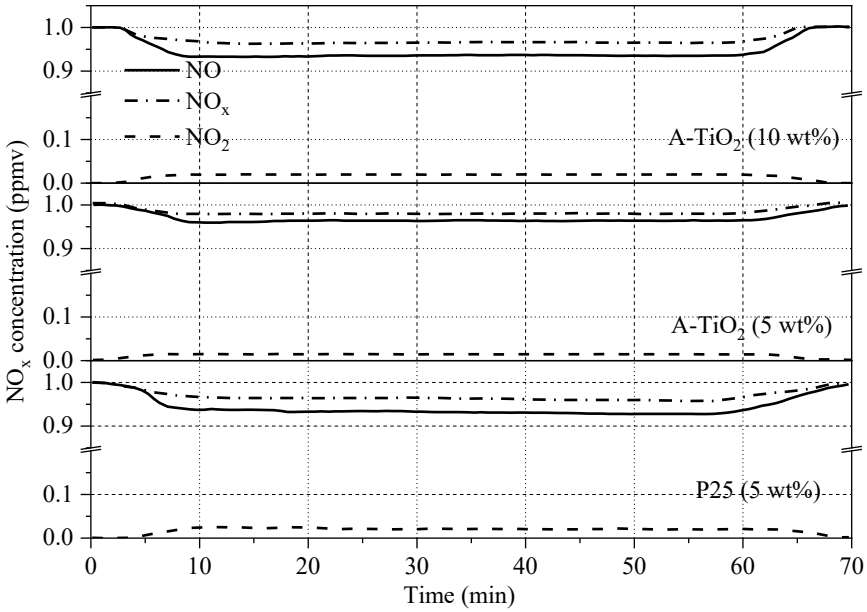

Fig. 5-7. NO_x removal performance of the manufactured photocatalytic mortars under UV-A lamp.

Meanwhile, the maximum removal of NO using P25 (5 wt.%) mixed mortar was 0.93 ppmv. NO_2 production rate was found to be proportional to NO removal rate in both A-TiO_2 and P25 mixed mortar as exhibited in **Fig. 5-7**. As shown in **Table 5-3**, the average NO_2 concentration in the reactor increased from 0.03 µmol to 0.08 µmol, 0.01 µmol to 0.13 µmol, and 0.02 µmol to 0.14 µmol for mortar blocks containing A-TiO_2 (5%), A-TiO_2 (10%), and P25 (5%) respectively, under UV irradiation of 70 min.

At equal wt.%, A-TiO_2 showed 50% less NO removal efficiency compared to P25. Results in **Fig. 5-5** and **5-6** indicated a significant difference in NO_x removal behavior for photocatalytic (A-TiO_2 or P25) NPs and photocatalyst (A-TiO_2 or P25) mixed mortar. The corresponding NPs under continuous UV light showed a decreasing trend (see **Fig. 5-6**) during NO removal, which was not the scenario in the case of prepared mortar blocks. Possibly, the synergistic effects of the cementitious materials on TiO_2 NPs were the prevailing reasons (Ohama & Van Gemert, 2011). It has been reported that the final product of NO removal using TiO_2 is NO_3^- (see **Fig. 5-1**), which can react with Ca in surrounding hydrated cement and produces $Ca(NO_3)_2$ rather than inhibiting the photocatalytic activity of TiO_2 through adsorption on photoactive sites (Chen et al., 2018; Seo & Yun, 2017) or regeneration of NO under UV (El Zein et al., 2013). Hence, the photodegradation of NO remained almost constant under the UV lamp.

As mentioned before, the apparent density of A-TiO_2 was significantly higher than that of P25, which leads to its poorer NO abatement rate than P25. Despite the notable difference (almost 6 times) in density, the extent of photoactivity only reduced by 50%. It is presumed that complex interactions between cement and A-TiO_2 NPs, along with physical properties of mortar contributed towards improved removal of NO (Kim et al., 2017; Pérez-Nicolás et al., 2017). Park et al. (2014) prepared TiO_2 from flocculation of dye wastewater and their TiO_2 performed at par with commercial P25 for the removal of atmospheric NO_x, since the apparent density of their TiO_2 was not very high compared with P25. Therefore, improvement in physical properties of A-TiO_2 developed in the current study could further enhance the extent of photoactivity. Moreover, from **Fig. 5-7**, it is evident that A-TiO_2 at 10 wt.% in mortar performed similarly as with P25 (5 wt.%). The A-TiO_2 used in this study was prepared from recycling sludge, so it is considerably cheaper compared to P25. Therefore, the problem concerning high apparent density can be counterbalanced by increasing the amount of A-TiO_2 used.

5.6 Conclusions

In the present study, $TiCl_4$ was used to conduct flocculation in algae bloomed lake water, and the accompanying jar tests showed superior turbidity, COD and TP removal compared with PAC. TiO_2 NPs were prepared by annealing $TiCl_4$ flocculated sludge. XRD and EDX analyses confirmed the generation of anatase TiO_2 with some level of impurities on the annealed TiO_2 NPs. In addition, photocatalytic mortar blocks were prepared by mixing TiO_2 generated from flocculated sludge. Followings are some of the important finding of the study:

- When the coagulant dose varied from 0.1 to 0.3 g/L in algae enriched wastewater, $TiCl_4$ was found superior in removing turbidity, COD and TP compared with commercially available PAC. More importantly, $TiCl_4$ removed almost 97% of the effluent TP at a coagulant dose of 0.3 g/L.

- The prepared A-TiO_2 NPs effectively removed 85.7% of gaseous acetaldehyde under UV-A exposure for 120 min, and by considering the pseudo-1st order kinetic reaction, the reaction rate constant was found as 0.0169 min^{-1}, which is approximately 54.34% of commercially available P25. Additionally, in a continuous flow reaction, under UV-A irradiation for 60 min, the as-prepared A-TiO_2 NPs was found to remove approximately 28% of NO on average. The A-

TiO_2 mixed mortar blocks prepared in this study showed 50% less NO_x removal efficiency compared to P25 mixed mortar blocks under UV irradiance.

Although the prepared A-TiO_2 showed reduced photoactivity compared with P25, it was recovered from algal flocculated sludge which otherwise would have required expensive disposal mechanisms for sustainable management. Hence, considering economic factors, the novel TiO_2 from flocculated algal sludge can contribute towards the increasing demand of P25 in the field of air treatment.

CHAPTER 6
Visible light activation of photocatalysts formed from the heterojunction of sludge-generated TiO_2 and g-CN towards NO removal

STATEMENT OF CONTRIBUTION OF AUTHORS

Title of Paper	Visible light activation of photocatalysts formed from the heterojunction of sludge-generated TiO_2 and g-CN towards NO removal		
Publication Status	☒Published ☐Accepted for Publication ☐Submitted for Publication		
Publication Details	**Hossain, S. M.**, Tijing, L., Suzuki, N., Fujishima, A., Kim, J.-H., & Shon, H. K. (2022). Visible light activation of photocatalysts formed from the heterojunction of sludge-generated TiO_2 and g-CN towards NO removal. *Journal of Hazardous Materials*, *422*. https://doi.org/10.1016/j.jhazmat.2021.126919		
PRINCIPLE AUTHOR			
Name of Principle Authors	Sayed Mukit Hossain **(Candidate)**		
Contribution	**Conceptualization, Data curation, Formal analysis, Investigation, Methodology, Validation, Writing – original draft.**		
Certification	This paper reports on original research I conducted during my Higher Degree by Research candidature and is not subject to any obligations or contractual agreements with a third party that would constrain its inclusion in this thesis. I am the primary author of this paper.		
Signature	Production Note: Signature removed prior to publication.	Date	30/11/2021
CO-AUTHOR CONTRIBUTIONS			
Name of Co-Author 1	Leonard Tijing		
Contribution	Validation, Writing – review & editing.		
Name of Co-Author 2	Norihiro Suzuki		
Contribution	Validation, Writing – review & editing.		
Name of Co-Author 3	Akira Fujishima		
Contribution	Validation, Writing – review & editing.		
Name of Co-Author 4	Jong-Ho Kim		
Contribution	Validation, Writing – review & editing.		
Name of Co-Author 5	Ho Kyong Shon		
Contribution	Supervision, Project administration, Resources, Funding acquisition, Validation, Writing - review and editing.		

6 Visible light activation of photocatalysts formed from the heterojunction of sludge-generated TiO_2 and g-CN towards NO removal

6.1 Abstracts

The feasibility of preparing TiO_2/g-CN heterojunction from Ti-incorporated dried dye wastewater sludge is explored in this study. Two reaction routes of composite formation were evaluated. In the initial approach, one-step calcination of dried sludge and melamine mixture @600 °C was carried out. Detailed morphological and chemical characterizations showed that the one-step calcination route did not create TiO_2/g-CN composites; instead, only N-doped anatase TiO_2 composites were formed. Moreover, due to the non-uniform composition of organic content in the dried sludge, it was not easy to control the N doping level by varying melamine content (0 – 100%) in the precursor mix. However, successful formation of anatase TiO_2 and g-CN was observed when a two-step calcination route was followed, i.e., via synthesis of anatase TiO_2 from dried sludge, and later development of heterojunction by calcining (@550 °C) the TiO_2 and melamine mixture. X-ray diffraction along with infrared and X-ray photoelectron spectroscopy verified the effective heterojunction. In addition, maximum atmospheric NO removal under UV and visible light were observed for the prepared composite when the melamine content in the precursor mixture was 70%. After 1 hour of UV and visible light irradiation, the best TiO_2/g-CN composite removed 25.71% and 13.50% of NO, respectively. Optical characterization suggested that the enhanced NO oxidation under UV/visible light was due to the bandgap narrowing and diminished photogenerated electron-hole recombination.

6.2 Introduction

Environmental problems and the impending energy crises are becoming more troublesome as global industrial operations grow in size and complexity. More environmentally acceptable methods are urgently needed. Photocatalytic technology, which uses the sun as a power source, has emerged as one of the most promising breakthroughs in this area. TiO_2 is especially beneficial among the many photocatalytic compounds available since it is inexpensive, chemically stable, and non-toxic (Asahi et al., 2014). Furthermore, the hierarchical nanostructures of TiO_2 nanoparticles have been studied in-depth, and research has concluded that they represent efficient photocatalysts that offer a large surface area and the porous structure required to facilitate enhanced harvesting of light (Nasirian et al., 2017). Significant attempts have been made to improve

TiO_2's photocatalytic performance, and a number of strategies have been suggested, including morphology modulation, doping elements, and coupling with alternate semiconductors (Z. Zhang et al., 2019). Research has shown, in particular, that heterojunction forming through a hybrid of narrow optical bandgap semiconductors and TiO_2 is a viable means of improving photocatalytic efficiency (S. Zhang et al., 2019).

In order to resolve the problem of light response, graphic nitride nanosheets (g-CN) were used to manufacture TiO_2 composites to generate efficient visible photocatalysts on the premise that g-CN is a feasible contending agent for superior TiO_2 composites (Giannakopoulou et al., 2017; H. Liu et al., 2019; Papailias et al., 2017). g-CN represents an abundantly available novel polymeric semiconductor free of metal and behaves in a stable way (Jinzhu Ma et al., 2016). It also has a narrow bandgap (in the region of 2.7 eV) and is characterized by a unique energy band structure (Huang et al., 2015). To potentially increase light utilization and enhance the movement of photogenerated carriers, it can be coupled with TiO_2. For instance, to prepare TiO_2/g-C_3N_4 composites, Tan et al. (2018) used a simple melamine-involved vapor deposition process. It was observed that the resulting substance demonstrated positive evolution of hydrogen under visible light. To synthesize core-shell TiO_2@g-C_3N_4 composites that showed reliable stability and enhanced properties, Ma et al. (2018) used a dual-step self-assembly approach. In addition, Wang et al. (2017) accelerated the tetracycline photocatalytic degradation by using a technique involving quantum thick graphitic g-CN polymerization on the surface of anatase nanosheets with the underlying purpose of creating a quantum heterojunction core-shell TiO_2@g-C_3N_4. To prepare g-C_3N_4@TiO_2 core-shell standardized photocatalysts with 0 – 3 nm ultrathin g-CN layer on TiO_2 nanorods, Y. Wang et al. (2018) used a sol-gel process. The association between the thickness of the g-CN nanosheets that shaped the surface of the core-shell, and the photocatalytic activity was also studied. Besides, the porosity and surface area of g-CN nanosheets also significantly influence the level of light absorbed and the efficiency with which the charge carriers are transported, which directly influences the photocatalytic function (Dong et al., 2011). Previous studies have concluded that the development of mesoporous structure g-CN nanosheets represents one of the most effective methods of enhancing photocatalytic performance (Dong et al., 2011; Y. Huang et al., 2019; Huang et al., 2015). Compared to bulk g-CN, mesoporous g-CN nanosheets have been found to offer a range of enhanced characteristics, such as a significantly larger surface area, a higher level of porosity,

increased charge separation, a higher degree of flexibility, and more efficient photogenerated electrons (Xia et al., 2019).

Conventionally, TiO_2 is produced using chemical-intensive methods, such as chloride, sulfate, and alkoxide (Shon et al., 2007a). The issue is that the procedures for producing TiO_2 generate a lot of wastewaters, which includes a lot of strong acid and chloride/sulfate ions in high concentrations. As a result, a sustainable TiO_2 production method would be much appreciated. Hence, Shon et al. (2007a) have proposed a novel technique, which can replace the conventional sludge recycling techniques like membrane bioreactor with inherent problems like membrane fouling (Sepehri & Sarrafzadeh, 2018). They have proposed a facile Ti salt-based coagulation-flocculation method for subsequent anatase TiO_2 recovery. Consequently, one prevalent and cost-effective method of treating wastewater is coagulation. In recent times, titanium (Ti) coagulants have emerged as an alternative to Fe and Al salts (M. M. Mian & G. J. Liu, 2019; Z. Wang et al., 2018c; Y. X. Zhao, B. Y. Gao, G. Z. Zhang, Q. B. Qi, et al., 2014). One of the most substantial benefits of Ti coagulants is that they have low toxicity (Lee et al., 2008). Furthermore, it is possible to convert Ti coagulation sludge into products that add value, such as TiO_2 photocatalysts (Park et al., 2014; Shon et al., 2014; Zhao et al., 2013). As such, it is widely expected that Ti coagulants can help overcome the issues associated with the use of conventional Al/Fe salt coagulants. Back in 1916, a soluble Ti complex was employed as an $Al_2(SO_4)_3$ additive and was found to enhance the effectiveness of color removal and significantly reduce the amount of time taken for precipitation (Block, 1916). Later, as a coagulant for water treatment systems, $Ti(SO_4)_2$ was used in 1937 (Upton & Buswell, 1937). Over the last twenty years, due to the developments observed in the Ti industry, a range of Ti coagulants, ranging from polymerized salts (!!! INVALID CITATION !!!) to simple salts (J. Xu et al., 2018) have been researched. Depending on the floc properties, hydrolysis characteristics, and coagulation mechanisms, Ti offers several advantages. During coagulation, Ti flocs rapidly grow to a large size and have a brief sedimentation time; hence, they can be used in smaller tanks (H. K. Shon et al., 2009a; Shon et al., 2007a). The enhanced Ti sedimentation performance can also reduce the expense and complexity associated with sludge dewatering by decreasing the amount of Ti sludge. Additionally, the concentration of residual metals in Ti effluent is significantly lower than that associated with Al/Fe effluents; as such, Ti coagulation represents an appropriate pre-treatment for a variety of advanced wastewater treatments without the threat of the

coagulant residues causing secondary pollution (Lee et al., 2008). Most importantly, it is possible to calcine sludge that contains Ti into the form of functional TiO_2 (H. Shon et al., 2009a). In addition to lowering the sludge treatment costs, this offers a myriad of benefits.

As a result, the goal of this research was to address two significant environmental issues: titania recovery from undesired wastewater sludge and titania activation under visible light for NO photooxidation. Although mesoporous g-CN has been successfully used in conjunction with commercially available titania for visible light activation, research has yet to investigate the use of sludge-generated titania as a starting point for the composite. This research aimed to fill this knowledge gap by synthesizing a novel TiO_2/g-CN composite using Ti-incorporated dry sludge as the basis for TiO_2 development. A template-free method was employed by which a precursor combination of Ti-incorporated sludge/S-TiO_2 and melamine was used to achieve heterojunction. The advanced morphological, chemical, and optical classifications of the as-synthesized composites were conducted. The photocatalytic studies were performed following ISO 17198-1 (2018) (ISO, 2018) and ISO 22197-1 (2007) (ISO, 2016) standards to evaluate the NO_x photooxidation capacity of the prepared composites under visible and UV light irradiance, respectively.

6.3 Thermal analysis

TGA and DSC analysis were conducted to evaluate the phase transition of 1:1 ratio precursor (dried sludge, melamine) and various blends, i.e., sludge:melamine, SM0:melamine, NP400:melamine, and P25:melamine, within the temperature range of 25 °C to 600 °C. An alumina crucible with a lid reproduced the true sample calcination thermal condition during the thermal examination. **Fig. 6-1** summarizes the above TGA and DSC results, showing the formation heat and the final residue. When calcinating only the dry sludge, the color of the incinerated sludge shifted from black to white as the temperature rose. The sample 's black color could be attributed to the remaining organic matter at lower temperatures. Thermal treatment of dry sludge up to 100 °C mainly reduced the quantity of water, while the organic matter was eliminated between 100 °C and 600 °C. 34.83% of the final residue was estimated, which is compatible with the relevant studies (H. Shon et al., 2009a; Shon et al., 2008b; Shon et al., 2007a).

Moreover, by integrating the area beneath the endothermic peak at ~350 °C, the heat of formation (ΔH_f) for SM0 was estimated at 155.55 $J.g^{-1}$. However, the yield was reduced to 15.04% when dried sludge and melamine mix (equal proportion) was calcined up to 600 °C. Presumably, such minimal yield could create difficulty towards successful TiO_2/g-CN composite preparation through a one-step calcination route. However, the composite formation can be confirmed from the increased ΔH_f value from 155.55 $J.g^{-1}$ to 289.98 $J.g^{-1}$. On the other hand, the calcination of SM0 and melamine mix provided a residue of 32.45% and further reduced the ΔH_f value to 264.56 $J.g^{-1}$. A substantial decrease in the organic content of the SM0 compared to the dried sludge could be the possible reason behind the reduced ΔH_f value. To compare the phase transformation results and the possible formation of TiO_2/g-CN heterojunction, commercially available NP400 and P25 were used in the precursor mix instead of dried sludge/SM0 during TGA and SC analysis. The estimated ΔH_f value for NP400 and P25 was 259.25 $J.g^{-1}$ and 237.74 $J.g^{-1}$, respectively, which infers the possibility of TiO_2/g-CN composite formation from one-step and two-step calcination routes. The endothermic plateau at 300 °C – 350 °C could suggest the thermal condensation of melamine into g-CN in all four instances (Hossain et al., 2021). Furthermore, inside the above temperature range, the rapid initial decrease of the sample weight may be due to the condensation of melamine into melem (Dong et al., 2014). Subsequently, the condensation of melem to g-CN may be due to the incremental decrease in weight at the peak temperature (Thomas et al., 2008).

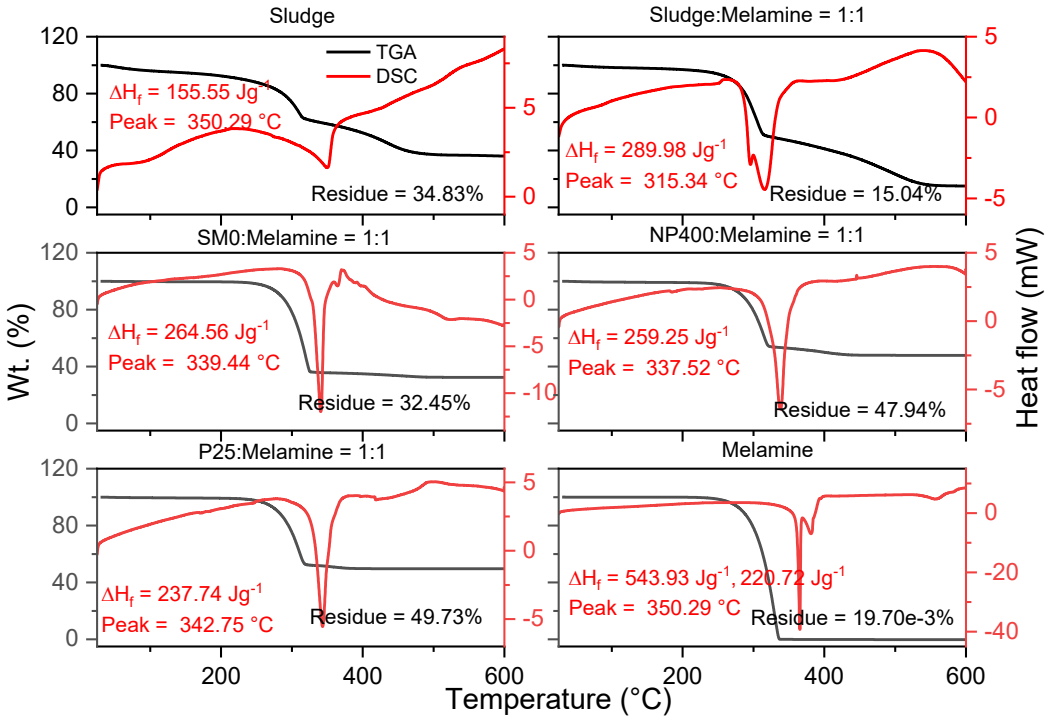

Fig. 6-1. TGA-DSC results for sludge only, sludge:melamine, SM0:melamine, NP400:melamine, P25:melamine, and melamine only, within the temperature range of 25 °C to 600 °C. All blend samples are in 1:1 ratio.

6.4 Composites from sludge (one-step calcination)

6.4.1 Structural attributes

All the prepared composites listed in **Table 3-2** underwent a thorough investigation, employing XRD, of their phase structure. The XRD patterns for the composites that underwent preparation using the one-step calcination of melamine mixes and Ti-incorporated dried sludge in various ratios are illustrated in **Fig. 6-2(a)** and **(b)**. In **Fig. 6-2(a)** the TiO_2 anatase crystal planes for (101), (103), (004), (112), (200), (105), (211), (204), (116), (220), (215), and (224) are represented in the dominant diffraction peaks (JCPDS No 21-1272) (Huan Liu et al., 2019). Increasing the levels of melamine within the precursor mix did not lead to significant changes in peak intensity (Zhou et al., 2015). We must note that diffraction peak positions for SM0, in which just the sludge was calcined, stayed in place in samples SM30 to SM90 even when melamine was added to the precursor mix (30% – 90%). Thus, we can say that incorporating melamine into the precursor mix does not significantly affect the crystal phase for the generated anatase TiO_2. We did see negative shifts in the value for the dominant anatase (101) plane with the as-prepared samples SM30 – SM90; this may be attributed to heterojunction of TiO_2

and g-CN or foreign elements (N) appearing within the crystal lattice (Fig. 3 (b)) (Zhang et al., 2014). Nevertheless, we did not observe any characteristic peaks for g-CN for samples that underwent preparation through the calcination of a melamine/dried sludge mixture. However, with SM100 which had a precursor mix of 100% melamine, a pair of characteristic g-CN peaks at ~13.0 (100) and ~17.5 (002) was observed. The crystal plane reflects the in-plane duplication by trigonal N-bridging of the tris-triazine units (100) and the inter-plane stacking of the aromatic conjugate structure (002) (Song et al., 2016; Wang et al., 2015).

We have determined the effective surface area (S_{BET}) and pore size (d_p) distribution for the as-prepared composites and NP400 by employing N_2 physisorption isotherms. **Fig. 6-2(c)** shows graphs for the adsorbed N_2 volume (@STP) plotted against relative pressure (P/P_0). As well as NP400, every prepared sample manifested type IV isotherm, in accordance with IUPAC categorization, confirming that the samples contained mesopores (Troppová et al., 2018). In addition, the as-prepared composites exhibited a type H2 hysteresis loop, which may be a result of cavitation-oriented evaporation within a limited range of pore necks (Thommes et al., 2015). **Fig. 6-2(d)** shows PSD of the synthesized samples, calculated employing the adsorption data with the BJH method. The estimation of the S_{BET} for SM0 was 85.82 m^2/g, higher than that found in commercially manufactured NP400 (66.65 m^2/g). It was important to notice that as the content of melamine inside the precursor mix increased, the S_{BET} values of the composites dropped marginally. With the maximum level of melamine within the precursor mix (90%), the S_{BET} estimation was 72.05 m^2/g. Similar to NP400, every as-prepared sample exhibited mesoporous characteristics, as shown in **Figs. 6-2(c)** and **(d)**.

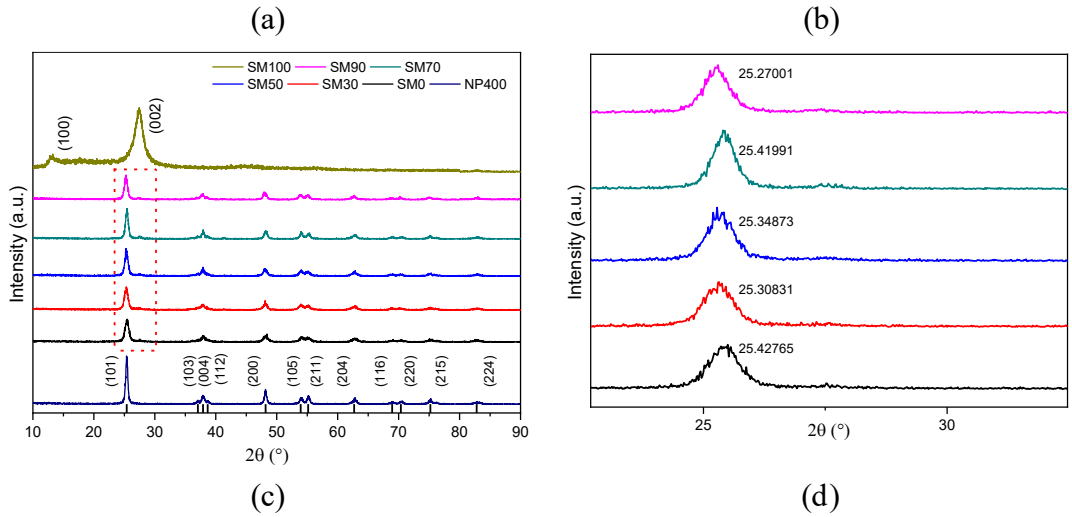

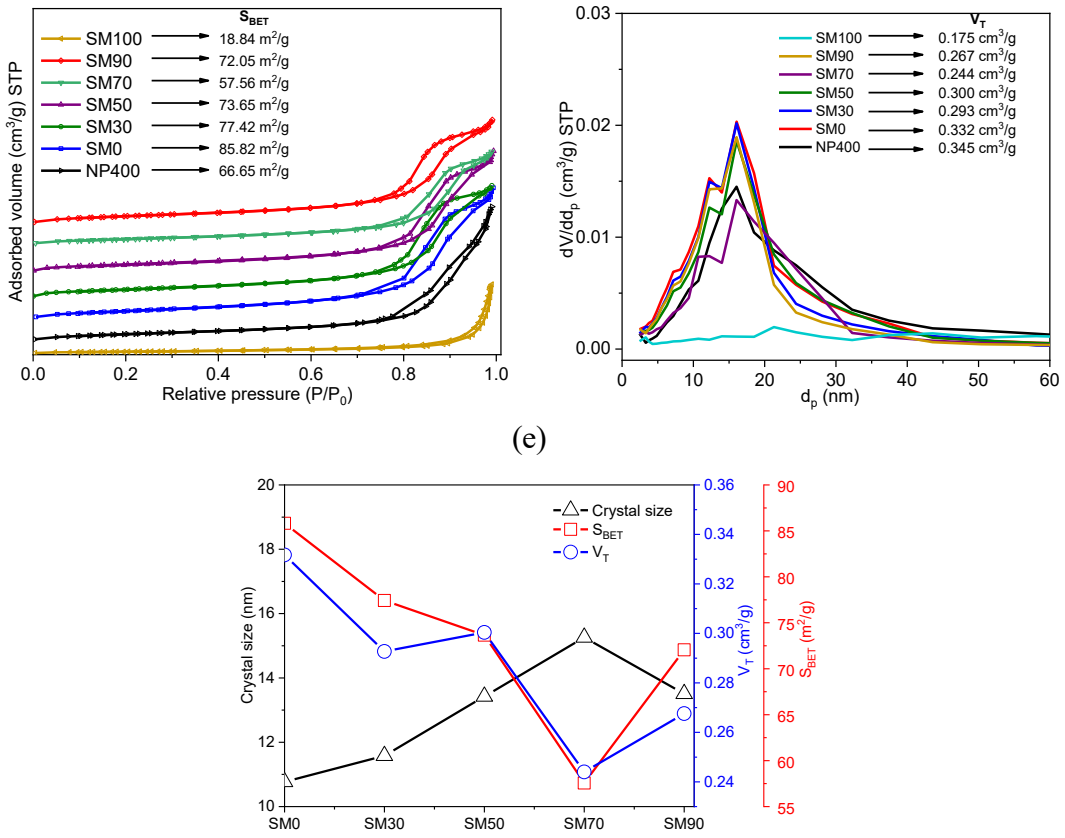

Fig. 6-2. (a – b) XRD patterns (c) N_2 adsorption-desorption isotherm (d) BJH PSDs of SM0 – SM100 and NP400; (e) Correlation between the crystal size, S_{BET}, and V_T of the samples SM0 – SM100.

Scherrer's equation was employed around the dominant plane (101) for the anatase TiO_2 for evaluating the influence of the as-synthesized samples on size of crystals; the outcomes can be seen in **Fig. 6-2(e)**.

$$D = \frac{K\lambda}{FWHM \times cos\theta} \qquad (6\text{-}1)$$

In this equation, crystal size is represented by , K is Scherrer's constant, λ is wavelength, FWHM is full width at half maxima, and θ is Bragg's angle. Looking at the crystal sizes shown in **Fig. 6-2(e)**, it can be seen that mixing melamine into the dried sludge for the precursor mix SM0 – SM90 slightly increased the crystal size (10.76 nm – 13.50 nm). Thus, their S_{BET} values correspondingly decreased as melamine content increased.

6.4.2 FTIR and XPS analysis

For further validation of the presence of anatase TiO_2 and g-CN within the as-synthesized composites, FTIR analysis was employed, the results of which are shown in **Fig. 6-3(a)**. For samples SM0 – SM90, the broad absorption peaks from 400 – 700 cm^{-1} is attributed

to stretching modes Ti-O and Ti-O-Ti of the TiO_2 (Chao Liu et al., 2016). Additionally, we can attribute the broad absorption band from 3000 – 3700 cm^{-1} to O-H stretching applied to the adsorbed H_2O within the samples (Huan Liu et al., 2019; Troppová et al., 2018). All the characteristic g-CN peaks can be seen within the as-synthesized SM100. A range of absorption bands was found in SM100, with a wavelength range between 1230 cm^{-1} and 1600 cm^{-1} (see **Fig. 6-3(a)**), this being chiefly attributed to C-N stretching with the aromatic section of g-CN (Giannakopoulou et al., 2017; Papailias et al., 2017). No characteristic g-CN peaks were found in any of the samples (SM10 – SM90) created from the calcination of the sludge/melamine mixture.

XPS analysis was undertaken to provide more details of the chemical composition of the as-synthesized samples as well as their oxidation states. The wide-angle XPS survey for the as-synthesized samples (see **Fig. 6-3(b)**) indicates significant photoelectron peaks for Ti 2p and O 1s that are clearly apparent with binding energies of 458 eV and 530 eV for samples SM0 – SM90 (Qian et al., 2014). Due to g-CN formation, SM100 was the only sample displaying peaks for N 1s and C 1s (Thomas et al., 2008). The deconvoluted N 1s, O1s, and Ti 2p spectra for the as-prepared samples are shown in **Fig. 6-3(c)** to **6-3(e)**, respectively. We can see that for SM30 – SM90, minor peak intensities of around 400 eV were observed, which may be a result of interstitial nitrogen doping with the TiO_2 lattice (Qian et al., 2014; Wu et al., 2010). Three convoluted peaks in the N 1s spectra for SM100 were also found, these being at 398.48 eV (pyridinic N), 399.28 eV (pyrrolic N), and 400.98 eV (graphitic N) (Y. Huang et al., 2019; Jiang et al., 2018; H. Liu et al., 2019). There were peaks at 530.88 eV and 529.56 eV in the narrow-angle O 1s SM0, for which the XRD findings showed anatase TiO_2 was all that was present (Qian et al., 2014). These peaks may be attributed to O_2^- lattice (529.56 eV) and OH^- (530.88 eV), confirming that TiO_2 is formed in the prepared samples. In all the samples from SM30 – SM90, a minor peak is found around 532.0 eV as a result of nitrogen and oxygen being present within the same lattice (Diker et al., 2014). Investigating the Ti 2p narrow scan (**Fig. 6-3(e)**) for the prepared samples (SM0 – SM90), we have discovered significant peaks at 457 – 459 eV and 463 – 465 eV, which manifest the characteristics of Ti $2p_{3/2}$ and Ti $2p_{1/2}$ (Cui et al., 2020; Wang et al., 2013). Thus, we are justified in presuming that Ti within the as-prepared samples represents the Ti^{4+} form. Therefore, based on the FTIR and XPS results, we found no heterojunction of g-CN and anatase TiO_2; instead, the calcination of Ti-incorporated dried sludge and melamine only resulted in solely N-doped TiO_2. Thus, we

proceeded to test a two-step calcination route for successful heterojunction between anatase titania and g-CN to improve the resulting composite material.

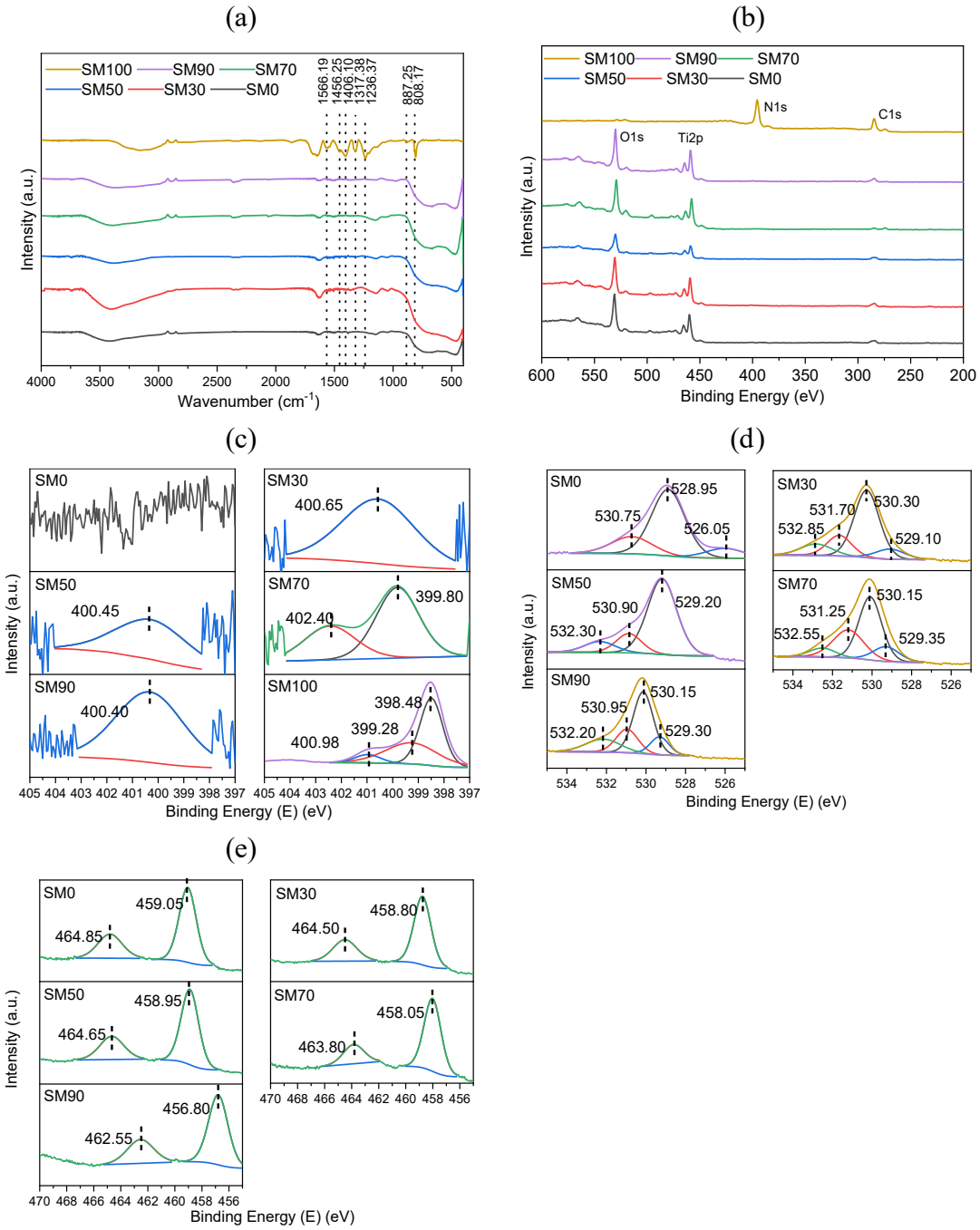

Fig. 6-3. (a) FTIR and (b) XPS spectra of the samples SM0 – SM100; high resolution (c) N 1s, (d) O 1s, and (e) Ti 2p scan of sample SM0 – SM100.

Table 6-1. Elemental composition of the composite samples SM0 – SM100, from XPS analysis.

Name	C (at.%)	N (at.%)	Ti (at.%)	O (at.%)
SM0	5.66		38.9	55.44
SM30	13.42	1.21	31.92	53.45
SM50	15.57	1.39	30.54	52.49
SM70	10.38	1.1	34.05	54.47
SM90	13	1.32	32.82	52.87
SM100	43.4	55.11		1.5

6.5 Heterojunction of SM0 and g-CN (two-step calcination)

6.5.1 Photocatalytic performance

Since anatase titania was the precursor for the heterojunction in the two-step calcination route, the photoactivity of the synthesized photocatalysts was initially assessed, followed by advanced characterization of the best photoactive samples. By making an estimation of the degree of NO oxidation using UV and visible light irradiance, we could assess the photoactivity of the samples synthesized with two-step calcination. We also compared the composite photoactivity with that of commercially produced NP400. **Fig. 6-4(a)** shows the NO, NO_2, and NO_x concentration variation patterns for the as-prepared composites TM0 – TM100 under UV irradiation, while **Fig. 6-4(c)** shows the patterns under visible light irradiation. Additionally, **Figs. 6-4(b)** and **(d)** illustrate the NO removal, NO_2 production, and NO_3^-selectivity of the prepared composites alongside NP400 under UV and visible light, respectively.

For all the experiments, ~7.50 μmol of NO was inserted into the reactor. Regardless of the light type (either UV or visible), removal patterns match those of the as-prepared composites. With every sample under examination, it was seen that NO and NO_x concentrations began to fall as soon as light irradiation started (of either type) and achieved a minimum concentration after 5 min of irradiance. As a result of the instrument's default factory settings, there was very little response lag at either end of the irradiation process. The fact that NO began to degrade as soon as light irradiance commenced rapidly may be attributed to the dual influence of adsorption and photooxidation at the photocatalytic sites for the respective catalysts (Hossain, Park, Kang, Kim, et al., 2020; Hossain et al., 2021). There was very little photoactivity with

either form of light irradiation (this UV or visible) with the TM0 created using two-step calcination of flocculation-generated dye wastewater; this does not agree with the results of some similar research (Park et al., 2014). Only 5.02% (**Fig. 6-4(a)**) and 4.05% (**Fig. 6-4(c)**) of NO were removed by an hour of UV and visible light irradiation. We may attribute the steady decline in TM0 efficiency in removing NO with visible/UV light irradiation because the photocatalytic sites were saturated with protoxidized byproducts (i.e., NO_2, NO_3^-) (Park et al., 2014; Rhee et al., 2018). When commercial NP400 is employed for the photodegradation of atmospheric NO, similar removal patterns are demonstrated. Nevertheless, with an identical scenario, NP400 removed 23% NO under UV light, and 9% under visible light. It is interesting to note that unlike TM0 and NP400, the as-prepared composites TM30 – TM100 demonstrated stability in levels of NO and NO_x removal after an hour of irradiation (UV/visible), which may indicate better photoactivity (**Fig. 6-4(a)** and **(c)**).

As shown in **Fig. 6-4(b)**, NO removal was significantly improved for our prepared composites when subjected to UV irradiation due to melamine being incorporated into the precursor mix. TM70 had the most significant NO (25.71%) and NO_x (11.15%) removal levels, approximately 5 times higher than TM0. When the TM70 composite was synthesized, it had a precursor mix of approximately 70% melamine. Increasing the melamine content above 70% led to a reduction of photoactivity, so that 1 h of UV irradiation on TM90 caused a NO_x reduction of approximately a quarter (3.25%) of that of TM70. **Fig. 6-4(d)** demonstrates that TM70 displayed the highest removal rates of NO (13.5%) and NO_x (12.4%) when irradiated with visible light resulting in an enhanced NO_3^- selectivity of 91.85%. As the melamine proportion of the precursor mix rose, the NO removal when irradiated with visible light rose from 4.05% (TM0) to 13.5% (TM70). As with UV radiation, it was shown that NO removal gradually fell as the melamine content was increased over the 70% threshold, with NO removal levels for TM90 being 8.2% and for TM100 being 7.0%. It has been noted that the composites $NO_{3^-\text{selectivity}}$ rose with visible light irradiation as a greater percentage of melamine was added to the precursor mix but began to fall when this proportion went over 70%.

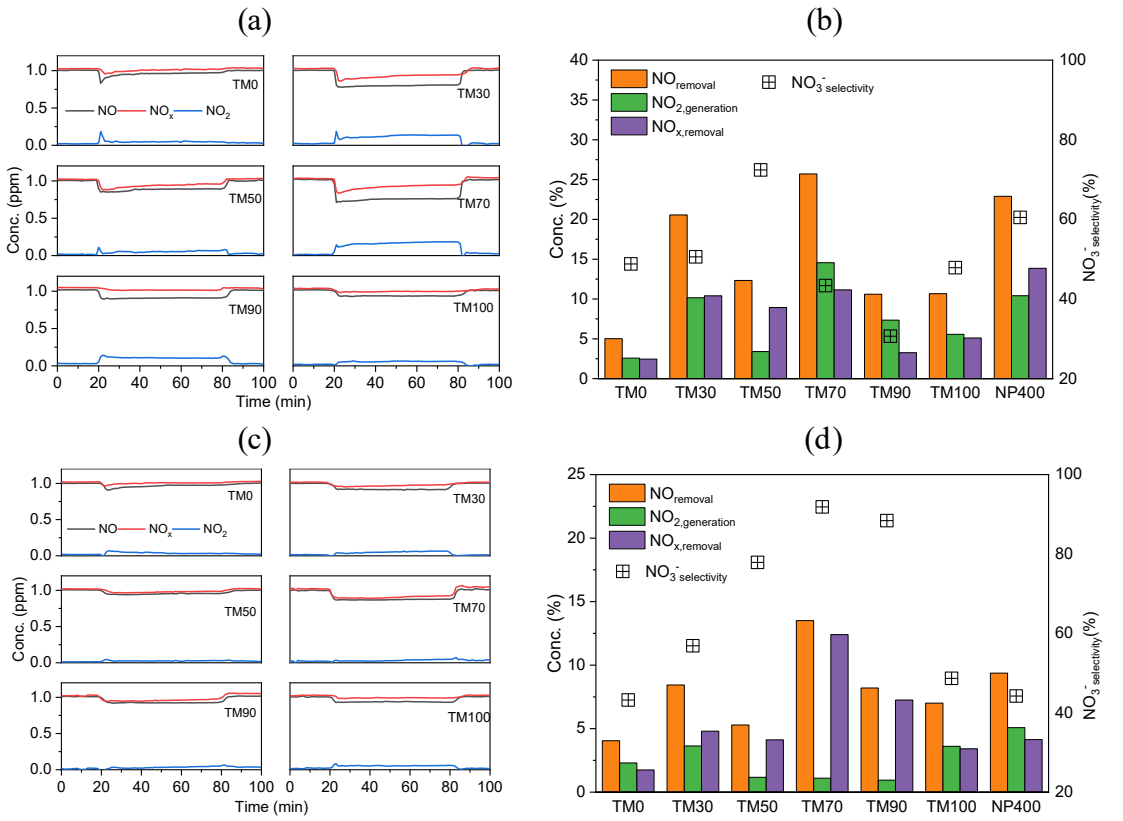

Fig. 6-4. NO, NO_x, NO_2 conc. patterns and summarized % removal under UV irradiance (a – b), under visible light irradiance (c – d).

6.5.2 Structural attributes

On the basis of the superior photoactivity found in the prepared composites, we undertook XRD analysis on the samples TM70 – TM100, comparing the patterns with those of SM0 and NP400. **Table 6-2** and **Fig. 6-5(a)** show that the prepared TM70 and TM90 employing SM0 for a precursor comprises chiefly anatase structure. Additionally, for both TM70 and TM90, a characteristic g-CN peak around 2θ~27.5° (002) was found, demonstrating the inter-planar assembly of the conjugated aromatic system (Yuan et al., 2020). When only melamine underwent calcination, g-CN (TM100) was formed with dominant peaks around 2θ = 13.04° and 27.58°, the former being attributed to the N-bridged repetition for $C_6H_3N_7$ units, and the latter as the inter-planar assembly for the conjugated aromatic system (Du et al., 2020; Huan Liu et al., 2019; Wang et al., 2013). **Fig. 6-5(a)** clearly demonstrates that the synthesized SM0/g-CN heterojunction preserved the anatase planes for SM0, and no significant changes occurred to 2θ. In addition, the anatase planes retained their peaks no matter how the ratio of SM0 and melamine was adjusted within the precursor mix, which agrees well with previous research (Giannakopoulou et al., 2017; Jinzhu Ma et al., 2016). When the melamine was increased

from 70% to 90%, there is a broader, elevated peak in the region at ~27.50°. The fact that the composite TM90 had a higher peak intensity of g-CN in comparison with TM70 may be attributed to improved crystallinity. Taking these facts and examining **Fig. 6-5(a)**, it becomes clear that our prepared composites showed a superposition of characteristic XRD peaks with SM0 and g-CN. Thus, we can assume that when the melamine and SM0 mix underwent calcination, g-CN gathered on the face of SM0 without interfering with either component's crystal lattice structures.

Fig. 6-5(b) shows the FTIR spectra for the as-prepared TM70 – TM100 compared to those of the precursor SM0 and the commercially available NP400. Apart from TM100, every sample in **Fig. 6-5(b)** exhibited a substantial absorption peak between 400 – 700 cm^{-1} as a result of the Ti-O and Ti-O-Ti stretching mode (Yu Huang et al., 2019). For TM70 and TM90, the broad absorption band between 3000 – 3700 cm^{-1} may result from the adsorbed H_2O on our samples undergoing O-H stretching; the vibration of N-H from the other NH_2 groups may also be a cause (Papailias et al., 2017). The FTIR peaks were around 808.17 cm^{-1} in the as-prepared TM70 – TM100 as a result of the skeletal triazine cycles' bending mode (Dong et al., 2014). A series of absorption bands around the wavelengths 1230 – 1600 cm^{-1} was also observed, which can be attributed to the aromatic part undergoing C-N stretching (Wang et al., 2015). As the g-CN content of the synthesized samples rose, the g-CN characteristic FTIR peaks widened and sharpened. It was also interesting to note that looking at the FTIR spectra for the prepared composites, the broad peak around 400 – 700 cm^{-1} shifted slightly towards a higher wavelength (see **Fig. 6-5(b)**), in congruence with other related research on composites (Song et al., 2016). We presumed that the g-CN within the composite promoted modifications on the surface chemical environment of SM0. Past research has demonstrated that as a result of close heterojunction, the molecular orbits of the different components will interact, and so the fact that the Ti-O-Ti stretching modes for the as-synthesized composites undergo a shift; this leads us to assume that the significant heterojunction between g-CN and SM0 is adjacent.

Fig. 6-5(c) shows significant spikes in photoelectron activity for C 1s, N 1s, Ti 2p, and O 1s corresponding to binding energies of 286, 400, 458, and 530 eV for the as-prepared TM70 and TM90 (Troppová et al., 2018). Characteristic peaks for C 1s and N 1s are visible on the wide-angle survey scan of TM100. **Fig. 6-5(d – g)** illustrates the narrow scan spectra of C 1s, N 1s, Ti 2p, and O 1s of the as-prepared composite TM70 – TM100

as well as their corresponding peak positions. We used Lorentz peak fitting to deconvolute the XPS peaks in the narrow scan. From XRD and FTIR analysis, it was shown that TM70 and TM90 both contained g-CN, and so we may ascribe N-C=N_2 characteristics and coordinates as a g-CN peak to the deconvoluted C 1s peak at 288.08 eV (see **Fig. 6-5(d)**) (Papailias et al., 2017). As there is no visible C-Ti peak, this confirms that there was no chemical reaction between g-CN and anatase TiO_2, but there was an effective heterojunction.

Examining the high resolution N 1 spectra for the as-synthesized TM70 – TM100 dominant peak related to triazine rings showed that sp2 hybridized C=N-C was present at ~398.58 eV. Additionally, a peak for tertiary N-$(C)_3$ was found at ~399 and for N-H groups at ~401 eV (see **Fig. 6-5(e)**) (Giannakopoulou et al., 2017). For the prepared TM70 and TM90, the O 1s spectra generally fitted, as shown in **Fig. 6-5(f)**) to ~529.5, ~531, and ~532, offering clear confirmation that the lattice O_2^- and O_2^-ions/OH^- groups are present (Yu Huang et al., 2019). In **Fig. 6-5(g)** we can see the Ti 2p spectra for the as-prepared TM70 and TM90 composite. We can see substantial peaks for these composites at ~458.5 and ~464 eV; these are characteristic peaks of Ti $2p_{3/2}$ and Ti $2p_{1/2}$, confirming the presence of Ti as Ti^{4+} species (Jiang et al., 2018). In comparison to TM70, as quantities of g-CN within the samples rose, we could see that the prepared TM90 experienced a positive 0.10 eV shift. We can attribute this finding to the closeness of electronic interactions of used SM0 and g-CN, confirming the formation of compact composites. This positive shift may also be attributed to the composite formation increasing the electron density on Ti (Hossain et al., 2021).

(a) (b)

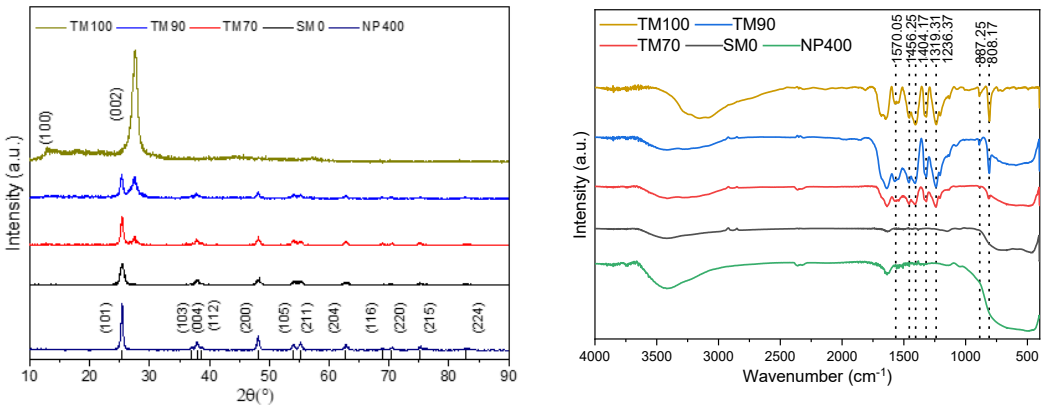

(c) (d)

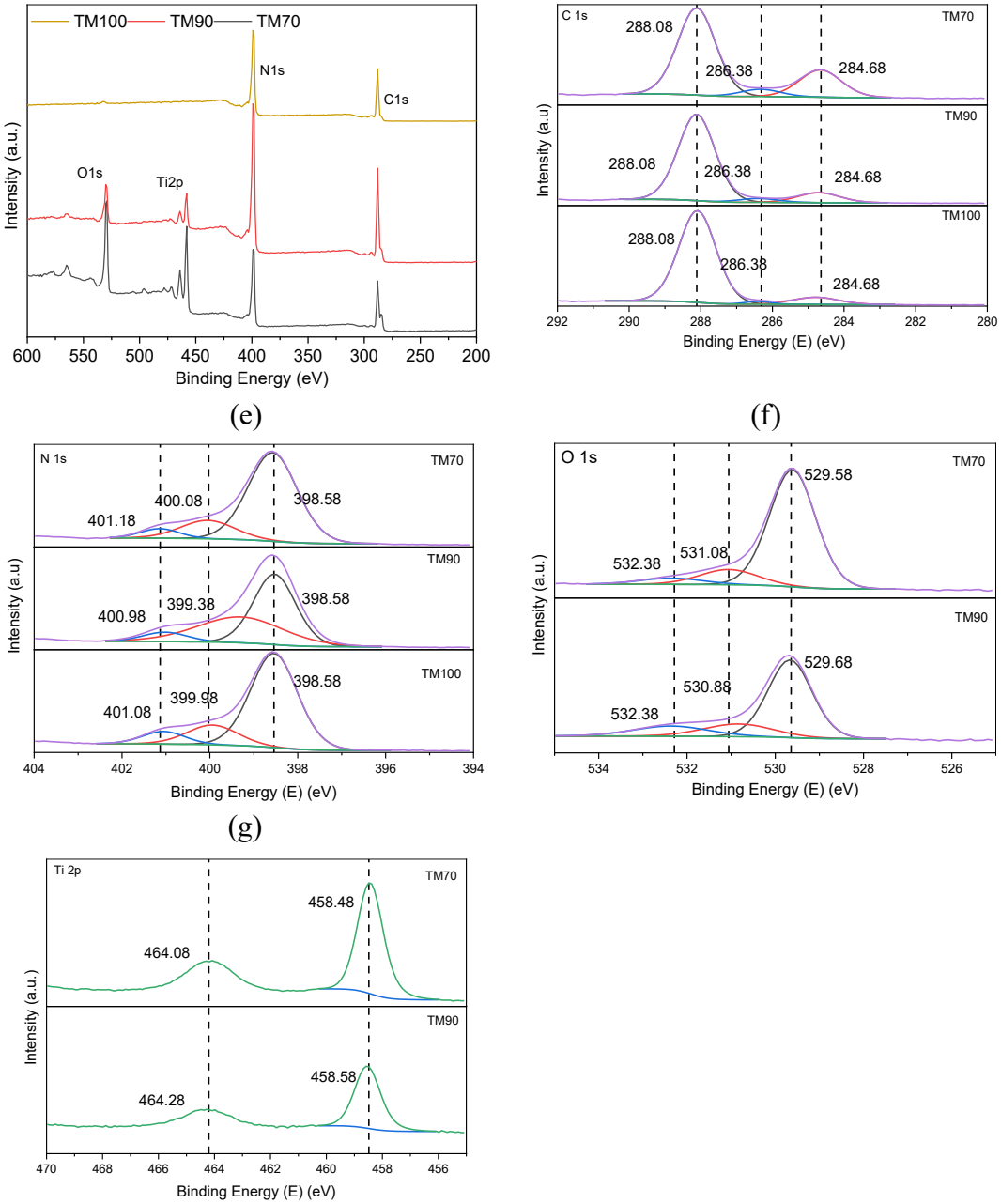

Fig. 6-5. (a) XRD and (b) FTIR patterns of SM0, TM70, TM90, TM100, and NP400; (c) broad angle XPS spectra, and high resolution (d) N 1s, (e) C 1s, (f) O 1s, and (g) Ti 2p scan of sample TM70 – TM100.

6.5.3 Optical attributes

UV-vis was used to determine the optical energy bandgap (E_g) for TM70, and the light absorption data was placed in the UV-Vis range. E_g for TM70 was ascertained by employing the extrapolation technique for the Kubelka-Munk function; the results can be seen in **Fig. 6-6(a – c)**. A comparison is made of the DRS analysis for TM70 with TM100, SM0, and NP400, showing clearly that the bandgap narrowed. In **Fig. 6-6(a)** and **(b)**, we

can see the pattern of F(R) function and the absorbance spectra for as-prepared samples SM0, TM0, TM100, and NP400. **Fig. 6-6(a)** shows that prepared TM70 absorbed more light in the UV region in comparison to TM100 and therefore was significantly more efficient at the removal of NO_x when irradiated with UV light. TM70 also demonstrated better light absorption outside the UV range in comparison to SM0 and NP400. A superposition for the material's light absorption spectra was noted, confirming that heterojunction had been successfully achieved. The same sort of attributes has been found with photocatalysts synthesized through heterojunction of commercially produced titania and enriched nitrogen precursors such as urea, melamine and others (Yuan et al., 2020). **Fig. 6-6(d)** illustrates the (F (R)hv)n against hv for the samples, with energy bandgaps calculated via extrapolation from the matching graphs. It was shown that the energy bandgaps were 3.43 eV for NP400, 3.20 eV for SM0, 2.69 eV for TM70, and 2.61 eV for TM100. Additionally, the conduction band (CB) and valence band (VB) edges for g-CN and TiO_2 were estimated by employing the equations below.

$$E_{CB} = E_{VB} - E_g \qquad (6\text{-}2)$$

$$E_{VB} = X - E_0 + 0.5\, E_g \qquad (6\text{-}3)$$

The CB and VB edges of the semiconductor are respectively represented by E_{CB} and E_{VB}. In addition, average electronegativity is represented by X (5.81 eV for anatase TiO_2 and 4.64 eV for g-CN), and the energy of free electrons adjacent to NHE is represented by E_0 (4.5 eV) (Hossain et al., 2021). For additional evaluation of TM70's photooxidation mechanism, we undertook PL analysis, with the derived spectrum then undergoing comparison with the PL spectra for SM0, TM90, and TM100 (**Fig. 6-6(d)**). It is generally accepted that a semiconductor's PL spectrum may provide useful information regarding its rates of photo-induced charge separation when subjected to light irradiation (Yu et al., 2020). A robust quasi-asymmetric PL spectrum was found with the prepared composites, with a maximum peak at around ~438 nm. This peak corresponded with the point at which the photogenerated e^-/h^+ pairs recombine after being generated inside the photocatalysts. **Fig. 6-6(d)** shows that TM70 had a considerably lower PL intensity in the same peak position than TM90 and TM100. This generally implies lower recombination rates.

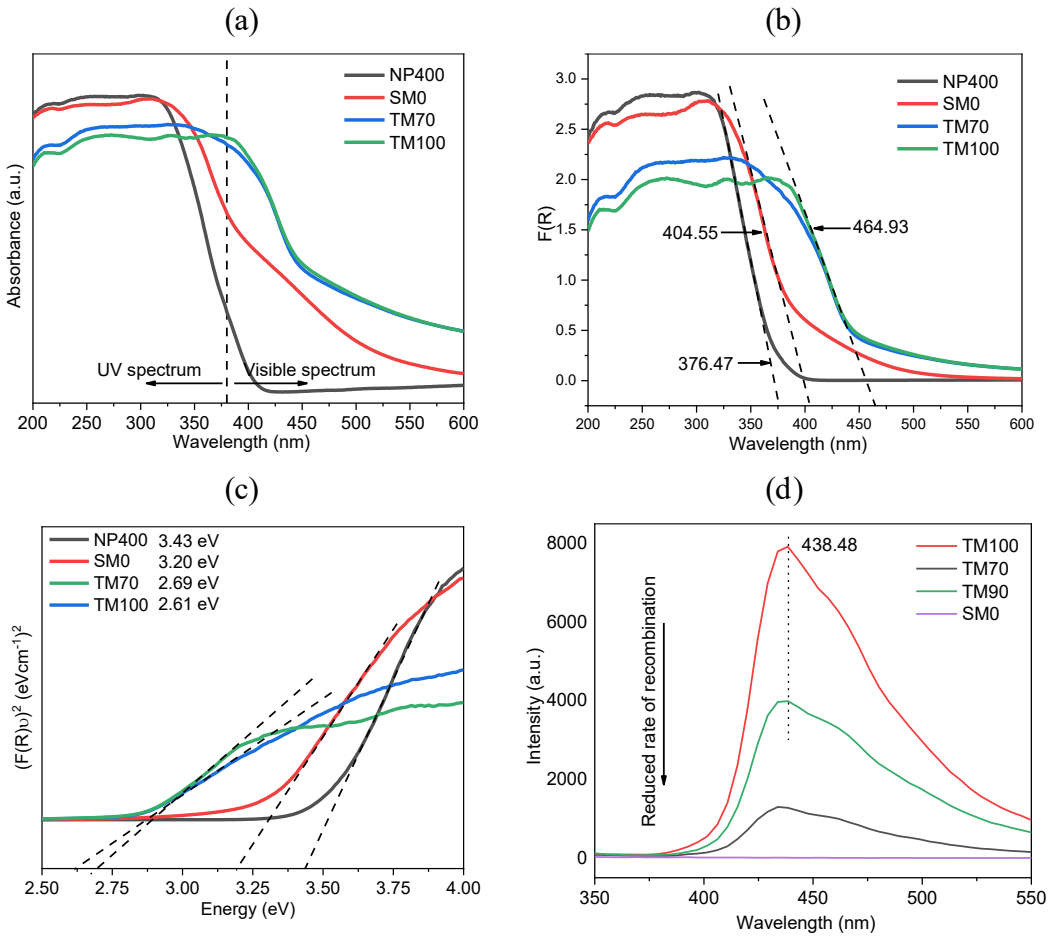

Fig. 6-6. UV-vis DRS (a) absorbance vs. wavelength, (b) (F(R) vs. wavelength), (c) converted Kubelka-Munk function vs. energy of absorbed light, and (d) PL spectra of the samples SM0, TM70, TM100, and NP400.

6.5.4 Stability and photocatalytic mechanism

The stability of the representative composite TM70 was explored by undertaking NO removal recycling experiments irradiated with UV light (**Fig. 6-7**). The as-prepared TM70 was subjected to as many as 5 runs of recycling experiments. Each cycle lasted 30 min; a 5 min stopping period was inserted between each run for consideration. Photoactivity showed very low levels of decay following five cycles, showing that the as-prepared composite is highly stable and reusable. After the first 30 min run of UV radiation, it was estimated that NO removal stood at 15.88%; by the end of the 5th run, this had only fallen to 11.35% (**Fig. 6-7(b)**). This mild decrease demonstrates that NO oxidized byproducts are present at the active photocatalytic regions. Interestingly, nitrate selectivity was retained in the 1st run (approximately 42%) and had risen slightly by the 5th run (42.3%).

We found two primary reasons for the enhanced photoactivity of the TM70 composite examined here when exposed to UV/Visible irradiation, based on the previously stated advanced characterizations for the as-prepared samples. First, the optical bandgap is narrowed, and second, the recombination rate of the photogenerated e^-/h^+ pair is reduced (**Fig. 6-6(d)**). When g-CN was combined with SM0, the optical bandgap of TM70 was reduced from 3.20 eV to 2.69 eV. The optical bandgap for TM100 (g-CN) was determined to be 2.61 eV in **Fig. 6-6(c)**. Thus, we may ascribe the narrowing of the bandgap of TM 70 to the presence of g-CN in the composite. With TM70, a redshift (464.93 nm) was detected, similar to that seen with g-CN, which enabled photoactivity to be triggered when exposed to visible light (Papailias et al., 2017; Song et al., 2016; Troppová et al., 2018). In addition, as compared to g-CN and TM90 (melamine concentration more than 70%), as-prepared TM70 showed a drop in the intensity of PL spectra, suggesting that the degree of charge recombination has decreased. Therefore, the prepared composites exhibited greater photoactivity when subjected to both visible light and UV light. Following on from this, the rising improvements in NO_x removal when subjected to UV/visible light irradiation and the rising intensity in the PL spectra (**Fig. 6-6(d)**) exhibited similar patterns (TM100 < TM90 < TM70).

It is widely agreed that it is generally the active species, e.g., superoxide ($\cdot O_2^-$) and hydroxyl ($\cdot OH$) radicals created by redox reactions that involve photogenerated e^-/h^+ pairs and adsorbed O_2/OH^- groups from the irradiated photocatalyst that are chiefly responsible for photocatalytic NO oxidation (Hossain, Park, Kang, Mun, et al., 2020; Hossain et al., 2021; Jinzhu Ma et al., 2016; Papailias et al., 2017; Song et al., 2016). If photogenerated e^- is to be effective in the production of $\cdot O_2^-$, there must be greater negativity at the CB edge for the photocatalyst compared to the redox potential for $O_2/\cdot O_2^-$ (0.33 eV vs NHE) (Jinzhu Ma et al., 2016). The standard redox potential of $OH^-/\cdot OH$ is 1.99 eV compared to NHE, and so VB needs a more positive position if the generation of $\cdot OH$ radicals from the h^+ are to occur. The estimations of optical bandgaps in this research, as well as the CB and VB positions for SM0 and g-CN, indicate that the as-synthesized composite is a type II heterojunction photocatalyst. Thus, the SM0 and the g-CN within the TM70 composite are subject to excitation when subjected to UV irradiation, generating photo-induced e^- and h^+ for CB and VB, respectively. Because the CB for g-CN (-1.16 eV) is more negative in comparison with SM0 (-0.29 eV), the photogenerated e^- moves to the CB of SM0. Subsequently the reaction between e^- and adjacent O_2 and H_2O creates $\cdot O_2^-$

and ·OH radicals. Conversely, photo-induced h^+ on the very positive VB of SM0 (+2.91 eV) moves to the lower positivity VB of g-CN (+1.45 eV), reacting with adsorbed H_2O and generating ·OH radicals. Subsequently, these newly created $\cdot O_2^-$ and ·OH radicals subject the NO to oxidization, and it turns to NO_2 or NO_3^-. Several previous studies have shown that the main species in the oxidation of NO to NO_3^- is $\cdot O_2^-$ (Jiang et al., 2018; Jinzhu Ma et al., 2016). Thus, on the basis of the discovered nitrated selectivity shown by prepared samples, we may conclude that $\cdot O_2^-$ and ·OH radicals are both primary active species in the oxidation of NO when irradiated with UV light. Conversely, when the TM70 composites were subjected to visible light irradiation, g-CN was the only element experiencing excitation, so the photogenerated e^- can move to SM0 and easily generate $\cdot O_2^-$, however, it is not possible for the h^+ on the VB to apply direct oxidation to turn H_2O/OH^- into ·OH radicals. Thus $\cdot O_2^-$ is the primary species for oxidation of NO when subject to visible light. With the prepared samples, the nitrated sensitivity estimation supports the assertions above, with visible light activation of the composites demonstrating upward trends (see **Fig. 6-4(d)**). Hence, with the increase in melamine content, a bell-shaped pattern in nitrate selectivity was observed under visible light (**Fig. 6-4(d)**). Melamine content in the precursor mix above 70% resulted in increased charge recombination rate (**Fig. 6-6(d)**) and reduced photon adsorption (**Fig. 6-6(a)**. Hence, the NO_2 generation rate of TM90 and TM100 increased, which caused the reduction in NO_3^- selectivity.

Table 6-2. Comparative key features of the NP400, SM0, and TM70

Name	**S_{BET}**	**Crystal size, D**	**V_T**	**E_g**	**Absorption edge, λ**	**NO_x removal**		**Remarks**
						Under UV	**Under visible light**	
	m^2/g	nm	cm^3/g	eV	nm	%	%	
NP400	66.65	18.8	0.35	3.43	376.47	22.20	9.37	Commercial anatase TiO_2

Name	S_{BET}	Crystal size, D	V_T	E_g	Absorption edge, λ	NO_x removal		Remarks
						Under UV	Under visible light	
SM0	85.82	9.72	0.33	3.20	404.55	12.54	4.05	Sludge-generated anatase TiO_2
TM70	36.82	25.34	0.26	2.69	464.93	25.71	13.5	TiO_2/g-CN composite from SM0 @70% melamine content.

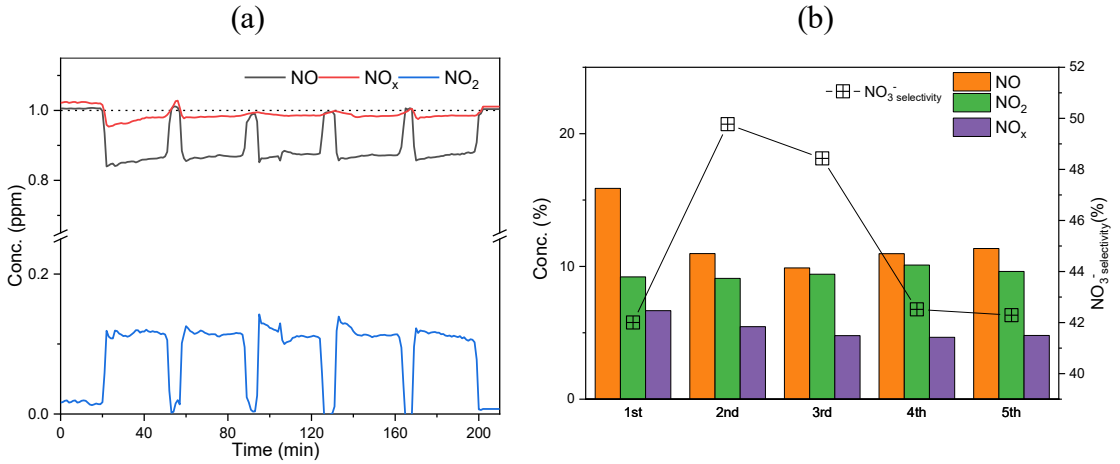

Fig. 6-7. Recycling NO photooxidation experiments for photostability of TM70 (a) conc. patterns in ppm, (b) removal efficiencies.

6.6 Conclusion

The goal of the analysis was to prepare the heterojunction of anatase TiO_2/g-CN by using Ti-incorporated dried sludge as the precursor for anatase titania. XRD, FTIR, and XPS research verified the active preparation of the TiO_2/g-CN heterojunction anatase. The addition of g-CN had a marginal influence on the composition of the crystal and the scale of the titanium precursor used. Maximum NO removal was recorded for the TiO_2/g-CN

composite, which has a melamine content of 70% in the precursor mix. The subsequent UV-vis DRS performed on the best performing composite depicted that the energy bandgap was decreased from 3.20 eV (sludge-generated TiO_2) to 2.61 eV. Hence, in both UV and visible regions, the absorption band of the composite was significantly increased. Moreover, owing to the bandgap narrowing, a distinct redshift in the light wavelength (464.93 nm) absorption was observed. Therefore, relative to pristine sludge-generated TiO_2, UV light absorption was decreased. Furthermore, the PL analysis showed an inhibited recombination rate of e^-/h^+ pairs produced, which is favorable for the easy generation of $\cdot O_2^-$ and $\cdot OH$ radicals for NO_x photodegradation. The elimination of NO_x under UV light where no melamine was used in the precursor mixed was just 2.45%, which was improved in the optimized composite and discovered as 11.15% by considering NO_3^-selectivity. A similar pattern was observed under the visible light irradiation, where the bare TiO_2 removed around 1.70% and the g-CN optimized sample removed about 12.4% of NO_x. Hence, based on the advanced characterizations and NO photooxidation performance, the two-step calcination of the Ti-incorporated dried sludge and melamine could be a viable approach towards preparing visible light active photocatalysts.

CHAPTER 7
Synthesis and NO_x removal performance of anatase S-TiO_2/g-CN heterojunction formed from dye wastewater sludge

STATEMENT OF CONTRIBUTION OF AUTHORS

Title of Paper	Synthesis and NO_x removal performance of anatase S-TiO_2/g-CN heterojunction formed from dye wastewater sludge		
Publication Status	☒Published ☐Accepted for Publication ☐Submitted for Publication		
Publication Details	**Hossain, S. M.**, Park, H., Kang, H. J., Mun, J. S., Tijing, L., Rhee, I., Kim, J. H., Jun, Y. S., & Shon, H. K. (2021). Synthesis and NO_x removal performance of anatase S-TiO_2/g-CN heterojunction formed from dye wastewater sludge. *Chemosphere*, *275*, 130020. https://doi.org/10.1016/j.chemosphere.2021.130020		
PRINCIPLE AUTHOR			
Name of Principle Authors	Sayed Mukit Hossain **(Candidate)**		
Contribution	**Conceptualization, Data curation, Formal analysis, Investigation, Methodology, Validation, Writing – original draft.**		
Certification	This paper reports on original research I conducted during my Higher Degree by Research candidature and is not subject to any obligations or contractual agreements with a third party that would constrain its inclusion in this thesis. I am the primary author of this paper.		
Signature	Production Note: Signature removed prior to publication.	Date	30/11/2021
CO-AUTHOR CONTRIBUTIONS			
Name of Co-Author 1	Heeju Park		
Contribution	Data analysis, investigation, and data curation.		
Name of Co-Author 2	Hui-Ju Kang		
Contribution	Data analysis, investigation, and data curation.		
Name of Co-Author 3	Jong Seok Mun		
Contribution	Data analysis, investigation, and data curation.		
Name of Co-Author 4	Leonard Tijing		
Contribution	Writing - review and editing, Funding acquisition.		
Name of Co-Author 5	Inkyu Rhee		
Contribution	Writing - review and editing.		
Name of Co-Author 6	Jong-Ho Kim		
Contribution	Writing - review and editing, Funding acquisition.		
Name of Co-Author 7	Young-Si Jun		
Contribution	Writing - review and editing, Resources.		
Name of Co-Author 8	Ho Kyong Shon		
Contribution	Supervision, Project administration, Resources, Funding acquisition, Validation, Writing - review and editing.		

7 Synthesis and NO_x removal performance of anatase S-TiO_2/g-CN heterojunction formed from dye wastewater sludge

7.1 Abstract

In this study, sludges generated from Ti-based flocculation of dye wastewater were used to retrieve photoactive titania (S-TiO_2). It was heterojunctioned with graphitic carbon nitride (g-CN) to augment photoactivity under UV/visible light irradiance. Later the as-prepared samples were utilized to remove nitrogen oxides (NO_x) in the atmospheric condition through photocatalysis. Heterojunction between S-TiO_2 and g-CN was prepared through facile calcination (@550 °C) of S-TiO_2 and melamine mix. Advanced sample characterization was carried out and documented extensively. Successful heterojunction was confirmed from the assessment of morphological and optical attributes of the samples. Finally, the prepared samples' level of photoactivity was assessed through photooxidation of NO_x under both UV and visible light irradiance. Enhanced photoactivity was observed in the prepared samples irrespective of the light types. The best sample, STC4, was found to remove 15.18% and 9.16% of ambient NO after 1 h of UV and visible light-based photooxidation. In STC4, the mixing ratio of S-TiO_2, to melamine was maintained as 1:3. Moreover, the optical bandgap of STC4 was found as 2.65 eV, where for S-TiO_2, it was 2.83 eV. Hence, the restrained rate of photogenerated charge recombination and tailored energy bandgap of the as-prepared samples were the primary factors for enhancing photoactivity.

7.2 Introduction

In conventional wastewater treatment plants, coagulation and flocculation have been employed for generations for the removal of particulate matters either in suspension or colloidal form. In general, settling basin and mechanical filtration can easily separate the pollutants in suspension but found ineffective in removing colloidal particles (Zhao & Li, 2019). Meanwhile, coagulation and flocculation can readily remove various water-induced contaminants of the colloidal genre, e.g., materials causing turbidity, metal oxides, persistent toxic compounds, organic materials, stable emulsions, etc. (Hussain et al., 2019; Xia et al., 2018; W. Zhang et al., 2018). Traditionally, various types of Al and Fe salts are used as coagulants; however, they are induced with the significant drawbacks of unwanted sludge generation and effects of trace metals (Al/Fe) in subsequent effluent (J. Xu et al., 2018). Recently, Ti-based salts ($TiCl_4$, $TiSO_4$, and PTC) are found to perform on par with the Al and Fe based coagulants (Chi et al., 2019; X. Wang et al., 2018; Z.

Wang et al., 2018a). Ti (IV) coagulation has been effectively applied to treat water and wastewater enriched with various types of pollutants, such as inorganic colloids (Z. Wang et al., 2018a), natural organic matter with varying molecular weight (Wan et al., 2019), algae (Chi et al., 2019; J. Xu et al., 2018), trace nanoparticles (Aziz et al., 2018), phosphorous (Jeon & Ahn, 2018), arsenic (Y. Sun et al., 2013) and many more. Additionally, H. K. Shon et al. (2009a) affirmed equivalent pollutant removal comparing conventional coagulants ($FeCl_3$ & $Al_2(SO_4)_3$) and steady titania recovery from the flocculated sludge (Shon et al., 2007a). Photo-catalytically active anatase TiO_2 were prepared through incineration of $TiCl_4$ flocculated sludge at a temperature of 600 °C to 800 °C. Shortly after, Lee et al. (2008), studied the aquatic toxicity of residual Ti after $TiCl_4$ coagulation. They observed negligible toxicity at a chemical dose of 150 mg/L. Furthermore, the ready titania from flocculated sludge showed low toxicity compared to commercially available TiO_2 (P-25). Hence Ti-based coagulation possesses the potential to mitigate the human health and high chroma index issues of residual Al and Fe after treatment (Lee et al., 2008; Okour, Shon, et al., 2009; Shon et al., 2008b). To date, titania nanoparticles (NPs) and nanofibers (NFs) have been developed by utilizing the coagulated sludge of drinking water, seawater, biologically treated sewage effluent, wastewater from the printing press, dye wastewater and algae bloomed surface water (El Saliby et al., 2009; El Saliby et al., 2010b; Jong Beom Kim et al., 2010; Okour, El Saliby, et al., 2009). The provision of resource recovery as titania (TiO_2) and negligible aquatic toxicity of residual Ti established the background of the current study.

Initially, Fujishima and Honda (1972) announced the revolutionary study on TiO_2 electrode sensitization for H_2O electrolysis. Since then, many research groups have examined the possibility of using TiO_2 as photocatalysts for the hydrolysis of H_2O, towards numerous practical implications (Haider et al., 2019; Wang et al., 2019). Moreover, TiO_2 is cost-effective, non-toxic as a photocatalytic substance, and has reasonably good reactivity and stability in both aqueous and atmospheric environments (Diebold, 2003). TiO_2 has mostly been developed for the application of highly dispersed standalone photocatalysts, dye-sensitized solar cells, and the UV/visible light irradiated degradation of organic and inorganic pollutants through photocatalysis (Asahi et al., 2014; Nasirian et al., 2017). However, the main shortcoming of TiO_2 that has hindered its practical application is its wide energy bandgap of ~3.2 eV (Nasirian et al., 2017). Hence, standalone utilization of TiO_2 for photocatalysis can only be facilitated by light irradiation

in the UV region. Moreover, due to having large energy bandgap, the rate of recombination of the developed photoinduced electron/hole (e^-/h^+) pair is elevated, which substantially suppresses the photoactivity of TiO_2 (Asahi et al., 2014). Hence, to overcome the limitations associated with a large energy bandgap, a number of strategies were utilized to augment the photocatalytic efficiencies of TiO_2. To date, the most common strategies that have been employed includes self-structural adjustment, metal/noble metal/non-metal doping, sensitization, and heterojunction with other suitable semiconductors (Asahi et al., 2014; Nasirian et al., 2017). Among the techniques mentioned above, the heterojunction of semiconductors has stirred outstanding interest in recent years. In the last decades, an N modified TiO_2 was synthesized through pyrolysis of the precursor mix of TiO_2 and urea/melamine at 400 °C, which showed notable photoactivity within the visible light spectrum (Kobayakawa et al., 2005). The aforementioned visible light activation was attributed to the highly condensed melamine products such as melam, melem, and melon, which are the predecessors of graphitic carbon nitride (g-CN) (S. Zhang et al., 2019). These research results recommended that the products created from further condensation of melamine can potentially sensitize titania for visible light activation, which may have created an inspirational route of TiO_2/g-CN heterojunction formation. Hence, an extensive research study has been conducted on visible light-sensitive g-CN, focusing on their composition, and structural arrangement to manage the necessary transformation of light energy into usable chemical energy (Santosh Kumar et al., 2018; Ong, 2017; Tan et al., 2018; Xiao et al., 2018).

The backbone of g-CN, a nonmetal-based semiconductor, is constructed as a conjugated polymeric system and contains the earth abundant C and N atoms (B. Xu et al., 2018). The polymeric layers are being constructed with s-triazine ($C_3H_3N_3$) or heptazine ($C_6H_3N_7$) units interlinked by tertiary amine groups, and the layer atoms are considered in the arrangement of honeycomb. (Santosh Kumar et al., 2018). The $C_3H_3N_3$ or $C_6H_3N_7$ based 2D layers remain interconnected through weak van der Waals forces. Hence, due to the presence of aromatic heterocycles, including prevailing van der Waals forces within the polymeric sheets, g-CN is thermally durable up to 600 °C in atmospheric conditions (S. Zhang et al., 2019). Also, g-CN showed superior chemical stabilities in solvents like water, alcohols, ethers, and several weak acids. Moreover, the optical bandgap of g-CN is narrower (~2.7 eV), and with respect to normal hydrogen electrode at pH= 7, the conduction band (CB) and valence band (VB) location could be estimated as -1.31 and

+1.40 eV, respectively (Zhou et al., 2019). Hence, as a photocatalyst, the extraordinary advantages of g-CN include favorable electro-optical properties and superior visible light sensitivity due to narrow energy bandgap. For the preparation of photocatalytic heterojunction, molecular level chemical modification can easily be applied to facilitate favorable surface properties of g-CN. Moreover, several studies inferred that g-CN showed outstanding compatibility as a host nanomaterial while composited with diverse inorganic NPs (Huang et al., 2020; Yu et al., 2020; Zhou et al., 2019). However, the prompt recombination of the photogenerated e^-/h^+ pairs and the inferior active surface area is still two vital disadvantages limiting the photoactivity of g-CN. Therefore, developing novel answers to surmount these barriers are of significant importance.

Over the past decades, a substantial increase in atmospheric nitrogen oxides (NO_x; NO + NO_2) has been observed, and photooxidation of NO_x is one of the most prominent solutions for this problem (Jinzhu Ma et al., 2016; Papailias et al., 2017). Many research groups nowadays have focused on this topic and developed a number of efficient photocatalysts to oxidize NO_x into a more neutral product. The suitable positioning of the CB and VB edge of anatase TiO_2 and g-CN, along with the 2D sheet like structure of g-CN, favors successful heterojunction. It has been reported that g-CN could form a thin layer on TiO_2 NPs, while heterojunction is formed (Jiang et al., 2018). Additionally, type II heterojunction has been reported for anatase TiO_2/g-CN composites due to the placement of their CB and VB edges (Jinzhu Ma et al., 2016). Therefore, photogenerated e^- and h^+ can migrate between the band edges of TiO_2 and g-CN, facilitating the hindered rate of recombination. Giannakopoulou et al. (2017) demonstrated an easy solvent-free mechanical mixing followed by calcination technique to tailor the energy bandgap of TiO_2/g-CN, to facilitate NO oxidation. They oxidized an initial concentration of 1 ppm NO under both visible (7000 lux) and UV (10 Wm^{-2}) light irradiation. After 40 min of irradiance, they attained a maximum of 38% and 42% of removal for visible and UV light, respectively. Papailias et al. (2017) similarly removed NO_x using TiO_2/g-CN with a removal rate of 18% and 22.5% after 30 min by using visible and UV irradiation, respectively. This was attained by modifying the surface morphology of the as-prepared photocatalysts with the assistance of $CaCO_3$. Recently, Yu Huang et al. (2019) used a simple ultrasonic exfoliation technique and synthesized Ti^{3+} TiO_2/p-CN composite for the purpose of NO_x oxidation. Using an initial NO concentration of 400 ppb, a removal percentage of 25.8% after 30 min of irradiation was reported.

Despite numerous studies conducted for NO_x removal using TiO_2/g-CN composites, in most cases, commercially available titania was used as the precursor of TiO_2, which increases costs for photocatalyst synthesis. Therefore, in this study, we have synthesized a novel TiO_2/g-CN heterojunction by using sludge generated titania (S-TiO_2) as the precursor of TiO_2. We have used a template-free approach and utilized the precursor mix of S-TiO_2 and melamine for successful heterojunction. Advanced chemical, morphological and optical characterizations of as-synthesized samples have been conducted. ISO 22197-1 (2007) and ISO 17198-1 (2018) was followed to evaluate the prepared samples' NO_x photooxidation capacity under UV and visible light, respectively. Besides, nitrate selectivity of the ready samples was assessed and based on the advanced characterizations, a possible photooxidation scheme was proposed.

7.3 Photocatalytic activity

The photoactivity of the synthesized samples was assessed through estimating the extent of NO oxidation under UV and visible light irradiance. In addition, the photoactivity of the as-prepared samples were compared with standalone use of S-TiO_2, NP400, and g-CN. **Fig. 7-1** and **7-2** show the NO, NO_2, and NO_x concentration trends of as-prepared samples, STC1 – STC6, S-TiO_2, NP400, and g-CN, under light (UV/visible) irradiance. Moreover, the detailed results of total NO and NO_x removal along with NO_2 generation during 1 h of light irradiation are tabulated in **Table 7-1** (UV light) and **7-2** (visible light). For each experiment, 7.58 ± 0.069 µmol NO was inserted in the reactor, and irrespective of the light types (UV/visible), both S-TiO_2 and NP400 showed similar NO removal profile as illuminated in **Fig. 7-1(a)** and **(h)**, respectively. For all the samples examined, the NO and NO_x concentrations initiated to decrease instantly at the light irradiance (UV/visible) and reached the minimum concentration of NO and NO_x within 5 min of light irradiation. Negligible response lag was witnessed at the beginning and the end of the light irradiation due to the instrument's default factory setup. The rapid degradation of NO at the starting of the light irradiance could be attributed to the dual effects of adsorption and photooxidation on the photocatalytic sites of the respective samples. Later, due to saturation of the photocatalytic sites with the protoxidized by-products (i.e., NO_2, NO_3^-), the NO removal efficiencies tend to decrease gradually (Park et al., 2014). **Fig. 7-1** and **7-2** show that the gradual decrease in NO and NO_x removal with irradiation time is dominant in S-TiO_2 and NP400. Interestingly, compared to anatase titania (S-TiO_2 and NP400), the as-prepared samples (STC1-STC6) and g-CN showed stable NO and NO_x

removal within 1 h of irradiation (UV/visible), which could be the indication of superior photoactivity.

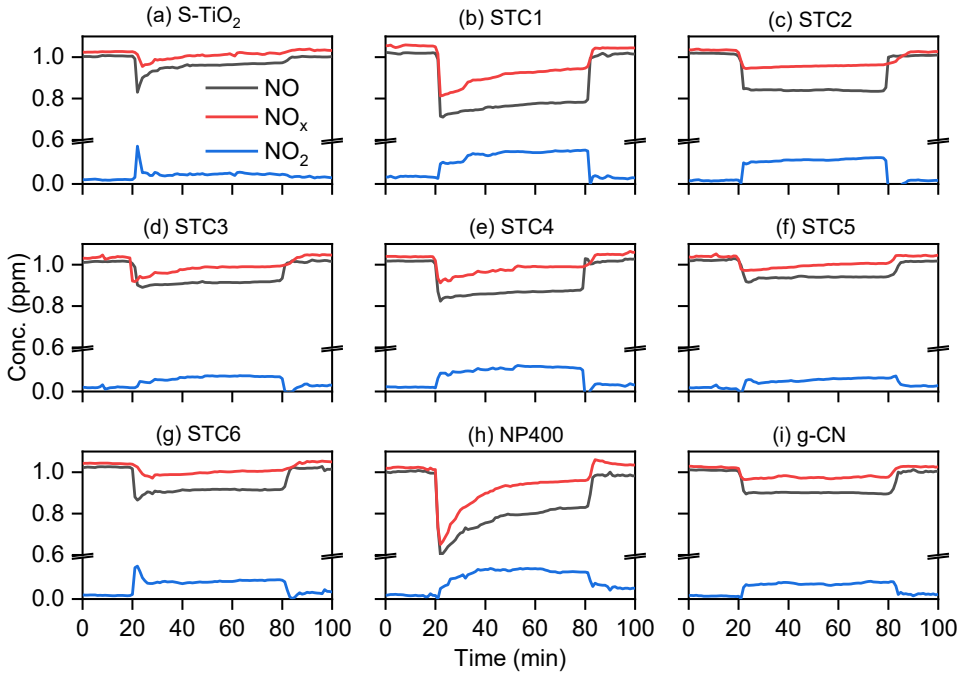

Fig. 7-1. NO_x removal profile for S-TiO_2, STC1 – STC4, and g-CN, under UV irradiation.

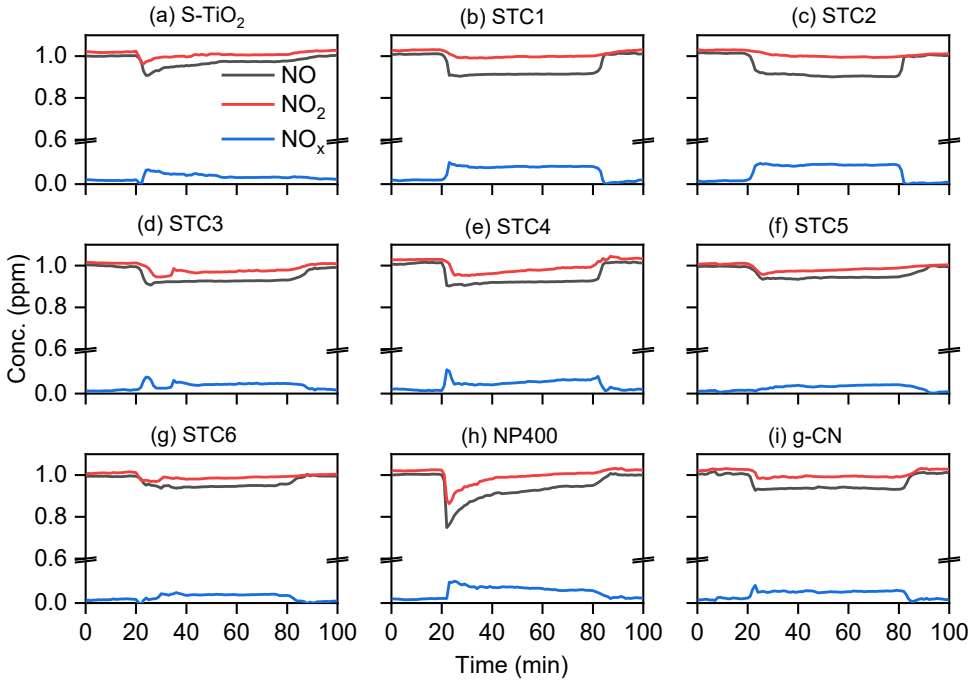

Fig. 7-2. NOx removal profile for S-TiO2, STC1 – STC4, and g-CN, under visible light irradiation.

Table 7-1. Detailed NO_x oxidation data under UV irradiation for the prepared composites.

Sample	NO_{input}	$NO_{removal}$	Removal	$NO_{2,input}$	$NO_{2,generation}$	Generation	$NO_{x,input}$	$NO_{x,removal}$	Removal	NO_3^- Selectivity
	µmol	µmol	%	µmol	µmol	%	µmol	µmol	%	%
S-TiO_2	7.52	0.38	5.02	0.19	0.19	2.57	7.71	0.18	2.45	41.90
STC1	7.63	1.93	25.25	0.24	0.84	10.99	7.87	1.09	14.26	48.80
STC2	7.58	1.29	17.03	0.10	0.77	10.10	7.68	0.53	6.92	56.48
STC3	7.58	0.76	9.99	0.17	0.33	4.29	7.75	0.43	5.66	40.63
STC4	7.64	1.16	15.18	0.18	0.61	7.98	7.82	0.55	7.20	56.66
STC5	7.64	0.61	7.96	0.16	0.26	3.43	7.79	0.34	4.50	47.43
STC6	7.65	0.82	10.74	0.17	0.47	6.12	7.82	0.34	4.50	56.53
NP400	7.44	1.70	22.90	0.13	0.77	10.41	7.71	1.03	13.85	60.49
g-CN	7.55	0.81	10.67	0.13	0.42	5.57	7.69	0.39	5.11	47.87

Table 7-2. Detailed NO_x oxidation data under visible light irradiation for the prepared composites.

Sample	NO_{input}	$NO_{removal}$	Removal	$NO_{2,input}$	$NO_{2,generation}$	Generation	$NO_{x,input}$	$NO_{x,removal}$	Removal	NO_3^- Selectivity
	µmol	µmol	%	µmol	µmol	%	µmol	µmol	%	%
S-TiO_2	7.50	0.30	4.05	0.13	0.17	2.30	7.63	0.13	1.75	46.20
STC1	7.57	0.72	9.58	0.14	0.49	6.49	7.70	0.23	3.09	43.21
STC2	7.55	0.74	9.82	0.09	0.59	7.86	7.64	0.15	2.03	32.25

Sample	NO_{input}	$NO_{removal}$	Removal	$NO_{2,input}$	$NO_{2,generation}$	Generation	$NO_{x,input}$	$NO_{x,removal}$	Removal	NO_3^- Selectivity
	µmol	µmol	%	µmol	µmol	%	µmol	µmol	%	%
STC3	7.47	0.53	7.10	0.11	0.23	3.07	7.58	0.30	4.03	20.67
STC4	7.58	0.69	9.16	0.14	0.28	3.75	7.72	0.41	5.40	56.76
STC5	7.46	0.38	5.04	0.08	0.18	2.41	7.54	0.20	2.66	58.95
STC6	7.45	0.35	4.74	0.09	0.19	2.55	7.54	0.16	2.19	52.78
NP400	7.51	0.70	9.37	0.16	0.38	5.08	7.66	0.31	4.14	44.21
g-CN1	7.54	0.53	7.01	0.14	0.27	3.61	7.68	0.26	3.41	48.67

Fig. 7-3(a) and **(b)** reveal the corresponding NO removal, NO_2 generation, and NO_3^- selectivity of the as-synthesized samples along with S-TiO_2, NP400, and g-CN under UV and visible light, respectively. The S-TiO_2 prepared from flocculation of dye wastewater showed very limited photoactivity under any kind of light irradiation, whether UV or visible light, which is in contrast with some related studies (El Saliby et al., 2012). Under 1 h of UV and visible light irradiation, S-TiO_2 only removed 0.378 µmol and 0.303 µmol of NO, respectively (see **Table 7-1** and **7-2**), which is around 5% of the total NO inserted in the reactor. On the other hand, with the same setup, NP400 showed around 22.89% and 9.36% NO removal under UV and visible light, respectively. As **Fig. 7-3(a)** illustrates, the prepared samples under UV irradiation showed significant improvement in NO removal. STC1 showed the maximum NO removal of 25.25%, which is around 5 times higher compared to S-TiO_2. During the synthesis of the sample STC1, the precursor mix contained around 33.33% of melamine, and in the following samples, the melamine contents were increased as 50%, 66.67%, 75%, 80%, and 83.33%. With increased melamine content in the precursor mix, at 50% melamine content, the NO and NO_x removal get reduced to 17.03% and 6.92%, respectively. Later, at 75% melamine content, the sample showed enhanced NO_x removal of 7.82%, and a further increase in melamine content within the precursor showed a consecutive reduction in NO and NO_x removal. One dominant trait that has been observed is, with increased melamine proportion in the precursor mix, the NO_3^- selectivity of the samples showed an increasing trend and begun to decline while the melamine proportion exceeded 75% of the initial mix.

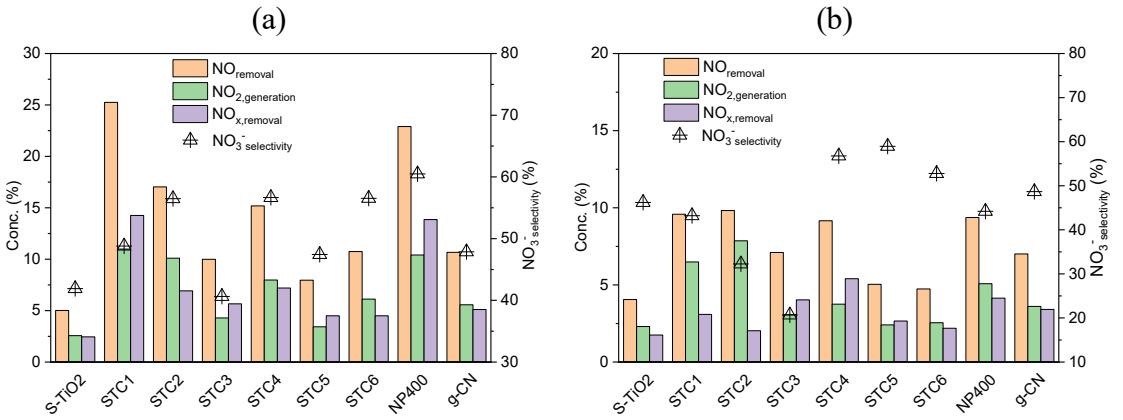

Fig. 7-3. NO_x removal and NO_3^-selectivity of the as-prepared samples under 1 h of (a) UV light, and (b) visible light irradiation.

Fig. 7-3(b) shows that STC4 achieved the maximum NO_x removal of 5.4% under visible light due to superior NO_3^- selectivity of 56.76%. As illustrated in **Table 7-2**, in total, 7.63

± 0.067 µmol NO_x was inserted in the reactor under visible light irradiation of 1 h for each sample. At the end of 1h of visible light irradiation, STC4 was found to remove around 0.41 µmol of NO_x, whereas S-TiO_2, NP400, and g-CN removed around 0.13 µmol, 0.31 µmol, and 0.25 µmol, respectively. For NO_3^- selectivity under visible light, a similar pattern was observed as photooxidation under UV light. Initially, selectivity increased with the increase in the precursor mix's melamine content, and after 80%, it started to decrease.

7.4 Morphological attributes

7.4.1 XRD and BET analysis

XRD was conducted to identify the phase configuration of the synthesized samples, and the patterns were compared with commercially available NP400 and laboratory prepared g-CN and S-TiO_2. **Fig. 7-4(b)** shows that the prepared S-TiO_2 using dye wastewater is mainly of anatase form. The corresponding anatase crystal planes that were found are, (101), (103), (004), (112), (200), (105), (211), (204), (116), (220), (215), and (224) (JCPDS No. 21-1272) (Xia et al., 2019; Yu et al., 2020; X. Zhang et al., 2019). On the other hand, the g-CN prepared in this study showed two characteristic peaks around 2θ of 13.04° and 27.58°, representing the spacing between the adjacent lattice planes of 0.693 and 0.324 nm respectively (Wang et al., 2015). The dominant crystal plans observed in g-CN are depicted in **Fig. 7-4(b)**, where plane (100) corresponds to the N-bridged repetition of $C_6H_3N_7$ units and (600) explains the inter-planer assembling of the conjugated aromatic system (Dong et al., 2015).

From **Fig. 7-4(a)**, it is obvious that the synthesized S-TiO_2/g-CN heterojunction preserved the anatase planes of S-TiO_2, and no significant shift in 2θ was observed. Additionally, the peaks for anatase planes remained intact irrespective of the variations in weight ratios of S-TiO_2 and melamine in the precursor mix, which are in coherence with relevant studies (Tan et al., 2018; Troppová et al., 2018; Zhenyu Wang et al., 2018). At lower melamine content of almost up to 50% of the precursor mix, no characteristic XRD pattern of g-CN was found within the prepared samples. Presumably, this could be due to the formation of negligible amounts of g-CN in the samples. However, once the melamine proportion was twice than that of S-TiO_2 in the precursor mix, an obvious peak around 27.58° (2θ) depicted the presence of characteristics (002) plane of g-CN. With a further increase in melamine content during the synthesis of the samples, the peak around 27.58°

became wider and steeper. The enhancement in peak intensity for g-CN in the consecutive samples (STC1 to STC6) could be attributed to the better crystallinity (Dong et al., 2015).

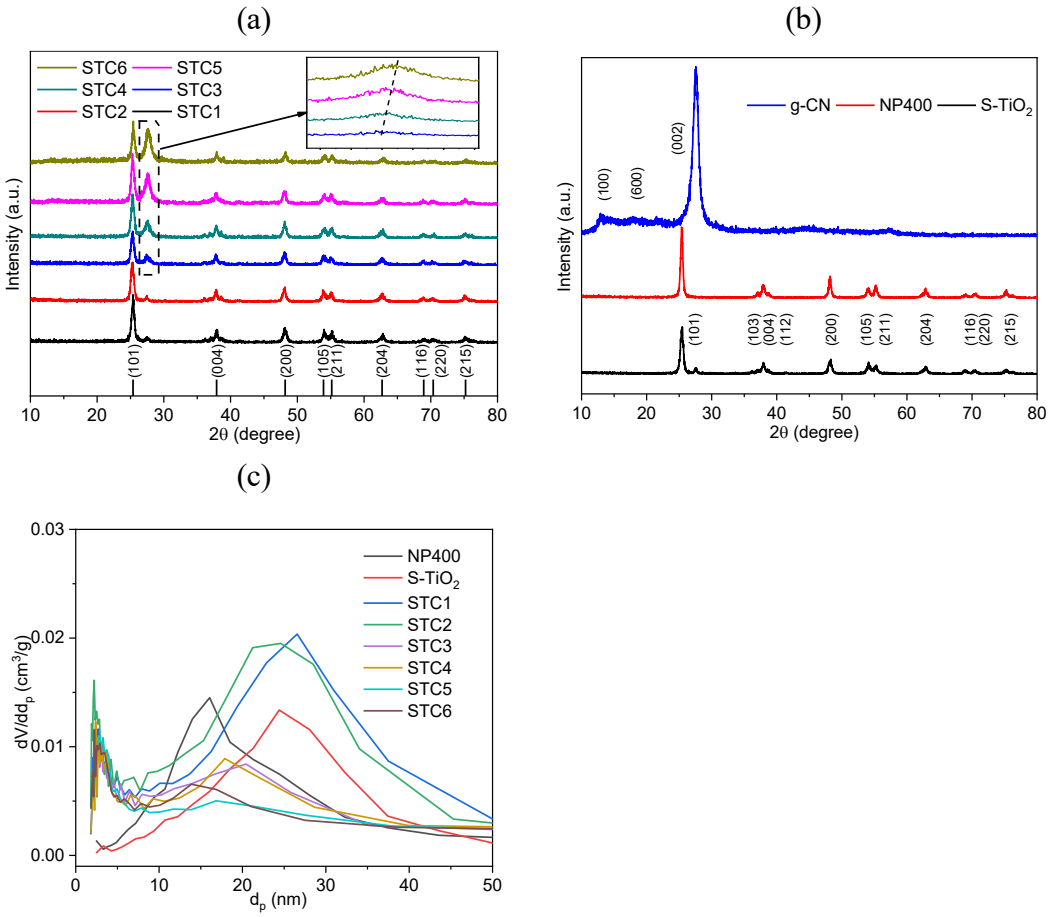

Fig. 7-4. XRD images of the (a) as-prepared samples STC1 to STC6, and (b) NP400, g-CN and S-TiO_2; (c) evaluated pore size distribution (BJH adsorption) of the as-prepared samples.

Additionally, with the increased content of g-CN in the samples, the (002) lattice plane of g-CN tends to shift slightly toward high 2θ value, due to the reduced gallery distance of the basic aromatic sheets in g-CN. Moreover, due to slight increase in the total content of the precursor mix, there could be a slight increase in the internal temperature during the synthesis, which could be the reason behind the slight shift of the (002) plane of the composited g-CN (Dong et al., 2015; Wang et al., 2015). More melamine in the precursor mix will also generate more ammonia, HCN and CN_x gases which render the atmosphere in furnace were more reductive. Compared to standalone calcination of melamine, the calcination of S-TiO_2 mixed melamine tends to destroy the in-plane periodic $C_6H_3N_7$ units; hence, the lattice plane of g-CN around 13.04° was diminished in the as-prepared samples (Kočí et al., 2017). From the above discussion and by using **Fig. 7-4**, it is evident that the

prepared samples exhibited superposition of the characteristics XRD peaks of both S-TiO_2 and g-CN. Hence, it can be presumed that during the calcination of the dry mix of S-TiO_2 and melamine, g-CN was assembled on the facade of S-TiO_2, without affecting the crystal lattice arrangement of either of the components.

Moreover, to evaluate the effects on crystal size of the as-synthesized samples, scherrer's equation (Giannakopoulou et al., 2017; Papailias et al., 2017; Song et al., 2016) was utilized at the dominant plane (101) of the anatase TiO_2, and the results are reported in **Table 7-3**.

$$= \frac{K\lambda}{FWHM \times \cos\theta} \qquad (7\text{-}1)$$

Here, represents the crystal size, while K, λ, FWHM, and θ are the Scherrer's constant, wavelength, full width at half maxima, and Bragg's angle. From the crystal sizes reported in **Table 7-3**, incorporation of g-CN with S-TiO_2 did not show any remarkable changes. The average crystal size of the synthesized samples was determined as 15.42 ± 0.66 nm, which was similar to the pristine S-TiO_2 (15.40 nm).

The effective surface area (S_{BET}) and pore size (d_p) distribution of the as-prepared samples and pristine S-TiO_2 were determined by utilizing N_2 physisorption isotherms. **Table 7-3** depicted the respective S_{BET} values and pore volumes (V_T) of the as-synthesized samples. Furthermore, the d_p distribution curves evaluated using BJH technique were incorporated in **Fig. 7-4(c)**. S-TiO_2 showed a comparable surface area to commercially available NP400. From the S_{BET} values tabulated in **Table 7-3**, a declining trend was observed with the increase of g-CN content in the synthesized samples. Besides, from **Fig. 7-4(c)** it is evident that both S-TiO_2 and NP400 showed mesoporous traits, where integration of g-CN in the samples showed the combination of mesoporous and microporous nature (pore size distribution of STC1 – STC4).

Table 7-3. Estimated FWHM and crystal size of the samples along the dominant anatase (101) plan of TiO_2, effective surface area (S_{BET}), and total pore volume (V_T).

ID	**2θ (degree)**	**FWHM**	**Crystal size (nm)**	**S_{BET} (m^2/g)**	**V_T (cm^3/g)**
S-TiO_2	25.41	0.529	15.40	51.69	0.31
STC1	25.31	0.475	16.23	45.45	0.31

ID	2θ (degree)	FWHM	Crystal size (nm)	S_{BET} (m^2/g)	V_T (cm^3/g)
STC2	25.28	0.548	14.87	52.33	0.31
STC3	25.31	0.533	15.29	35.0	0.29
STC4	25.33	0.501	16.26	33.69	0.26
STC5	25.34	0.550	14.80	30.47	0.23
STC6	25.44	0.540	15.08	30.40	0.23
NP400	25.40	0.370	21.87	66.65	0.34

7.4.2 FT-IR spectra

To further validate the occurrence of S-TiO_2 and g-CN in the as-synthesized samples, Fourier-transform infrared spectroscopy (FT-IR) analysis was conducted, and the findings were compared with individual FT-IR of S-TiO_2, NP400, and g-CN. The FT-IR spectra of the synthesized samples STC1 – STC6 are illustrated in **Fig. 7-5(a)**, while **Fig. 7-5(b)** depicted the FT-IR patterns of S-TiO_2, NP400, and g-CN. For S-TiO_2 and NP400, the broad absorption peak across 400 – 700 cm^{-1} (**Fig. 7-5(b)**) can be allocated to the Ti-O and Ti-O-Ti stretching forms (Huan Liu et al., 2019). Additionally, the broad absorption band around 3000 – 3700 cm^{-1} can be ascribed to the O-H stretching of the adsorbed H_2O on the samples (Kočí et al., 2017; Papailias et al., 2017). The prepared g-CN showed FT-IR peaks around 808.24 cm^{-1} due to the bending mode of skeletal triazine cycles (B. Zhang et al., 2018). For g-CN, a series of absorption bands were found within the wavelength range of 1200 – 1600 cm^{-1}, as shown in **Fig. 7-5(b)**, which are mainly attributed to the C-N stretching of the aromatic part (Troppová et al., 2018). Besides, the wide absorption band within 3000 – 3500 cm^{-1} could also be due to the vibration of N-H from the remaining NH_2 groups (Du et al., 2020).

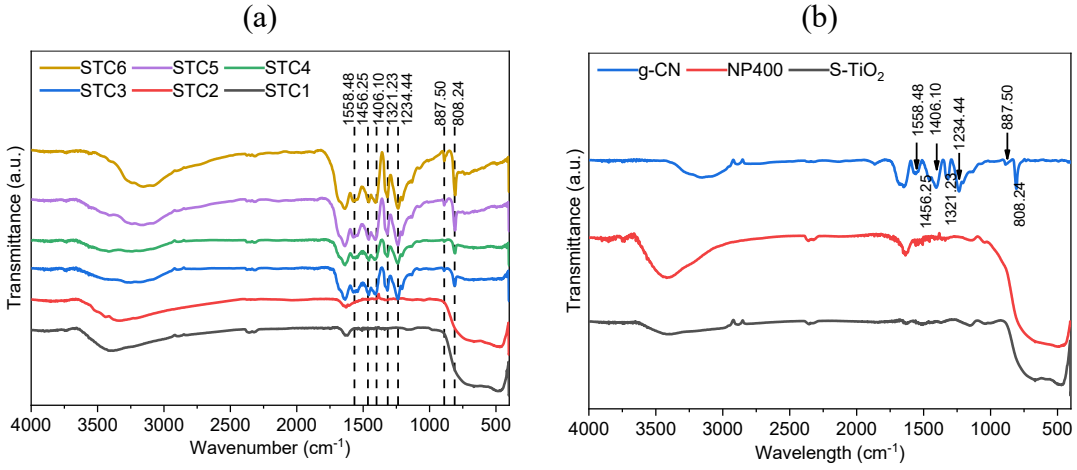

Fig. 7-5. FT-IR patterns of the (a) as-prepared samples STC1 to STC6, and (b) NP400, g-CN and S-TiO_2.

From **Fig. 7-5(a)**, STC1 and STC2 only showed the characteristics absorption bands for Ti-O and Ti-O-Ti stretching modes, whereas presence of g-CN was not confirmed which corresponds well with the obtained XRD data. On the other hand, all other samples starting from STC3 to STC6 evidently showed the absorption bands for the aromatic C-N stretching and anatase TiO_2. Additionally, with increased g-CN content in the synthesized samples, the comparative intensity of the characteristics FT-IR peaks for g-CN became broader and steeper. Another interesting finding from assessing the FT-IR spectra of the prepared samples was a slight shift of the wide peak across 400 – 700 cm^{-1} towards greater wavenumber (see **Fig. 7-5(a)**), which is in coherence with relevant composite studies (Giannakopoulou et al., 2017; Song et al., 2016). Presumably, the presence of g-CN in the sample modified the chemical environment on the surface of S-TiO_2, and relevant studies confirmed that interaction between the molecular orbitals of the separate components happens due to close heterojunction (Song et al., 2016). Hence, the shift in the Ti-O-Ti stretching modes of the as-synthesized samples may infer robust heterojunction at the edge of S-TiO_2 and g-CN.

7.4.3 Electron Microscopy

To authenticate the compositions and morphology of the as-prepared samples, scanning electron microscope (SEM) was conducted, and the SEM images of STC1 to STC6 are illustrated in **Fig. 7-6(a – f)**. Additionally, for comparison purposes, SEM images of S-TiO_2 and g-CN are incorporated in **Fig. 7-6(g) and (h)**, respectively. As a representative of the as-prepared samples transmission electron microscopy (TEM) image of STC4 is incorporated in **Fig. 7-8** at varying magnifications. The prepared g-CN exhibited the presence of a 2D layer sheet structure together with a fairly smooth and flat facade, where the S-TiO_2 prepared from wastewater was found as irregular structure (**Fig. 7-8(a)**). From **Fig. 7-7**, based on the energy-dispersive X-ray spectroscopy (EDX) results, S-TiO_2 showed the presence of the C atom (8.50%), which is in coherence with former relevant research (Shon et al., 2007a). In a number of previous studies, recovered TiO_2 from wastewater sludge inferred the presence of doped C in the as-prepared samples, and the presence of prevailing organic compounds was concluded as the source of the doped C atoms (H. Shon et al., 2009a; Shon et al., 2007a).

By observing the SEM image of STC1 to STC6 (**Fig. 7-6**), it is clear that the incorporation of melamine in the precursor mix reduced the agglomeration of S-TiO_2 NPs and more uniform dispersion was observed (Giannakopoulou et al., 2017). Accordingly, based on the EDX result presented in **Fig. 7-7**, the presence of C, N, O, and Ti atoms was confirmed in the samples, and with increased melamine content during synthesis, the proportion of g-CN tends to increase. Based on the EDX and SEM results, no g-CN were formed in the STC1 and STC2; however, the presence of C atoms was observed in the as-prepared samples. Initially, by comparing S-TiO_2 and STC1, the atomic proportion of C was reduced from 8.50% to 5%. Further increase of melamine in STC2 enhanced the C content (7.37%) of the sample.

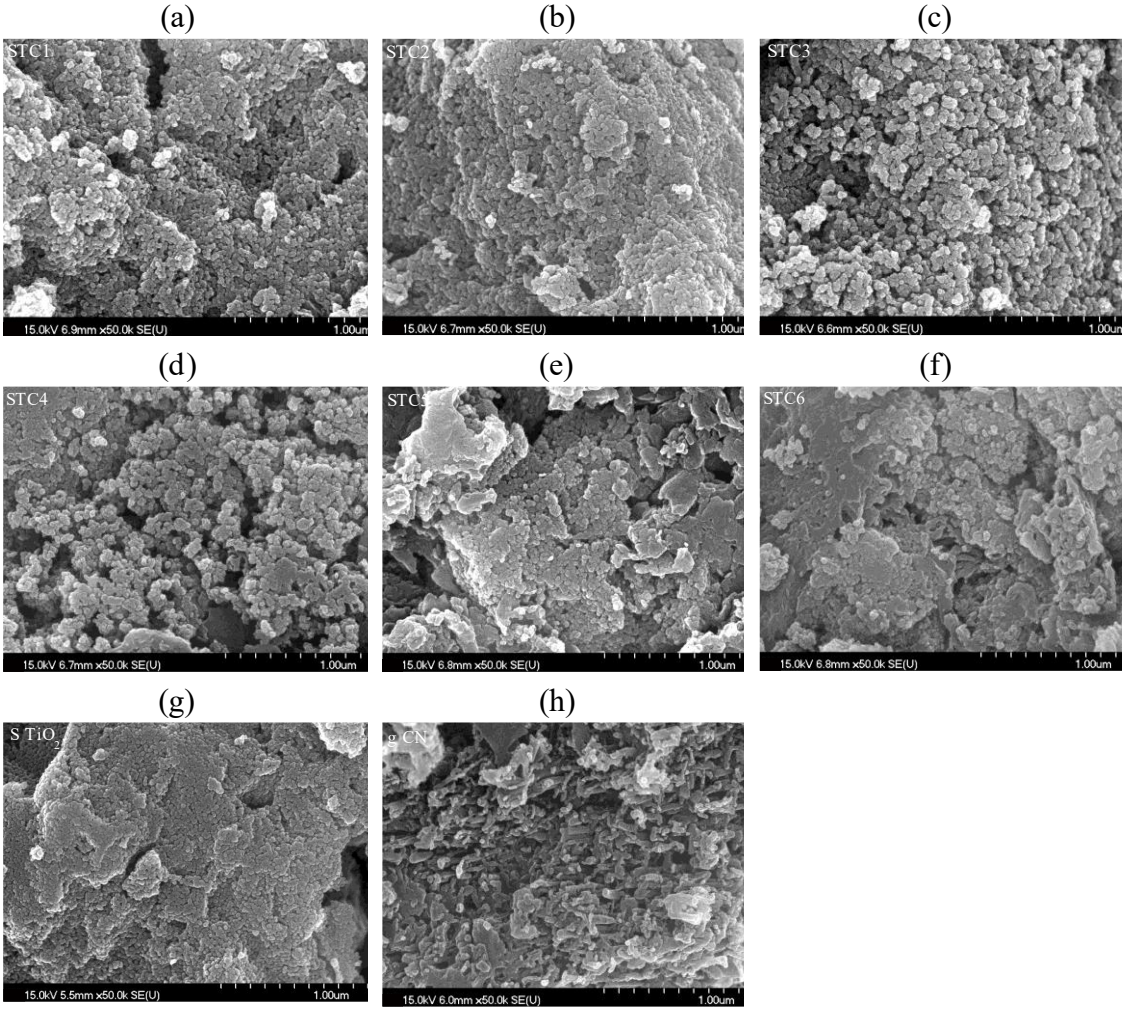

Fig. 7-6. SEM images of (a-f) as-prepared composites STC1 to STC6, (g) S-TiO_2, and (h) g-CN.

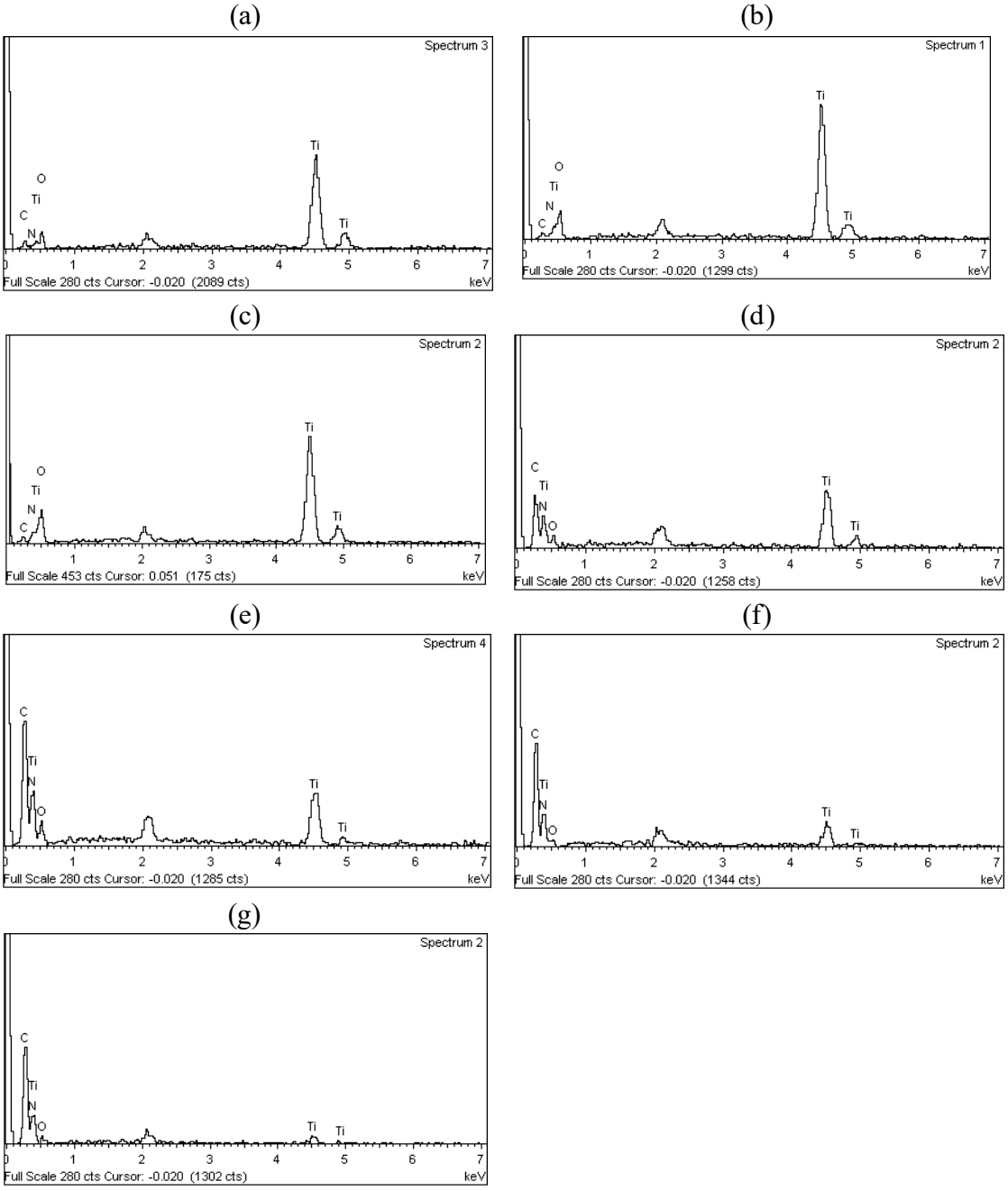

Fig. 7-7. EDX results of S-TiO_2 (a) and STC1 – STC6 (b – g).

In STC3, i.e., in the initial mix while the melamine content was 150% of S-TiO_2, the occurrence of g-CN was observed in the TEM and EDX (**Fig. 7-7**) results. As shown in **Fig. 7-8**, the TEM of STC4, depicted the presence of 2D sheet like g-CN along with a considerable amount of somewhat spaced sphere-shaped NPs (S-TiO_2). Moreover, in the TEM image of STC4, transparent lattice fringes at a distance of 0.352 and 0.238 nm were detected, which can be assigned to the anatase lattice planes (101) and (004), respectively (Wei et al., 2016; Zhang et al., 2014).

The TEM image of STC4 (**Fig. 7-8**) and SEM image of STC3-STC6 (**Fig. 7-6**) explicitly showed the successful grafting of S-TiO_2 over the g-CN nanosheets. In the as-prepared samples, S-TiO_2 NPs appear denser and more compact due to the excellent heterojunction effect and found beneficial for the transfer of photogenerated e^-/h^+ pairs. The TEM image shows laminar structure of g-CN, loaded with dense and uniformly distributed S-TiO_2 NPs without any apparent accumulation, demonstrating a strong fusion between S-TiO_2 and g-CN.

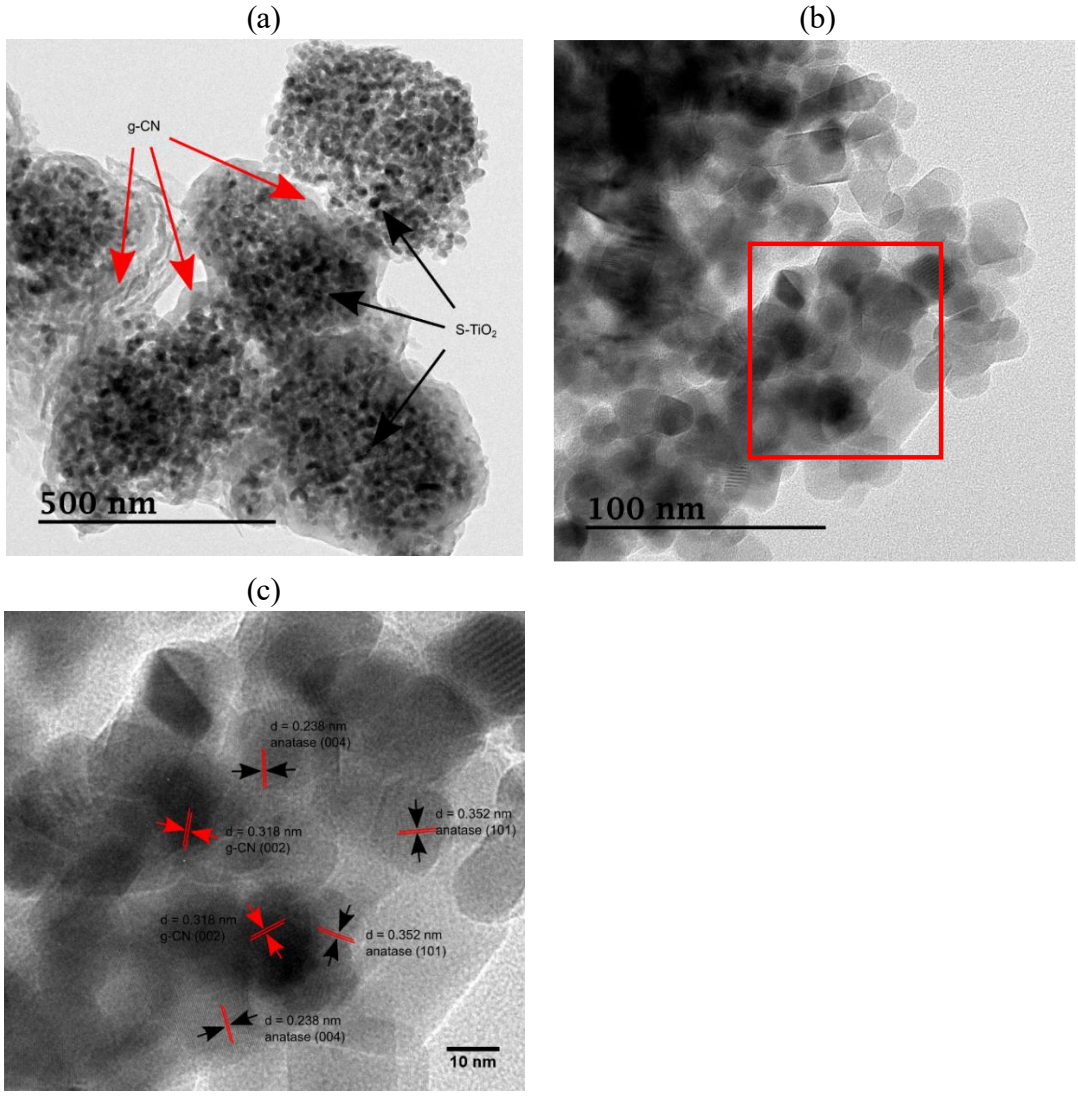

Fig. 7-8. TEM images of the as-prepared STC4 at varying scale ((a) 500 nm, (b) 100 nm, and (c) 10 nm) showing the presence of S-TiO_2 and g-CN.

7.4.4 XPS spectra

To have an in-depth idea concerning the oxidation states and the chemical compositions of the prevailing components in the as-synthesized samples, X-ray photoelectron spectroscopy (XPS) analysis was conducted. **Fig. 7-9** illuminated the wide-angle XPS

survey spectra of the as-synthesized samples. From the **Fig. 7-9**, the sharp photoelectron peaks for C 1s, N 1s, Ti 2p, and O 1s are clearly visible across the binding strengths of 286, 400, 458, and 530 eV (K. Li et al., 2015; Huan Liu et al., 2019). Based on the survey spectra, peaks for Ti 2p and O 1s has significantly reduced in the samples STC5 and STC6. Besides, the prepared g-CN revealed the characteristics C 1s and N 1s peaks on the wide-angle survey scan.

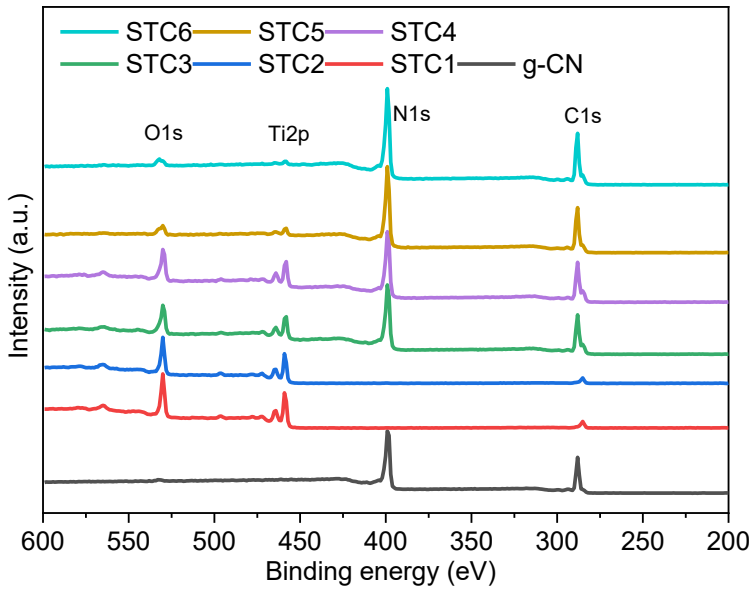

Fig. 7-9. Wide band XPS spectra of STC1-STC6 and g-CN.

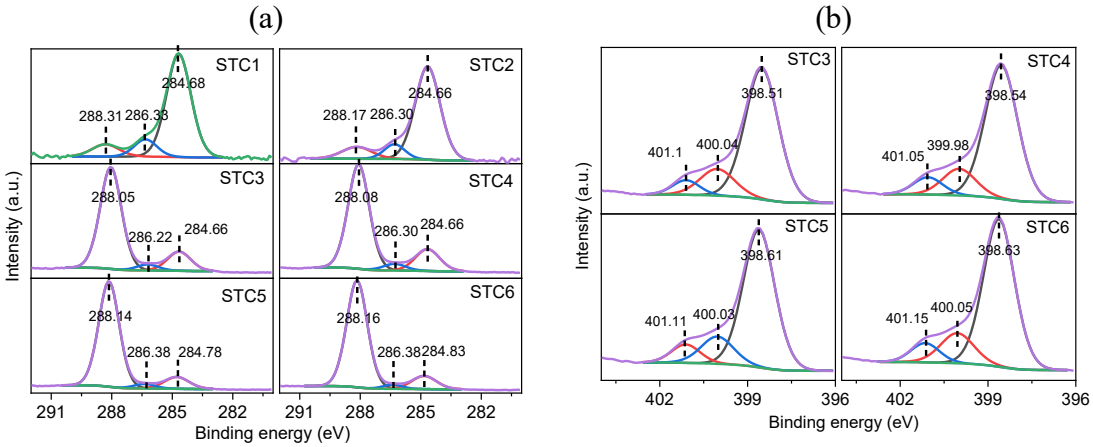

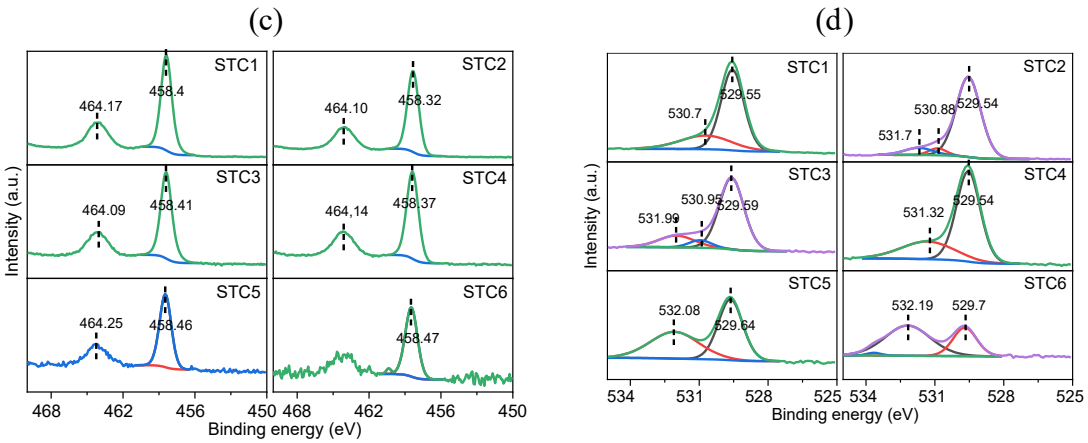

Fig. 7-10. High resolution survey scan of (a) C 1s, (b) N 1s, (c) Ti 2p, and (d) O 1s for the synthesized STC1 to STC6.

Fig. 7-10(a – d) shows the high resolution survey spectra C 1s, N 1s, Ti 2p, and O 1s, respectively, for the as-prepared samples STC1 to STC6. Besides, the peak positions, along with the atomic proportions of the narrow scans for the corresponding samples, are tabulated in **Table 7-4**. Lorentz peak fitting was utilized for the deconvolution of the narrow scan XPS peaks. Based on the FT-IR and XRD analysis, the presence of g-CN was not found in STC1 and STC2; hence the deconvoluted 3 C 1s peaks shown in **7-10(a)** could be attributed to adventitious carbon as Sp^2 hybridized C-C (284.70 eV), C-O-C (286.30 eV) and O-C=O (288.20 eV) bond present as defects (Zhou et al., 2014). While for the prepared g-CN, STC3, STC4, STC5, and STC6, the dominant C 1s narrow scan peak was found around ~288.10 eV, which can be assigned to N-C=N_2 coordination and characteristics peak for g-CN (H. Liu et al., 2019; Thomas et al., 2008). Additionally, the absence of no visible peak for C-Ti confirmed that there were no chemical reactions between S-TiO_2 and g-CN, rather successful heterojunction was prepared.

Except for STC1 and STC2, from the narrow survey N 1s spectra of the as-synthesized samples dominant peak for triazine rings, i.e., sp^2 hybridized C=N-C was found around ~398.54 eV (Caudillo-Flores et al., 2019). Moreover, peaks for tertiary N-$(C)_3$ and N-H group were found around ~399.98 and 401.05 eV(Li et al., 2019; Huan Liu et al., 2019). Moreover, the peak positions were in coherence with the laboratory-made g-CN (**Table 7-4**). In STC1 and STC2, characteristic peaks for g-CN were absent, and very low concentration of N atoms was found in doped condition, which was 0.8% and 0.7%, respectively, which could be the reason for enhanced NO_x removal beneath UV light. The O 1s spectra of the as-prepared samples could mainly be fitted around 529.55 and 530.7

eV, which clearly confirms the presence of lattice O^{2-} and O_2^- ions/OH^- groups respectively (Yu Huang et al., 2019).With the increase of g-CN in the prepared samples, the peak around 530.7 eV tends to shift towards higher binding energy, which inferred that g-CN firmly combines with the oxygen groups presented on the facade of S-TiO_2. **Fig. 7-10(b)** indicates the Ti 2p bands of the as-prepared samples STC1 to STC6. Sharp peaks around 458.66 and 464.41 eV has been observed in the samples, which are characteristic peaks of Ti 2p3/2 and Ti 2p1/2 and confirms that Ti is present as Ti^{4+} species (Song et al., 2016). Compared to S-TiO_2, with increased amounts of g-CN in the samples, a negative shift was observed in the prepared samples (**Table 7-4**). This phenomenon can be attributed to the close electronic interaction between the used S-TiO_2 and g-CN, which confirms compact sample formation. Additionally, the negative shift could be due to the increased electron density on Ti from the sample formation.

Table 7-4. Narrow scan peaks positions and atomic % of C 1s, N 1s, Ti 2p, and O 1s, for the prepared composites, S-TiO_2 and g-CN.

	S-TiO_2		**STC1**		**STC2**		**STC3**		**STC4**		**STC5**		**STC6**		**g-CN**	
Narrow scan	**Peak (eV)**	**At. (%)**	**Peak (eV)**	**At. (%)**	**Peak (eV)**	**At. (%)**	**Peak (eV)**	**At. (%)**	**Peak (eV)**	**At. (%)**	**Peak (eV)**	**At. (%)**	**Peak (eV)**	**At. (%)**	**Peak (eV)**	**At. (%)**
C1s A	284.6	4.23	284.68	19.03	284.66	19.95	288.05	30.29	288.08	29.45	288.14	35.23	288.16	36.16	288.09	37.87
C1s B	288.8	4.21	288.31	2.5	288.17	3.07	284.66	6.19	284.66	7.03	284.78	4.73	284.83	5.29	284.79	3.7
C1s C	291.37	4.2	286.33	2.96	286.3	2.62	286.22	1.79	286.3	2	286.38	1.58	286.4	1.3	286.39	0.86
O1s A	533.13	29.99	529.55	41.81	529.54	48.99	529.59	10.15	529.54	10.08	529.64	2.97	532.19	2.45	532.22	1.16
O1s B	534.3	14.42	530.7	16.11	530.88	3.04	531.99	2.44	531.32	4.42	532.08	2.61	529.7	1.21	529.61	0.14
O1s C	532.09	15.24			531.7	5.15	530.95	0.98					533.66	0.07		
O1s D	535.38	7.51														
N1s A			399.58	0.8	399.14	0.7	398.51	34.2	398.54	32.81	398.61	39.08	398.63	39.64	398.54	41.61
N1s B							400.04	7.33	399.98	6.66	401.11	4.73	400.05	8.67	399.94	9.55
N1s C							401.1	3.11	401.05	3.85	400.03	8	401.15	4.73	401.05	5.11
Ti2p A	458.66	11.92	464.17	3.86	458.32	16.45	464.09	1.2	458.37	3.69	458.46	1.05	458.47	0.47		
Ti2p B	464.41	8.29	458.4	12.93	464.10	0.05	458.41	2.3	464.14	0.01	464.25					

7.5 Optical traits and photocatalytic mechanism

Based on the detailed morphological and chemical characterizations, STC3, STC4, STC5, and STC6 were the successful S-TiO_2/g-CN heterojunctions. Additionally, among the aforementioned samples, maximum photoactivity was observed by STC4 under both UV and visible light irradiance (see **Fig. 7-3**). Therefore, to further evaluate the photooxidation mechanism of STC4, PL analysis was performed, and the respective spectrum was compared with PL spectra of S-TiO_2 and g-CN (**Fig. 7-11(a)**). It is well established that the PL spectra of the semiconductors can infer valuable insights on the rate of photoinduced charge separation, while irradiated with light.

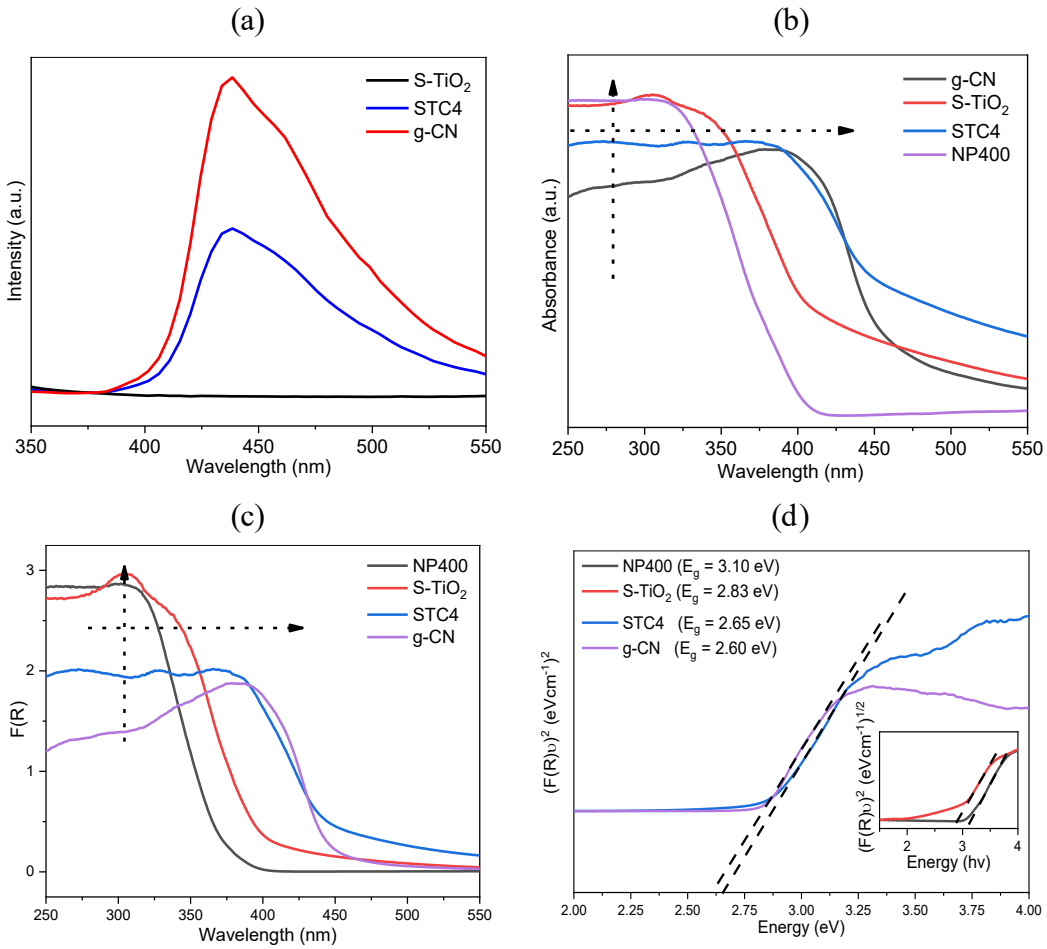

Fig. 7-11. (a) PL spectra, (b) UV-vis DRS (absorbance vs. wavelength), (c) UV-vis DRS (F(R) vs. wavelength), (d) converted Kubelka-Munk function vs. energy of absorbed light of STC4, S-TiO_2, g-CN, and NP400.

The prepared g-CN displayed a strong quasi-asymmetric PL spectrum, and the maximum peak was found around ~400 nm. This peak corresponds to the recombination of photoinduced e^-/h^+ pairs generated within the g-CN (Wang et al., 2013; J. Yu et al., 2013).

Based on **Fig. 7-11(a)**, compared to g-CN, STC4 showed much lower PL intensity at a similar peak position. Normally, lower PL intensity means a lower rate of recombination (Troppová et al., 2018). Moreover, the minimal recombination rate of S-TiO_2 is understandable as in the visible light spectrum, light absorption by S-TiO_2 was also minimal.

Additionally, for the determination of the optical energy bandgap (E_g) of STC4, UV-vis DRS was employed, and the light absorption data was reported in the UV-Vis range. By using the extrapolation technique on the modified Kubelka-Munk function, E_g for STC4 was determined, and the findings are depicted in **Fig 7-11(b – d)** (Giannakopoulou et al., 2017). **Fig. 7-11(b)** and **(c)** illustrate the absorbance spectra and the pattern of F(R) function of the as-prepared superior sample (STC4), and the results were compared with g-CN, S-TiO_2, and commercially available NP400. From **Fig. 6(b)**, the prepared STC4 showed superior light absorption in the UV region compared to g-CN hence showed significant improvement in removing NO_x under UV light irradiation. On the other hand, compared to NP400 and S-TiO_2, STC4 showed expanded light absorption beyond the UV range. A superposition of the material's light absorption spectra was observed, which also confirmed successful heterojunction. Similar attributes were reported for the photocatalysts synthesized by heterojunction of commercially available titania and nitrogen enriched precursors like (melamine, urea etc.) (Papailias et al., 2017; Song et al., 2016). Additionally, **Fig. 7-11(d)** shows the $(F(R)h\nu)^n$ (n = 1/2 and 2) vs. hν graph of the samples, and the energy bandgaps were determined through the extrapolation of the corresponding graphs. The energy bandgaps were determined as 2.60, 2.65, 2.83, and 3.10 eV for g-CN, STC4, S-TiO_2, and NP400, respectively. Besides, the CB and VB edge of S-TiO_2 and g-CN was estimated by using the following equations (Zhou et al., 2019),

$$E_{CB} = E_{VB} - E_g \qquad (7\text{-}2)$$

$$E_{VB} = X - E_0 + 0.5\, E_g \qquad (7\text{-}3)$$

Here, E_{CB} and E_{VB} represents the CB and VB edge of the semiconductor. Additionally, X and E_0 represents the average electronegativity and the energy of a free electrons next to NHE. Based on the relevant studies, for anatase TiO_2 and g-CN, the value of electronegativity can be assigned as 5.81, and 4.64 eV, respectively, and E_0 can be taken as 4.5 eV (Zhou et al., 2019). Hence, the E_{VB} of S-TiO_2 and g-CN can be estimated as +2.73 eV and +1.5 eV, respectively; also, the corresponding E_{CB} will be -0.11 eV and -

1.22 eV. According to the above discussion, the primary factor that has been contributed towards the superior photoactivity of STC4 was the reduced energy bandgap due to the successful formation of heterojunction. Interestingly, despite having reduced S_{BET}, STC4 (33.69 m^2/g) showed extended NO_x oxidation compared to S-TiO_2 (51.69 m^2/g). The possible reason for negligible photoactivity of the prepared S-TiO_2 could be the result of a greater amount of adventitious carbon or Sp2 hybridized defects, as explained with EDX and XPS analysis. On the other hand, the reduced PL intensity of STC4 compared to g-CN confirms the reduced recombination rate; hence, enhanced photoactivity. Based on the assessment of the optical traits of the prepared STC4, the photocatalytic reaction mechanism can be proposed as shown in **Fig. 7-12**.

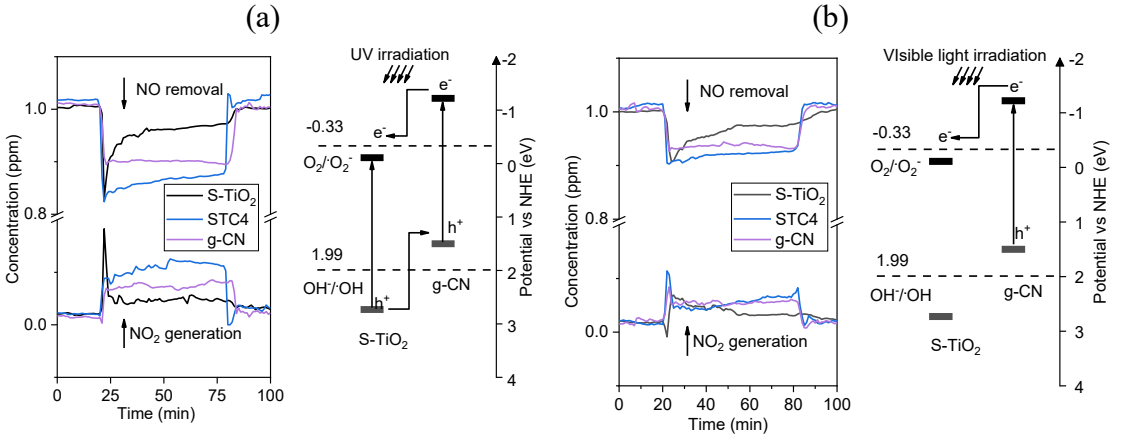

Fig. 7-12. Proposed photooxidation scheme for NO_x using S-TiO_2/g-CN under UV (a) and visible light (b) irradiation.

Under UV irradiance, both S-TiO_2 and g-CN within the as-synthesized sample get excited, and the photoinduced e^- transfer from the VB towards the CB of the respective components (Troppová et al., 2018). Hence, the photoinduced e^-/h^+ pair gets generated, as shown in **Fig 7-12(a)**. Following the charge separation, the e^- generated on the CB of g-CN favors transferring towards the CB of S-TiO_2 due to less negative CB edge (Song et al., 2016). On the other hand, the h^+ generated on the VB of S-TiO_2 migrates towards the less positive VB of g-CN (Papailias et al., 2017). Consequently, the lifetime of the photoinduced e^-/h^+ pairs get increased, leading to superior photoactivity. From the inhibited PL spectrum of the as-synthesized STC4, it is evident that the photoinduced charge separation rate got augmented, leading to an enhanced lifetime of e^-/h^+ pairs (Jinzhu Ma et al., 2016). Later, the photoinduced e^- can readily reduce the adjacent O_2 into $\cdot O_2^-$, while the h^+ on the VB reacts with adsorbed H_2O and generates $\cdot OH$ radicals

(Jinzhu Ma et al., 2016; Papailias et al., 2017). It is well established that the active species $\cdot O_2^-$ and ·OH are the two significant radicals that can promptly oxidize NO_x into more neutral nitrate salts. However, when STC4 was irradiated under visible light, only g-CN became excited, and the photoinduced e^-/h^+ pairs were generated on the respective CB and VB (Jinzhu Ma et al., 2016). Similarly, due to the less negative position of the CB of S-TiO_2, the e^- from g-CN migrates to the S-TiO_2 and restrain the rate of charge recombination. Later, the photoinduced e^-/h^+ pairs can readily produce the active species ($\cdot O_2^-$ and ·OH) for the effective photooxidation of NO_x. Hence, under UV and visible light irradiation the dominant photocatalytic reactions could be as follows,

$$e^- + O_2 \rightarrow .O_2^- \quad (7\text{-}4)$$

$$h^+ + H_2O\ (OH^-) \rightarrow .OH \quad (7\text{-}5)$$

$$.O_2^- + NO \rightarrow NO_3^- \quad (7\text{-}6)$$

$$.OH + NO \rightarrow NO_2 \quad (7\text{-}7)$$

$$NO_2 + .OH \rightarrow NO_3^- \quad (7\text{-}8)$$

One interesting phenomenon observed during the Photooxidation of NO under UV/visible light was an enhancement in the $NO_3^-{}_{selectivity}$ of the prepared heterojunctions compared to the precursor S-TiO_2. Under UV and visible light irradiation, the $NO_3^-{}_{selectivity}$ of S-TiO_2 was reported as 41.90% (see **Table 7-1**) and 42.20% (see **Table 7-2**), respectively, which was substantially increased for STC4 and were found as 56.66% and 56.76%, respectively. Perhaps the incorporation of g-CN played a vital role due to the favorable V_{CB}/V_{VB} position. Compared to S-TiO_2 (-0.11 eV), the CB edge of g-CN (-1.22 eV) was found more negative; hence, the reduction potential of the photogenerated e^- in STC4 was higher to reduce O_2 into $\cdot O_2^-$ (Z. Wang et al., 2016). On the other hand, less positive V_{VB} of g-CN (+1.5 eV) in STC4 reduced the generation rate of ·OH, as the redox potential of OH^-/·OH (2.37 eV) is higher (Hossain et al., 2021; Z. Wang et al., 2016). Therefore, it can be presumed that the $\cdot O_2^-$ played the primary role in the complete photooxidation of NO. Moreover, the enhanced $NO_3^-{}_{selectivity}$ of STC4 depicted that compared to ·OH, the oxidation potential of $\cdot O_2^-$ for NO to NO_3^- conversion is higher, explaining the significant NO_2 generation during standalone use of S-TiO_2. The aforementioned phenomena are coherent with most of the TiO_2/g-CN based atmospheric NO removal studies, where $\cdot O_2^-$

was claimed to be the primary reactive species (Jiang et al., 2018; Jinzhu Ma et al., 2016; Papailias et al., 2017; Z. Wang et al., 2016).

7.6 Conclusion

The objectives of the study were to prepare TiO_2/g-CN samples by utilizing sludge generated TiO_2 and increase the removal of atmospheric NO_x under UV and visible light irradiation. Successful preparation of S-TiO_2/g-CN samples was confirmed through XRD, SEM, TEM, FT-IR, and XPS analysis. Detailed surface characterizations demonstrated that g-CN enhanced the dispersion of S-TiO_2. Moreover, g-CN had negligible impacts on the crystal structure and size of the utilized S-TiO_2 precursor. Among the successfully prepared samples, maximum NO_x removal was reported for STC4, wherein the precursor mix of the melamine content was 3 times higher than the S-TiO_2. UV-vis DRS conducted on STC4 revealed that the energy bandgap was reduced to 2.65 eV from 2.83 eV from S-TiO_2. Hence, the absorption band of STC4 was significantly increased in both UV and visible regions. Besides, PL analysis showed inhibited recombination rate of generated e^-/h^+ pairs, which is favorable to readily generate $\cdot O_2^-$ and $\cdot OH$ radicals for photodegradation of NO_x. Finally, based on the evaluated optical traits, a simplified schematic is proposed for NO_x removal under UV and visible light irradiation. By considering NO_3^- selectivity, the NO_x removal under UV light by S-TiO_2 was reported only 2.45%, which was increased in STC4 and found as 7.2%. Again, under visible light, the NO_x removal of 1.75% by S-TiO_2 was increased to 5.4% by utilizing STC4. However, compared to commercially available NP400, the NO_x removal of STC4 was found inferior, but this synthesis route of TiO_2/g-CN heterojunction has significant potential to promote sustainability through the utilization of unwanted sludge from the water treatment plant and reduction in synthesis cost of the photocatalysts.

CHAPTER 8
Modified hydrothermal route for synthesis of photoactive anatase TiO_2/g-CN nanotubes from sludge generated TiO_2

STATEMENT OF CONTRIBUTION OF AUTHORS

Title of Paper	Modified Hydrothermal Route for Synthesis of Photoactive Anatase TiO_2/g-CN Nanotubes from Sludge Generated TiO_2		
Publication Status	☒Published ☐Accepted for Publication ☐Submitted for Publication		
Publication Details	**Hossain, S. M.**, Park, H., Kang, H.-J., Mun, J. S., Tijing, L., Rhee, I., Kim, J.-H., Jun, Y.-S., & Shon, H. K. (2020). Modified Hydrothermal Route for Synthesis of Photoactive Anatase TiO_2/g-CN Nanotubes from Sludge Generated TiO_2. *Catalysts*, *10*(11). https://doi.org/10.3390/catal10111350		
PRINCIPLE AUTHOR			
Name of Principle Authors	Sayed Mukit Hossain **(Candidate)**		
Contribution	**Conceptualization, Data curation, Formal analysis, Investigation, Methodology, Validation, Writing – original draft.**		
Certification	This paper reports on original research I conducted during my Higher Degree by Research candidature and is not subject to any obligations or contractual agreements with a third party that would constrain its inclusion in this thesis. I am the primary author of this paper.		
Signature	Production Note: Signature removed prior to publication.	Date	30/11/2021
CO-AUTHOR CONTRIBUTIONS			
Name of Co-Author 1	Heeju Park		
Contribution	Data analysis, investigation, and data curation.		
Name of Co-Author 2	Hui-Ju Kang		
Contribution	Data analysis, investigation, and data curation.		
Name of Co-Author 3	Jong Seok Mun		
Contribution	Data analysis, investigation, and data curation.		
Name of Co-Author 4	Leonard Tijing		
Contribution	Writing - review and editing, Supervision.		
Name of Co-Author 5	Inkyu Rhee		
Contribution	Data analysis, investigation, and data curation.		
Name of Co-Author 6	Jong-Ho Kim		
Contribution	Writing - review and editing, Funding acquisition.		
Name of Co-Author 7	Young-Si Jun		
Contribution	Writing - review and editing, Resources.		
Name of Co-Author 8	Ho Kyong Shon		
Contribution	Supervision, Project administration, Resources, Funding acquisition, Validation, Writing - review and editing.		

8 Modified hydrothermal route for synthesis of photoactive anatase TiO_2/g-CN nanotubes from sludge generated TiO_2

8.1 Abstract

Titania nanotube was prepared from sludge generated TiO_2 (S-TNT) through a modified hydrothermal route and successfully composited with graphitic carbon nitride (g-CN) through a simple calcination step. Advanced characterization techniques such as X-ray diffraction, scanning and transmission electron microscopy, infrared spectroscopy, X-ray photoelectron spectroscopy, UV-visible diffuse reflectance spectroscopy, and photoluminescence analysis were utilized to characterize the prepared samples. A significant improvement in morphological and optical bandgap was observed. The effective surface area of the prepared composite increased three folds compared to sludge generated TiO_2. The optical bandgap has been narrowed to 3.00 eV from 3.18 eV in the pristine sludge generated TiO_2 nanotubes. The extent of photoactivity of the prepared composites was investigated through photooxidation of NO_x in a continuous flow reactor. Due to extended light absorption of the as-prepared composite, under visible light, 19.62% of NO removal was observed. On the other hand, under UV irradiation, due to bandgap narrowing, although the light absorption got compromised, the impact on photoactivity was compensated by the increased effective surface area of 153.61 m^2/g. Hence, under UV irradiance, the maximum NO removal was attained as 32.44% after 1 h of light irradiation. The proposed facile method in this study for the heterojunction of S-TNT and g-CN could significantly contribute to resource recovery from water treatment plants and photocatalytic atmospheric pollutant removal.

8.2 Introduction

Over the last few years, wastewater generation has increased at an exponential rate. The increase in the global population, which makes the biggest contribution to the depletion of wastewater, remains a major issue for water security (Xue et al., 2019). While the adoption of wastewater recycling methods has successfully addressed many of the pollution problems that result from the introduction of polluted water into the natural environment, the hazardous sludge that is generated during the physiochemical treatment of wastewater remains a major concern (M. M. Mian & G. Liu, 2019; Pavithra et al., 2019). In recent times, Shon et al. (2007a) described a cutting-edge method of sludge reuse that involved the synthesis of titania from Ti salt based flocculated sludge. Through the use of Ti-salts, viz., titanium tetrachloride ($TiCl_4$), titanium sulfate ($Ti(SO_4)_2$), and

polymerized $TiCl_4/Ti(SO_4)_2$ within water flocculation, it is possible to calcine the sludge to generate TiO_2, which represents a useful byproduct (Okour, Shon, et al., 2009; H. Shon et al., 2009b; H. K. Shon et al., 2009b). Previous studies found that approximately 40 mg of anatase titania can readily be produced from the flocculation and calcination of a liter of secondary sewage effluent (Hossain et al., 2019). As such, it was concluded that Ti-based salts as coagulants represent an effective means of addressing some of the environmental concerns that are linked with the generation of large volumes of sludge from conventional coagulants (Chi et al., 2019; M. M. Mian & G. J. Liu, 2019; Z. Wang et al., 2018a, 2018c).

Researchers have concentrated their attention on titanium dioxide (TiO_2) because it provides a greater degree of stability, high photoactivity, wide surface area, commercial availability, and non-toxicity (Chao Liu et al., 2016; Nasirian et al., 2017). Moreover, TiO_2 has been utilized in a range of applications including solar cells (H. Yu et al., 2013), paints (Yu et al., 2018), photocatalysis (Yu et al., 2020), and UV shielding (Asahi et al., 2014; Lee et al., 2008). Within these various contexts, TiO_2 is deemed to represent one of the most attractive semiconductors in the field of photocatalysis due to its ability to limit environmental pollution (Lee et al., 2008). A broad range of TiO_2 morphologies has been explored in the current literature to improve the use of photocatalysts as suspension or photoelectrodes. Subsequently, one of the most frequently explored morphologies are aligned TiO_2 nanotubes (TNTs) (Cui et al., 2020; Gao et al., 2016; Wei et al., 2016). The significant focus on TNTs could be attributed to their improved reactivity and desirable structural geometry. Specifically, the photoconversion productivities of nanotubular arrays of TiO_2 have been found to be particularly high because of the orthogonal carrier separation and the high charge transfer rate (Gao et al., 2016). A simple TNT synthesis process was proposed by Kasuga et al. (1998) through the hydrothermal treatment of titania nanoparticles in a NaOH based aqueous solution and reported the formation of nanotubes with an effective surface area of 400 m^2/g having a diameter of 8 nm.

As TNTs have a wide variety of applications, they were expected to have a more beneficial impact on photocatalytic applications than other forms of titania such as nanoparticles, colloidal, and alternative structures (El Saliby et al., 2012; Han et al., 2014). Some researchers have hypothesized that the as-synthesized Na/H-titanate nanotubes can degrade organic pollutants at a higher level of efficiency than alternative methods (J. Li et al., 2007; Okour et al., 2010). The augmentation in photocatalytic activities of the TNTs

is commonly attributed to their tubular structure, increased rate of sedimentation, and augmented effective surface area (El Saliby et al., 2012; Okour et al., 2010). Additionally, Okour et al. (2010) investigated the post-treatment of titanate nanotubes as a means of preparing thiourea-doped titanate nanofibers. They found that thiourea-doped TNTs delivered superior performance in decaying acetone under UV and visible light. They attributed this performance to the fact that nanotubes have a smaller crystallite and larger specific surface area.

Nevertheless, TiO_2 can only be excited by UV light at wavelengths below 380 nm because it exhibits a wide bandgap (Asahi et al., 2014). Unfortunately, only around 3 – 5% of sunlight contains UV light under 400 nm; as such, there is a low efficiency of solar energy conversion (Jinzhu Ma et al., 2016; Song et al., 2016). Hence, researchers have employed non-metal dopants for example, nitrogen (N) (T.-H. Kim et al., 2013; Kobayakawa et al., 2005) and sulfur (S) (Asahi et al., 2014) to increase the photoactivity of TiO_2 within the visible light region. Studies revealed that N-doped atoms reduce the optical bandgap of TiO_2 and, thereby, enhance its responsiveness to visible light irradiation (Nolan et al., 2012). There is a wide belief that N atoms act as a viable replacement for lattice oxygen atoms in a TiO_2 structure (Asahi et al., 2014; Wu et al., 2010). They serve to modify the bandgap of the catalyst such that it is within the visible light region. There is a potential to combine the impact of multiple dopants where dopants are renowned for changing the structure of TiO_2, as doing so can enhance photooxidation activity under visible light (T.-H. Kim et al., 2013). In addition, heterojunctions can be constructed by merging TiO_2 with alternative semiconductors that exhibit a narrow bandgap to explore an alternative pathway by which it is possible to increase the visible light response of TiO_2-based catalysts (Jinzhu Ma et al., 2016; Papailias et al., 2017). Heterojunctions are capable of producing an effective photogenerated charge separation between the TiO_2 substrate and the associated semiconductors in a similar manner to dye sensitized TiO_2. This plays a vital role in improving the performance of photocatalysts based on semiconductors.

Lately, as a heterojunction constituent of TiO_2, the 2D graphitic carbon nitride (g-CN) has been found to attract growing attention due to its suitable optical band edge positions, superior chemical stability, and the light absorption capacity in the visible light spectrum (Y. Huang et al., 2019; H. Liu et al., 2019; Yu et al., 2020). When composite photocatalyst is prepared by using anatase TiO_2 and 2D g-CN, the optical band edge positions (g-CN: −1.1 eV and +1.6 eV; TiO_2: −0.1 eV and +3.1 eV) of the constituents remain intact, and

a type II heterojunction interface is formed (Giannakopoulou et al., 2017; Jiang et al., 2018). Therefore, during light irradiation, it is possible for the photoinduced electrons (e^-) and holes (h^+) to travel between the valency band (VB) and conduction band (CB) of TiO_2 and g-CN (Jinzhu Ma et al., 2016). This serves to result in extended charge carrier separation within the heterojunction. Multiple studies have attempted to synthesize TiO_2/g-CN heterostructures as a means of achieving a wide light absorption range and high photoinduced charge separation productivity through the use of a heterojunction approach (Jiang et al., 2018; Kočí et al., 2017; Jinzhu Ma et al., 2016).

One of the most significant environmental issues of the contemporary era concerns the atmospheric pollution that is caused by nitrogen oxides (NO_x). It has been found that anthropogenic activities, such as burning fossil fuels and the denitrification of nitrate salts from the topsoil, are the primary atmospheric NO_x sources (Papailias et al., 2017). Hence, there has been a notable increase in the concentration of atmospheric NO_x over the last few decades. This is evident in the dense haze that can be observed because of the use of secondary aerosols. Thankfully, compared to conventional atmospheric NO_x removal techniques, photocatalysis can readily remove gaseous NO_x at significantly lower concentration (ppb level), which mimics the ambient atmospheric condition (Yu Huang et al., 2019; Jiang et al., 2018). Moreover, the removal of atmospheric NO_x through photooxidation could facilitate sustainability by using the large-scale application of renewable solar energy at mild reaction conditions (Yu Huang et al., 2019).

To date, a number of studies have been conducted to prepare heterojunction between titanate nanotubes and g-CN using commercially available precursors for TiO_2 sources, such as tetrabutyl titanate (Han et al., 2014; Wei et al., 2016), Ti foils (Gao et al., 2016), and commercial TiO_2 powders (Zhang et al., 2014). Insufficient amounts of studies have been found concerning the synthesis of single/composite photocatalysts by using the sludge generated TiO_2 (M. M. Mian & G. J. Liu, 2019; Z. Wang et al., 2018c; Zhao et al., 2013). To the author's advice, this is the first study to achieve an effective heterojunction of titanate nanotubes formed by sludge with g-CN. Consequently, the objectives of the study were to evaluate the feasibility of fabricating heterojunction between sludge generated TiO_2 nanotubes and melamine exfoliated g-CN for superior atmospheric NO removal under an extended irradiation spectrum. Initially, for removing impurities from sludge generated TiO_2 and the fabrication of H-titania nanotubes (H-TNTs), a modified hydrothermal approach was employed. Later, to enhance visible light absorption of the

as-prepared S-TNTs, a one-step template-free route was utilized to facilitate heterojunction between 1D S-TNTs and 2D g-CN. To assess the morphological and optical attributes of the as-prepared samples, advanced characterizations were carried out. Besides, following ISO 22197-1 (2007) (ISO, 2016) and ISO 17198-1 (2018) (ISO, 2018), the NO_x photooxidation potentials of the as-prepared samples were evaluated under UV and visible light, respectively.

8.3 Morphological attributes

8.3.1 XRD and BET results

To understand the crystallographic structure and phase, XRD patterns were obtained for the as-prepared samples and compared with standard charts. **Fig. 8-1(a)** compares the XRD patterns of the prepared composites S-TNT1 and S-TNT2 with prepared H-TNT, S-TNT, S-TiO_2, and g-CN. As shown in **Fig. 8-1(a)**, the prepared S-TiO_2 was perfectly indexed as anatase titania (JCPDS No. 21-1272) (Wei et al., 2016; Zhang et al., 2014). The XRD pattern of the prepared nanotubes (S-TNT, STNT1, and STNT2) shows that the phase structure and the crystallinity of S-TiO_2 remained intact after the modified hydrothermal treatment (Okour et al., 2010). However, before calcining H-TNT at 550 °C into S-TNT, the crystallographic development of anatase titania was insignificant. Scherrer's equation was utilized to estimate the crystal size of the anatase TiO_2 at the crystal plane (101) (Wei et al., 2016). The calculated crystal sizes were 15.40 nm, 16.44 nm, 15.79 nm, and 15.83 nm for S-TiO_2, S-TNT, S-TNT1, and S-TNT2, respectively. Hence, nanotube formation and composite preparation by utilizing S-TiO_2 showed negligible effects on the crystal size and phase. One interesting finding was the small peak around the 2θ value of 27.5°, which denotes the formation of little amounts of rutile (110) phase in S-TiO_2. According to the study conducted by Liao et al. (1997), anatase titania started converted to the rutile phase at the temperature above 550 °C, which is in coherence with the formation of the rutile phase in S-TiO_2. However, due to the presence of various impurities in the Ti incorporated sludge, the phase transformation is negligible even at 600 °C. Besides, Shon et al. (2007a) argued that while calcining Ti induced sludges, rutile titania becomes the dominant form of titania when the temperature is above 800 °C. Nevertheless, while calcining with melamine level of impurities increased in the precursor may have diminished the peak around 27.5° in the as-prepared samples (S-TNT, S-TNT1, and S-TNT2).

In comparison, the prepared g-CN nanosheets showed characteristics peaks around 2θ of 13.10° and 27.50°, which represent the Miller indices (hkl) value of (100) and (002), respectively (Thomas et al., 2008). The crystal planes, as mentioned earlier, correspond to the periodic in-plane arrangement of N-bridged tri-s-triazine repeating units (100) and the graphitic stacking of the conjugated aromatic system (002), with an estimated lattice spacing of 0.693 nm and 0.324 nm, respectively (Dong et al., 2014). Due to the negligible loading of g-CN, no visible characteristic peaks were observed in the prepared composites S-TNT1 and S-TNT2 (Gu et al., 2014). However, the composite formation of S-TNT with g-CN showed a negative shift in 2θ from 25.50° to 25.35° for the anatase (101) plane, which may have indicated the successful formation of S-TNT/g-CN composite (Song et al., 2016).

BET analysis was conducted with the help of N_2 adsorption-desorption isotherm, to assess the amendments in porosity due to nanotube and nanotube-based composite formation by employing S-TiO_2. For the as-prepared samples, graphs for the adsorbed volume of N_2 (@STP) versus relative pressure (P/P_0) is demonstrated in **Fig. 8-1(b)**. Additionally, for better comparison, BET assessment results of a commercially available anatase TiO_2 (NP400) has been compared with the prepared S-TiO_2. Along with NP400, all the prepared samples showed type IV(a) isotherm, according to IUPAC categorization, which confirms the existence of mesopores in the samples (Thommes et al., 2015). Additionally, the prepared S-TiO_2 showed a type H2 (b) hysteresis loop, wherein cavitation-oriented evaporation in slender array of pore necks could be the possible reason. However, after the formation of nanotubes (S-TNT), the hysteresis loops shifted to type H3, and later incorporation of g-CN with S-TNT changed the hysteresis loop to type H4 (Thommes et al., 2015). Also, an increase in the BET surface area of S-TNT2 was due to micropores' development compared to the other samples. Hence, the composite S-TNT2 was presumed to be a combination of micro and mesoporous structure (Thommes et al., 2015), which is further clarified by the pore size distribution curves depicted in **Fig. 8-1(c)**.

Using the adsorption data and the Barrett-Joyner-Halenda (BJH) method, the pore size distributions of the corresponding samples are depicted in **Fig. 8-1(c)**. The effective BET surface area (S_{BET}) of S-TiO_2 and NP400 were determined to be 51.69 m^2/g and 66.65 m^2/g, respectively. A slight reduction in the S_{BET} value of S-TiO_2 can be explained from the extended pore size distribution over a larger pore diameter (> 20 nm). On the other hand, after the fabrication of S-TNT from S-TiO_2, the S_{BET} values increased to 88.55 m^2/g,

and the pore size distribution shifted towards lower pore diameter, with a maximum pore diameter of 15 nm. Later incorporation of g-CN further increased the surface areas to 100.80 m^2/g and 153.61 m^2/g for S-TNT1 and S-TNT2, respectively (see **Fig. 8-1(b)**). Moreover, the larger effective surface area of S-TNT2 supports the shifting of pore size distribution curve towards lower pore diameter, and the maximum pore diameter was found to be half (5.82 nm) comparing S-TNT1 (12.90 nm).

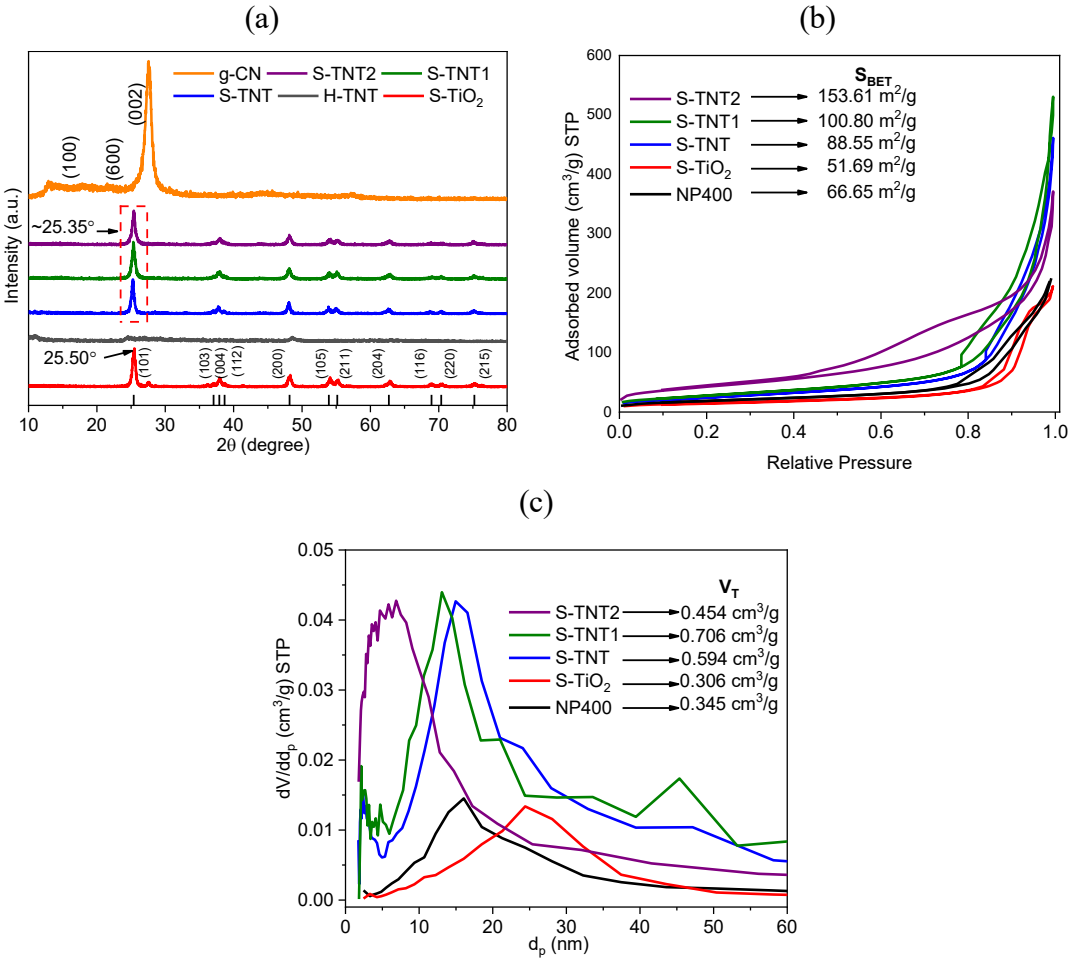

Fig. 8-1. (a) XRD patterns of the as-prepared samples S-TiO_2, H-TNT, S-TNT, S-TNT1, and S-TNT2; N_2 adsorption-desorption isotherms (b) and the pore size distribution (BJH adsorption) curves (c) of commercially available NP400 along with as-prepared S-TiO_2, S-TNT, S-TNT1, and S-TNT2.

8.3.2 Electron Microscopy (SEM and TEM images)

Fig. 8-2 and **Fig. 8-3** shows the SEM images and energy-dispersive X-ray (EDX) spectra of the as-prepared samples, respectively. The SEM image of the prepared S-TiO_2 (**Fig. 8-2(a)**) showed somewhat dispersed spherical-shaped particles and the EDX spectra confirm the existence of TiO_2 along with the presence of a considerable amount of C

(9.56 at.%) atoms (**Fig. 8-3(a)**), which is in coherence with previous studies, where the source of these C has been presumed as the organic contents of the precursor wastewater (M. M. Mian & G. J. Liu, 2019; Shon et al., 2007a). After the hydrothermal treatment, the prepared H-TNT also showed high carbon content along with the formation of nanotubes with a length of several μm and a diameter of 50 to 100 nm (**Fig. 8-2(b)**. Further calcination at 550 °C for 3 h seems to preserve the nanotubes' features and showed enhancement in tube length of the prepared S-TNT (**Fig. 8-2(c)**).

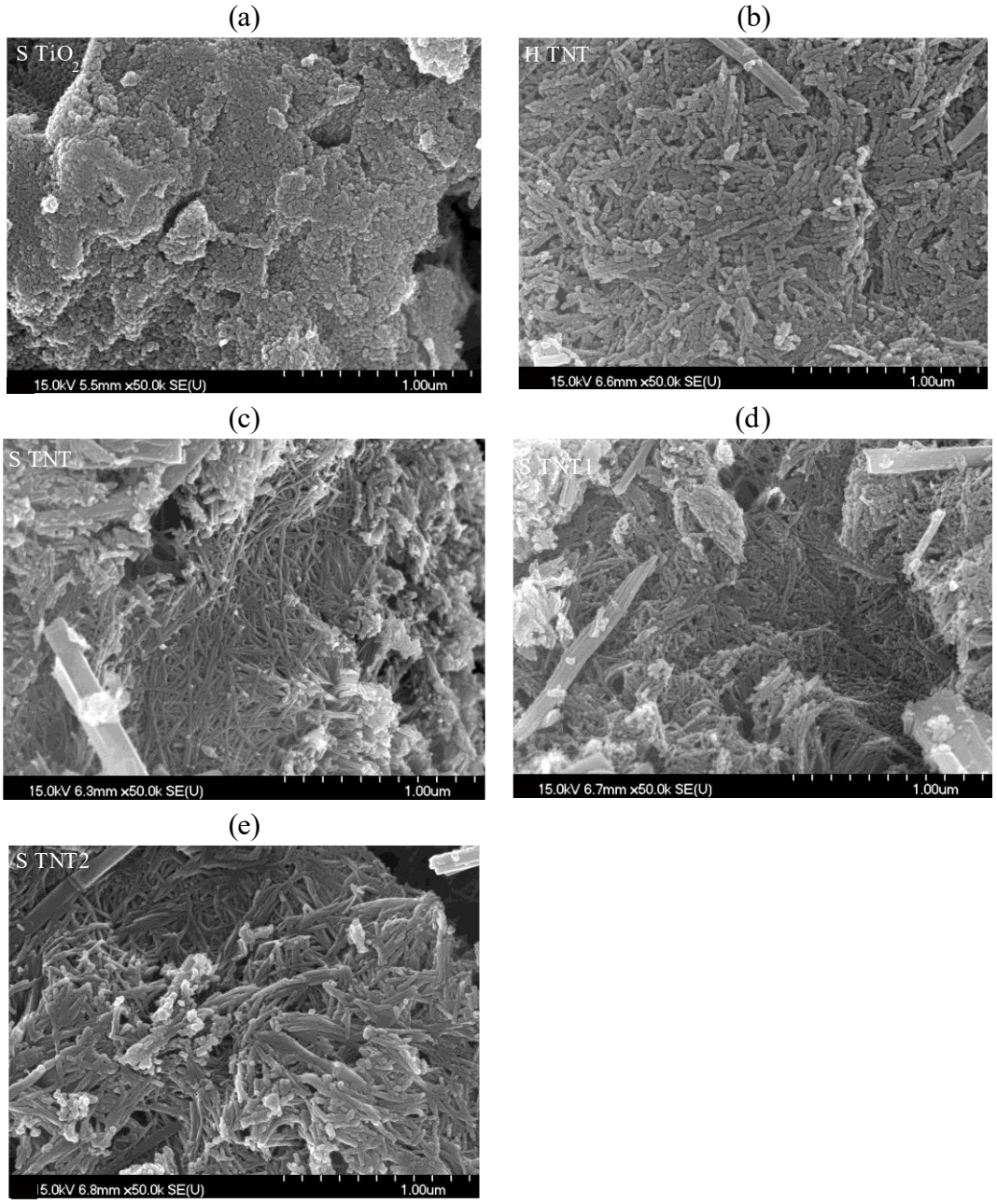

Fig. 8-2. SEM images of (a) S-TiO_2, (b) H-TNT, (c) S-TNT, (d) S-TNT1, and (e) S-TNT2.

Moreover, extended calcination seems to reduce the amounts of C (3.29 at.%) content in S-TNT, which may have significant impacts in photoactivity of the prepared S-TNT (see **Fig. 8-3(c)**). The SEM images of the as-prepared S-TNT1 and S-TNT2 show that the nanotube features of the H-TNT precursor remained intact with further length extension and surface smoothening of the nanotubes. Nevertheless, from the SEM image, it is hard to indicate the presence of 2D g-CN plates in the prepared composites (S-TNT1, and S-TNT2). Presumably, some of the 2D g-CN nanosheets were present covering the surface of the prepared nanotubes (Wei et al., 2016). Moreover, the EDX analysis of S-TNT1 (**Fig. 8-3(d)**) and S-TNT2 (**Fig. 8-3(e)**) confirmed the presence of small amounts C (19~40 at.%) and N (2~5 at.%) atoms in the prepared composites.

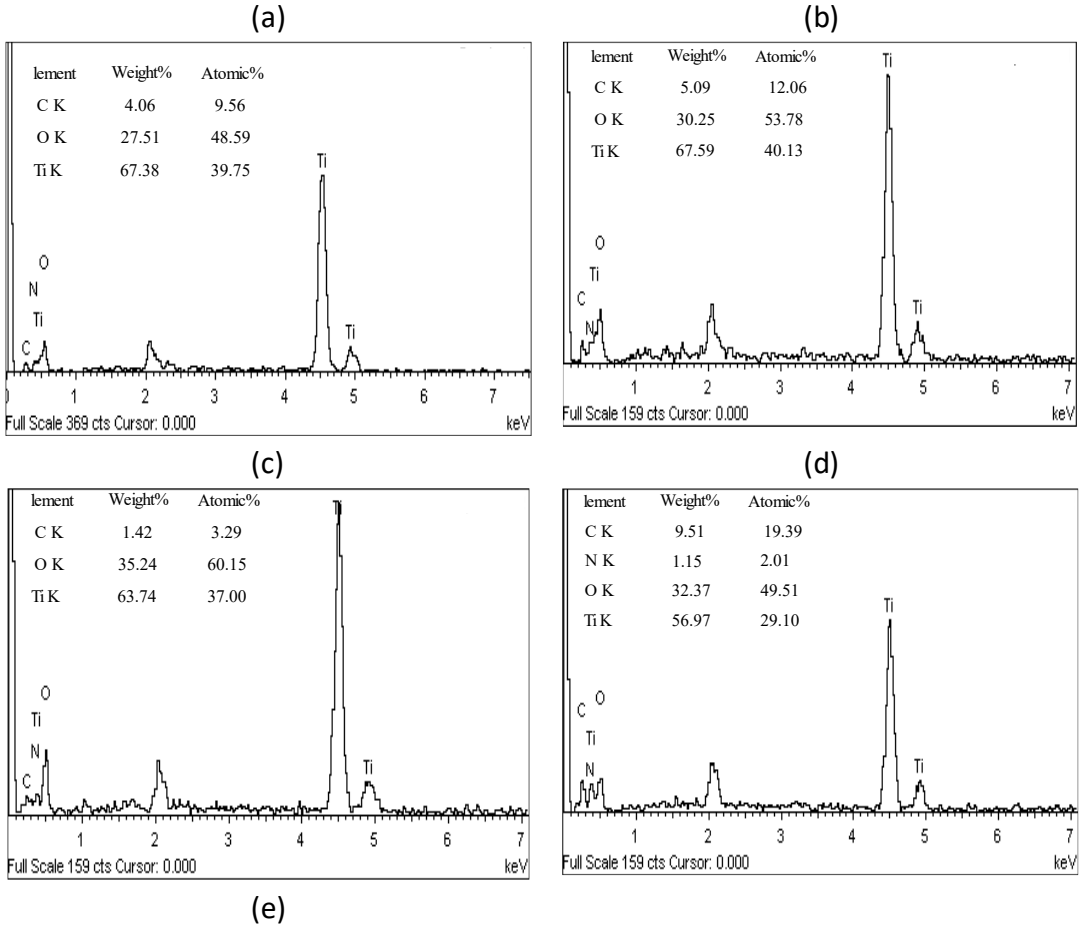

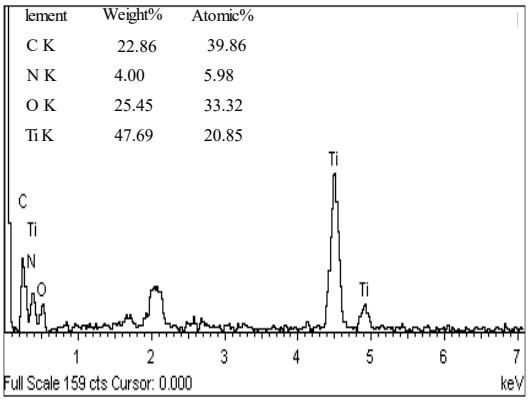

Fig. 8-3. EDX spectra of (a) S-TiO_2, (b) H-TNT, (c) S-TNT, (d) S-TNT1, and (e) S-TNT2.

To further assess the microstructure of the as-prepared S-TiO_2 and confirm the presence of g-CN in the prepared composite (S-TNT2), TEM analysis was conducted, and the corresponding images are illustrated in **Fig. 8-4**. The average crystal size of the as-synthesized S-TiO_2 depicted in **Fig. 8-4(a)** corresponds well with the aforementioned XRD spectra of S-TiO_2. Moreover, as shown in **Fig. 8-4(b)**, lattice fringes were found with the distances of 0.352 nm, 0.238 nm, and 0.188 nm, which confirm the presence of anatase (101), (004), and (200) planes (Gu et al., 2014; Han et al., 2014). From the TEM image of S-TNT (**Fig. 8-4(c)**), the presence of g-CN nanosheets can easily be found in/on the surface of S-TNT. Similar, lattice fringes as S-TiO_2 were found in the TEM image of S-TNT2 (**Fig. 8-4(d)**), and additionally, lattice fringes with the distance of 0.318 nm were found, confirming the presence of g-CN (002) nanosheets (Dong et al., 2014; Thomas et al., 2008).

(**a**) (**b**)

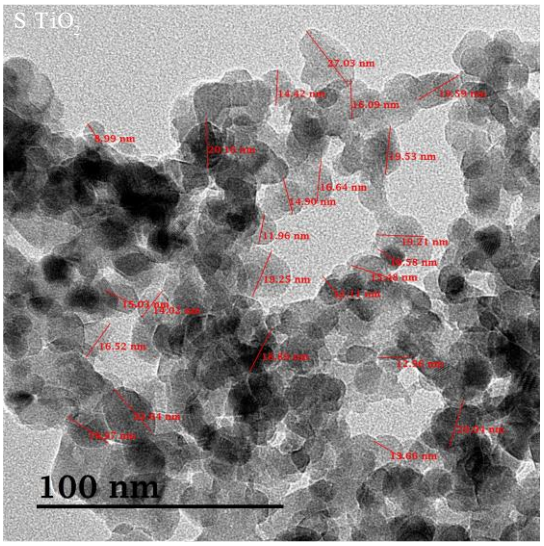

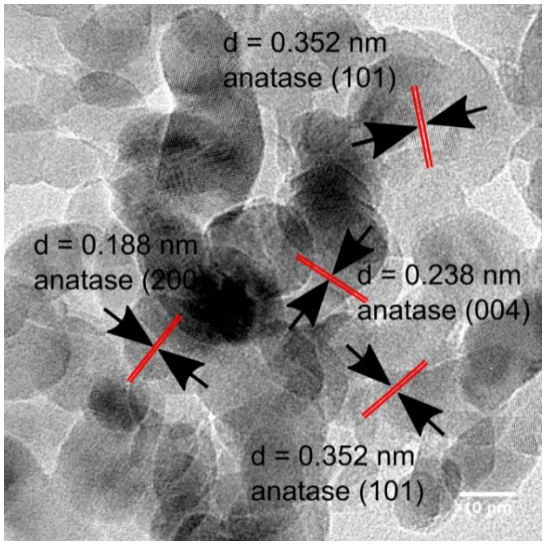

(c) (d)

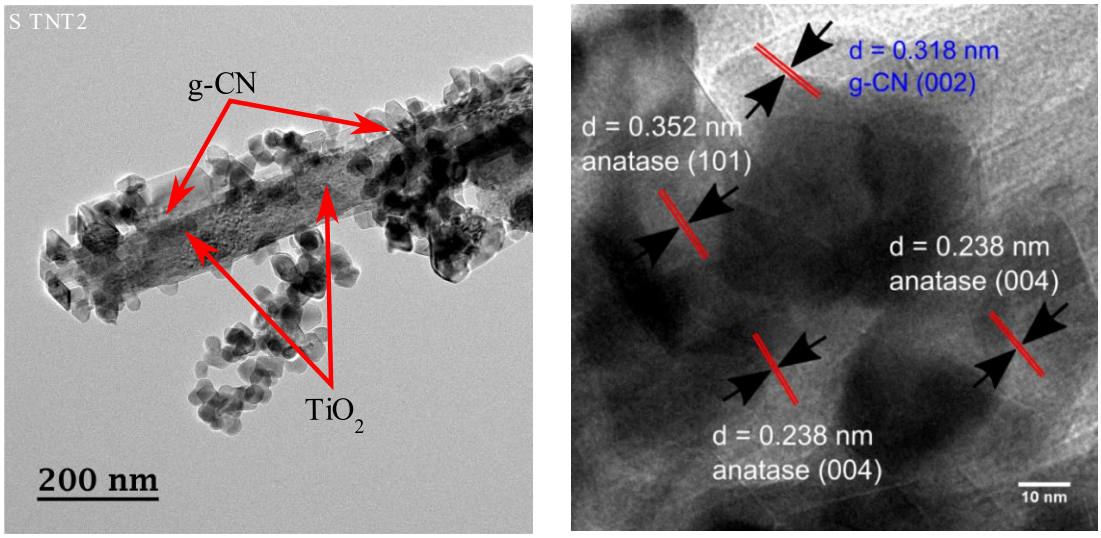

Fig. 8-4. TEM images of the as-prepared S-TiO_2 (a – b) and S-TNT2 (c – d).

8.3.3 FTIR and XPS spectra

FTIR spectra of the as-prepared composites and the single-component samples were compared to investigate the chemical structure for the validation of the presence of TiO_2 and g-CN. As shown in **Fig. 8-5(a)**, except for g-CN, all the samples showed a broad absorption peak around 450 – 600 cm^{-1}, which can be assigned to Ti-O-Ti stretching modes and confirms the presence of TiO_2 in the samples (Huang et al., 2020; Zhou et al., 2019). Another broad absorption peak was observed within the range of 3000 – 3650 cm^{-1}, which could be due to the stretching mode of O-H generated from the adsorbed water on the samples (Zhou et al., 2019). For pure g-CN, the peaks around 809.70 cm^{-1} and 3200 cm^{-1} could be dedicated to the stretching mode of s-triazine rings and N-H stretching of the remaining NH_x (x = 1, 2) groups (Dong et al., 2014). As shown in **Fig. 8-5(a)**, a series of absorption bands were found within the wavelength range of 1200 – 1600 cm^{-1}, which are due to the N-containing carbon of the core aromatic rings of g-CN (Wei et al., 2016). A zoomed-in image was provided within **Fig. 8-5(a)** to identify that increasing N content via the addition of a more g-CN content in synthesis processes. Although through EDX analysis, we have confirmed the presence of a small amount of C and N atoms in S-TNT1, it showed no characteristics peaks for g-CN. On the other hand, S-TNT2 showed the apparent presence of g-CN and confirmed the successful preparation of S-TNT/g-CN composite.

To further evaluate the as-prepared single element and composite sample's chemical compositions, XPS analysis was conducted. **Fig. 8-5(b)** illustrated the broad-angle scan, where **Fig. 8-5(c – f)** presented the deconvoluted C 1s, N 1s, Ti 2p, and O 1s spectra of

the as-prepared samples. The wide-angle survey scan shown in **Fig. 8-5(b)** shows that the presence of Ti 2p, O 1s, and C 1s spectra was confirmed in the prepared samples. Additionally, only the composite S-TNT2 showed any wide scan peak for the binding energies of N 1s. For the prepared composites S-TNT1 and S-TNT2, the C 1s (**Fig. 8-5(c)**) and N 1s (**Fig. 8-5(d)**) spectra were investigated to confirm the formation of g-CN within the composite. From **Fig. 8-5(d)**, characteristics N 1s peaks for g-CN were found in S-TNT2 but not in S-TNT1. A negligible amount of N atom was found in the composite, which may have been present in the doped condition. The FTIR spectrum of S-TNT1 is also in coherence with these results. From the N 1s spectra of S-TNT2, three convoluted peaks were found around 397.38, 398.76, and 400.22 eV, which can be assigned to pyridinic N, pyrrolic N, and graphitic N, respectively (Gao et al., 2016; Han et al., 2014). Besides, from the C 1s scan (**Fig. 8-5(c)**) of S-TNT2, a dominant peak for N-C=N_2 coordination was found around 288.08 eV (Gao et al., 2016). Additionally, due to the incorporation of g-CN with S-TNT in S-TNT2, the Ti 2p and O 1s scan's peak positions showed a positive shift of ~0.1 eV. The absence of no visible peak for C-Ti confirmed that there were no chemical reactions between S-TNT and g-CN, rather successful heterojunction was prepared.

(a) (b)

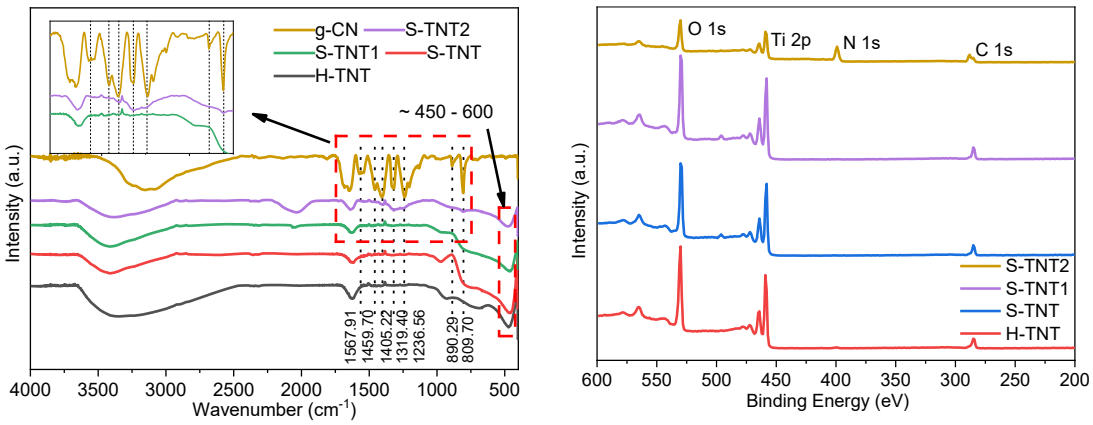

s(c) (d)

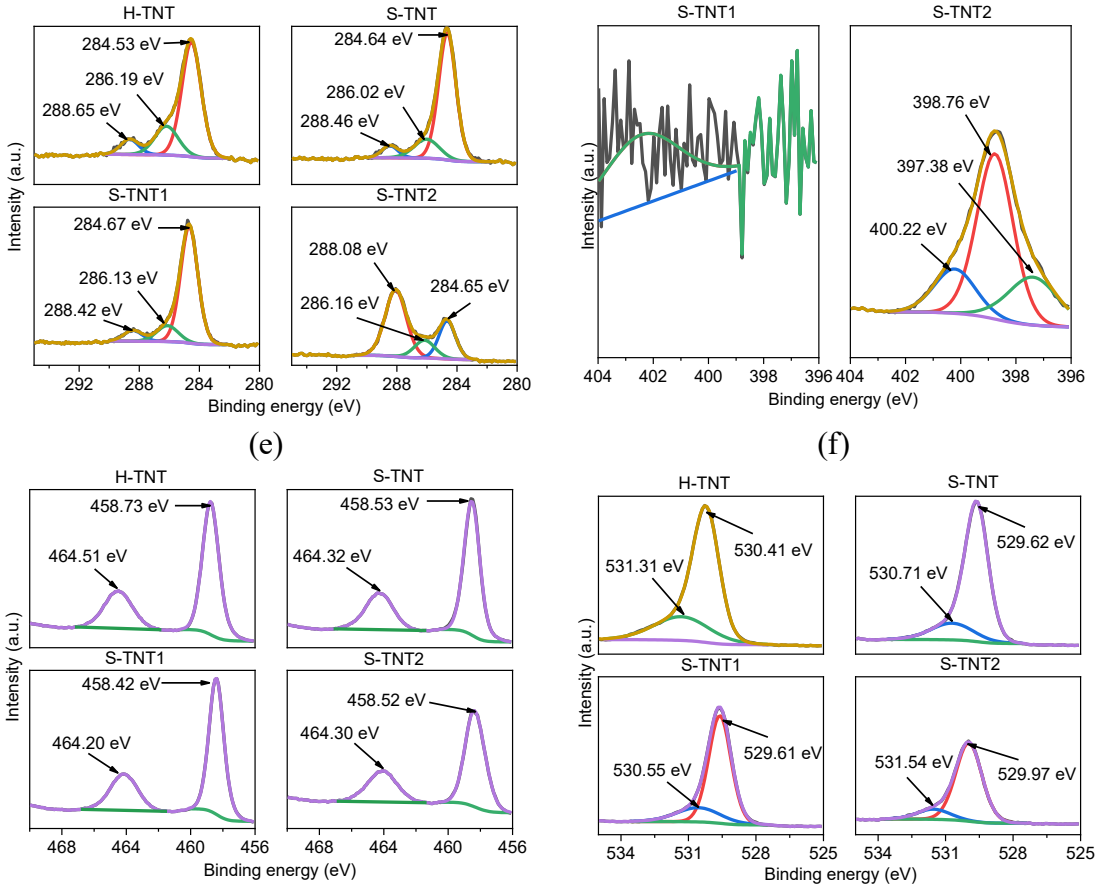

Fig. 8-5. (a) FTIR spectra and (b) wide-angle survey scan of the as-prepared composites; high resolution survey scan of (a) C 1s, (b) N 1s, (c) Ti 2p, and (d) O 1s for H-TNT, S-TNT, S-TNT1, and S-TNT2.

By investigating the Ti 2p narrow scan (**Fig. 8-5(e)**) of the prepared H-TNT, sharp peaks were found around 458.73 eV and 464. 51 eV, which can be ascribed to the characteristic peaks of Ti $2p_{3/2}$ and Ti $2p_{1/2}$ (Han et al., 2014). Hence, it is safe to presume that the Ti in H-TNT is present in the Ti^{4+} form. Besides, from the O 1s scan of H-TNT (**Fig. 8-5(f)**), the peaks around 530.41 eV and 531.31 eV could be assigned for O^{2-} lattice and OH^- respectively, which confirms the formation of TiO_2 in H-TNT (Wang et al., 2013). Similar peaks were observed in Ti 2p and O 1s scan of S-TNT; however, a negative shift of ~0.2 eV was observed due to the reduction of impurities, i.e., extra H and C atoms. Hence, based on the FTIR and XPS results, it can be presumed that successful heterojunction was prepared in S-TNT2 without compromising any of their chemical features. However, lower melamine content in the precursor mix (H-TNT:Melamine = 2:1) of S-TNT1 caused N/C doped S-TNT synthesis, which has modified the optical and photocatalytic attributes of the sample.

8.4 Optical traits (PL and UV-Vis DRS)

It is necessary to evaluate the compound's inherent optical traits to assess the in-depth mechanism of photoactivity of the photoactive semiconductor. Hence, DRS UV-Vis analysis was conducted to elucidate the amendment in the light absorption range and estimate the optical bandgap of the composites (S-TNT1 and S-TNT2). The findings associated with DRS UV-Vis are depicted in **Fig. 8-6(a – c)**. The absorbance spectra of S-TNT2 presented in **Fig. 8-6(a)** showed distinct enhancement in the visible light region, hence compared to S-TNT and S-TNT1, light absorption under UV spectra got reduced for obvious reasons. The distinction is more evident in **Fig. 8-6(b)**, where the sequence of light absorption wavelength edges was found as, g-CN (452.62 nm) > S-TNT2 (434.10 nm) > S-TNT1 (404.92 nm) > S-TNT (403.00 nm). Using the Kubelka-Munk function and through the process of extrapolation, the optical bandgaps of the as-prepared samples were estimated and depicted in **Fig. 8-6(c)** (Song et al., 2016; Troppová et al., 2018). Bandgap narrowing was observed in the prepared S-TNT2 compared to S-TNT and S-TNT1. Besides, the CB and VB position of the semiconductors were determined using the following equations,

$$E_{CB} = E_{VB} - E_g \qquad (8\text{-}1)$$

$$E_{VB} = X - E_0 + 0.5\, E_g \qquad (8\text{-}2)$$

Where E_{CB} and E_{VB} are CB and VB potential, X is the mean (geometric mean of the component atoms) electronegativity of the semiconductor. E_0 is the energy of free electrons against the normal hydrogen electrode (NHE), and E_g is the energy bandgap of the semiconductor. Based on the relevant articles, for anatase TiO_2 and g-CN, the value of electronegativity can be ascribed as 5.81, and 4.64 eV, respectively, and E_0 can be taken as 4.5 eV (Giannakopoulou et al., 2017). Hence, the E_{VB} of S-TNT and g-CN can be estimated as +2.90 eV and +1.5 eV, respectively; also, the corresponding E_{CB} will be -0.28 eV and -1.22 eV.

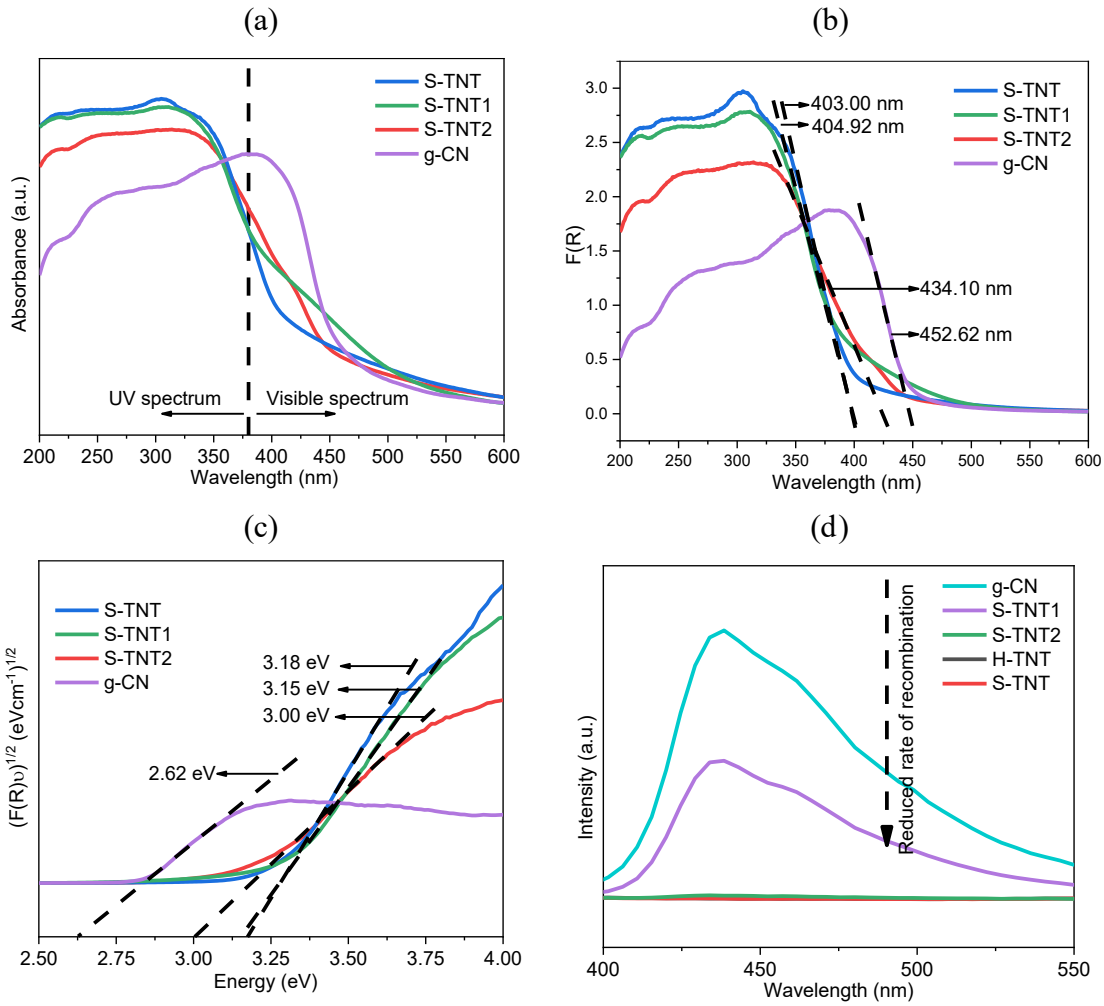

Fig. 8-6. (a) UV-vis DRS (absorbance vs. wavelength), (b) UV-vis DRS (F(R) vs. wavelength), (c) converted Kubelka-Munk function vs. energy of absorbed light, and (d) PL spectra of the as-prepared S-TNT, S-TNT1, STNT2, and g-CN.

In addition, to assess the rate of recombination of the photogenerated e^-/h^+ pairs, PL analysis was conducted. Based on relevant studies, PL spectra have been found to be an effective strategy to assess the photoactivity of a semiconductor (Han et al., 2014). The estimated PL spectra of the as-prepared samples are presented in **Fig. 8-6(d)**. The laboratory-made g-CN showed a semi asymmetric band around the maximum wavelength of ~439 nm, and similar peaks with reduced intensity were found for the prepared composites (S-TNT1 and S-TNT2). Based on the PL spectra, the recombination rate for S-TNT2 is minimal under visible light; hence, it is photoactivity should be maximum. On the other hand, S-TiO_2 and H-TNT showed a straight line as PL spectra in the visible light region, which is evident as light absorption was minimal **(Fig. 8-6(a))**.

8.5 Photoactivity

8.5.1 NO_x removal

The as-synthesized sample's photoactivity was evaluated by investigating the extent of atmospheric NO_x removal under both UV and visible light irradiation in a continuous flow reactor. Moreover, the range of NO_x photooxidation is compared with commercially available NP400. **Fig. 8-7(a)** and **Fig. 8-8(a)** presents the NO_x removal patterns and overall NO_x removal under 1 h of UV irradiation on the prepared samples, respectively. Compared to NP400, the prepared nanotubes showed a stable NO_x removal pattern. Under UV irradiation, S-TNT2 was found to be most effective in removing atmospheric NO, around 32.44% NO removal with a nitrate selectivity of 48.19% (see **Fig. 8-8(a)**). Compared to S-TiO_2, g-CN, and NP400, the extent of photooxidation using S-TNT under UV light was 6.4, 3.04, and 1.5 times higher. Similarly, under visible light, the prepared nanotubes showed a stable NO_x removal pattern (**Fig. 8-7(b)**), and S-TNT2 reported maximum removal. Under 1 h of visible light irradiation, S-TNT2 was found to remove 19.62% (**Fig. 8-8(b)**) of NO, which was about 4.8, 3.7, 2.09, and 2.8 times higher than S-TiO_2, S-TNT, NP400, and g-CN, respectively. Moreover, under visible light, S-TNT2 showed superior nitrate selectivity of almost 60%.

To further assess the stability of the prepared composite, recycle experiments up to 5 runs were carried out by using UV irradiation on the as-prepared S-TNT2 (see **Fig. 8-7(c)**). Each cycle was continued for 30 min with a 5 min stopping period that was considered between each run. After 5 cycles, the photoactivity showed negligible decay, demonstrating the high stability and reusability of the as-prepared composites. After 30 min of UV irradiation in the 1st run, total NO removal was estimated to be 33.58%, which was only reduced to 29.72% at the end of the 5th run (**Fig. 8-8(c)**). Moreover, the mild decreasing pattern confirms the presence of NO oxidized by-products on the active photocatalytic sites. Interestingly, the nitrate selectivity was preserved in the 1st four runs (around 51%) and reduced slightly in the 5th run (47.85%).

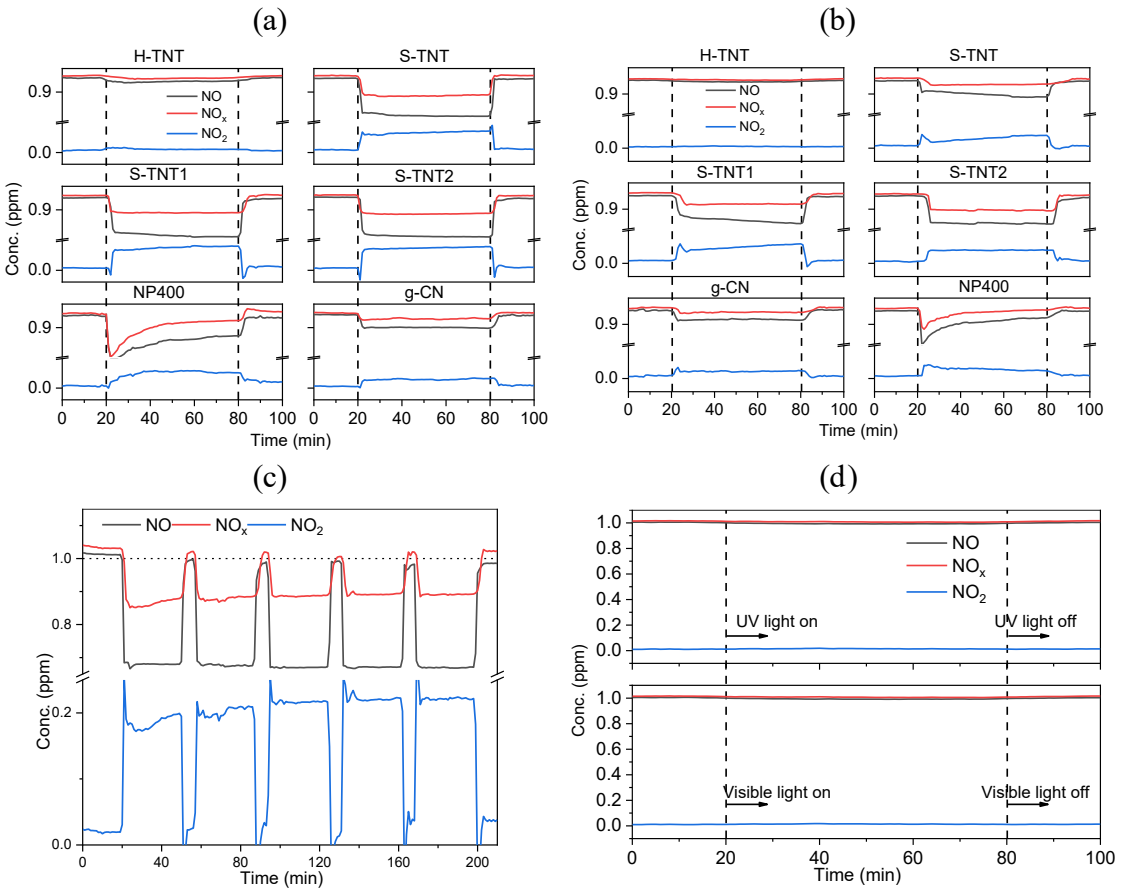

Fig. 8-7. Concentration patterns of NO, NO_2, and NO_x in the continuous flow reactor of the as-synthesized samples along with NP400, under UV (a) and visible light (b); (c) recycling experiments for NO removal under UV irradiation over S-TNT2; (d) NO_x concentration profile under light irradiation (UV/visible) without the presence of any photocatalysts.

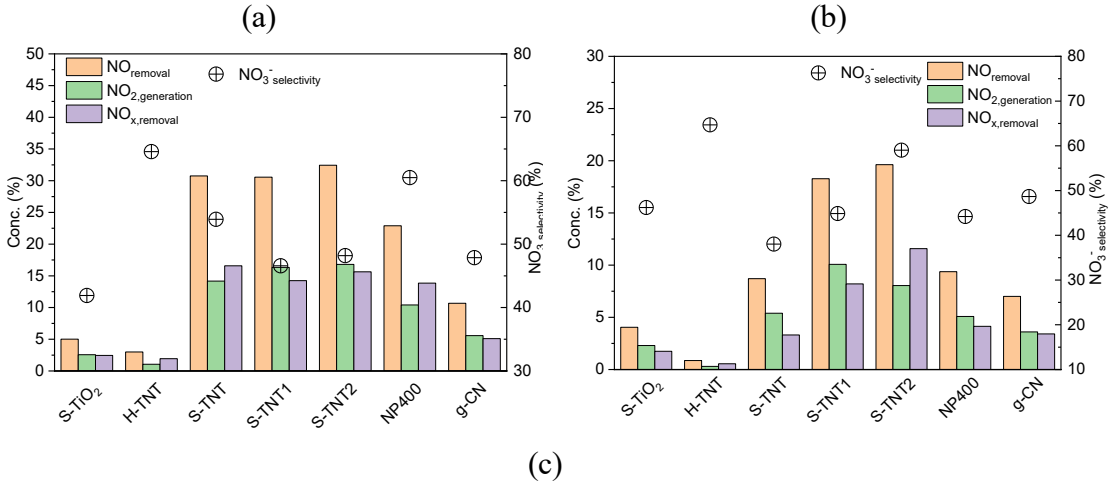

(c)

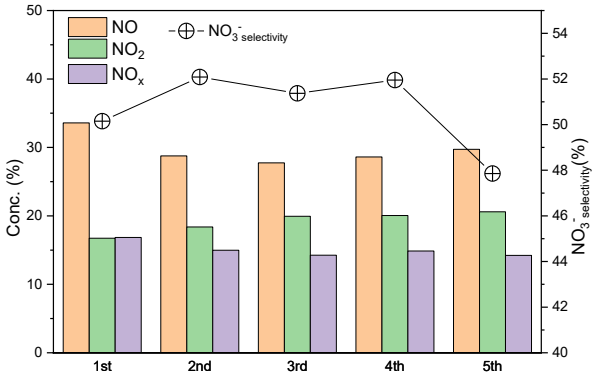

Fig. 8-8. Estimated $NO_{removal}$, $NO_{2,generation}$, $NO_{x,removal}$ and $NO_3^-{}_{selectivity}$ profile of the as-synthesized samples along with NP400, under UV (a) and visible light (b); (c) recycling experiments for NO removal under UV irradiation over S-TNT2.

8.5.2 Mechanism of NO_x removal

Based on the aforementioned advanced characterization of the as-prepared samples, three key reasons have been found that have contributed towards the enhanced photoactivity (under UV/Visible irradiation) of the studied S-TNT/g-CN (S-TNT2) composite. These primary reasons are (a) enhancement of the effective surface area, (b) narrowed optical bandgap, and (c) reduced recombination rate of photogenerated e^-/h^+ pairs.

(a) Enhancement of effective surface area: The successful S-TNT/g-CN heterojunction was observed in the as-synthesized S-TNT2, which showed an effective surface area of 153.61 m^2/g. The pristine S-TiO_2 and S-TNT showed the S_{BET} values of 51.69 m^2/g and 88.55 m^2/g, respectively. Hence, during the photooxidation of NO_x under either UV or visible light irradiance, S-TNT2 provided a significantly high amount of active photooxidation sites (Troppová et al., 2018). In the case of visible light irradiance, it was evident to have a high extent of NO_x removal, due to narrowed bandgap (**Fig. 8-6(c)**), and reduced charge recombination rate (**Fig. 8-6(d)**) along with the increased active sites (Kočí et al., 2017; Jinzhu Ma et al., 2016; Papailias et al., 2017). However, from the UV-Vis DRS spectra, it was apparent that the UV regime's light absorption was reduced for S-TNT2 compared to S-TNT (**Fig. 8-6(a)**). Irrespective of reduced UV light absorption, the prepared S-TNT2 showed enhancement in NO removal from 30.75% (S-TNT) to 32.44%, due to the dominant effect of effective surface area. Hence, visible light photo-activation of S-TNT/g-CN was possible without compromising the photoactivity under UV irradiance.

(b) Narrowed optical bandgap: Due to the incorporation of g-CN with S-TNT, the optical bandgap of S-TNT2 was reduced to 3.00 eV from 3.18 eV (S-TNT). As shown in **Fig. 8-6(c)**, the optical bandgap of g-CN was reported as 2.62 eV; hence, the narrowing of bandgap in S-TNT2 may be attributed to the presence of g-CN in the composite (Giannakopoulou et al., 2017; Yu Huang et al., 2019). Therefore, similar to g-CN, a redshift (**Fig. 8-6(b)**) was observed in S-TNT2, leading to activation of photoactivity under visible light.

(c) Reduced recombination rate of photogenerated e^-/h^+ pairs: In comparison to g-CN, the as-prepared S-TNT2 showed reduced intensity in PL spectra, which indicates the extent of charge recombination is decreased (Jiang et al., 2018). Hence the photoactivity of the prepared composites improved under both UV and visible light. Consequently, the trend of improvement in NO_x removal under UV/visible light (**Fig. 8-8**) and the increase in the intensity of the PL spectra (**Fig. 8-6(d)**) showed a similar pattern (g-CN < S-TNT1 < S-TNT2).

It is generally accepted that photocatalytic NO oxidation mainly comprises the active species such as superoxide ($\cdot O_2^-$) and hydroxyl ($\cdot OH$) radicals produced from redox reactions involving photogenerated e^-/h^+ pairs and adsorbed O_2 and OH^- groups on the irradiated photocatalyst (Jinzhu Ma et al., 2016; Papailias et al., 2017). For the photogenerated e^- to produce $\cdot O_2^-$ effectively, the CB edge of the photocatalyst must be more negative than the redox potential of $O_2/\cdot O_2^-$ (0.33 eV vs. NHE). Alternatively, the standard redox potential for $OH^-/\cdot OH$ is 1.99 eV against NHE; hence, the position of VB needed to be more positive for the h^+ to generate $\cdot OH$ radicals. Based on the estimated CB and VB edge position of the prepared samples (S-TNT and g-CN), **Fig. 8-9** presents the proposed schematic for NO removal under UV/Visible irradiance. The estimated optical bandgaps along with the CB and VB position of S-TNT and g-CN of this study suggested the as-synthesized composite to be of type II heterojunction photocatalyst (Troppová et al., 2018).

Under UV irradiance, both S-TNT and g-CN in the composite (S-TNT2) get excited and generates photoinduced e^- and h^+ in their respective CB and VB. As the CB of g-CN (-1.22 eV) is more negative compared to S-TNT (-0.28 eV), the photogenerated e^- migrates towards the CB of S-TNT (Jinzhu Ma et al., 2016). Later, e^- reacts with surrounding O_2 and H_2O to generate $\cdot O_2^-$ and $\cdot OH$ radicals. On the other hand, the photoinduced h^+ on the

highly positive VB of S-TNT (+2.90 eV) migrate towards less positive VB of g-CN (+1.50 eV) and reacts with the adsorbed H_2O to generate ·OH radicals. Later, the generated $\cdot O_2^-$ and OH^- radicals oxidize the NO into NO_2 or NO_3^- (Jiang et al., 2018; Kočí et al., 2017; Jinzhu Ma et al., 2016). Relevant works reported that under both UV and visible light, the primary species for NO oxidation to NO_3^- is the $\cdot O_2^-$(Jinzhu Ma et al., 2016). Hence, based on the reported nitrated selectivity of the prepared nanotubes (S-TNT = 53.90%, S-TNT1 = 46.59%, and S-TNT2 = 48.19%), it is safe to presume that both $\cdot O_2^-$ and ·OH radicals are primary active species for NO oxidation under UV light. The following equations summarize the underlying reactions when UV light is irradiated upon S-TNT2.

$$e^- + O_2 \rightarrow \cdot O_2^- \text{ (Primary active species)} \quad (8\text{-}3)$$

$$e^- + O_2 + H_2O \rightarrow \cdot OH \text{ (Primary active species)} \quad (8\text{-}4)$$

$$h^+ + OH^- \rightarrow \cdot OH \text{ (Primary active species)} \quad (8\text{-}5)$$

$$\cdot OH + NO \rightarrow NO_2 \quad (8\text{-}6)$$

$$\cdot O_2^- + NO \rightarrow NO_3^- \quad (8\text{-}7)$$

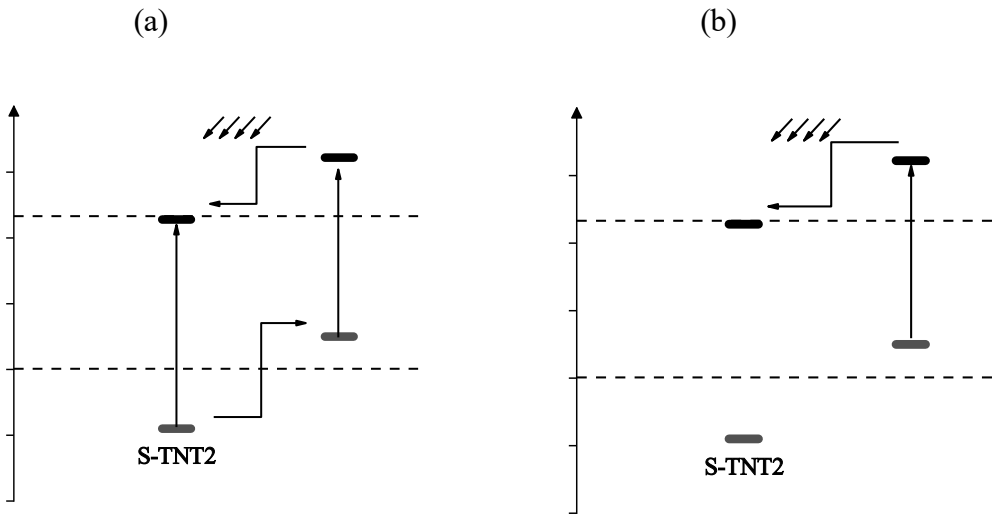

Fig. 8-9. Proposed schematic of NO removal mechanism for the as-prepared S-TNT/g-CN composites, S-TNT2 under (a) UV irradiance, (b) visible light.

Alternatively, under visible light irradiation on TiO_2/g-CN composites, only g-CN got excited, and the photogenerated e^- can migrate to S-TNT and readily produce $\cdot O_2^-$ but the h^+ on the VB cannot directly oxidize H_2O/OH^- to ·OH radicals (Jinzhu Ma et al., 2016). Hence, $\cdot O_2^-$ should be the primary reason for NO oxidation under visible light. The

estimated nitrated selectivity of the prepared nanotubes also supports the above postulates, and consecutive visible light activation of the composites showed an increasing trend (see **Fig. 8-8(b)**). Therefore, **Equations (8-3) to (8-7)** summarize the underlying reactions of visible light induced photooxidation of NO. However, the discussion mentioned above confirmed that the e^- and h^+ generated reactive species shown in **equation (8-4) and (8-5)** are the secondary active species during photooxidation under visible light.

8.6 Conclusions

The study reported the successful application of a NaOH based hydrothermal treatment for the preparation of sludge generated TiO_2/g-CN nanotubes. Through advanced characterization and UV/visible light induced photooxidation of NOx in a continuous flow reactor, the following postulates were deduced,

- NaOH based modified hydrothermal treatment of TiO_2 generated from sludges of dye wastewater can produce H-titanate after successive acid wash and lead to the preparation of pure anatase TiO_2 nanotubes through calcination.
- Facile calcination of sludge generated H-titanate, and an equal part of melamine mix at a temperature of 550°C@3h can successfully produce anatase TiO_2/g-CN nanotubes with severely increased effective surface area compared to the pristine nanotubes prepared by only calcining H-titanate.
- Due to bandgap narrowing, the prepared TiO_2/g-CN nanotubes showed a redshift in light absorption (434.10 nm). Hence, UV light absorption was reduced compared to pristine TiO_2 nanotubes, but the several-fold increase in effective surface area counterbalanced that drawback.

Under visible light irradiation of 1 h, the as-synthesized TiO_2/g-CN nanotubes showed almost 20% of NO removal with an enhanced nitrate selectivity of 59.02%, which is a significant improvement compared to pristine sludge generated TiO_2 nanotubes.

CHAPTER 9
CONCLUSIONS AND RECOMMENDATIONS

9 Conclusions and recommendations

9.1 Conclusions

9.1.1 Resolving the low pH problem of Ti- salt based flocculation and successful preparation of Ca-doped TiO_2

To address the issue of low pH during Ti salt based flocculation, Ca-doped TiO_2 was manufactured. The effects of employing $Ca(OH)_2$ as a coagulant aid on $TiCl_4$ coagulation performance and the characteristics of the recovered TiO_2 were investigated in this study. The photoactivity of the produced TiO_2 was compared to NP-400 under UV-A irradiation, and the results of the coagulation efficiency were thoroughly compared with the usage of $TiCl_4$ independently. $TiCl_4$ was first used to coagulate and flocculate synthetic wastewater. The optimum dosage of coagulant was identified by testing the turbidity, DOC, and zeta potential of the treated water. The effects on effluent pH, turbidity, and DOC removal were further studied using $Ca(OH)_2$ as a coagulant aid. Maximum turbidity and DOC removal were determined to be at 11.63 and 14.54 mg Ti/L, respectively, when $TiCl_4$ was used alone. As a result of fast water deprotonation at the optimum coagulant dosage, the effluent's pH fell below 3.77. A neutral pH of 7.26, on the other hand, was achieved by simultaneously administering 32.40 mg Ca/L and 14.54 mg Ti/L when $Ca(OH)_2$ was used as a coagulant aid. When $TiCl_4$ was used in conjunction with $Ca(OH)_2$, the turbidity removal was enhanced by 54.28%, and the DOC removal was comparable to that achieved when $TiCl_4$ was used alone. Using the collected sludge, TiO_2 was produced by incinerating it at 600 °C for 2 h. When the Ca-doped TiO_2 was analyzed using XRD, only an anatase phase was detected, as well as the presence of a high atomic proportion of Ca (4.14 %). Thus, a substantial quantity of Ca atoms hindered the TiO_2 phase, and there was no apparent presence of CaO. The commercially available NP-400 and a produced undoped TiO_2 both exhibit comparable CH_3CHO removal rates after UV irradiation. However, the Ca-doped TiO_2 formed with the optimal dosage of $Ca(OH)_2$ demonstrated minimal photoactivity when exposed to UV light. A large proportion of Ca inside the doped TiO_2 seemed to have an adverse effect on the specific surface area and photoactivity under ultraviolet light. However, photodegradation (under UV-A) of the CH_3CHO utilizing Ca-doped TiO_2 was significantly improved at lower $Ca(OH)_2$ doses (< 15 mg Ca/L).

9.1.2 Feasibility of photoactive TiO_2 generation from algae bloomed surface water

To explore the feasibility of preparing photoactive TiO_2 from algae bloomed surface water, $TiCl_4$ was used as a coagulant, and its coagulation efficiency was justified by comparing it with commercially available poly aluminum chloride. Coagulation efficiency was determined using conventional jar tests, and $TiCl_4$ was found superior to commercially available poly aluminum chloride. At an optimal dosage of 0.3 g Ti/L, turbidity, COD, and TP removal rates were 99.8%, 66.7%, and 96.9%, respectively. In addition, TiO_2 nanoparticles were extracted from the flocculated sludge. The existence of just the anatase phase was verified by SEM, EDX, and XRD investigation. After being exposed to a UVA lamp with a light intensity of 10 W/m^2, the recovered TiO_2 was shown to be effective in removing gaseous CH_3CHO and NO_x. Besides, the TiO_2 mixed mortar blocks produced in this research effectively removed nitrogen oxide from the atmosphere when exposed to UV light. Under UVA exposure for 120 min, the produced anatase TiO_2 successfully eliminated 85.7% of gaseous acetaldehyde, and the reaction rate constant was determined to be 0.0169 min^{-1}, which is about 54.34% of commercially available P25. Furthermore, during UVA irradiation for 60 min in a continuous flow process, the as-prepared TiO_2 was shown to remove about 28% of NO on average. Comparing the NO_x removal effectiveness of algal TiO_2 mixed mortar blocks produced in this research to that of P25 mixed mortar blocks under UV irradiation, it was discovered that the former had 50% less efficiency. Despite the fact that the produced anatase TiO_2 had lower photoactivity than P25, it was recovered from algal flocculated sludge, which would have needed costly disposal methods for long-term management. When economic considerations are taken into account, the novel TiO_2 derived from flocculated algal sludge may help to meet the growing need for commercial titania in air treatment.

9.1.3 Visible light activation of sludge generated TiO_2

9.1.3.1 Feasibility of sludge generated TiO_2 and g-CN heterojunction

For visible light activation, the feasibility of preparing TiO_2/g-CN heterojunction from Ti-incorporated dried dye wastewater sludge was explored. Dye wastewater was obtained from a wastewater treatment plant in Daegu, South Korea, for the purpose of Ti-based flocculation and coagulation. The flocculated wastewater was subsequently dried for 48 h in a lab oven set at 100 °C before the blackish dried flocculated sludge was ground into powder form using a mortar and pestle. Later, two reaction routes of composite formation were evaluated. In the initial approach, one-step calcination of dried sludge and melamine

mixture at 600 °C was carried out. Detailed morphological and chemical characterizations showed that the one-step calcination route did not create TiO_2/g-CN composites; instead, only N-doped anatase TiO_2 composites were formed. Moreover, due to the non-uniform composition of organic content in the dried sludge, it was not easy to control the N doping level by varying melamine content (0 - 100%) in the precursor mix. However, successful formation of anatase TiO_2 and g-CN was observed when a two-step calcination route was followed, i.e., via synthesis of anatase TiO_2 from dried sludge and later development of heterojunction by calcining (550 °C) the TiO_2 and melamine mixture. X-ray diffraction along with infrared and X-ray photoelectron spectroscopy verified the effective heterojunction. TGA and DSC analysis were conducted to evaluate the phase transition of 1:1 ratio precursor and various blends, i.e., sludge:melamine, sludge generated TiO_2:melamine, NP400:melamine, and P25:melamine, within the temperature range of 25 – 600 °C. The yield was reduced to 15.04% when dried sludge and melamine mix were calcined to 600 °C. The composite formation was confirmed from the increased heat of formation from 155.55 $J \cdot g^{-1}$ to 289.98 $J \cdot g^{-1}$. To compare the phase transformation results and the possible formation of TiO_2/g-CN heterojunction, commercially available NP400 and P25 were used in the precursor mix instead of dried sludge during TGA and DSC analysis. The estimated heat of formation for NP400 and P25 was 259.25 $J \cdot g^{-1}$ and 237.74 $J \cdot g^{-1}$, respectively, which inferred the possibility of TiO_2/g-CN composite formation from two-step calcination routes. In addition, maximum atmospheric NO removal under UV and visible light were observed for the prepared composite when the melamine content in the precursor mixture was 70%. After 1 h of UV and visible light irradiation, the best TiO_2/g-CN composite removed 25.71% and 13.50% of NO, respectively. Optical characterization suggested that the enhanced NO oxidation under UV/visible light was due to the bandgap narrowing and diminished photo- generated electron-hole recombination. It has been noted that the composites $NO_3^-{}_{selectivity}$ rose with visible light irradiation as a greater percentage of melamine was added to the precursor mix but began to fall when this proportion went over 70%.

9.1.3.2 Tailoring of optical energy bandgap and optimization of TiO_2/g-CN heterojunction

To further optimize the photoactivity of the synthesized visible light active TiO_2/g-CN from sludge generated TiO_2, alteration of optical bandgap was investigated in detail. In this study, photoactive titania was recovered from sludges produced by Ti-based

flocculation of dye effluent. It was heterojunctioned with g-CN to improve photoactivity in the presence of UV/visible light. A simple one-step synthesis method was used to produce pure g-CN, and the conjugated sludge generated TiO_2/g-CN. The combination made up of sludge generated TiO_2 and melamine was annealed in a box furnace for the production of the sample. The annealing process was carried out at normal atmospheric pressure. Various samples were produced by varying the weight percent of melamine to TiO_2 in the mixture, and a calcination temperature of 550 °C was used throughout the process. The photocatalytic removal of NO_x from the atmosphere was accomplished using the samples as they were produced. It was possible to create a heterojunction between TiO_2 and g-CN via simple calcination (at 550 °C) of sludge generated TiO_2 and melamine mix. From the evaluation of the samples' morphological and optical characteristics, it was ascertained that they formed a successful heterojunction. Moreover, g-CN had minimal effects on the crystal structure and size of the TiO_2 precursor used in the experiment. The degree of photoactivity of the produced samples was determined by measuring the amount of NO_x oxidized under both UV and visible light irradiance. Regardless of the light types used, the prepared samples showed increased photoactivity. The best sample removed 15.18 % and 9.16 % of ambient NO after 1 h of UV/visible light-based photooxidation, respectively. It was determined that the mixing ratio of sludge produced TiO_2 to melamine was kept at 1:3 in the optimum sample. Additionally, the optical bandgap of the optimized sample was determined to be 2.65 eV, compared to 2.83 eV for the sludge generated TiO_2. In both the UV and visible areas, the absorption band of the heterojunctioned TiO_2/g-CN was substantially enhanced. Furthermore, the PL study revealed an inhibited recombination rate of produced e^-/h^+ pairs, which is advantageous for easily generating $\cdot O_2^-$ and $\cdot OH$ radicals for NO_x photodegradation. As a result, the controlled rate of photogenerated charge recombination and the tailored energy bandgap of the as-prepared samples were the main drivers in increasing photoactivity in the experiments. Although the NO_x removal efficiency of synthesized sludge generated TiO_2/g-CN was found to be inferior to that of commercially available NP400, this synthesis route of TiO_2/g-CN heterojunction has considerable potential to promote sustainability through the utilization of undesired sludge from water treatment plants and a rebate in the cost of the photocatalysts.

9.2 Enhancement of photoactivity of sludge generated TiO_2 under UV/Visible light

Titania nanotubes were produced from sludge generated TiO_2 using a modified hydrothermal method and effectively composited with g-CN using a simple calcination procedure in order to increase the degree of photoactivity of the material. Advanced characterization methods were used to analyze the produced samples, such as XRD/TEM, SEM/XPS, UV-visible DRS, and PL analysis. After a series of acid washes, a NaOH-based modified hydrothermal treatment of TiO_2 produced from dye wastewater sludges was found to yield H-titanate, which was then be calcined to form pure anatase TiO_2 nanotubes. The successful production of anatase TiO_2/g-CN nanotubes may be achieved by calcining sludge generated H-titanate with an equivalent proportion of melamine mix at 550 °C for 3 h. A substantial improvement in morphological and optical bandgap was found. The produced composite has a threefold increase in effective surface area when compared to TiO_2 synthesized by sludge. Compared to the 3.18 eV optical bandgap in pristine sludge generated TiO_2, the optical bandgap has been reduced to 3.00 eV. Because of the narrowing of the bandgap, the produced TiO_2/g-CN nanotubes exhibited a redshift in light absorption (434.10 nm). The degree of photoactivity of the produced composites was examined through photooxidation of NO_x in a continuous flow reactor. Although light absorption was impaired during UV irradiation due to bandgap narrowing, the influence on photoactivity was offset by the increased effective surface area of 153.61 m^2/g. Thus, after 1 h of light irradiation, the highest NO elimination was 32.44 % under UV irradiance. After 1 h of visible light irradiation, the as-synthesized TiO_2/g-CN nanotubes removed almost 20% of NO with a 59.02 % increase in nitrate selectivity, which is a substantial improvement above pure sludge produced TiO_2 nanotubes. By using TiO_2 nanotubes and g-CN in heterojunction, the suggested technique may substantially contribute to resource recovery from water treatment facilities as well as photocatalytic air pollution elimination.

9.3 Recommendations

This study developed a number of sludge-generated titania from both synthetic and real wastewater to photocatalytically activate under UV and visible light irradiation. The photoactivity of the synthesized photocatalysts was assessed based on atmospheric NO_x removal, which optimized the synthesis parameters. Successful photoactive TiO_2s were generated from synthetic secondary sewage effluent, eutrophic river water, and industry-grade dye wastewater. Moreover, a novel photoactive composite was generated from dye

wastewater, which can get effectively activated under visible light towards removing atmospheric NO_x and preserving the UV activation equally. Nonetheless, there are a few limitations in this research and room for improvement. The following suggestions are made in order to address the study's issues:

- Modification (foreign element doping/co-doping) of the optical attributes of sludge-generated TiO_2 is possible by incorporating target element incorporated coagulant aids during the coagulation and flocculation phase of the Ti salt-based coagulants. However, this study reported that controlling the doping is difficult by optimizing the coagulant and coagulant aid dose during flocculation. Instead, the synthesis of photoactive TiO_2 can be designed by varying the coagulant dose to target the photoactivity of the final photocatalyst as a variable.
- Photoactive TiO_2 was successfully synthesized in this study by utilizing the flocculated eutrophic wastewater sludges and was incorporated in mortar blocks for effective NO_x removal. However, the algal content of the flocculated sludge may impact the long-term performance of the photocatalysts, which was not incorporated in this study. Hence, further study on this aspect would ascertain substantial insight on this issue.
- This study reported efficient heterojunction of g-CN with sludge-generated TiO_2, which unfolded the possibility of compositing other graphene nanocomposites along with dye and quantum dot sensitization of the sludge-generated TiO_2.
- The TiO_2/g-CN composites prepared from sludge-generated TiO_2, and melamine showed substantial improvement in morphological and optical attributes, resulting in promising band-gap modification to get photocatalytically activated under UV and visible light separately. However, the combined effect or the performance under the solar spectrum was not assessed in this study. The work can be further extended by designing the material for solar activation.
- A facile hydrothermal treatment of the synthesized dye wastewater sludge generated TiO_2 revealed that optimized melamine content for photocatalyst design varied substantially for TiO_2 nanoparticles compared to nanotubes, which was not further investigated in this study. The author presumed that the effect of extra hydrothermal treatment weakened the crystallinity of the TiO_2 nanotubes. However, there is a possibility that the heterojunction of TiO_2-g-CN nanotubes

can be further optimized by varying the calcination temperature from 550 °C to a lower range.

- Future studies should consider experiments with more types of real wastewater. The life-cycle cost assessment could also be considered, which can facilitate the comparison with other conventional coagulants.

10 References

Akpan, U. G., & Hameed, B. H. (2011a). Enhancement of the photocatalytic activity of TiO2by doping it with calcium ions. *Journal of Colloid and Interface Science*, *357*, 168-178. https://doi.org/10.1016/j.jcis.2011.01.014

Akpan, U. G., & Hameed, B. H. (2011b). Enhancement of the photocatalytic activity of TiO(2) by doping it with calcium ions. *J Colloid Interface Sci*, *357*(1), 168-178. https://doi.org/10.1016/j.jcis.2011.01.014

An, B., Lee, S., Kim, H.-G., Zhao, D., Park, J.-A., & Choi, J.-W. (2019). Organic/inorganic hybrid adsorbent for efficient phosphate removal from a reservoir affected by algae bloom. *Journal of Industrial and Engineering Chemistry*, *69*, 211-216. https://doi.org/10.1016/j.jiec.2018.09.029

Angelo, J., Andrade, L., Madeira, L. M., & Mendes, A. (2013). An overview of photocatalysis phenomena applied to NO_x abatement. *J Environ Manage*, *129*, 522-539. https://doi.org/10.1016/j.jenvman.2013.08.006

Arain, R. A., Khatri, Z., Memon, M. H., & Kim, I.-S. (2013). Antibacterial property and characterization of cotton fabric treated with chitosan/AgCl–TiO2 colloid. *Carbohydrate polymers*, *96*(1), 326-331. https://www.sciencedirect.com/science/article/abs/pii/S0144861713003573?via%3Dihub

Asahi, R., Morikawa, T., Irie, H., & Ohwaki, T. (2014). Nitrogen-doped titanium dioxide as visible-light-sensitive photocatalyst: designs, developments, and prospects. *Chem Rev*, *114*(19), 9824-9852. https://doi.org/10.1021/cr5000738

Aziz, H. A., Razak, M. H. A., Rahim, M. Z. A., Kamar, W., Abu Amr, S. S., Hussain, S., & Van Leeuwen, J. (2018). Evaluation and comparison the performance of titanium and zirconium(IV) tetrachloride in textile wastewater treatment. *Data Brief*, *18*, 920-927. https://doi.org/10.1016/j.dib.2018.03.113

Babko, A., Gridchina, G., & Nabivanets, B. (1962). Study of titanium (IV) in hydrochloric acid by dialysis and ion-exchange chromatography. *Russian Journal of Inorganic Chemistry*, *7*, 66-70.

Baca, M., Kukulka, W., Cendrowski, K., Mijowska, E., Kalenczuk, R. J., & Zielinska, B. (2019). Graphitic Carbon Nitride and Titanium Dioxide Modified with 1D and 2D Carbon Structures for Photocatalysis [Review]. *Chemsuschem*, *12*(3), 612-620. https://doi.org/10.1002/cssc.201801642

Bahadori, A., Clark, M., & Boyd, B. (2013). *Essentials of water systems design in the oil, gas, and chemical processing industries*. Springer Science & Business Media.

Banerjee, S., Dionysiou, D. D., & Pillai, S. C. (2015). Self-cleaning applications of TiO2 by photo-induced hydrophilicity and photocatalysis. *Applied Catalysis B: Environmental*, *176*, 396-428.

Barakwan, R., Trihadiningrum, Y., & Bagastyo, A. (2019). Characterization of Alum Sludge from Surabaya Water Treatment Plant, Indonesia. *Journal of Ecological Engineering*, *20*(5), 7-13. https://doi.org/10.12911/22998993/104619

Batault, F., Thevenet, F., Hequet, V., Rillard, C., Le Coq, L., & Locoge, N. (2015). Acetaldehyde and acetic acid adsorption on TiO2 under dry and humid conditions. *Chemical Engineering Journal*, *264*, 197-210. https://doi.org/10.1016/j.cej.2014.10.089

Behzadnia, A., Montazer, M., Rashidi, A., & Rad, M. M. (2014). Sonosynthesis of nano TiO2 on wool using titanium isopropoxide or butoxide in acidic media producing multifunctional fabric. *Ultrasonics sonochemistry*, *21*(5), 1815-1826. https://www.sciencedirect.com/science/article/abs/pii/S1350417714000984?via%3Dihub

Bianchi, C. L., Gatto, S., Pirola, C., Naldoni, A., Di Michele, A., Cerrato, G., Crocellà, V., & Capucci, V. (2014). Photocatalytic degradation of acetone, acetaldehyde and toluene in

gas-phase: Comparison between nano and micro-sized TiO_2. *Applied Catalysis B: Environmental*, *146*, 123-130. https://doi.org/10.1016/j.apcatb.2013.02.047

Bjerrum, J., Schwarzenbach, G., & Sillen, L. (1958). Inorganic ligands. *Stability constants of metal-ion complexes. IUPAC special publication*(7).

Block, J. W. (1916). Coagulant for filtering. In: Google Patents.

Boonen, E., & Beeldens, A. (2012). Photocatalytic roads: from lab tests to real scale applications. *European Transport Research Review*, *5*(2), 79-89. https://doi.org/10.1007/s12544-012-0085-6

Boonen, E., & Beeldens, A. (2014). Recent Photocatalytic Applications for Air Purification in Belgium. *Coatings*, *4*(3), 553-573. https://doi.org/10.3390/coatings4030553

Boonprakob, N., Wetchakun, N., Phanichphant, S., Waxler, D., Sherrell, P., Nattestad, A., Chen, J., & Inceesungvorn, B. (2014). Enhanced visible-light photocatalytic activity of g-C3N4/TiO2 films. *J Colloid Interface Sci*, *417*, 402-409. https://doi.org/10.1016/j.jcis.2013.11.072

Bratby, J. (2006). *Coagulation and flocculation in water and wastewater treatment*. IWA publishing.

Buettner, K. M., & Valentine, A. M. (2012). Bioinorganic chemistry of titanium. *Chem Rev*, *112*(3), 1863-1881. https://doi.org/10.1021/cr1002886

Burnat, B., Robak, J., Batory, ., Leniart, A., Piwoński, I., Skrzypek, S., & Brycht, M. (2015). Surface characterization, corrosion properties and bioactivity of Ca-doped TiO_2 coatings for biomedical applications. *Surface and Coatings Technology*, *280*, 291-300. https://doi.org/10.1016/j.surfcoat.2015.09.018

Castro, Y., & Durán, A. (2016). Ca doping of mesoporous TiO_2 films for enhanced photocatalytic efficiency under solar irradiation. *Journal of Sol-Gel Science and Technology*, *78*(3), 482-491. https://doi.org/10.1007/s10971-016-3988-1

Caudillo-Flores, U., Muñoz-Batista, M. J., Luque, R., Fernández-García, M., & Kubacka, A. (2019). g-C3N4/TiO2 composite catalysts for the photo-oxidation of toluene: Chemical and charge handling effects. *Chemical Engineering Journal*, *378*. https://doi.org/10.1016/j.cej.2019.122228

Chai, B., Peng, T., Mao, J., Li, K., & Zan, L. (2012). Graphitic carbon nitride (g-C3N4)-Pt-TiO2 nanocomposite as an efficient photocatalyst for hydrogen production under visible light irradiation. *Phys Chem Chem Phys*, *14*(48), 16745-16752. https://doi.org/10.1039/c2cp42484c

Chekli, L., Corjon, E., Tabatabai, S. A. A., Naidu, G., Tamburic, B., Park, S. H., & Shon, H. K. (2017). Performance of titanium salts compared to conventional $FeCl_3$ for the removal of algal organic matter (AOM) in synthetic seawater: Coagulation performance, organic fraction removal and floc characteristics. *J Environ Manage*, *201*, 28-36. https://doi.org/10.1016/j.jenvman.2017.06.025

Chekli, L., Eripret, C., Park, S. H., Tabatabai, S. A. A., Vronska, O., Tamburic, B., Kim, J. H., & Shon, H. K. (2017). Coagulation performance and floc characteristics of polytitanium tetrachloride (PTC) compared with titanium tetrachloride (TiCl 4) and ferric chloride (FeCl 3) in algal turbid water. *Separation and Purification Technology*, *175*, 99-106. https://doi.org/10.1016/j.seppur.2016.11.019

Chekli, L., Galloux, J., Zhao, Y. X., Gao, B. Y., & Shon, H. K. (2015). Coagulation performance and floc characteristics of polytitanium tetrachloride (PTC) compared with titanium tetrachloride (TiCl4) and iron salts in humic acid–kaolin synthetic water treatment. *Separation and Purification Technology*, *142*, 155-161. https://doi.org/10.1016/j.seppur.2014.12.043

Chen, J. J., Yeh, H. H., & Tseng, I. C. (2009). Effect of ozone and permanganate on algae coagulation removal--pilot and bench scale tests. *Chemosphere*, *74*(6), 840-846. https://doi.org/10.1016/j.chemosphere.2008.10.009

Chen, L., Zhou, X., Jin, B., Luo, J., Xu, X., Zhang, L., & Hong, Y. (2016). Heterojunctions in g-C3N4/B-TiO2 nanosheets with exposed {001} plane and enhanced visible-light

photocatalytic activities. *International Journal of Hydrogen Energy*, *41*(18), 7292-7300. https://doi.org/10.1016/j.ijhydene.2016.03.137

Chen, X.-F., Lin, S.-r., & Kou, S.-C. (2018). Effect of composite photo-catalysts prepared with recycled clay brick sands and nano-TiO_2 on methyl orange and NO_x removal. *Construction and Building Materials*, *171*, 152-160. https://doi.org/10.1016/j.conbuildmat.2018.03.099

Chen, Y., Huang, W., He, D., Situ, Y., & Huang, H. (2014). Construction of heterostructured g-C(3)N(4)/Ag/TiO(2) microspheres with enhanced photocatalysis performance under visible-light irradiation. *ACS Appl Mater Interfaces*, *6*(16), 14405-14414. https://doi.org/10.1021/am503674e

Cheng, W. P., & Chi, F. H. (2002). A study of coagulation mechanisms of polyferric sulfate reacting with humic acid using a fluorescence-quenching method. *Water Research*, *36*(18), 4583-4591. https://doi.org/10.1016/s0043-1354(02)00189-6

Cheng, W. P., Chi, F. H., Li, C. C., & Yu, R. F. (2008). A study on the removal of organic substances from low-turbidity and low-alkalinity water with metal-polysilicate coagulants. *Colloids and Surfaces A: Physicochemical and Engineering Aspects*, *312*(2-3), 238-244.

Cheng, X., Yu, X., Xing, Z., & Yang, L. (2016). Synthesis and characterization of N-doped TiO_2 and its enhanced visible-light photocatalytic activity. *Arabian Journal of Chemistry*, *9*, S1706-S1711. https://doi.org/10.1016/j.arabjc.2012.04.052

Chi, Y., Tian, C., Li, H., & Zhao, Y. (2019). Polymerized Titanium Salts for Algae-Laden Surface Water Treatment and the Algae-Rich Sludge Recycle toward Chromium and Phenol Degradation from Aqueous Solution. *ACS Sustainable Chemistry & Engineering*, *7*(15), 12964-12972. https://doi.org/10.1021/acssuschemeng.9b02016

Comba, P., & Merbach, A. (1987). The titanyl question revisited. *Inorganic Chemistry*, *26*(8), 1315-1323.

Crittenden, J. C., Howe, K. J., Hand, D. W., Tchobanoglous, G., & Trussell, R. R. (2012). *Principles of water treatment*. Wiley.

Cui, L., Liu, S., Wang, F., Li, J., Song, Y., Sheng, Y., & Zou, H. (2020). Growth of uniform g-C3N4 shells on 1D TiO2 nanofibers via vapor deposition approach with enhanced visible light photocatalytic activity. *Journal of Alloys and Compounds*, *826*. https://doi.org/10.1016/j.jallcom.2020.154001

Damma, D., Boningari, T., Ettireddy, P. R., Reddy, B. M., & Smirniotis, P. G. (2018). Direct Decomposition of NOx over TiO2 Supported Transition Metal Oxides at Low Temperatures. *Industrial & Engineering Chemistry Research*, *57*(49), 16615-16621. https://doi.org/10.1021/acs.iecr.8b03532

deKrafft, K. E., Wang, C., & Lin, W. (2012). Metal-organic framework templated synthesis of Fe2O3/TiO2 nanocomposite for hydrogen production. *Advanced Materials*, *24*(15), 2014-2018. https://doi.org/10.1002/adma.201200330

Deng, M., Wu, X., Zhu, A., Zhang, Q., & Liu, Q. (2019). Well-dispersed TiO2 nanoparticles anchored on Fe3O4 magnetic nanosheets for efficient arsenic removal. *J Environ Manage*, *237*, 63-74. https://doi.org/10.1016/j.jenvman.2019.02.037

DeWolfe, J. (2003). *Guidance manual for coagulant changeover*. American Water Works Association.

Diebold, U. (2003). The surface science of titanium dioxide. *Surface science reports*, *48*(5-8), 53-229. https://doi.org/10.1016/s0167-5729(02)00100-0

Diker, H., Varlikli, C., & Stathatos, E. (2014). N-doped titania powders prepared by different nitrogen sources and their application in quasi-solid state dye-sensitized solar cells. *International Journal of Energy Research*, *38*(7), 908-917. https://doi.org/10.1002/er.3091

Dobias, B., & Stechemesser, H. (2005). *Coagulation and Flocculation* (Vol. 126). Taylor & Francis https://doi.org/10.1201/9781420027686

Dong, F., Li, Y., Wang, Z., & Ho, W.-K. (2015). Enhanced visible light photocatalytic activity and oxidation ability of porous graphene-like g-C3N4 nanosheets via thermal exfoliation. *Applied Surface Science*, *358*, 393-403. https://doi.org/10.1016/j.apsusc.2015.04.034

Dong, F., Ou, M., Jiang, Y., Guo, S., & Wu, Z. (2014). Efficient and Durable Visible Light Photocatalytic Performance of Porous Carbon Nitride Nanosheets for Air Purification. *Industrial & Engineering Chemistry Research*, *53*(6), 2318-2330. https://doi.org/10.1021/ie4038104

Dong, F., Wang, Z., Sun, Y., Ho, W. K., & Zhang, H. (2013). Engineering the nanoarchitecture and texture of polymeric carbon nitride semiconductor for enhanced visible light photocatalytic activity. *J Colloid Interface Sci*, *401*, 70-79. https://doi.org/10.1016/j.jcis.2013.03.034

Dong, F., Wu, L., Sun, Y., Fu, M., Wu, Z., & Lee, S. C. (2011). Efficient synthesis of polymeric g-C3N4 layered materials as novel efficient visible light driven photocatalysts. *Journal of Materials Chemistry*, *21*(39). https://doi.org/10.1039/c1jm12844b

Dougna, A. A., Gombert, B., Kodom, T., Djaneye-Boundjou, G., Boukari, S. O., Leitner, N. K. V., & Bawa, L. M. (2015). Photocatalytic removal of phenol using titanium dioxide deposited on different substrates: Effect of inorganic oxidants. *Journal of Photochemistry and Photobiology A: Chemistry*, *305*, 67-77.

Du, X., Bai, X., Xu, L., Yang, L., & Jin, P. (2019). Visible-light activation of persulfate by TiO2/g-C3N4 photocatalyst toward efficient degradation of micropollutants. *Chemical Engineering Journal*. https://doi.org/10.1016/j.cej.2019.123245

Du, X., Bai, X., Xu, L., Yang, L., & Jin, P. (2020). Visible-light activation of persulfate by TiO2/g-C3N4 photocatalyst toward efficient degradation of micropollutants. *Chemical Engineering Journal*, *384*, 123245. https://doi.org/10.1016/j.cej.2019.123245

Duan, J., & Gregory, J. (2003). Coagulation by hydrolysing metal salts. *Advances in colloid and interface science*, *100*, 475-502.

Einaga, H., & Komatsu, Y. (1981). Hydrolytic precipitation reaction of titanium(IV) from (Na, H)Cl aqueous solution. *Journal of Inorganic and Nuclear Chemistry*, *43*(10), 2443-2448. https://doi.org/10.1016/0022-1902(81)80279-5

El Saliby, I., Okour, Y., Shon, H. K., Kandasamy, J., Lee, W. E., & Kim, J.-H. (2012). TiO_2 nanoparticles and nanofibres from $TiCl_4$ flocculated sludge: Characterisation and photocatalytic activity. *Journal of Industrial and Engineering Chemistry*, *18*(3), 1033-1038. https://doi.org/10.1016/j.jiec.2011.12.002

El Saliby, I. J., Okour, Y. H., Shon, H. K., Vigneswaran, S., Kandasamy, J., & Kim, J. H. (2009). Detailed investigation on the effect of washing TiO_2 prepared from Ti-salts flocculated wastewater sludge. *Journal of Advanced Oxidation Technologies*, *12*(2), 194-201. <Go to ISI>://WOS:000269856800007

El Saliby, I. J., Shon, H. K., Okour, Y. H., Vigneswaran, S., Senthilnanthanan, M., & Kandasamy, J. (2010a). Production of titanium dioxide nanoparticles and nanostructures from dye wastewater sludge-characterisation and evaluation of photocatalytic activity. *Journal of Advanced Oxidation Technologies*, *13*(1), 15-20. <Go to ISI>://WOS:000274182800002

El Saliby, I. J., Shon, H. K., Okour, Y. H., Vigneswaran, S., Senthilnanthanan, M., & Kandasamy, J. (2010b). Production of titanium dioxide nanoparticles and nanostructures from dye wastewater sludge - characterisation and evaluation of photocatalytic activity. *Journal of Advanced Oxidation Technologies*, *13*(1), 15-20. <Go to ISI>://WOS:000274182800002

El Zein, A., Bedjanian, Y., & Romanias, M. N. (2013). Kinetics and products of HONO interaction with TiO_2 surface under UV irradiation. *Atmospheric Environment*, *67*, 203-210. https://doi.org/10.1016/j.atmosenv.2012.11.016

Everett, D. (1988). Basic Principles of Colloid Science, Royal Soc. *Chem., Whitstable*.

Fajrina, N., & Tahir, M. (2019). A critical review in strategies to improve photocatalytic water splitting towards hydrogen production [Review]. *International Journal of Hydrogen Energy*, *44*(2), 540-577. https://doi.org/10.1016/j.ijhydene.2018.10.200

Ferri, D., & Riccio, G. (1985). On the hydrolysis of the titanium (IV) ion in chloride media. *Polyhedron*, *4*(1), 15-22.

Flynn Jr, C. M. (1984). Hydrolysis of inorganic iron (III) salts. *Chemical Reviews*, *84*(1), 31-41.
Fujishima, A., & Honda, K. (1972). Electrochemical photolysis of water at a semiconductor electrode. *Nature*, *238*(5358), 37-38. https://doi.org/10.1038/238037a0
Fujishima, A., Zhang, X., & Tryk, D. A. (2008). TiO2 photocatalysis and related surface phenomena. *Surface science reports*, *63*(12), 515-582.
Gallus, M., Ciuraru, R., Mothes, F., Akylas, V., Barmpas, F., Beeldens, A., Bernard, F., Boonen, E., Boreave, A., Cazaunau, M., Charbonnel, N., Chen, H., Daele, V., Dupart, Y., Gaimoz, C., Grosselin, B., Herrmann, H., Ifang, S., Kurtenbach, R., Maille, M., Marjanovic, I., Michoud, V., Mellouki, A., Miet, K., Moussiopoulos, N., Poulain, L., Zapf, P., George, C., Doussin, J. F., & Kleffmann, J. (2015). Photocatalytic abatement results from a model street canyon. *Environ Sci Pollut Res Int*, *22*(22), 18185-18196. https://doi.org/10.1007/s11356-015-4926-4
Gan, Y., Li, J., Zhang, L., Wu, B., Huang, W., Li, H., & Zhang, S. (2021). Potential of titanium coagulants for water and wastewater treatment: Current status and future perspectives. *Chemical Engineering Journal*, *406*. https://doi.org/10.1016/j.cej.2020.126837
Gan Yonghai, W. B., Li Haojie,Li Jingbiao,Li Runsheng,Zhang Shujuan. (2020). Preparation and application evaluation of a novel titanium coagulant. *Inorganic Chemicals Industry*, *52*(9), 1-5. https://doi.org/10.11962/1006-4990.2020-0249
Gao, Z. D., Qu, Y. F., Zhou, X., Wang, L., Song, Y. Y., & Schmuki, P. (2016). Pt-Decorated g-C3N4/TiO2 Nanotube Arrays with Enhanced Visible-Light Photocatalytic Activity for H2 Evolution. *ChemistryOpen*, *5*(3), 197-200. https://doi.org/10.1002/open.201500219
Ghanem, A., Badawy, A., Ismail, N., Tian, Z. R., Rehim, M. A., & Rabia, A. (2014). Photocatalytic activity of hyperbranched polyester/TiO2 nanocomposites. *Applied Catalysis A: General*, *472*, 191-197.
Ghernaout, B., Ghernaout, D., & Saiba, A. (2012). Algae and cyanotoxins removal by coagulation/flocculation: A review. *Desalination and Water Treatment*, *20*(1-3), 133-143. https://doi.org/10.5004/dwt.2010.1202
Giannakopoulou, T., Papailias, I., Todorova, N., Boukos, N., Liu, Y., Yu, J., & Trapalis, C. (2017). Tailoring the energy band gap and edges' potentials of g-C 3 N 4 /TiO 2 composite photocatalysts for NO x removal. *Chemical Engineering Journal*, *310*, 571-580. https://doi.org/10.1016/j.cej.2015.12.102
Graham, N., Gang, F., Fowler, G., & Watts, M. (2008). Characterisation and coagulation performance of a tannin-based cationic polymer: A preliminary assessment. *Colloids and Surfaces A: Physicochemical and Engineering Aspects*, *327*(1-3), 9-16.
Gregory, J., & Duan, J. (2001). Hydrolyzing metal salts as coagulants. *Pure and Applied Chemistry*, *73*(12), 2017-2026.
Gu, L., Wang, J., Zou, Z., & Han, X. (2014). Graphitic-C(3)N(4)-hybridized TiO(2) nanosheets with reactive {001} facets to enhance the UV- and visible-light photocatalytic activity. *J Hazard Mater*, *268*, 216-223. https://doi.org/10.1016/j.jhazmat.2014.01.021
Gupta, K. K., Jassal, M., & Agrawal, A. K. (2007). Functional finishing of cotton using titanium dioxide and zinc oxide nanoparticles. *Research Journal of Textile and Apparel*, *11*(3), 1-10.
Hahn, H. H., Hoffmann, E., & Odegaard, H. (2007). *Chemical Water and Wastewater Treatment IX*. IWA publishing.
Haider, Z., Cho, H.-i., Moon, G.-h., & Kim, H.-i. (2019). Minireview: Selective production of hydrogen peroxide as a clean oxidant over structurally tailored carbon nitride photocatalysts [Review]. *Catalysis Today*, *335*, 55-64. https://doi.org/10.1016/j.cattod.2018.11.067
Hameed, Y. T., Idris, A., Hussain, S. A., Abdullah, N., Man, H. C., & Suja, F. (2018). A tannin–based agent for coagulation and flocculation of municipal wastewater as a pretreatment for biofilm process. *Journal of Cleaner Production*, *182*, 198-205. https://doi.org/10.1016/j.jclepro.2018.02.044
Han, C., Wang, Y., Lei, Y., Wang, B., Wu, N., Shi, Q., & Li, Q. (2014). In situ synthesis of graphitic-C3N4 nanosheet hybridized N-doped TiO2 nanofibers for efficient

photocatalytic H2 production and degradation. *Nano Research*, *8*(4), 1199-1209. https://doi.org/10.1007/s12274-014-0600-2

Harifi, T., & Montazer, M. (2014). Fe3+: Ag/TiO2 nanocomposite: synthesis, characterization and photocatalytic activity under UV and visible light irradiation. *Applied Catalysis A: General*, *473*, 104-115.

Hay, S. O., Obee, T., Luo, Z., Jiang, T., Meng, Y., He, J., Murphy, S. C., & Suib, S. (2015). The viability of photocatalysis for air purification. *Molecules*, *20*(1), 1319-1356. https://doi.org/10.3390/molecules20011319

Henderson, R. K., Parsons, S. A., & Jefferson, B. (2010). The impact of differing cell and algogenic organic matter (AOM) characteristics on the coagulation and flotation of algae. *Water Res*, *44*(12), 3617-3624. https://doi.org/10.1016/j.watres.2010.04.016

Hossain, S. M., Park, H., Kang, H.-J., Kim, J. B., Tijing, L., Rhee, I., Jun, Y.-S., Shon, H. K., & Kim, J.-H. (2020). Preparation and Characterization of Photoactive Anatase TiO2 from Algae Bloomed Surface Water. *Catalysts*, *10*(4). https://doi.org/10.3390/catal10040452

Hossain, S. M., Park, H., Kang, H.-J., Mun, J. S., Tijing, L., Rhee, I., Kim, J.-H., Jun, Y.-S., & Shon, H. K. (2020). Modified Hydrothermal Route for Synthesis of Photoactive Anatase TiO_2/g-CN Nanotubes from Sludge Generated TiO_2. *Catalysts*, *10*(11). https://doi.org/10.3390/catal10111350

Hossain, S. M., Park, H., Kang, H. J., Mun, J. S., Tijing, L., Rhee, I., Kim, J. H., Jun, Y. S., & Shon, H. K. (2021). Facile synthesis and characterization of anatase TiO_2/g-CN composites for enhanced photoactivity under UV-visible spectrum. *Chemosphere*, *262*, 128004. https://doi.org/10.1016/j.chemosphere.2020.128004

Hossain, S. M., Park, M. J., Park, H. J., Tijing, L., Kim, J. H., & Shon, H. K. (2019). Preparation and characterization of TiO2 generated from synthetic wastewater using TiCl4 based coagulation/flocculation aided with Ca(OH)2. *J Environ Manage*, *250*, 109521. https://doi.org/10.1016/j.jenvman.2019.109521

Hou, X., Wang, C.-W., Zhu, W.-D., Wang, X.-Q., Li, Y., Wang, J., Chen, J.-B., Gan, T., Hu, H.-Y., & Zhou, F. (2014). Preparation of nitrogen-doped anatase TiO2 nanoworm/nanotube hierarchical structures and its photocatalytic effect. *Solid State Sciences*, *29*, 27-33.

Huang, J., Li, D., Li, R., Chen, P., Zhang, Q., Liu, H., Lv, W., Liu, G., & Feng, Y. (2020). One-step synthesis of phosphorus/oxygen co-doped g-C3N4/anatase TiO2 Z-scheme photocatalyst for significantly enhanced visible-light photocatalysis degradation of enrofloxacin. *J Hazard Mater*, *386*, 121634. https://doi.org/10.1016/j.jhazmat.2019.121634

Huang, Q., Hu, Y., He, G., Lin, C., & Wei, C. (2018). Photocatalytic oxidation of nitrogen oxides over {001}TiO2: the influence of F(-) ions. *Environ Sci Pollut Res Int*, *25*(35), 35342-35351. https://doi.org/10.1007/s11356-018-3435-7

Huang, X., Gao, B., Yue, Q., Wang, Y., & Li, Q. (2018). Effects of polytitanium chloride and polyaluminum chloride pre-treatment on ultrafiltration process: Floc properties and membrane fouling. *Journal of the Taiwan Institute of Chemical Engineers*, *88*, 193-200. https://doi.org/10.1016/j.jtice.2018.03.057

Huang, Y., Wang, P., Wang, Z., Rao, Y., Cao, J.-j., Pu, S., Ho, W., & Lee, S. C. (2019). Protonated g-C3N4/Ti3+ self-doped TiO2 nanocomposite films: Room-temperature preparation, hydrophilicity, and application for photocatalytic NO removal. *Applied Catalysis B: Environmental*, *240*, 122-131. https://doi.org/10.1016/j.apcatb.2018.08.078

Huang, Y., Wang, P. G., Wang, Z. Y., Rao, Y. F., Cao, J. J., Pu, S. Y., Ho, W. K., & Lee, S. C. (2019). Protonated g-C3N4/Ti( )(3+)self-doped TiO2 nanocomposite films: Room-temperature preparation, hydrophilicity, and application for photocatalytic NOx removal. *Applied Catalysis B-Environmental*, *240*, 122-131. https://doi.org/10.1016/j.apcatb.2018.08.078

Huang, Z. a., Sun, Q., Lv, K., Zhang, Z., Li, M., & Li, B. (2015). Effect of contact interface between TiO2 and g-C3N4 on the photoreactivity of g-C3N4/TiO2 photocatalyst: (0 0 1) vs (1 0 1) facets of TiO2. *Applied Catalysis B: Environmental*, *164*, 420-427. https://doi.org/10.1016/j.apcatb.2014.09.043

Humayun, M., Raziq, F., Khan, A., & Luo, W. (2018). Modification strategies of TiO2 for potential applications in photocatalysis: a critical review. *Green Chemistry Letters and Reviews*, *11*(2), 86-102.

Hussain, S., Awad, J., Sarkar, B., Chow, C. W. K., Duan, J., & van Leeuwen, J. (2019). Coagulation of dissolved organic matter in surface water by novel titanium (III) chloride: Mechanistic surface chemical and spectroscopic characterisation. *Separation and Purification Technology*, *213*, 213-223. https://doi.org/10.1016/j.seppur.2018.12.038

ISO. (2009). ISO 679: 2009: Cement test methods–Determination of strength. In: ISO Geneva, Switzerland.

ISO. (2016). 22197-1: Fine Ceramics (Advanced Ceramics, Advanced Technical Ceramics)—Test Method for air-purification Performance of Semiconducting Photocatalytic Materials—Part 1: Removal of Nitric Oxide. In *ISO: Geneva, Switzerland* (pp. 13). Switzerland.

ISO. (2018). 17168-1: Fine ceramics (advanced ceramics, advanced technical ceramics) — Test method for air-purification performance of semiconducting photocatalytic materials under indoor lighting environment — Part 1: Removal of nitric oxide. *ISO: Geneva, Switzerland*.

Jarvis, P., Jefferson, B., Gregory, J., & Parsons, S. A. (2005). A review of floc strength and breakage. *Water Res*, *39*(14), 3121-3137. https://doi.org/10.1016/j.watres.2005.05.022

Jarvis, P., Sharp, E., Pidou, M., Molinder, R., Parsons, S. A., & Jefferson, B. (2012). Comparison of coagulation performance and floc properties using a novel zirconium coagulant against traditional ferric and alum coagulants. *Water Research*, *46*(13), 4179-4187. https://www.sciencedirect.com/science/article/abs/pii/S004313541200303X?via%3Dihub

Jeon, K.-J., & Ahn, J.-H. (2018). Evaluation of titanium tetrachloride and polytitanium tetrachloride to remove phosphorus from wastewater. *Separation and Purification Technology*, *197*, 197-201. https://doi.org/10.1016/j.seppur.2018.01.016

Jeon, K. J., Kim, J. H., & Ahn, J. H. (2017). Phosphorus Removal Characteristics of Titanium Salts Compared with Aluminum Salt. *Water Environ Res*, *89*(8), 739-743. https://doi.org/10.2175/106143017X14839994522902

Jiang, G., Cao, J., Chen, M., Zhang, X., & Dong, F. (2018). Photocatalytic NO oxidation on N-doped TiO2/g-C3N4 heterojunction: Enhanced efficiency, mechanism and reaction pathway. *Applied Surface Science*, *458*, 77-85. https://doi.org/10.1016/j.apsusc.2018.07.087

Jiang, J. Q., & Kim, C. G. (2008). Comparison of Algal Removal by Coagulation with Clays and Al-based Coagulants. *Separation Science and Technology*, *43*(7), 1677-1686. https://doi.org/10.1080/01496390801973615

Jo, Y. K., Lee, J. M., Son, S., & Hwang, S.-J. (2019). 2D inorganic nanosheet-based hybrid photocatalysts: Design, applications, and perspectives [Review]. *Journal of Photochemistry and Photobiology C: Photochemistry Reviews*, *40*, 150-190. https://doi.org/10.1016/j.jphotochemrev.2018.03.002

Kandi, D., Martha, S., & Parida, K. M. (2017). Quantum dots as enhancer in photocatalytic hydrogen evolution: A review [Review]. *International Journal of Hydrogen Energy*, *42*(15), 9467-9481. https://doi.org/10.1016/j.ijhydene.2017.02.166

Kaneko, M., & Okura, I. (2002). *Photocatalysis: science and technology*. Springer.

Karafas, E. S., Romanias, M. N., Stefanopoulos, V., Binas, V., Zachopoulos, A., Kiriakidis, G., & Papagiannakopoulos, P. (2019). Effect of metal doped and co-doped TiO_2 photocatalysts oriented to degrade indoor/outdoor pollutants for air quality improvement. A kinetic and product study using acetaldehyde as probe molecule. *Journal of Photochemistry and Photobiology A: Chemistry*, *371*, 255-263. https://doi.org/10.1016/j.jphotochem.2018.11.023

Karapati, S., Giannakopoulou, T., Todorova, N., Boukos, N., Antiohos, S., Papageorgiou, D., Chaniotakis, E., Dimotikali, D., & Trapalis, C. (2014). TiO_2 functionalization for efficient

NO_x removal in photoactive cement. *Applied Surface Science*, *319*, 29-36. https://doi.org/10.1016/j.apsusc.2014.07.162

Kasuga, T., Hiramatsu, M., Hoson, A., Sekino, T., & Niihara, K. (1998). Formation of titanium oxide nanotube. *Langmuir*, *14*(12), 3160-3163.

Kim, J.-H., Cho, D. L., Kim, G.-J., Gao, B., & Shon, H. K. (2011). Titania Nanomaterials Produced from Ti-Salt Flocculated Sludge in Water Treatment. *Catalysis Surveys from Asia*, *15*(2), 117-126. https://doi.org/10.1007/s10563-011-9115-y

Kim, J. B., Lee, K. W., Park, S. M., Shon, H. K., Shahid, M., El Saliby, I., Lee, W. E., Kim, G. J., & Kim, J. H. (2013). Preparation of iron-doped titania from flocculated sludge with iron-titanium composite coagulant. *J Nanosci Nanotechnol*, *13*(6), 4106-4109. https://doi.org/10.1166/jnn.2013.7017

Kim, J. B., Park, H. J., Shon, H. K., Cho, D. L., Kim, G. J., Choi, S. W., & Kim, J. H. (2010). Preparation of TiO2 nanoparticle from Ti-salt flocculated sludge with dye wastewater. *J Nanosci Nanotechnol*, *10*(5), 3260-3265. https://doi.org/10.1166/jnn.2010.2316

Kim, J. B., Seol, D.-H., Shon, H. K., Kim, G.-J., & Kim, J.-H. (2010). Preparation and Characterization of Titania Nanoparticles from Titanium Tetrachloride and Titanium Sulfate Flocculation of Dye Wastewater. *Journal of the Japan Petroleum Institute*, *53*(3), 167-172. https://doi.org/10.1627/jpi.53.167

Kim, J. H., Cho, D. L., Kim, G. J., Gao, B., & Shon, H. K. (2011). Titania nanomaterials produced from Ti-salt flocculated sludge in water treatment. *Catalysis Surveys from Asia*, *15*(2), 117-126. https://doi.org/10.1007/s10563-011-9115-y

Kim, T.-H., Rodríguez-González, V., Gyawali, G., Cho, S.-H., Sekino, T., & Lee, S.-W. (2013). Synthesis of solar light responsive Fe, N co-doped TiO2 photocatalyst by sonochemical method. *Catalysis Today*, *212*, 75-80. https://doi.org/10.1016/j.cattod.2012.09.014

Kim, Y. K., Hong, S. J., Kim, H. B., & Lee, S. W. (2017). Evaluation of In-Situ NOx Removal Efficiency of Photocatalytic Concrete in Expressways. *KSCE Journal of Civil Engineering*, *22*(7), 2274-2280. https://doi.org/10.1007/s12205-017-0028-9

Knauss, K. G., Dibley, M. J., Bourcier, W. L., & Shaw, H. F. (2001). Ti (IV) hydrolysis constants derived from rutile solubility measurements made from 100 to 300 C. *Applied Geochemistry*, *16*(9-10), 1115-1128.

Kobayakawa, K., Murakami, Y., & Sato, Y. (2005). Visible-light active N-doped TiO2 prepared by heating of titanium hydroxide and urea. *Journal of Photochemistry and Photobiology A: Chemistry*, *170*(2), 177-179. https://doi.org/10.1016/j.jphotochem.2004.07.010

Kočí, K., Reli, M., Troppová, I., Šihor, M., Kupková, J., Kustrowski, P., & Praus, P. (2017). Photocatalytic decomposition of N2O over TiO2/g-C3N4 photocatalysts heterojunction. *Applied Surface Science*, *396*, 1685-1695. https://doi.org/10.1016/j.apsusc.2016.11.242

Kumar, S., Karthikeyan, S., & Lee, A. (2018). g-C3N4-Based Nanomaterials for Visible Light-Driven Photocatalysis [Review]. *Catalysts*, *8*(2), 47, Article 74. https://doi.org/10.3390/catal8020074

Kumar, S., Karthikeyan, S., & Lee, A. F. (2018). g-C3N4-Based Nanomaterials for Visible Light-Driven Photocatalysis [Review]. *Catalysts*, *8*(2), 47, Article 74. https://doi.org/10.3390/catal8020074

Lee, B. C., Kim, S., Shon, H. K., Vigneswaran, S., Kim, S. D., Cho, J., Kim, I. S., Choi, K. H., Kim, J. B., Park, H. J., & Kim, J. H. (2008). Aquatic toxicity evaluation of TiO2 nanoparticle produced from sludge of TiCl4 flocculation of wastewater and sea water. *Journal of Nanoparticle Research*, *11*(8), 2087-2096. https://doi.org/10.1007/s11051-008-9574-x

Lei, J., Chen, Y., Shen, F., Wang, L., Liu, Y., & Zhang, J. (2015). Surface modification of TiO2 with g-C3N4 for enhanced UV and visible photocatalytic activity. *Journal of Alloys and Compounds*, *631*, 328-334. https://doi.org/10.1016/j.jallcom.2015.01.080

Lei, J., Chen, Y., Wang, L., Liu, Y., & Zhang, J. (2015). Highly condensed g-C3N4-modified TiO2 catalysts with enhanced photodegradation performance toward acid orange 7. *Journal of Materials Science*, *50*(9), 3467-3476. https://doi.org/10.1007/s10853-015-8906-3

Li, C., Lou, Z., Yang, Y., Wang, Y., Lu, Y., Ye, Z., & Zhu, L. (2019). Hollowsphere Nanoheterojunction of g-C3N4@TiO2 with High Visible Light Photocatalytic Property. *Langmuir*, *35*(3), 779-786. https://doi.org/10.1021/acs.langmuir.8b03867

Li, C., Sun, Z., Xue, Y., Yao, G., & Zheng, S. (2016). A facile synthesis of g-C3N4/TiO2 hybrid photocatalysts by sol–gel method and its enhanced photodegradation towards methylene blue under visible light. *Advanced Powder Technology*, *27*(2), 330-337. https://doi.org/10.1016/j.apt.2016.01.003

Li, F., Jiang, J.-Q., Wu, S., & Zhang, B. (2010). Preparation and performance of a high purity poly-aluminum chloride. *Chemical Engineering Journal*, *156*(1), 64-69. https://doi.org/10.1016/j.cej.2009.09.034

Li, G., Nie, X., Chen, J., Jiang, Q., An, T., Wong, P. K., Zhang, H., Zhao, H., & Yamashita, H. (2015). Enhanced visible-light-driven photocatalytic inactivation of Escherichia coli using g-C3N4/TiO2 hybrid photocatalyst synthesized using a hydrothermal-calcination approach. *Water Res*, *86*, 17-24. https://doi.org/10.1016/j.watres.2015.05.053

Li, H., Zhou, L., Wang, L., Liu, Y., Lei, J., & Zhang, J. (2015). In situ growth of TiO2 nanocrystals on g-C3N4 for enhanced photocatalytic performance. *Phys Chem Chem Phys*, *17*(26), 17406-17412. https://doi.org/10.1039/c5cp02554k

Li, J., Ma, W., Chen, C., Zhao, J., Zhu, H., & Gao, X. (2007). Photodegradation of dye pollutants on one-dimensional TiO2 nanoparticles under UV and visible irradiation. *Journal of Molecular Catalysis A: Chemical*, *261*(1), 131-138. https://doi.org/10.1016/j.molcata.2006.08.018

Li, K., Gao, S., Wang, Q., Xu, H., Wang, Z., Huang, B., Dai, Y., & Lu, J. (2015). In-Situ-Reduced Synthesis of Ti(3)(+) Self-Doped TiO(2)/g-C(3)N(4) Heterojunctions with High Photocatalytic Performance under LED Light Irradiation. *ACS Appl Mater Interfaces*, *7*(17), 9023-9030. https://doi.org/10.1021/am508505n

Li, T., Zhu, Z., Wang, D., Yao, C., & Tang, H. (2006). Characterization of floc size, strength and structure under various coagulation mechanisms. *Powder technology*, *168*(2), 104-110.

Li, Y., Peng, S., Jiang, F., Lu, G., & Li, S. (2007). Effect of doping TiO_2 with alkaline-earth metal ions on its photocatalytic activity. *Journal of the Serbian Chemical Society*, *72*, 393-402.

Li, Y., Sun, Y., Ho, W., Zhang, Y., Huang, H., Cai, Q., & Dong, F. (2018). Highly enhanced visible-light photocatalytic NO x purification and conversion pathway on self-structurally modified g-C 3 N 4 nanosheets. *Science Bulletin*, *63*(10), 609-620. https://doi.org/10.1016/j.scib.2018.04.009

Liao, L., & Zhang, P. (2018). Preparation and Characterization of Polyaluminum Titanium Silicate and its Performance in the Treatment of Low-Turbidity Water. *Processes*, *6*(8). https://doi.org/10.3390/pr6080125

Liao, S. C., Mayo, W. E., & Pae, K. D. (1997). Theory of high pressure/low temperature sintering of bulk nanocrystalline TiO2. *Acta Materialia*, *45*(10), 4027-4040. https://doi.org/10.1016/s1359-6454(97)00087-6

Liberti, A., Chiantella, V., & Corigliano, F. (1963). Mononuclear hydrolysis of titanium (IV) from partition equilibria. *Journal of Inorganic and Nuclear Chemistry*, *25*(4), 415-427.

Lin, W., Xie, X., Wang, X., Wang, Y., Segets, D., & Sun, J. (2018). Efficient adsorption and sustainable degradation of gaseous acetaldehyde and o-xylene using rGO-TiO_2 photocatalyst. *Chemical Engineering Journal*, *349*, 708-718. https://doi.org/10.1016/j.cej.2018.05.107

Lisowski, P., Colmenares, J. C., Mašek, O., Lisowski, W., Lisovytskiy, ., Kamińska, A., & Łomot, . (2017). ual Functionality of TiO2/Biochar Hybrid Materials: Photocatalytic Phenol Degradation in the Liquid Phase and Selective Oxidation of Methanol in the Gas Phase. *ACS Sustainable Chemistry & Engineering*, *5*(7), 6274-6287. https://doi.org/10.1021/acssuschemeng.7b01251

Liu, C., Wang, J., Cao, Z., Chen, W., & Bi, H. (2016). Variation of dissolved organic nitrogen concentration during the ultrasonic pretreatment to *Microcystis aeruginosa*. *Ultrason Sonochem*, *29*, 236-243. https://doi.org/10.1016/j.ultsonch.2015.09.017

Liu, C., Zhang, L., Liu, R., Gao, Z., Yang, X., Tu, Z., Yang, F., Ye, Z., Cui, L., Xu, C., & Li, Y. (2016). Hydrothermal synthesis of N-doped TiO 2 nanowires and N-doped graphene heterostructures with enhanced photocatalytic properties. *Journal of Alloys and Compounds*, *656*, 24-32. https://doi.org/10.1016/j.jallcom.2015.09.211

Liu, H., Xia, T., Shon, H. K., & Vigneswaran, S. (2011). Preparation of titania-containing photocatalysts from metallurgical slag waste and photodegradation of 2,4-dichlorophenol. *Journal of Industrial and Engineering Chemistry*, *17*(3), 461-467. https://doi.org/10.1016/j.jiec.2010.10.029

Liu, H., Yu, D., Sun, T., Du, H., Jiang, W., Muhammad, Y., & Huang, L. (2019). Fabrication of surface alkalinized g-C3N4 and TiO2 composite for the synergistic adsorption-photocatalytic degradation of methylene blue. *Applied Surface Science*, *473*, 855-863. https://doi.org/10.1016/j.apsusc.2018.12.162

Liu, H., Yu, D. Q., Sun, T. B., Du, H. Y., Jiang, W. T., Muhammad, Y., & Huang, L. (2019). Fabrication of surface alkalinized g-C3N4 and TiO2 composite for the synergistic adsorption-photocatalytic degradation of methylene blue. *Applied Surface Science*, *473*, 855-863. https://doi.org/10.1016/j.apsusc.2018.12.162

Liu, L., Chu, X., Chen, P., Xiao, Y., & Hu, J. (2016). Effects of water quality on inactivation and repair of *Microcystis viridis* and *Tetraselmis suecica* following medium-pressure UV irradiation. *Chemosphere*, *163*, 209-216. https://doi.org/10.1016/j.chemosphere.2016.08.027

Liu, Y., Hu, D., Min, Z., & Liu, S. (2014). *Synthesis of Calcium Doped TiO2 Nanomaterials and Their Visible Light Degradation Property* Proceedings of the International Conference on Material and Environmental Engineering (ICMAEE 2014), https://download.atlantis-press.com/article/11451.pdf

Liu, Z., Wei, H., Li, A., & Yang, H. (2019). Enhanced coagulation of low-turbidity micro-polluted surface water: Properties and optimization. *J Environ Manage*, *233*, 739-747. https://doi.org/10.1016/j.jenvman.2018.08.101

Lobanov, F., Savostina, V., Serzhenko, L., & Peshkova, V. (1969). Distribution Study of Complex Formation by Titanium (IV) with Thenoyltrifluoroacetonate and Hydroxide Ions. *Russ. J. Inorg. Chem*, *14*, 562-565.

Lokshin, E., & Belikov, M. (2003). Water purification with titanium compounds to remove fluoride ions. *Russian journal of applied chemistry*, *76*(9), 1466-1471.

Lu, J., Wang, Y., Huang, J., Fei, J., Cao, L., & Li, C. (2017). In situ synthesis of mesoporous C-doped TiO2 single crystal with oxygen vacancy and its enhanced sunlight photocatalytic properties. *Dyes and Pigments*, *144*, 203-211.

Lu, X., Wang, Q., & Cui, D. (2010). Preparation and Photocatalytic Properties of g-C3N4/TiO2 Hybrid Composite. *Journal of Materials Science & Technology*, *26*(10), 925-930. https://doi.org/10.1016/s1005-0302(10)60149-1

Lu, X., Xu, Y., Sun, W., Sun, Y., & Zheng, H. (2017). UV-initiated synthesis of a novel chitosan-based flocculant with high flocculation efficiency for algal removal. *Sci Total Environ*, *609*, 410-418. https://doi.org/10.1016/j.scitotenv.2017.07.192

Ma, J., & Liu, W. (2002). Effectiveness and mechanism of potassium ferrate(VI) preoxidation for algae removal by coagulation. *Water Res*, *36*(4), 871-878. https://doi.org/10.1016/s0043-1354(01)00282-2

Ma, J., Tan, X., Yu, T., & Li, X. (2016). Fabrication of g-C3N4/TiO2 hierarchical spheres with reactive {001} TiO2 crystal facets and its visible-light photocatalytic activity. *International Journal of Hydrogen Energy*, *41*(6), 3877-3887. https://doi.org/10.1016/j.ijhydene.2015.12.191

Ma, J., Wang, C., & He, H. (2016). Enhanced photocatalytic oxidation of NO over g-C3N4-TiO2 under UV and visible light. *Applied Catalysis B: Environmental*, *184*, 28-34. https://doi.org/10.1016/j.apcatb.2015.11.013

Ma, L., Wang, G., Jiang, C., Bao, H., & Xu, Q. (2018). Synthesis of core-shell TiO 2 @g-C 3 N 4 hollow microspheres for efficient photocatalytic degradation of rhodamine B under

visible light. *Applied Surface Science*, *430*, 263-272. https://doi.org/10.1016/j.apsusc.2017.07.282

Maggos, T., Plassais, A., Bartzis, J. G., Vasilakos, C., Moussiopoulos, N., & Bonafous, L. (2008). Photocatalytic degradation of NO_x in a pilot street canyon configuration using TiO_2-mortar panels. *Environ Monit Assess*, *136*(1-3), 35-44. https://doi.org/10.1007/s10661-007-9722-2

Mamaghani, A. H., Haghighat, F., & Lee, C.-S. (2017). Photocatalytic oxidation technology for indoor environment air purification: The state-of-the-art. *Applied Catalysis B: Environmental*, *203*, 247-269. https://doi.org/10.1016/j.apcatb.2016.10.037

Martinez-Oviedo, A., Ray, S. K., Nguyen, H. P., & Lee, S. W. (2019). Efficient photo-oxidation of NO_x by Sn doped blue TiO_2 nanoparticles. *Journal of Photochemistry and Photobiology A: Chemistry*, *370*, 18-25. https://doi.org/10.1016/j.jphotochem.2018.10.032

Matilainen, A., Vepsalainen, M., & Sillanpaa, M. (2010). Natural organic matter removal by coagulation during drinking water treatment: a review. *Advances in Colloid and Interface Science*, *159*(2), 189-197. https://doi.org/10.1016/j.cis.2010.06.007

McConnell, R., Islam, T., Shankardass, K., Jerrett, M., Lurmann, F., Gilliland, F., Gauderman, J., Avol, E., Kunzli, N., Yao, L., Peters, J., & Berhane, K. (2010). Childhood incident asthma and traffic-related air pollution at home and school. *Environ Health Perspect*, *118*(7), 1021-1026. https://doi.org/10.1289/ehp.0901232

McKay, R. B. (1994). *Technological applications of dispersions* (Vol. 52). CRC Press.

McManamon, C., O'Connell, J., Delaney, P., Rasappa, S., Holmes, J. D., & Morris, M. A. (2015). A facile route to synthesis of S-doped TiO2 nanoparticles for photocatalytic activity. *Journal of Molecular Catalysis A: Chemical*, *406*, 51-57.

Mian, M. M., & Liu, G. (2019). Sewage sludge-derived TiO_2/Fe/Fe_3C-biochar composite as an efficient heterogeneous catalyst for degradation of methylene blue. *Chemosphere*, *215*, 101-114. https://doi.org/10.1016/j.chemosphere.2018.10.027

Mian, M. M., & Liu, G. J. (2019). Sewage sludge-derived TiO_2/Fe/Fe_3C-biochar composite as an efficient heterogeneous catalyst for degradation of methylene blue. *Chemosphere*, *215*, 101-114. https://doi.org/10.1016/j.chemosphere.2018.10.027

Na, S.-H., Shon, H. K., Kim, J. B., Park, H. J., & Kim, J.-H. (2011). Preparation and characterization of titania nanoparticle produced from Ti-flocculated sludge with paper mill wastewater. *Journal of Industrial and Engineering Chemistry*, *17*(2), 277-281. https://doi.org/10.1016/j.jiec.2011.02.022

Na, S. H., Shon, H. K., Kim, J. B., Park, H. J., Cho, D. L., Saliby, I. E., & Kim, J. H. (2010). Recycling of excess sludge using titanium tetrachloride ($TiCl_4$) as a flocculant aid with alkaline-thermal hydrolysis. *Journal of Industrial and Engineering Chemistry*, *16*(1), 96-100. https://doi.org/10.1016/j.jiec.2010.01.013

Naceradska, J., Novotna, K., Cermakova, L., Cajthaml, T., & Pivokonsky, M. (2019). Investigating the coagulation of non-proteinaceous algal organic matter: Optimizing coagulation performance and identification of removal mechanisms. *J Environ Sci (China)*, *79*, 25-34. https://doi.org/10.1016/j.jes.2018.09.024

Naseri, A., Samadi, M., Pourjavadi, A., Moshfegh, A. Z., & Ramakrishna, S. (2017). Graphitic carbon nitride (g-C3N4)-based photocatalysts for solar hydrogen generation: recent advances and future development directions [Review]. *Journal of Materials Chemistry A*, *5*(45), 23406-23433. https://doi.org/10.1039/c7ta05131j

Nasirian, M., Lin, Y., Bustillo-Lecompte, C., & Mehrvar, M. (2018). Enhancement of photocatalytic activity of titanium dioxide using non-metal doping methods under visible light: A review. *International Journal of Environmental Science and Technology*, *15*(9), 2009-2032.

Nasirian, M., Lin, Y. P., Bustillo-Lecompte, C. F., & Mehrvar, M. (2017). Enhancement of photocatalytic activity of titanium dioxide using non-metal doping methods under visible light: a review. *International Journal of Environmental Science and Technology*, *15*(9), 2009-2032. https://doi.org/10.1007/s13762-017-1618-2

Nasirian, M., & Mehrvar, M. (2016). Modification of TiO2 to enhance photocatalytic degradation of organics in aqueous solutions. *Journal of environmental chemical engineering*, *4*(4), 4072-4082.

Nolan, N. T., Synnott, D. W., Seery, M. K., Hinder, S. J., Van Wassenhoven, A., & Pillai, S. C. (2012). Effect of N-doping on the photocatalytic activity of sol-gel TiO2. *J Hazard Mater*, *211-212*, 88-94. https://doi.org/10.1016/j.jhazmat.2011.08.074

Noman, M. T., Ashraf, M. A., & Ali, A. (2019a). Synthesis and applications of nano-TiO2: a review. *Environ Sci Pollut Res Int*, *26*(4), 3262-3291. https://doi.org/10.1007/s11356-018-3884-z

Noman, M. T., Ashraf, M. A., & Ali, A. (2019b). Synthesis and applications of nano-TiO 2: a review. *Environ Sci Pollut Res Int*, *26*, 1-30.

Ohama, Y., & Van Gemert, D. (2011). *Applications of Titanium Dioxide Photocatalysis to Construction Materials* (Vol. 5). Springer. https://doi.org/10.1007/978-94-007-1297-3

Okour, Y., El Saliby, I., Shon, H. K., Vigneswaran, S., Kim, J. H., Cho, J., & Kim, I. S. (2009). Recovery of sludge produced from Ti-salt flocculation as pretreatment to seawater reverse osmosis. *Desalination*, *247*(1-3), 53-63. https://doi.org/10.1016/j.desal.2008.12.012

Okour, Y., Shon, H. K., & El Saliby, I. (2009). Characterisation of titanium tetrachloride and titanium sulfate flocculation in wastewater treatment. *Water Sci Technol*, *59*(12), 2463-2473. https://doi.org/10.2166/wst.2009.254

Okour, Y., Shon, H. K., El Saliby, I. J., Naidu, R., Kim, J. B., & Kim, J. H. (2010). Preparation and characterisation of titanium dioxide (TiO2) and thiourea-doped titanate nanotubes prepared from wastewater flocculated sludge. *Bioresour Technol*, *101*(5), 1453-1458. https://doi.org/10.1016/j.biortech.2009.06.096

Okour, Y., Shon, H. K., Liu, H., Kim, J. B., & Kim, J. H. (2011). Seasonal variation in the properties of titania photocatalysts produced from Ti-salt flocculated bioresource sludge. *Bioresour Technol*, *102*(9), 5545-5549. https://doi.org/10.1016/j.biortech.2010.11.060

Ong, W.-J. (2017). 2D/2D Graphitic Carbon Nitride (g-C3N4) Heterojunction Nanocomposites for Photocatalysis: Why Does Face-to-Face Interface Matter? [Review]. *Frontiers in Materials*, *4*, 10, Article Unsp 11. https://doi.org/10.3389/fmats.2017.00011

Oskooei, A. B., Koohsorkhi, J., & Mehrpooya, M. (2019). Simulation of plasma-assisted catalytic reduction of NOx, CO, and HC from diesel engine exhaust with COMSOL. *Chemical Engineering Science*, *197*, 135-149. https://doi.org/10.1016/j.ces.2018.12.009

Pan, J., Dong, Z., Wang, B., Jiang, Z., Zhao, C., Wang, J., Song, C., Zheng, Y., & Li, C. (2019). The enhancement of photocatalytic hydrogen production via Ti3+ self-doping black TiO2/g-C3N4 hollow core-shell nano-heterojunction. *Applied Catalysis B: Environmental*, *242*, 92-99. https://doi.org/10.1016/j.apcatb.2018.09.079

Pan, J. H., Zhao, X. S., & Lee, W. I. (2011). Block copolymer-templated synthesis of highly organized mesoporous TiO2-based films and their photoelectrochemical applications. *Chemical Engineering Journal*, *170*(2-3), 363-380. https://doi.org/10.1016/j.cej.2010.11.040

Papailias, I., Todorova, N., Giannakopoulou, T., Yu, J., Dimotikali, D., & Trapalis, C. (2017). Photocatalytic activity of modified g-C 3 N 4 /TiO 2 nanocomposites for NOx removal. *Catalysis Today*, *280*, 37-44. https://doi.org/10.1016/j.cattod.2016.06.032

Park, S. M., Chekli, L., Kim, J. B., Shahid, M., Shon, H. K., Kim, P. S., Lee, W.-S., Lee, W. E., & Kim, J.-H. (2014). NO removal of mortar mixed with titania produced from Ti-salt flocculated sludge. *Journal of Industrial and Engineering Chemistry*, *20*(5), 3851-3856. https://doi.org/10.1016/j.jiec.2013.12.090

Pavithra, K. G., P, S. K., V, J., & P, S. R. (2019). Removal of colorants from wastewater: A review on sources and treatment strategies. *Journal of Industrial and Engineering Chemistry*, *75*, 1-19. https://doi.org/10.1016/j.jiec.2019.02.011

Perelshtein, I., Applerot, G., Perkas, N., Grinblat, J., & Gedanken, A. (2012). A one-step process for the antimicrobial finishing of textiles with crystalline TiO2 nanoparticles. *Chemistry*, *18*(15), 4575-4582. https://doi.org/10.1002/chem.201101683

Pérez-Nicolás, M., Navarro-Blasco, I., Fernández, J. M., & Alvarez, J. I. (2017). Atmospheric NO_x removal: Study of cement mortars with iron- and vanadium-doped TiO_2 as visible light–sensitive photocatalysts. *Construction and Building Materials*, *149*, 257-271. https://doi.org/10.1016/j.conbuildmat.2017.05.132

Qian, W., Greaney, P. A., Fowler, S., Chiu, S.-K., Goforth, A. M., & Jiao, J. (2014). Low-Temperature Nitrogen Doping in Ammonia Solution for Production of N-Doped TiO2-Hybridized Graphene as a Highly Efficient Photocatalyst for Water Treatment. *ACS Sustainable Chemistry & Engineering*, *2*(7), 1802-1810. https://doi.org/10.1021/sc5001176

Reddy, P. V. L., Kim, K. H., Kavitha, B., Kumar, V., Raza, N., & Kalagara, S. (2018). Photocatalytic degradation of bisphenol A in aqueous media: A review. *J Environ Manage*, *213*, 189-205. https://doi.org/10.1016/j.jenvman.2018.02.059

Reichwaldt, E. S., & Ghadouani, A. (2012). Effects of rainfall patterns on toxic cyanobacterial blooms in a changing climate: between simplistic scenarios and complex dynamics. *Water Res*, *46*(5), 1372-1393. https://doi.org/10.1016/j.watres.2011.11.052

Renault, F., Sancey, B., Badot, P.-M., & Crini, G. (2009). Chitosan for coagulation/flocculation processes–an eco-friendly approach. *European Polymer Journal*, *45*(5), 1337-1348.

Rhee, I., Lee, J. S., Kim, J. B., & Kim, J. H. (2018). Nitrogen Oxides Mitigation Efficiency of Cementitious Materials Incorporated with TiO(2) [Article]. *Materials (Basel)*, *11*(6), Article 877. https://doi.org/10.3390/ma11060877

Roy, N., Sohn, Y., Leung, K. T., & Pradhan, D. (2014). Engineered electronic states of transition metal doped TiO2 nanocrystals for low overpotential oxygen evolution reaction. *The Journal of Physical Chemistry C*, *118*(51), 29499-29506.

Schwartz-Narbonne, H., Jones, S. H., & Donaldson, D. J. (2019). Indoor Lighting Releases Gas Phase Nitrogen Oxides from Indoor Painted Surfaces. *Environmental Science & Technology Letters*, *6*(2), 92-97. https://doi.org/10.1021/acs.estlett.8b00685

Semerjian, L., & Ayoub, G. (2003). High-pH–magnesium coagulation–flocculation in wastewater treatment. *Advances in Environmental Research*, *7*(2), 389-403.

Sendi, R. K. (2018). Electric and dielectric behaviors of (Ca, Ta)-doped TiO_2 thick film varistor obtained by screen printing. *Results in Physics*, *8*, 758-763. https://doi.org/10.1016/j.rinp.2018.01.012

Seo, D., & Yun, T. S. (2017). NOx removal rate of photocatalytic cementitious materials with TiO 2 in wet condition. *Building and Environment*, *112*, 233-240. https://doi.org/10.1016/j.buildenv.2016.11.037

Seo, G. T., Ohgaki, S., & Suzuki, Y. (1997). Sorption characteristics of biological powdered activated carbon in bpac-mf (biological powdered activated carbon-microfiltration) system for refractory organic removal. *Water Science and Technology*, *35*(7), 163-170. https://doi.org/10.1016/s0273-1223(97)00127-3

Sepehri, A., & Sarrafzadeh, M.-H. (2018). Effect of nitrifiers community on fouling mitigation and nitrification efficiency in a membrane bioreactor. *Chemical Engineering and Processing - Process Intensification*, *128*, 10-18. https://doi.org/10.1016/j.cep.2018.04.006

Shen, J., Yang, H., Shen, Q., Feng, Y., & Cai, Q. (2014). Template-free preparation and properties of mesoporous g-C3N4/TiO2 nanocomposite photocatalyst. *Crystengcomm*, *16*(10), 1868-1872. https://doi.org/10.1039/c3ce42513d

Shen, Q., Zhu, J., Cheng, L., Zhang, J., Zhang, Z., & Xu, X. (2011). Enhanced algae removal by drinking water treatment of chlorination coupled with coagulation. *Desalination*, *271*(1-3), 236-240. https://doi.org/10.1016/j.desal.2010.12.039

Shon, H., Okour, Y., El Saliby, I., Park, J., Cho, D., Kim, J.-B., Park, H.-J., & Kim, J.-H. (2009a). Preparation and Characterisation of Titanium dioxide Produced from Ti-salt Flocculated Sludge in Water Treatment. *Journal of the Korean Industrial and Engineering Chemistry*, *20*(3), 241-250.

Shon, H., Okour, Y., El Saliby, I., Park, J., Cho, D., Kim, J.-B., Park, H.-J., & Kim, J.-H. (2009b). Preparation and characterisation of titanium dioxide produced from Ti-salt flocculated sludge in water treatment. *Journal of the Korean Industrial and Engineering Chemistry*.

Shon, H., Okour, Y., El Saliby, I., Park, J., Cho, D., Kim, J.-B., Park, H.-J., & Kim, J.-H. (2009c). Preparation and characterisation of titanium dioxide produced from Ti-salt flocculated sludge in water treatment. *Journal of the Korean Industrial and Engineering Chemistry*, *11*(5), 1453-1458.

Shon, H., Phuntsho, S., Okour, Y., Cho, D.-L., KK, S., Li, J., Na, S.-H., Kim, J.-B., & Kim, J.-H. (2008a). Visible light responsive titanium dioxide (TiO2). *Journal of the Korean Industrial and Engineering Chemistry*.

Shon, H., Phuntsho, S., Okour, Y., Cho, D.-L., KK, S., Li, J., Na, S.-H., Kim, J.-B., & Kim, J.-H. (2008b). Visible light responsive titanium dioxide (TiO_2). *Journal of the Korean Industrial and Engineering Chemistry*, *19*(1), 1-16.

Shon, H. K., Okour, Y., Park, S. M., Kim, J. B., & Kim, J. H. (2014). Titania produced from Ti-salt flocculated sludge: photocatalytic activity under solar light. *J Nanosci Nanotechnol*, *14*(8), 6386-6389. https://doi.org/10.1166/jnn.2014.8292

Shon, H. K., Vigneswaran, S., Kandasamy, J., Zareie, M. H., Kim, J. B., Cho, D. L., & Kim, J. H. (2009a). Preparation and characterization of titanium dioxide (TiO_2) from sludge produced by $TiCl_4$ flocculation with $FeCl_3$, $Al_2(SO_4)_3$ and $Ca(OH)_2$ coagulant aids in wastewater. *Separation Science and Technology*, *44*(7), 1525-1543. https://doi.org/10.1080/01496390902775810

Shon, H. K., Vigneswaran, S., Kandasamy, J., Zareie, M. H., Kim, J. B., Cho, D. L., & Kim, J. H. (2009b). Preparation and Characterization of Titanium Dioxide (TiO2) from Sludge produced by TiCl4Flocculation with FeCl3, Al2(SO4)3and Ca(OH)2Coagulant Aids in Wastewater. *Separation Science and Technology*, *44*(7), 1525-1543. https://doi.org/10.1080/01496390902775810

Shon, H. K., Vigneswaran, S., Kim, I. S., Cho, J., Kim, G. J., Kim, J. B., & Kim, J. H. (2007a). Preparation of titanium dioxide (TiO_2) from sludge produced by titanium tetrachloride ($TiCl_4$) flocculation of wastewater. *Environ Sci Technol*, *41*(4), 1372-1377. https://doi.org/10.1021/es062062g

Shon, H. K., Vigneswaran, S., Kim, I. S., Cho, J., Kim, G. J., Kim, J. B., & Kim, J. H. (2007b). Preparation of titanium dioxide (TiO_2) from sludge produced by titanium tetrachloride ($TiCl_4$) flocculation of wastewater. *Environmental science & technology*, *41*(4), 1372-1377. https://www.ncbi.nlm.nih.gov/pubmed/17593744

Sillanpaa, M., Ncibi, M. C., Matilainen, A., & Vepsalainen, M. (2018). Removal of natural organic matter in drinking water treatment by coagulation: A comprehensive review. *Chemosphere*, *190*, 54-71. https://doi.org/10.1016/j.chemosphere.2017.09.113

Singh, R., Tripathy, T., Karmakar, G., Rath, S., Karmakar, N., Pandey, S., Kannan, K., Jain, S., & Lan, N. (2000). Novel biodegradable flocculants based on polysaccharides. *CURRENT SCIENCE-BANGALORE-*, *78*(7), 798-803.

Singh, R. P., Pal, S., Krishnamoorthy, S., Adhikary, P., & Ali, S. A. (2009). High-technology materials based on modified polysaccharides. *Pure and Applied Chemistry*, *81*(3), 525-547.

Siwinska-Stefanska, K., Fluder, M., Tylus, W., & Jesionowski, T. (2018). Investigation of amino-grafted TiO2/reduced graphene oxide hybrids as a novel photocatalyst used for decomposition of selected organic dyes. *J Environ Manage*, *212*, 395-404. https://doi.org/10.1016/j.jenvman.2018.02.030

Song, W., Zeng, Y., Wang, Y., Zhang, S., Zhong, Q., Wang, T., & Wang, X. (2019). Photo-induced strong active component-support interaction enhancing NO_x removal performance of CeO_2/TiO_2. *Applied Surface Science*, *476*, 834-839. https://doi.org/10.1016/j.apsusc.2019.01.190

Song, X., Hu, Y., Zheng, M., & Wei, C. (2016). Solvent-free in situ synthesis of g-C 3 N 4 /{0 0 1}TiO 2 composite with enhanced UV- and visible-light photocatalytic activity for NO

oxidation. *Applied Catalysis B: Environmental*, *182*, 587-597. https://doi.org/10.1016/j.apcatb.2015.10.007

Sood, S., Umar, A., Mehta, S. K., & Kansal, S. K. (2015). Highly effective Fe-doped TiO2 nanoparticles photocatalysts for visible-light driven photocatalytic degradation of toxic organic compounds. *Journal of Colloid and Interface Science*, *450*, 213-223. https://www.sciencedirect.com/science/article/abs/pii/S0021979715002775?via%3Dihub

Sugimoto, T., Zhou, X., & Muramatsu, A. (2002). Synthesis of uniform anatase TiO2 nanoparticles by gel-sol method. 1. Solution chemistry of Ti(OH)(4-n)+(n) complexes. *J Colloid Interface Sci*, *252*(2), 339-346. https://doi.org/10.1006/jcis.2002.8454

Sulaiman, S. N. A., Zaky Noh, M., Nadia Adnan, N., Bidin, N., & Ab Razak, S. N. (2018). Effects of photocatalytic activity of metal and non-metal doped Tio2 for Hydrogen production enhancement - A Review. *Journal of Physics: Conference Series*, *1027*, 012006. https://doi.org/10.1088/1742-6596/1027/1/012006

Sun, F., Pei, H.-Y., Hu, W.-R., Li, X.-Q., Ma, C.-X., & Pei, R.-T. (2013). The cell damage of *Microcystis* aeruginosa in PACl coagulation and floc storage processes. *Separation and Purification Technology*, *115*, 123-128. https://doi.org/10.1016/j.seppur.2013.05.004

Sun, Q., Hu, X., Zheng, S., Zhang, J., & Sheng, J. (2019). Effect of calcination on structure and photocatalytic property of N-TiO2/g-C3N4@diatomite hybrid photocatalyst for improving reduction of Cr(). *Environ Pollut*, *245*, 53-62. https://doi.org/10.1016/j.envpol.2018.10.121

Sun, Y., Zhou, G., Xiong, X., Guan, X., Li, L., & Bao, H. (2013). Enhanced arsenite removal from water by Ti(SO4)2 coagulation. *Water Res*, *47*(13), 4340-4348. https://doi.org/10.1016/j.watres.2013.05.028

Tahir, M., & Amin, N. S. (2015). Indium-doped TiO2 nanoparticles for photocatalytic CO2 reduction with H2O vapors to CH4. *Applied Catalysis B: Environmental*, *162*, 98-109.

Tahir, M. B., Sagir, M., & Shahzad, K. (2019). Removal of acetylsalicylate and methyl-theobromine from aqueous environment using nano-photocatalyst WO3-TiO2 @g-C3N4 composite. *J Hazard Mater*, *363*, 205-213. https://doi.org/10.1016/j.jhazmat.2018.09.055

Tan, S., Xing, Z., Zhang, J., Li, Z., Wu, X., Cui, J., Kuang, J., Zhu, Q., & Zhou, W. (2018). Ti3+-TiO2/g-C3N4 mesostructured nanosheets heterojunctions as efficient visible-light-driven photocatalysts. *Journal of Catalysis*, *357*, 90-99. https://doi.org/10.1016/j.jcat.2017.08.006

Tang, X., Zheng, H., Teng, H., Zhao, C., Wang, Y., Xie, W., Chen, W., & Yang, C. (2015). An alternative method for preparation of polyaluminum chloride coagulant using fresh aluminum hydroxide gels: Characterization and coagulation performance. *Chemical Engineering Research and Design*, *104*, 208-217. https://doi.org/10.1016/j.cherd.2015.08.009

Thanh Truc, N. T., Giang Bach, L., Thi Hanh, N., Pham, T. D., Thi Phuong Le Chi, N., Tran, D. T., Nguyen, M. V., & Nguyen, V. N. (2019). The superior photocatalytic activity of Nb doped TiO2/g-C3N4 direct Z-scheme system for efficient conversion of CO2 into valuable fuels. *J Colloid Interface Sci*, *540*, 1-8. https://doi.org/10.1016/j.jcis.2019.01.005

Thomas, A., Fischer, A., Goettmann, F., Antonietti, M., Müller, J.-O., Schlögl, R., & Carlsson, J. M. (2008). Graphitic carbon nitride materials: variation of structure and morphology and their use as metal-free catalysts. *Journal of Materials Chemistry*, *18*(41). https://doi.org/10.1039/b800274f

Thomas, D., Judd, S., & Fawcett, N. (1999). Flocculation modelling: a review. *Water Research*, *33*(7), 1579-1592.

Thomas, M., Bąk, J., & Królikowska, J. (2020). fficiency of titanium salts as alternative coagulants in water and wastewater treatment: short review. *Desalination and Water Treatment*, *208*, 261-272. https://doi.org/10.5004/dwt.2020.26689

Thommes, M., Kaneko, K., Neimark, A. V., Olivier, J. P., Rodriguez-Reinoso, F., Rouquerol, J., & Sing, K. S. W. (2015). Physisorption of gases, with special reference to the evaluation

of surface area and pore size distribution (IUPAC Technical Report). *Pure and Applied Chemistry*, *87*(9-10), 1051-1069. https://doi.org/10.1515/pac-2014-1117

Tripathy, T., & De, B. R. (2006). Flocculation: a new way to treat the waste water.

Troppová, I., Šihor, M., Reli, M., Ritz, M., Praus, P., & Kočí, K. (2018). Unconventionally prepared TiO 2 /g-C 3 N 4 photocatalysts for photocatalytic decomposition of nitrous oxide. *Applied Surface Science*, *430*, 335-347. https://doi.org/10.1016/j.apsusc.2017.06.299

Tsang, C. H. A., Li, K., Zeng, Y., Zhao, W., Zhang, T., Zhan, Y., Xie, R., Leung, D. Y. C., & Huang, H. (2019). Titanium oxide based photocatalytic materials development and their role of in the air pollutants degradation: Overview and forecast. *Environment International*, *125*, 200-228. https://doi.org/10.1016/j.envint.2019.01.015

Upton, W., & Buswell, A. (1937). Titanium salts in water purification. *Industrial & Engineering Chemistry*, *29*(8), 870-871.

Wan, Y., Huang, X., Shi, B., Shi, J., & Hao, H. (2019). Reduction of organic matter and disinfection byproducts formation potential by titanium, aluminum and ferric salts coagulation for micro-polluted source water treatment. *Chemosphere*, *219*, 28-35. https://doi.org/10.1016/j.chemosphere.2018.11.117

Wang, D., Saleh, N. B., Sun, W., Park, C. M., Shen, C., Aich, N., Peijnenburg, W., Zhang, W., Jin, Y., & Su, C. (2019). Next-Generation Multifunctional Carbon-Metal Nanohybrids for Energy and Environmental Applications [Review]. *Environ Sci Technol*, *53*(13), 7265-7287. https://doi.org/10.1021/acs.est.9b01453

Wang, H., Li, J., Ma, C., Guan, Q., Lu, Z., Huo, P., & Yan, Y. (2015). Melamine modified P25 with heating method and enhanced the photocatalytic activity on degradation of ciprofloxacin. *Applied Surface Science*, *329*, 17-22. https://doi.org/10.1016/j.apsusc.2014.12.049

Wang, J., Xu, W., Xu, J., Wei, D., Feng, H., & Xu, Z. (2016). Effect of aluminum speciation and pH on in-line coagulation/diatomite microfiltration process: correlations between aggregate characteristics and membrane fouling. *Journal of Molecular Liquids*, *224*, 492-501.

Wang, W., Fang, J., Shao, S., Lai, M., & Lu, C. (2017). Compact and uniform TiO2@g-C3N4 core-shell quantum heterojunction for photocatalytic degradation of tetracycline antibiotics. *Applied Catalysis B: Environmental*, *217*, 57-64. https://doi.org/10.1016/j.apcatb.2017.05.037

Wang, X.-j., Yang, W.-y., Li, F.-t., Xue, Y.-b., Liu, R.-h., & Hao, Y.-j. (2013). In Situ Microwave-Assisted Synthesis of Porous N-TiO2/g-C3N4 Heterojunctions with Enhanced Visible-Light Photocatalytic Properties. *Industrial & Engineering Chemistry Research*, *52*(48), 17140-17150. https://doi.org/10.1021/ie402820v

Wang, X.-K., Wang, C., Jiang, W.-Q., Guo, W.-L., & Wang, J.-G. (2012). Sonochemical synthesis and characterization of Cl-doped TiO_2 and its application in the photodegradation of phthalate ester under visible light irradiation. *Chemical Engineering Journal*, *189-190*, 288-294. https://doi.org/10.1016/j.cej.2012.02.078

Wang, X., Gan, Y., Guo, S., Ma, X., Xu, M., & Zhang, S. (2018). Advantages of titanium xerogel over titanium tetrachloride and polytitanium tetrachloride in coagulation: A mechanism analysis. *Water Res*, *132*, 350-360. https://doi.org/10.1016/j.watres.2017.12.081

Wang, X., Li, M., Song, X., Chen, Z., Wu, B., & Zhang, S. (2016). Preparation and Evaluation of Titanium-Based Xerogel as a Promising Coagulant for Water/Wastewater Treatment. *Environ Sci Technol*, *50*(17), 9619-9626. https://doi.org/10.1021/acs.est.6b03321

Wang, Y., Duan, J., Li, W., Beecham, S., & Mulcahy, D. (2016). Aqueous arsenite removal by simultaneous ultraviolet photocatalytic oxidation-coagulation of titanium sulfate. *J Hazard Mater*, *303*, 162-170. https://doi.org/10.1016/j.jhazmat.2015.10.021

Wang, Y., Yang, W., Chen, X., Wang, J., & Zhu, Y. (2018). Photocatalytic activity enhancement of core-shell structure g-C3N4@TiO2 via controlled ultrathin g-C3N4 layer. *Applied Catalysis B: Environmental*, *220*, 337-347. https://doi.org/10.1016/j.apcatb.2017.08.004

Wang, Z., Chen, M., Huang, Y., Shi, X., Zhang, Y., Huang, T., Cao, J., Ho, W., & Lee, S. C. (2018). Self-assembly synthesis of boron-doped graphitic carbon nitride hollow tubes for enhanced photocatalytic NOx removal under visible light. *Applied Catalysis B: Environmental*, *239*, 352-361. https://doi.org/10.1016/j.apcatb.2018.08.030

Wang, Z., Huang, Y., Ho, W., Cao, J., Shen, Z., & Lee, S. C. (2016). Fabrication of Bi2O2CO3/g-C3N4 heterojunctions for efficiently photocatalytic NO in air removal: In-situ self-sacrificial synthesis, characterizations and mechanistic study. *Applied Catalysis B: Environmental*, *199*, 123-133. https://doi.org/10.1016/j.apcatb.2016.06.027

Wang, Z., Wang, Y., Yu, C., Zhao, Y., Fan, M., & Gao, B. (2018a). The removal of silver nanoparticle by titanium tetrachloride and modified sodium alginate composite coagulants: floc properties, membrane fouling, and floc recycle. *Environ Sci Pollut Res Int*, *25*(21), 21058-21069. https://doi.org/10.1007/s11356-018-2240-7

Wang, Z., Wang, Y., Yu, C., Zhao, Y., Fan, M., & Gao, B. (2018b). The removal of silver nanoparticle by titanium tetrachloride and modified sodium alginate composite coagulants: floc properties, membrane fouling, and floc recycle. *Environ Sci Pollut Res Int*. https://doi.org/10.1007/s11356-018-2240-7

Wang, Z., Wang, Y., Yu, C., Zhao, Y., Fan, M., & Gao, B. (2018c). The removal of silver nanoparticle by titanium tetrachloride and modified sodium alginate composite coagulants: floc properties, membrane fouling, and floc recycle. *Environmental Science and Pollution Research*. https://doi.org/10.1007/s11356-018-2240-7

Wang, Z., Wang, Y., Yu, C., Zhao, Y., Fan, M., & Gao, B. (2018d). The removal of silver nanoparticle by titanium tetrachloride and modified sodium alginate composite coagulants: floc properties, membrane fouling, and floc recycle. *Environmental Science and Pollution Research*, *25*(21), 21058-21069. https://doi.org/10.1007/s11356-018-2240-7

Wei, J. C., Gao, B. Y., Yue, Q. Y., Wang, Y., & Lu, L. (2009). Performance and mechanism of polyferric-quaternary ammonium salt composite flocculants in treating high organic matter and high alkalinity surface water. *J Hazard Mater*, *165*(1-3), 789-795. https://doi.org/10.1016/j.jhazmat.2008.10.069

Wei, X., Shao, C., Li, X., Lu, N., Wang, K., Zhang, Z., & Liu, Y. (2016). Facile in situ synthesis of plasmonic nanoparticles-decorated g-C3N4/TiO2 heterojunction nanofibers and comparison study of their photosynergistic effects for efficient photocatalytic H2 evolution. *Nanoscale*, *8*(21), 11034-11043. https://doi.org/10.1039/c6nr01491g

Wei, Z., Liang, F., Liu, Y., Luo, W., Wang, J., Yao, W., & Zhu, Y. (2017). Photoelectrocatalytic degradation of phenol-containing wastewater by TiO2/g-C3N4 hybrid heterostructure thin film. *Applied Catalysis B: Environmental*, *201*, 600-606. https://doi.org/10.1016/j.apcatb.2016.09.003

Wesolowski, D. J., & Palmer, D. A. (1994). Aluminum speciation and equilibria in aqueous solution: V. Gibbsite solubility at 50 C and pH 3–9 in 0.1 molal NaCl solutions (a general model for aluminum speciation; analytical methods). *Geochimica et Cosmochimica Acta*, *58*(14), 2947-2969.

Wetchakun, K., Wetchakun, N., & Sakulsermsuk, S. (2019). An overview of solar/visible light-driven heterogeneous photocatalysis for water purification: TiO_2- and ZnO-based photocatalysts used in suspension photoreactors. *Journal of Industrial and Engineering Chemistry*, *71*, 19-49. https://doi.org/10.1016/j.jiec.2018.11.025

Wu, D., Long, M., Cai, W., Chen, C., & Wu, Y. (2010). Low temperature hydrothermal synthesis of N-doped TiO2 photocatalyst with high visible-light activity. *Journal of Alloys and Compounds*, *502*(2), 289-294. https://doi.org/10.1016/j.jallcom.2010.04.189

Wu, M., Zhang, J., Liu, C., Gong, Y., Wang, R., He, B., & Wang, H. (2018). Rational Design and Fabrication of Noble-metal-free NixP Cocatalyst Embedded 3D N-TiO2/g-C3N4 Heterojunctions with Enhanced Photocatalytic Hydrogen Evolution. *Chemcatchem*, *10*(14), 3069-3077. https://doi.org/10.1002/cctc.201800197

Wu, X., Yin, S., Dong, Q., Guo, C., Li, H., Kimura, T., & Sato, T. (2013). Synthesis of high visible light active carbon doped TiO2 photocatalyst by a facile calcination assisted solvothermal method. *Applied Catalysis B: Environmental*, *142*, 450-457.

Xia, X., Lan, S., Li, X., Xie, Y., Liang, Y., Yan, P., Chen, Z., & Xing, Y. (2018). Characterization and coagulation-flocculation performance of a composite flocculant in high-turbidity drinking water treatment. *Chemosphere*, *206*, 701-708. https://doi.org/10.1016/j.chemosphere.2018.04.159

Xia, Y., Xu, L., Peng, J., Han, J., Guo, S., Zhang, L., Han, Z., & Komarneni, S. (2019). TiO2@g-C3N4 core/shell spheres with uniform mesoporous structures for high performance visible-light photocatalytic application. *Ceramics International*, *45*(15), 18844-18851. https://doi.org/10.1016/j.ceramint.2019.06.118

Xiao, M., Luo, B., Wang, S., & Wang, L. (2018). Solar energy conversion on g-C3N4 photocatalyst: Light harvesting, charge separation, and surface kinetics [Review]. *Journal of Energy Chemistry*, *27*(4), 1111-1123. https://doi.org/10.1016/j.jechem.2018.02.018

Xiao, X., Liu, X., Cao, G., Zhang, C., Xia, L., Xu, W., & Xiao, S. (2015). Atomic layer deposition TiO2/Al2O3 nanolayer of dyed polyamide/aramid blend fabric for high intensity UV light protection. *Polymer Engineering & Science*, *55*(6), 1296-1302.

Xu, B., Ahmed, M. B., Zhou, J. L., Altaee, A., Xu, G., & Wu, M. (2018). Graphitic carbon nitride based nanocomposites for the photocatalysis of organic contaminants under visible irradiation: Progress, limitations and future directions [Review]. *Sci Total Environ*, *633*, 546-559. https://doi.org/10.1016/j.scitotenv.2018.03.206

Xu, J., Zhao, Y., Gao, B., & Zhao, Q. (2018). Enhanced algae removal by Ti-based coagulant: comparison with conventional Al- and Fe-based coagulants. *Environ Sci Pollut Res Int*, *25*(13), 13147-13158. https://doi.org/10.1007/s11356-018-1482-8

Xue, X., Cashman, S., Gaglione, A., Mosley, J., Weiss, L., Ma, X. C., Cashdollar, J., & Garland, J. (2019). Holistic Analysis of Urban Water Systems in the Greater Cincinnati Region: (1) Life Cycle Assessment and Cost Implications. *Water Res X*, *2*. https://doi.org/10.1016/j.wroa.2018.100015

Yan, H., & Yang, H. (2011). TiO2–g-C3N4 composite materials for photocatalytic H2 evolution under visible light irradiation. *Journal of Alloys and Compounds*, *509*(4), L26-L29. https://doi.org/10.1016/j.jallcom.2010.09.201

Yang, L., Hakki, A., Zheng, L., Jones, M. R., Wang, F., & Macphee, D. E. (2019). Photocatalytic concrete for NO_x abatement: Supported TiO_2 efficiencies and impacts. *Cement and Concrete Research*, *116*, 57-64. https://doi.org/10.1016/j.cemconres.2018.11.002

Yu, B., Meng, F., Khan, M. W., Qin, R., & Liu, X. (2020). Facile synthesis of AgNPs modified TiO2@g-C3N4 heterojunction composites with enhanced photocatalytic activity under simulated sunlight. *Materials Research Bulletin*, *121*. https://doi.org/10.1016/j.materresbull.2019.110641

Yu, H., Pan, J., Bai, Y., Zong, X., Li, X., & Wang, L. (2013). Hydrothermal synthesis of a crystalline rutile TiO2 nanorod based network for efficient dye-sensitized solar cells. *Chemistry*, *19*(40), 13569-13574. https://doi.org/10.1002/chem.201300999

Yu, J., Wang, S., Low, J., & Xiao, W. (2013). Enhanced photocatalytic performance of direct Z-scheme g-C3N4-TiO2 photocatalysts for the decomposition of formaldehyde in air. *Phys Chem Chem Phys*, *15*(39), 16883-16890. https://doi.org/10.1039/c3cp53131g

Yu, Q. L., Hendrix, Y., Lorencik, S., & Brouwers, H. J. H. (2018). Field study of NO_x degradation by a mineral-based air purifying paint. *Building and Environment*, *142*, 70-82. https://doi.org/10.1016/j.buildenv.2018.06.014

Yuan, N., Zhang, J., Zhang, S., Chen, G., Meng, S., Fan, Y., Zheng, X., & Chen, S. (2020). What Is the Transfer Mechanism of Photoexcited Charge Carriers for g-C3N4/TiO2 Heterojunction Photocatalysts? Verification of the Relative p–n Junction Theory. *The Journal of Physical Chemistry C*, *124*(16), 8561-8575. https://doi.org/10.1021/acs.jpcc.0c00422

Zaleska, A. (2008a). Doped-TiO2: A Review. *Recent Patents on Engineering*, *2*, 157-164. https://doi.org/10.2174/187221208786306289

Zaleska, A. (2008b). Doped-TiO_2: A Review. *Recent Patents on Engineering*, *2*(3), 157-164. https://doi.org/10.2174/187221208786306289

Zang, Y., Li, L., Xu, Y., Zuo, Y., & Li, G. (2014). Hybridization of brookite TiO2 with g-C3N4: a visible-light-driven photocatalyst for As3+ oxidation, MO degradation and water splitting for hydrogen evolution. *J. Mater. Chem. A*, *2*(38), 15774-15780. https://doi.org/10.1039/c4ta02082k

Zhang, B., Wang, Q., Zhuang, J., Guan, S., & Li, B. (2018). Molten salt assisted in-situ synthesis of TiO2/g-C3N4 composites with enhanced visible-light-driven photocatalytic activity and adsorption ability. *Journal of Photochemistry and Photobiology A: Chemistry*, *362*, 1-13. https://doi.org/10.1016/j.jphotochem.2018.05.009

Zhang, L., Jing, D., She, X., Liu, H., Yang, D., Lu, Y., Li, J., Zheng, Z., & Guo, L. (2014). Heterojunctions in g-C3N4/TiO2(B) nanofibres with exposed (001) plane and enhanced visible-light photoactivity. *J. Mater. Chem. A*, *2*(7), 2071-2078. https://doi.org/10.1039/c3ta14047d

Zhang, S., Gu, P., Ma, R., Luo, C., Wen, T., Zhao, G., Cheng, W., & Wang, X. (2019). Recent developments in fabrication and structure regulation of visible-light-driven g-C3N4-based photocatalysts towards water purification: A critical review [Review]. *Catalysis Today*, *335*, 65-77. https://doi.org/10.1016/j.cattod.2018.09.013

Zhang, W., Song, R., Cao, B., Yang, X., Wang, D., Fu, X., & Song, Y. (2018). Variations of floc morphology and extracellular organic matters (EOM) in relation to floc filterability under algae flocculation harvesting using polymeric titanium coagulants (PTCs). *Bioresour Technol*, *256*, 350-357. https://doi.org/10.1016/j.biortech.2018.02.011

Zhang, X., Song, H., Sun, C., Chen, C., Han, F., & Li, X. (2019). Photocatalytic oxidative desulfurization and denitrogenation of fuels over sodium doped graphitic carbon nitride nanosheets under visible light irradiation [Review]. *Materials Chemistry and Physics*, *226*, 34-43. https://doi.org/10.1016/j.matchemphys.2019.01.011

Zhang, Z., Bai, L., Li, Z., Qu, Y., & Jing, L. (2019). Review of strategies for the fabrication of heterojunctional nanocomposites as efficient visible-light catalysts by modulating excited electrons with appropriate thermodynamic energy [Review]. *Journal of Materials Chemistry A*, *7*(18), 10879-10897. https://doi.org/10.1039/c9ta02373a

Zhao, L., Liu, Y., Wang, L., Zhao, H., Chen, D., Zhong, B., Wang, J., & Qi, T. (2013). Production of Rutile TiO2 Pigment from Titanium Slag Obtained by Hydrochloric Acid Leaching of Vanadium-Bearing Titanomagnetite. *Industrial & Engineering Chemistry Research*, *53*(1), 70-77. https://doi.org/10.1021/ie4030598

Zhao, S., Chen, S., Yu, H., & Quan, X. (2012). g-C3N4/TiO2 hybrid photocatalyst with wide absorption wavelength range and effective photogenerated charge separation. *Separation and Purification Technology*, *99*, 50-54. https://doi.org/10.1016/j.seppur.2012.08.024

Zhao, Y.-x., & Li, X.-y. (2019). Polymerized titanium salts for municipal wastewater preliminary treatment followed by further purification via crossflow filtration for water reuse. *Separation and Purification Technology*, *211*, 207-217. https://doi.org/10.1016/j.seppur.2018.09.078

Zhao, Y., Gao, B., Zhang, G., Qi, Q., Wang, Y., Phuntsho, S., Kim, J.-H., Shon, H., Yue, Q., & Li, Q. (2014). Coagulation and sludge recovery using titanium tetrachloride as coagulant for real water treatment: A comparison against traditional aluminum and iron salts. *Separation and Purification Technology*, *130*, 19-27. https://doi.org/10.1016/j.seppur.2014.04.015

Zhao, Y., Phuntsho, S., Gao, B., & Shon, H. (2017). Polytitanium sulfate (PTS): Coagulation application and Ti species detection. *J Environ Sci (China)*, *52*, 250-258. https://doi.org/10.1016/j.jes.2016.04.008

Zhao, Y. X., Gao, B. Y., Cao, B. C., Yang, Z. L., Yue, Q. Y., Shon, H. K., & Kim, J. H. (2011). Comparison of coagulation behavior and floc characteristics of titanium tetrachloride

(TiCl4) and polyaluminum chloride (PACl) with surface water treatment. *Chemical Engineering Journal*, *166*(2), 544-550. https://doi.org/10.1016/j.cej.2010.11.014

Zhao, Y. X., Gao, B. Y., Shon, H. K., Cao, B. C., & Kim, J. H. (2011). Coagulation characteristics of titanium (Ti) salt coagulant compared with aluminum (Al) and iron (Fe) salts. *J Hazard Mater*, *185*(2-3), 1536-1542. https://doi.org/10.1016/j.jhazmat.2010.10.084

Zhao, Y. X., Gao, B. Y., Shon, H. K., Kim, J. H., & Yue, Q. Y. (2011). Effect of shear force, solution pH and breakage period on characteristics of flocs formed by Titanium tetrachloride (TiCl4) and Polyaluminum chloride (PACl) with surface water treatment. *J Hazard Mater*, *187*(1-3), 495-501. https://doi.org/10.1016/j.jhazmat.2011.01.064

Zhao, Y. X., Gao, B. Y., Shon, H. K., Wang, Y., Kim, J. H., & Yue, Q. Y. (2011). The effect of second coagulant dose on the regrowth of flocs formed by charge neutralization and sweep coagulation using titanium tetrachloride (TiCl4). *J Hazard Mater*, *198*, 70-77. https://doi.org/10.1016/j.jhazmat.2011.10.015

Zhao, Y. X., Gao, B. Y., Zhang, G. Z., Phuntsho, S., & Shon, H. K. (2014). Coagulation by titanium tetrachloride for fulvic acid removal: Factors influencing coagulation efficiency and floc characteristics. *Desalination*, *335*(1), 70-77. https://doi.org/10.1016/j.desal.2013.12.016

Zhao, Y. X., Gao, B. Y., Zhang, G. Z., Qi, Q. B., Wang, Y., Phuntsho, S., Kim, J. H., Shon, H. K., Yue, Q. Y., & Li, Q. (2014). Coagulation and sludge recovery using titanium tetrachloride as coagulant for real water treatment: A comparison against traditional aluminum and iron salts. *Separation and Purification Technology*, *130*, 19-27. https://doi.org/10.1016/j.seppur.2014.04.015

Zhao, Y. X., Phuntsho, S., Gao, B. Y., Yang, Y. Z., Kim, J. H., & Shon, H. K. (2015). Comparison of a novel polytitanium chloride coagulant with polyaluminium chloride: coagulation performance and floc characteristics. *J Environ Manage*, *147*, 194-202. https://doi.org/10.1016/j.jenvman.2014.09.023

Zhou, B., Hong, H., Zhang, H., Yu, S., & Tian, H. (2019). Heterostructured Ag/g-C3N4/TiO2 with enhanced visible light photocatalytic performances. *Journal of Chemical Technology & Biotechnology*, *94*(12), 3806-3814. https://doi.org/10.1002/jctb.6105

Zhou, J., Zhang, M., & Zhu, Y. (2015). Photocatalytic enhancement of hybrid C3N4/TiO2 prepared via ball milling method. *Phys Chem Chem Phys*, *17*(5), 3647-3652. https://doi.org/10.1039/c4cp05173d

Zhou, L., Zhang, H. Y., Sun, H. Q., Liu, S. M., Tade, M. O., Wang, S. B., & Jin, W. Q. (2016). Recent advances in non-metal modification of graphitic carbon nitride for photocatalysis: a historic review [Review]. *Catalysis Science & Technology*, *6*(19), 7002-7023. https://doi.org/10.1039/c6cy01195k

Zhou, M., Yu, J., Cheng, B., & Yu, H. (2005). Preparation and photocatalytic activity of Fe-doped mesoporous titanium dioxide nanocrystalline photocatalysts. *Materials Chemistry and Physics*, *93*(1), 159-163.

Zhou, S., Liu, Y., Li, J., Wang, Y., Jiang, G., Zhao, Z., Wang, D., Duan, A., Liu, J., & Wei, Y. (2014). Facile in situ synthesis of graphitic carbon nitride (g-C3N4)-N-TiO2 heterojunction as an efficient photocatalyst for the selective photoreduction of CO2 to CO. *Applied Catalysis B: Environmental*, *158-159*, 20-29. https://doi.org/10.1016/j.apcatb.2014.03.037

Zhou, X., Jin, B., Li, L., Peng, F., Wang, H., Yu, H., & Fang, Y. (2012). A carbon nitride/TiO2 nanotube array heterojunction visible-light photocatalyst: synthesis, characterization, and photoelectrochemical properties. *Journal of Materials Chemistry*, *22*(34). https://doi.org/10.1039/c2jm32686h

Zhu, J., Deng, Z., Chen, F., Zhang, J., Chen, H., Anpo, M., Huang, J., & Zhang, L. (2006). Hydrothermal doping method for preparation of Cr3+-TiO2 photocatalysts with concentration gradient distribution of Cr3+. *Applied Catalysis B: Environmental*, *62*(3-4), 329-335. https://doi.org/10.1016/j.apcatb.2005.08.013

Zong, L., Zhang, J., Lu, G., & Tang, Z. (2018). Controlled Synthesis of TiO2 Shape and Effect on the Catalytic Performance for Selective Catalytic Reduction of NOx with NH3.

Catalysis Surveys from Asia, *22*(2), 105-117. https://doi.org/10.1007/s10563-018-9244-7

Zou, X. X., Li, G. D., Wang, Y. N., Zhao, J., Yan, C., Guo, M. Y., Li, L., & Chen, J. S. (2011). Direct conversion of urea into graphitic carbon nitride over mesoporous TiO2 spheres under mild condition. *Chem Commun (Camb)*, *47*(3), 1066-1068. https://doi.org/10.1039/c0cc03530k